LBL-37348
UC-411

Center for Advanced Materials

CAM

Toward Quantitative STM: Scanning Tunneling Microscopy Study of Structure and Dynamics of Adsorbates on Transition Metal Surfaces

J.C. Dunphy
(Ph.D. Thesis)

May 1995

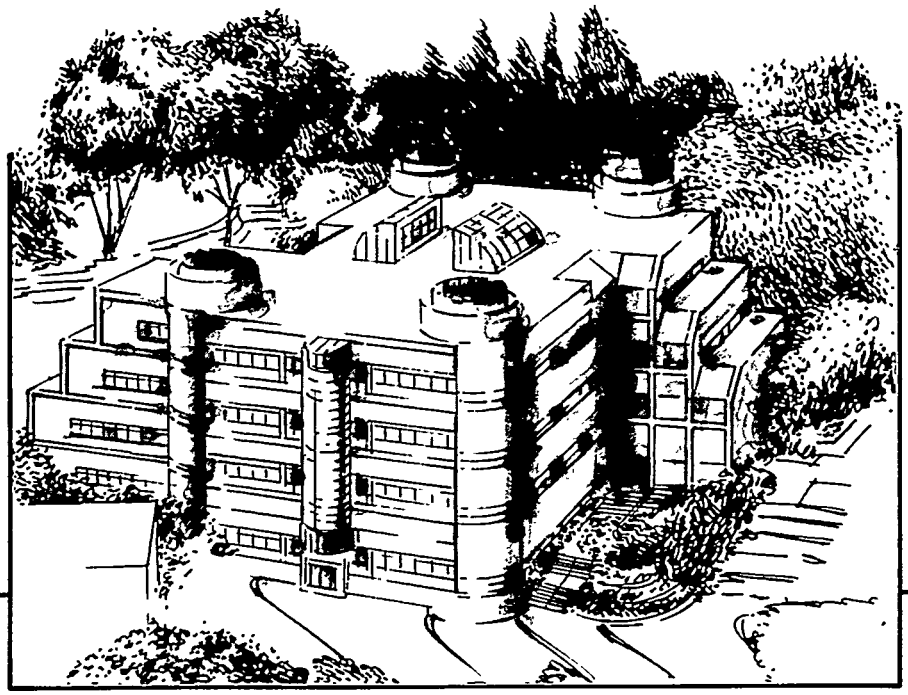

Materials and Chemical Sciences Division

Lawrence Berkeley Laboratory • University of California

ONE CYCLOTRON ROAD, BERKELEY, CA 94720 • (415) 486-4755

Prepared for the U.S. Department of Energy under Contract DE-AC03-76SF00098

LBL-37348
UC-411

Toward Quantitative STM: Scanning Tunneling Microscopy Study of Structure and Dynamics of Adsorbates on Transition Metal Surfaces

James Christopher Dunphy
Ph.D. Thesis

Department of Physics
University of California

and

Materials Sciences Division
Lawrence Berkeley Laboratory
University of California
Berkeley, California 94720

May 1995

This work was supported by the Director, Office of Energy Research, Office of Basic Energy Sciences, Materials Science Division, of the U.S. Department of Energy under Contract No. DE-AC03-76SF00098.

Toward Quantitative STM: Scanning Tunneling Microscopy Study of Structure and Dynamics of Adsorbates on Transition Metal Surfaces

by

James Christopher Dunphy

Toward Quantitative STM: Scanning Tunneling Microscopy Study of Structure and Dynamics of Adsorbates on Transition Metal Surfaces

by

James Christopher Dunphy

B.S. (Massachusetts Institute of Technology) 1989
M.S. (University of California at Berkeley) 1991

A dissertation submitted in partial satisfaction of the
requirements for the degree of
Doctor of Philosophy

in

Physics

in the

GRADUATE DIVISION

of the

UNIVERSITY of CALIFORNIA at BERKELEY

Committee in charge:
Professor Yuen-Ron Shen, Chair
Dr. Miquel B. Salmeron, Co-chair
Professor Gabor A. Somorjai
Professor Seamus Davis

1995

Abstract

Toward Quantitative STM:
Scanning Tunneling Microscopy Study of
Structure and Dynamics of Adsorbates on
Transition Metal Surfaces

by

James Christopher Dunphy

Doctor of Philosophy in Physics

University of California at Berkeley

Professor Yuen-Ron Shen, Chair
Dr. Miquel B. Salmeron, Co-chair

STM was applied to the study of chemisorbed sulfur layers on the Re(0001) and Mo(100) metal surfaces. As a function of coverage on both these surfaces sulfur orders into several different overlayer structures, which have been studied by dynamical LEED. STM images of all of these structures were obtained. The approximate location of the sulfur atoms in the structures was determined by inspection of the images, especially those of regions containing defects. The results are in agreement with those of LEED except for the $p(2x1)$ overlayer of sulfur on Mo(100).

The STM images were compared to calculations made with Electron Scattering Quantum Chemistry (ESQC) theory. The variation of contrast in experimental images is explained as a result of changes in STM tip termination structure. STM image contrast is a result of changes in the interference between different paths for the tunneling electrons. The simplest structure on the Mo(100) surface was used as a model for developing and testing a method of quantitative structure determination with the STM. Experimental STM images acquired under a range of tunneling conditions were compared to theoretical calculations of the images as a function of surface structure to determine the structure which

best fit. The results matched within approximately 0.1 Ångstroms a LEED structural determination.

At lower sulfur coverage the diffusion of sulfur atoms over the Re(0001) surface and the lateral interaction between these atoms were investigated by application of a new image analysis technique. The interaction between the sulfur and a coadsorbed CO layer was also studied, and CO was found to induce compression of the sulfur overlayer. A similar result was found for Au deposited on the sulfur covered Mo(100) surface.

The interaction between steps on the Mo surface was found to be influenced by sulfur adsorption and this observation was interpreted with the theory of equilibrium crystal shape.

Future work in this field can be greatly facilitated with an STM instrument which operates at cryogenic and variable sample temperatures. The design of such an instrument and its potential future applications are described.

Dedicated to my parents,

James F. Dunphy

and Katherine H. Dunphy

Table of Contents

List of Figures

List of Tables

Acknowledgments

I would like to thank my thesis advisor, Dr. Miquel Salmeron, for providing the opportunity to perform research in his group at LBL. His enthusiastic support and advice have made his group an exciting, enjoyable, and productive environment in which to work. I am also thankful to my advisor in the Berkeley physics department, Y.-Ron Shen for his helpful discussions. I would also like to thank Gabor Somorjai, who's enthusiasm first interested me in surface science. He provided many novel ideas and showed me how my research fit into the field of catalysis and surface chemistry.

The value of much of the work described here was greatly multiplied through the collaboration with Philippe Sautet who developed the ESQC STM theory and taught me how to apply it in my research. I owe Philippe many thanks for his friendship and encouragement. Frank Ogletree also deserves thanks for always taking the time to discuss my work, whether scientific results or more mundane technical problems, and to provide excellent advice on either. His great STM data acquisition and analysis software made the experiments possible. Claude Chapelier deserves credit for the design of the cryogenic STM system, but unfortunately had to leave Berkeley before having the satisfaction of seeing it work.

I would also like to acknowledge the help and friendship of the current and many former members of the Salmeron and Somorjai groups who are too numerous all to credit here. I owe Bob Hwang and Dave Zeglinski for their work in constructing the UHV STM system. I would like to thank Julio Gomez for first teaching me the operation of the UHV STM, and who was patient despite the many mistakes I made learning these techniques. I would particularly like to thank those in the STM group I have worked with most closely for their friendship and advice: Brian McIntyre, Heather Galloway, James Batteas, Stefan Behler, and JunFei Zheng.

I also owe many thanks to the excellent technical staff at LBL, including the machine shops in building 62, the plating shop, ceramic shop, and the photolab. Special thanks go to Joe Katz for his help with electronic problems. The cryostat construction was possible only because of the expert work in the physics department machine shop by Alex and George.

This work was supported in part by the Director, Office of Energy Research, Office of Basic Energy Sciences, Materials Science Division of the U.S. Department of Energy under contract no. DE-AC03-76SF00098.

I would also like to acknowledge Peet's coffee without which I'm sure I wouldn't have been as productive.

Chapter 1. INTRODUCTION

The surface is the largest and most important defect in solids which is neglected by the basic theories of solid state physics. These theories are based on a model of solids as infinite crystals, but no real solid can exist without having some of its atoms at the termination of its periodic structure. In macroscopic sized solids fewer than one in a million atoms is adjacent to the surface; thus bulk properties are little effected by its presence. On the other hand, the surface region is responsible for many observable properties of solids: chemical properties, catalytic activity[1], adhesion, friction, work function, and epitaxial growth.[2] The reduced dimensionality at surfaces may modify phenomena such as magnetism[3] and phase transitions with respect to the bulk, resulting in new physics worthy of study. In addition, new techniques have made possible the fabrication of nanoscale devices in which a large fraction of the atoms are in close contact with the surface and thus it may have a significant effect on bulk properties. Thus, surfaces are an important current area of study in solid state physics.

The invention of the Scanning Tunneling Microscopy (STM) in 1981-82 by Binnig and Rohrer[4-6] provided a new approach for the study of surfaces. STM is a particularly exciting and unique technique for probing surfaces. With the exception of Field Ion Microscopy (FIM),[7, 8] all of the dozens of previously available surface sensitive techniques are non-local. In these techniques the surface is probed with electrons, electromagnetic radiation, atoms, or ions, and one of the same is detected at an asymptotically far distance from the surface. The information provided by these techniques represents some macroscopic average over the surface. While some methods provide atomic scale information on the local environment of surface atoms, this information represents an average over a macroscopic region.

In contrast with these methods, STM[9-14] provides local atomic-scale information on both the physical and electronic structure of surfaces of conductors and semiconductors.

STM is much more widely applicable technique than FIM, which is limited to the small number of metals which can be fashioned into a sharp tip and tolerate high electric fields. Unlike most other surface science techniques, STM can work in a wide range of environments besides vacuum. For a number of problems in surface science, STM can provide information only indirectly accessible by other techniques. Because of these unique abilities, the use of this technique has grown exponentially. It is now applied in the fields of physics, surface chemistry, electrochemistry, and biology.

In the experiments described in this thesis the STM technique is applied to study single crystal metal surfaces covered with chemisorbed layers. These surfaces are good models of many real surfaces of interest, such as the active surfaces of catalysts and substrates for epitaxy. On the other hand, they have a simple enough structure for fundamental studies to be carried out. These surfaces are flat on the atomic scale, facilitating STM imaging of single atoms. Because they are highly uniform on a macroscopic scale, their composition and average local order can be characterized by techniques other than STM.

The aim of this work is twofold. First, it is to learn more about specific chemisorption systems of interest, namely sulfur on Re(0001) and Mo(100). Secondly, it is to improve the ability to interpret atomic scale STM images in general by improving the understanding of the mechanisms of contrast in the images and images of non-static surfaces. This portion of the work is quite general and can be adapted to a wide range of other systems. It can be subdivided into two areas, structure and dynamics.

While the STM apparatus is conceptually simple, the system producing the images, the nanoscopic tip-adsorbate-surface region, is quite complex and quantum mechanical in character.[9] Hence, it is still unclear precisely how an STM image represents local surface structure at the atomic scale. At this scale the physical and electronic structure of the surface, which together make up the image, are of nearly equal size and difficult to deconvolve. For this reason, nearly all STM images at this scale are interpreted

qualitatively. For instance, a maximum of a certain size may be associated with an adsorbed atom on the surface. While the quantity and distribution of such features can be easily measured from STM images, it is far from clear why a particular adsorbed atom should appear as a particular shape of feature. Its shape and size certainly carry information about the adsorption site and local structure around the atom. If this information could be interpreted, STM could provide much more information on the local atomic structure of surfaces than is currently possible.

Most STM experiments probe surfaces which are completely static. This is because STM image acquisition takes at least several seconds and changes in the surface structure during this time complicate image interpretation. There are a number of recent exceptions to this in which the surface structure changes due to chemical reactions were followed.[15] However, relatively little work had been done to probe dynamics on surfaces with STM, especially when the dynamics is fast with respect to the imaging time. This thesis includes the development of a method for studying dynamics at this time scale. This method provides a way through statistical mechanics analysis to measure quantitative energies of lateral interactions between adsorbates. Knowledge of these energies is fundamental to the understanding of surface processes governed by kinetics, such as catalysis and epitaxy.[2]

This thesis is organized into three main sections. The first several chapters contain background information on the experiments described later in the thesis and a description of the STM theory used to interpret the some of the results. The final portion briefly describes the construction of a new variable sample temperature STM system and some potential systems for study with it. The bulk of the thesis is the description of experiments on chemisorption systems, their results, and interpretation.

Within the introductory section, the principles underlying the scanning tunneling microscope are described. The experimental details of the preparation and characterization of the surfaces which were studied are discussed. In chapter 4, several widely referenced theories used for explaining and interpreting STM images are outlined, concentrating

specifically on Electron Scattering Quantum Chemistry (ESQC) theory[16, 17], which is used to interpret and explain the experimental results later in this thesis.

Following this preliminary discussion a number of experiments and their results are described. The first few chapters of this portion concentrates on the surface crystallography of the S on Re(0001) and S on Mo(100) systems. For each system a general introduction to the surface crystallography is given, and the results of STM experiments imaging sulfur structures are presented. The approximate surface structure of the sulfur overlayers is determined by a simple qualitative analysis of the images, especially those including defects and antiphase boundaries.

ESQC theory is applied to the simplest sulfur structure on each of these metals. On the Re(0001) system, the results provide insight into the mechanism of contrast in STM images including the influence of the tip on this contrast and the how surface structure affects STM images. In a more detailed theoretical analysis, one structure of sulfur on the Mo(100) surface was used as a model system for the development of a method for quantitative surface structure determination from STM images. In this method, ESQC calculations of STM images are compared with experimental data acquired in a new imaging mode to determine the precise structure of the sulfur overlayer.

The focus then shifts to dynamics on these surfaces. At low density and room temperature sulfur was found to be mobile on Re on the same time scale at which STM images are acquired. A new technique which allows the interactions of the diffusing sulfur atoms to be investigated is described as are the results of the application of this technique. The interaction of a second adsorbate, CO, on the surface with the mobile sulfur was also investigated. This coadsorption system is a good model for metal catalyst surfaces which are usual covered with more than one adsorbate. Coadsorption of gold with the sulfur layers on Mo(100) was also investigated as a potential model buried interface. The influence of sulfur adsorption on the size and distribution of steps on this surface was

studied and analyzed within the framework of the theory of the equilibrium shape of crystal surfaces.

In the final section of the thesis, the future of experiments in this area in discussed. Much more progress can be achieved with a new instrument with improved capabilities, most notably variable and low sample temperature. The design, construction, and initial tests of this instrument are described.

Chapter 1 References

[1] G.A. Somorjai. *Chemistry in Two Dimensions: Surfaces*. (Cornell University Press, Ithaca, 1981).

[2] J.A. Venables, G.D.T. Spiller and M. Handücken, Rep. Prog. Phys. **47** (1984) 399.

[3] L.M. Falicov, D.T. Pierce, S.D. Bader, R. Gronsky, K.B. Hathaway, H.J. Hopster, D.N. Lambeth, S.S.P. Parkin, G. Prinz and M. Salamon, J. Mater. Res. **5** (1990) 1299.

[4] G. Binnig, H. Rohrer, C. Gerber and E. Weibel, Phys. Rev. Lett. **49** (1982) 57.

[5] G. Binnig, H. Rohrer, C. Gerber and E. Weibel, Phys. Rev. Lett. **50** (1983) 120.

[6] G. Binnig, H. Rohrer, C. Gerber and E. Weibel, Appl. Phys. Lett. **40** (1982) 178.

[7] R. Gomer. *Field Emission and Field Ionization*. (Harvard University Press, Cambridge, MA, 1961).

[8] T. Tsong, Rep. Prog. Phys. **51** (1988) 759.

[9] M. Tsukada, K. Kobayashi, N. Isshiki and H. Kageshima, Surf. Sci. Rep. **13** (1991) 265.

[10] J.A. Golovchenko, Science **232** (1986) 48.

[11] P.K. Hansma and J. Tersoff, J. Appl. Phys. **61** (1987) 1.

[12] G. Binnig and H. Rohrer, Rev. Mod. Phys. **59** (1987) 615.

[13] J.E. Dumuth, U.K. Koehler and R.J. Hamers, J. Microsc. **152** (1988) 299.

[14] M. Salmeron and F. Ogletree, Prog. Solid St. Chem. **20** (1990) 235.

[15] L. Ruan, F. Besenbacher, I. Stensgaard and E. Laegsaard, Phys. Rev. Lett. **69** (1992) 3523.

[16] P. Sautet and C. Joachim, Ultramicroscopy **42-44** (1992) 115.

[17] P. Sautet and C. Joachim, Chem. Phys. Lett. **185** (1991) 23.

Chapter 2. SCANNING TUNNELING MICROSCOPY

2.1 Principle of Operation

The Scanning Tunneling Microscope (STM) was invented in 1981-82 by Binnig and Rohrer[1-3] and has since been widely used to study surfaces at the atomic scale. A number of reviews describing the STM technique and theory have now been published.[4-9] In an STM, a sharp conducting tip is brought extremely close (< 10 Ångstroms) to a conducting sample so that electron tunneling through the vacuum gap between the two can take place. The tunneling current is used as a probe of the sample to tip distance which is maintained constant with a feedback loop. Electron tunneling is highly localized to the small region at the end of the tip, providing STM with extremely high lateral spatial resolution of the order of 1 Ångstrom. Images of the surface are made by recording the tip height, tunneling current, or tunneling I(V) spectroscopy data while rastering the tip over the surface.

The STM is based on the phenomenon of electron tunneling. When two conductors, as shown in figure 2.1, are brought close enough together, electron conduction can occur across the gap between them. Ordinarily electrons, even free conduction electrons, cannot leave a conductor because a there is a potential barrier at the surface equal to the workfunction ϕ of the material above the Fermi level. This barrier, of order several electron volts, is far higher than kT so none of the electrons within the conductor are able to overcome it. However, as the barrier at the surface is not infinite, the Schrödinger equation,

$$H\psi - E\psi = 0, \tag{2.1}$$

indicates that the free electron wavefunctions do not discontinuously drop to zero outside of the surface. Instead they decay approximately exponentially into the vacuum. In a one dimensional model of the potential with $\phi_{tip} \cong \phi_{sample} = \phi << V_{bias}$, the decay rate can be

estimated from the solution of this equation using a Hamiltonian with terms for the kinetic and potential energy of an electron,

$$H = \frac{-\hbar^2}{2m}\nabla^2 + V(z). \tag{2.2}$$

The solution is an exponential decay of the wavefunction in the vacuum region $(z > 0)$,

$$\psi \propto \exp(-\kappa z) \text{ where } \kappa = \left(\frac{2m\phi}{\hbar^2} + k^2\right)^{1/2}, \tag{2.3}$$

where k is the momentum vector in the plane of the surface.

If another conductor is brought close enough to the surface of the first, the decaying

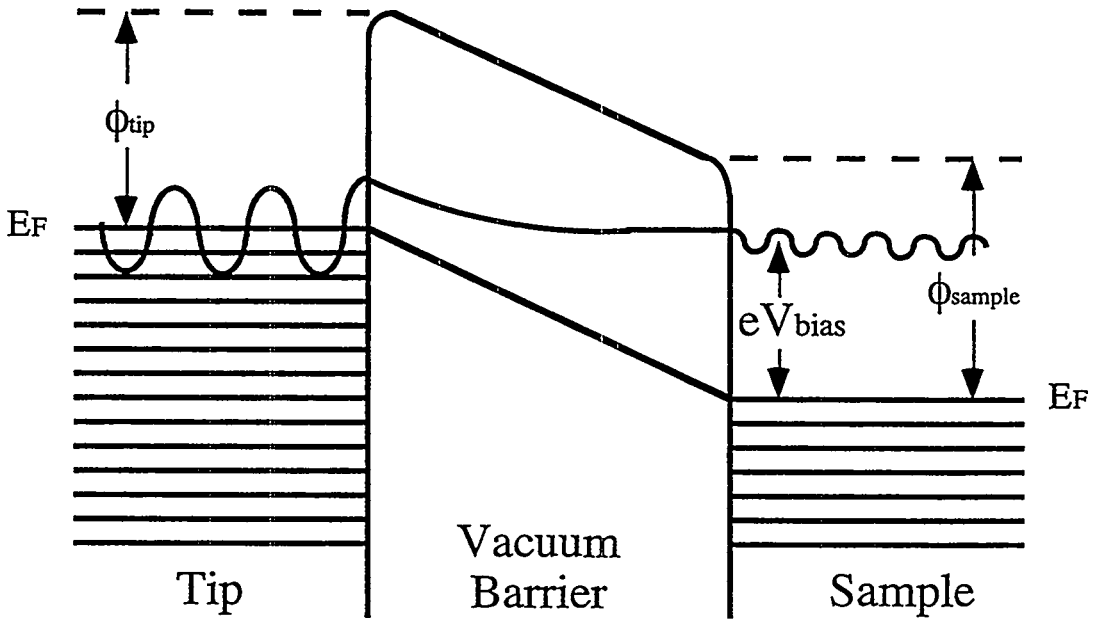

Figure 2.1 A Model Of The Tunneling Barrier

In an STM two conductors are brought close enough together so that their electron wavefunctions have a finite overlap. The wavefunctions decay exponentially outside of each conductor because the potential in the vacuum region is higher by the work function of the materials than the highest electron energy in the conductors (E_F). When a bias voltage is applied between the conductors, empty states in one overlap with full states in the other and a net current flow is produced.

wavefunction of each conductor may have a finite overlap in the gap between them, coupling the states of the two conductors, as is indicated for one state in figure 2.1. In equilibrium the coupling produces no net current through the gap. The Fermi level of the two conductors are equal, and thus states coupled across the gap are equally occupied.

However, when a bias voltage is applied between the two conductors, the Fermi level of one is shifted with respect to the other. States that in equilibrium are full on one side of the tunneling gap will overlap with states which are empty on the other side. This imbalance produces a net flow of electrons across the gap. This tunneling current (of order pA to nA) is proportional to the number of overlapped empty and filled states, and therefore proportional to the applied bias (of order mV to several V) in the case of a flat density of states on each side of the gap. It is also proportional to the square of the overlap of the wavefunctions on each side of the gap and thus decays with tip-sample distance approximately as

$$I \propto \exp(-2\kappa z), \tag{2.4}$$

where the decay rate specified in (2.3) is approximately one order of magnitude per Ångstrom for a barrier height ϕ of several electron volts. This formula, originally derived by Simmons[10], was later corrected to include the effect of different tip and sample workfunctions and a non-zero bias voltage.[11] Under these conditions the potential barrier between the two conductors is of a trapezoidal form as shown in figure 2.1. With this correction, the value of κ is found using an average workfunction of

$$\phi = \frac{1}{2}\left(\phi_{\text{tip}} + \phi_{\text{sample}}\right) - \left(E - \frac{eV}{2}\right), \tag{2.5}$$

where E is the energy of the electron above the Fermi level.

The exponential decay of the tunneling current with separation provides STM with its high spatial resolution which is on the atomic scale. While it is difficult to produce a tip with a single atomically sharp termination, this is not necessary to obtain high resolution. If the sample is a flat surface, or nearly so, it is only necessary that the tip have one asperity which is slightly closer to the surface than the rest of the atoms as shown in figure 2.2.

Due to the exponential decay of the tunneling current with distance, nearly all of the tunneling current will pass through the closest asperity, often consisting of a single atom. The lateral resolution of the STM will be roughly the electronic size of this atom.

2.2 Piezoelectric Elements

Besides the tip and sample, an STM includes a mechanism for mechanically positioning them close enough together for electron tunneling to occur and for controlling their relative position. This is generally done with piezoelectric elements.[12] These ferroelectric ceramic crystals are usually a lead titanate-zirconate solid solution which is

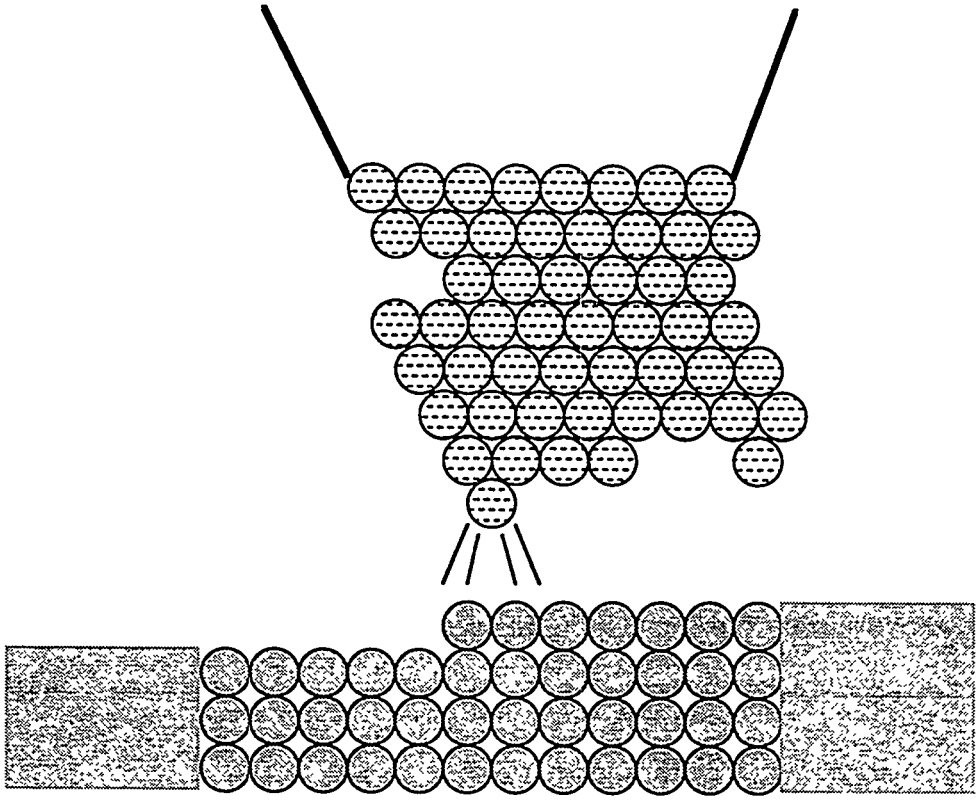

Figure 2.2 A Realistic STM Tip

Even if an STM tip does not end in a sharp point, there is usually one asperity which is several Ångstroms closer to the surface than the rest of the tip. Nearly all of the tunneling current goes through this point, giving the STM atomic resolution.

often doped with other metals to improve its electromechanical properties. Because these materials have asymmetric units cells with an electrical dipole moment, they slightly change their physical shape in response to an applied electric field. Depending on the polarity of the applied field, they lengthen in the direction of the field while contracting in the perpendicular plane and vice versa. A number of configurations are possible for using piezoelectric elements to control position in three dimensions. In the experiments described here, the piezoelectric material was shaped into a cylindrical tube with electrodes on the inside and outside of the tube for the application of the electric field. The outer electrode was cut lengthwise into four segments as shown in figure 2.3. Applying a voltage between any of the outer electrodes and the inner electrodes causes a lengthening or shortening of that quadrant of the tube, depending on the polarity. By applying a voltage between all of the outer sectors and the inner sector, the length of the tube can be changed. Applying the opposite sign of voltage to sectors on opposite sides of the tube causes the tube to bend in the plane of these sectors. Thus three dimensional positional control is achieved by applying x and y signals to the outer sectors and a z signal to the inner electrode. The magnitude of motion for these tubes is roughly 10-100 Ångstroms per applied volt, allowing a maximum range of several micrometers.

For larger scale motion needed to bring the tip into tunneling range of the sample, the piezoelectric tube range is not adequate. However, piezoelectric elements may be used to build linear translation motors which have a range of centimeters with a step size of a nanometer or less.

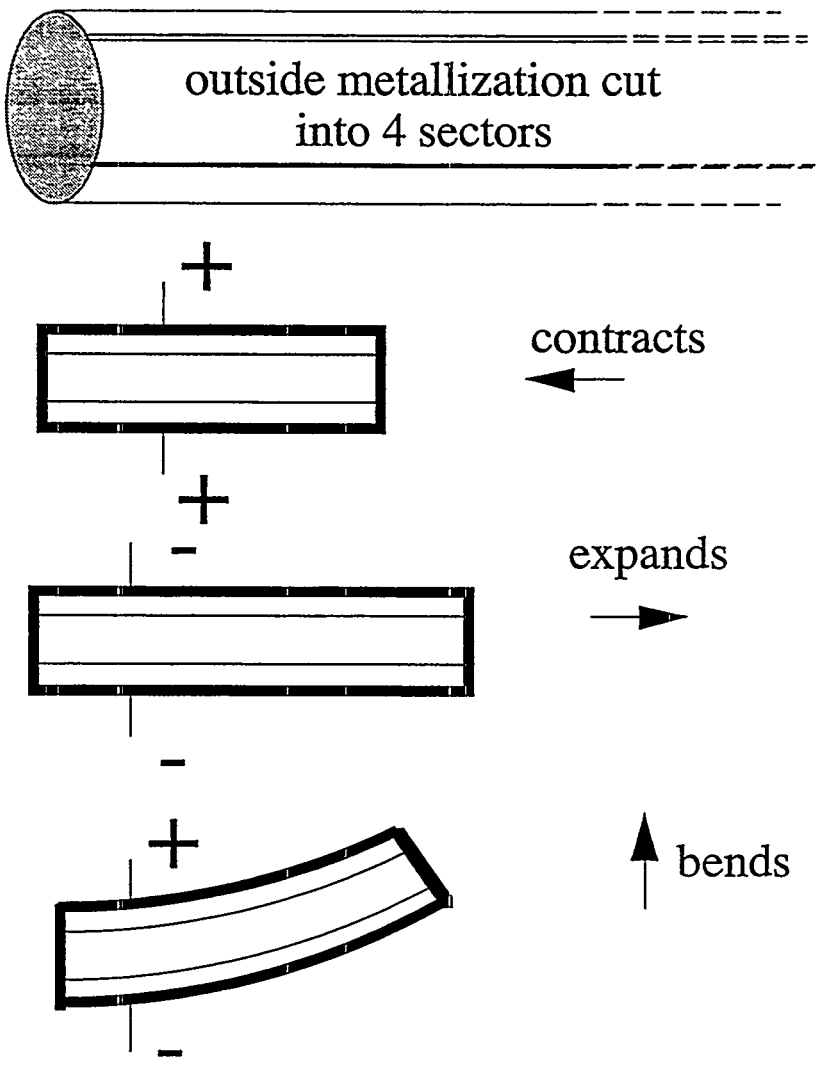

Figure 2.3 Piezoelectric Tube Positioner

Piezoelectric tube scanners are used to position the tip relative to the sample. The inside and outside of the tube are coated with metal electrodes. The outer electrode is cut into four sectors. By applying voltages between the inner an outer electrodes, the tube end motion can be controlled in x, y, and z with subatomic resolution.

2.3 Feedback Loop

In a working STM the tip-surface (z) distance is controlled by a feedback loop as shown in figure 2.4. The feedback loop attempts to keep the tip-sample distance such that the tunneling current is equal to an externally controlled setpoint value. The tunneling current of electrons between the tip and sample is measured and compared with the setpoint. The difference is sent into an electronic integrator which controls the z position of the tip. If the current is less than the setpoint, the tip is moved closer to the sample, while

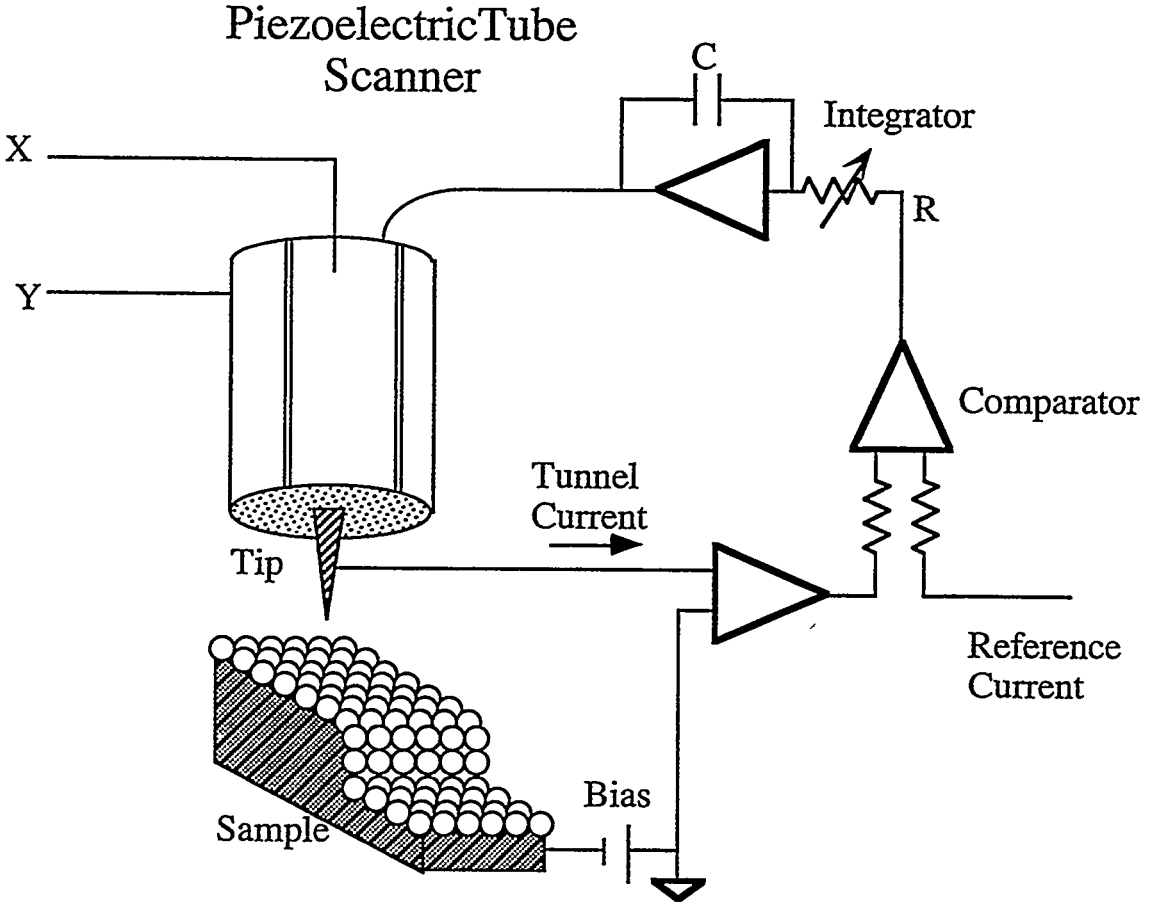

Figure 2.4 STM Model

A model of a Scanning Tunneling Microscope. A feedback loop maintains the z position of the tip such that the tunneling current is equal to a reference or setpoint value. Data is collected from one of a number of sources while the tip is rastered laterally across the surface.

if it is greater, the tip is moved back.

The response of the feedback loop can be described by

$$dz = SG(I - I_o)dt, \tag{2.6}$$

where S is the response of the piezoelectric positioner (m/V), G is the electronic gain (control voltage change per unit time per unit error in current), and I_o is the current setpoint. To first order the tunneling current can be expressed as

$$I = I_o + \left.\frac{dI}{dz}\right|_{I_o} (z - z_o) \ . \tag{2.7}$$

Therefore, the complete response of the feedback loop for a small perturbation depends on both the electronic control and the tunneling gap. The equation describing the response is

$$\frac{dz}{dt} = SG\left.\frac{dI}{dz}\right|_{I_o} (z - z_o) \ . \tag{2.8}$$

With the correct signs of S and G, the solution of this equation is an exponential decay of z toward the equilibrium value z_o with a time constant τ. In the frequency domain, the feedback loop responds by changing the tip position to correct for perturbations in the tunneling gap up to an angular frequency ω given by

$$\omega = \frac{1}{\tau} = SG\left.\frac{dI}{dz}\right|_{I_o} \ . \tag{2.9}$$

Above this frequency the response of the loop decays inversely with frequency. The cutoff frequency depends not only on the externally controllable gain G, but also on the tunneling gap parameter $\left.\frac{dI}{dz}\right|_{I_o}$ which is dependent on the setpoint I_o and the tip and surface composition.

An image is produced by rastering the tip laterally over the surface while collecting data from one of a number of sources: the tip to sample current, the feedback loop output, or a modulation in the tip to sample current produced by electrical or mechanical modulation of the tip. Several of the common imaging modes are shown in figure 2.5. The most common is the "topographic" or "constant current" mode. Topographic images are acquired by collecting the feedback loop output while tip is scanned slowly enough that the feedback loop can respond to and correct for changes in tunneling current. These images

are maps of the surface of constant tunneling current. This mode of imaging works well on surfaces which are rough, since the feedback loop is fast with respect to the scan rate and thus the tip is unlikely to contact the surface. On a large scale, these images can be interpreted simply as the topography of the surface. However, on an atomic scale electronic effects also play a role in shaping the image.

A second common imaging mode is the "current" or "constant height" mode. A "current" mode image is acquired by rastering the tip at a somewhat faster rate than that at which the feedback loop can respond while measuring the tunneling current value at each point. The image so produced is approximately of the derivative of the surface slope in the fast scanning direction. This mode is used when high scanning speed is required and the surface is flat. Because the feedback loop responds slowly, the tip is apt to catastrophically contact the surface if this imaging mode is used to image rough substrates. The interpretation of current mode image data is less straightforward than for topographic data because the image contrast is dependent on the scanning speed of the tip relative to the gain of the feedback loop.

Another mode of image acquisition "barrier height mode" measures the rate of decay of the tunneling current with tip-surface separation with a lockin technique. The tip position is controlled as in topographic mode, but the tip z position is modulated with a small (~0.1 Ångstrom) amplitude at a frequency above the cutoff of the feedback loop. The tunneling current response at this frequency is detected with a lockin. The measured signal is proportional to $\left.\frac{dI}{dz}\right|_{I_o}$, and can be directly related to the local surface workfunction through the model of tunneling described in section 2.1 and given in equations (2.4) and (2.5). Therefore, in this simple model, this measurement provides information on the local composition of the surface.

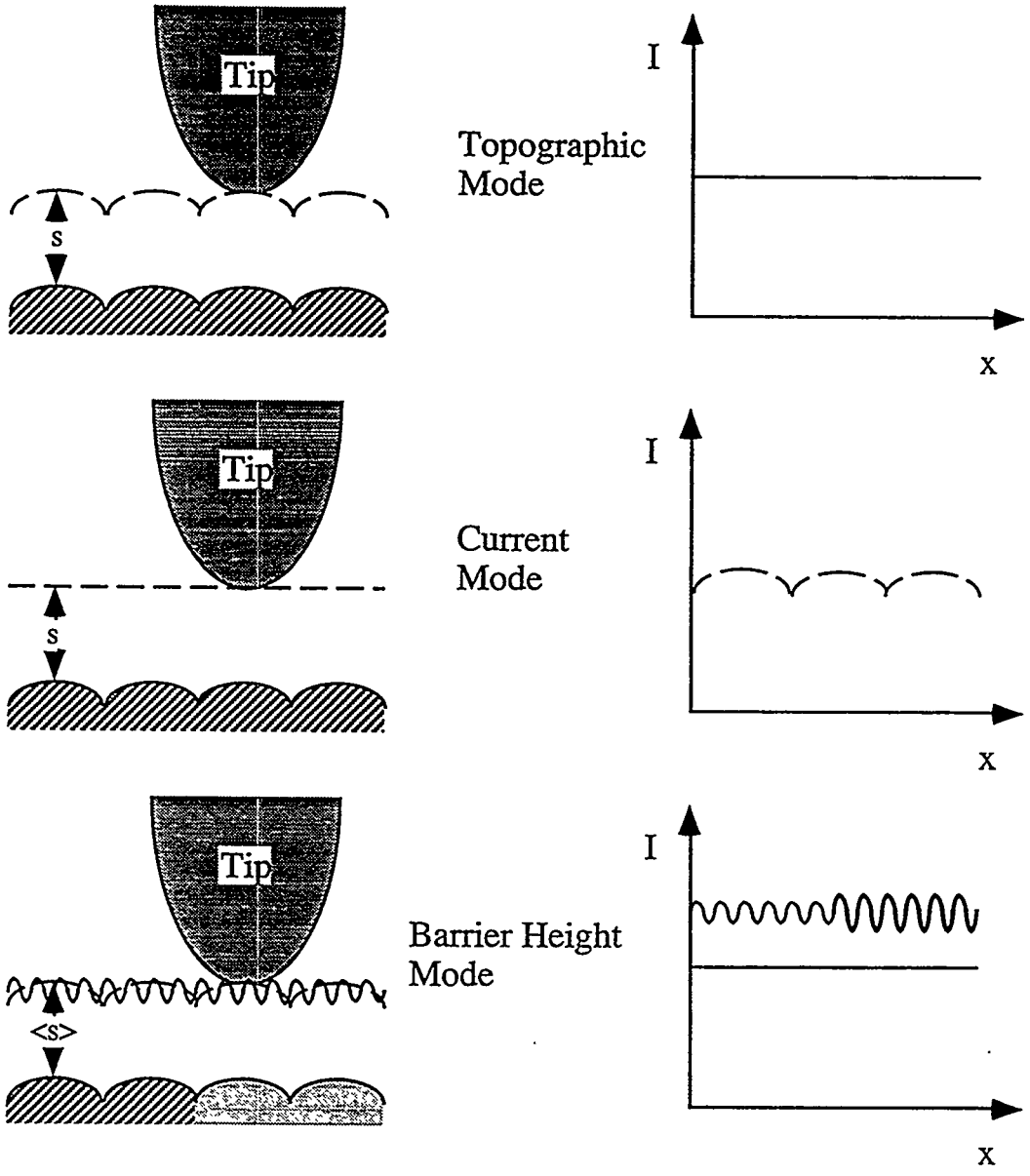

Figure 2.5 STM Imaging Modes

Three common modes of STM imaging: In topographic mode the tip height is recorded while it is adjusted to maintain constant tunneling current. In current mode the tunneling current is recorded while the tip is scanned over the surface at a rate slightly faster than the feedback loop can respond to the topographic features. In barrier height mode the tip height is modulated and the response of the tunneling current is detected with a lockin.

A number of other specialized data acquisition modes have also been developed. As indicated in figure 2.1, the tunneling current depends partially on the tip and surface density of states in the region near the Fermi level. Hence, the response of the tunneling current to a modulation of the bias voltage may be measured at each point providing rough spectroscopic information on the local density of states of the sample surface. Consecutive lines may be acquired at opposite bias polarity to compare the amplitude of tunneling into and out of a sample. It is possible, although slow, to acquire an entire I(V) tunneling spectrum at each data point, an imaging mode called Current Image Tunneling Spectroscopy (CITS).[13] These modes are particularly useful for the study of semiconductor materials which have a non-monotonic density of states, but are less useful when applied to metal substrates.

2.4 Theoretical and Practical Limits

There are both fundamental and practical limits to the resolution and speed with which an STM can probe a surface. These limits on resolution can be divided into three parts: lateral resolution, z resolution (perpendicular to the surface), and time resolution. The first of these, lateral resolution, is fundamentally limited by the deBroglie wavelength of the electrons which are tunneling to or from the surface. These electrons, with an energy of approximately the Fermi level of the material, have a wavelength of the Fermi wavelength, of order one Ångstrom. Therefore, a maximum or minimum in an STM image corresponding to the electrons around a particular atom on the surface will be smeared out by approximately this amount. In practice this is not important since the spacing of atoms on a surface is never closer than 2.5 Ångstroms. However, a real tip termination can have a size greater than a single atom and thus the resolution may be reduced below this theoretical limit.

While a finite time is required to accurately measure the tunneling current, in practice the time resolution of an STM is limited only by the mechanical stability of the microscope. As described in the previous section, the feedback loop response has a cutoff

frequency above which its response decreases. Topographic data points acquired faster than twice this frequency are not independent of each other. Current data can be acquired at a somewhat faster rate, but this risks crashing the tip into the surface if it is not flat. In principle, the cutoff frequency can be increased by increasing the gain G of the feedback electronics. However, the maximum achievable cutoff frequency is dependent on the mechanical stability of the microscope. At its mechanical resonance frequencies the physical response of the gap spacing to the feedback loop control signal, S, will increase by up to the quality factor Q of the mode and a phase shift in the response will occur. If the cutoff frequency is too high, the complete feedback loop gain at one of the lowest order resonance modes of the microscope (usually in the range 0.3 to 10 kHz) will exceed one, and the system will become unstable and begin to oscillate at this frequency. For operation, the electronic gain, and therefore the cutoff frequency, must be kept below the point at which this oscillation begins. This limits the maximum speed of data acquisition of most practical microscopes to several kHz in topographic mode (~10 seconds per image) and tens of kHz in current mode (~1 second per image).

The z resolution of an STM is limited by the noise involved in the detection of tunneling electrons which is used to monitor the tip position. There are several sources of noise in this measurement.[14] A fundamental source of noise is the "shot noise" derived from the quantization of electrons. Measuring a current is equivalent to counting the number of electrons passing per unit time. The noise involved in the count of N electrons is equal to the square root of N. Using nominal values of a bandwidth B of 1 kHz and a tunnel current of 1 nA, this produces a current noise equal to

$$I_{noise(RMS)} = \sqrt{2qIB} = 0.56 \text{ pA}, \tag{2.10}$$

where q is the charge of an electron. This corresponds to an RMS error in the current measurement of 0.056%. Assuming a tunneling gap with a decay rate of 1Å per order of magnitude in the current, this error corresponds to a z noise of 24 fm.

In addition to this statistical noise, there is noise associated with the electronics used to measure the current. In an STM current preamplifier the tunneling current is converted to a voltage and amplified by passing it through a resistor. This resistor produces a Johnson noise from thermal fluctuations within it. This voltage noise is equal to

$$V_{noise(RMS)} = \sqrt{4kTRB}. \tag{2.11}$$

With a preamplifier resistor of 10MΩ at room temperature and a bandwidth of 1kHz, this voltage noise is equivalent to

$$I_{noise(RMS)} = \sqrt{\frac{4kTB}{R}} = 1.3 \text{ pA} \tag{2.12}$$

in tunneling current or a topographic noise of 56 fm. This source of noise can be reduced by decreasing the temperature and increasing the size of the resistor, within practical limits.

These two sources of noise are generally much smaller than the actual noise found in real STM measurements, usually of order at least 1 pm (1000 fm). This noise comes from a number of experimental sources which are difficult to eliminate. Any real electronics produces 1/f noise resulting from changes in the contacts between components or within the components themselves. This noise dominates over the other sources of electronic noise at low frequencies. There is also noise associated with changes in the tunneling gap itself, such as diffusion of atoms on the tip and between the tip and surface.

Another important source of noise in STM is derived from mechanical (acoustic and building resonances) noise coupled into the tunneling gap. An STM must be vibrationally isolated from its environment so that the tunneling gap geometry will not change independently of the electronic control signals. This is usually accomplished by several layers of damped mass-spring systems on which the microscope rests. Even with these devices, vibrations from the building wall, cooling fans, speech, and other sources, are somewhat coupled into the tunneling gap. The combinations of all of the various sources of noise combine to limit the z resolution of most STMs to the range of 0.01 to 0.1 Ångstroms.

2.5 Application of STM to Chemisorption on Metals

Chemisorption of atoms and molecules onto single crystal metal surfaces is an important area where STM can be applied. These systems are good models for catalyst surfaces and substrates for epitaxy, but are highly uniform surfaces which can be systematically studied. In the past these systems have been studied by non-local techniques such as Low Energy Electron Diffraction (LEED) and Ion Scattering.

The first STM study of a chemisorption system was by Baro *et al.*[15] who imaged the oxygen induced reconstruction of the Ni(110) surface. They were able to resolve the (2x1) rows which form in the [100] direction separated by twice the lattice spacing distance. Complete molecules have been imaged on a number of surfaces. The first observation of molecular adsorbates was made by Ohtani *et al.*[16] These authors studied the ordered overlayer formed by CO and benzene on the Rh(111) surface. The benzene molecules appeared as threefold symmetric rings, while CO appeared as small bumps between the rings.

The work discussed in this thesis is on sulfur adsorbed on metals. Sulfur adsorbed on a number of metal surfaces has been imaged, including Al(111)[17], Re(0001)[18], Pt(111)[19, 20], Pd(111)[21], Cu(111)[22], Ni(110)[23], Ni(111)[24], and Cu(100)[25, 26]. With rare exception, adsorbed sulfur atoms appear as a maximum in STM images. Usually the underlying metal lattice is not simultaneously imaged, especially on close packed surfaces.

Chapter 2 References

[1] G. Binnig, H. Rohrer, C. Gerber and E. Weibel, Phys. Rev. Lett. **49** (1982) 57.

[2] G. Binnig, H. Rohrer, C. Gerber and E. Weibel, Phys. Rev. Lett. **50** (1983) 120.

[3] G. Binnig, H. Rohrer, C. Gerber and E. Weibel, Appl. Phys. Lett. **40** (1982) 178.

[4] M. Tsukada, K. Kobayashi, N. Isshiki and H. Kageshima, Surf. Sci. Rep. **13** (1991) 265.

[5] J.A. Golovchenko, Science **232** (1986) 48.

[6] P.K. Hansma and J. Tersoff, J. Appl. Phys. **61** (1987) 1.

[7] G. Binnig and H. Rohrer, Rev. Mod. Phys. **59** (1987) 615.

[8] J.E. Dumuth, U.K. Koehler and R.J. Hamers, J. Microsc. **152** (1988) 299.

[9] M. Salmeron and F. Ogletree, Prog. Solid St. Chem. **20** (1990) 235.

[10] J.G. Simmons, J. Appl. Phys. **34** (1963) 1793.

[11] M.C. Payne and J.C. Inkson, Surf. Sci. **159** (1985) 485.

[12] H. Jaffe and D.A. Berlincourt, Proceedings of the IEEE **53** (1965) 1372.

[13] R.J. Hamers, R.M. Tromp and J.E. Dumuth, Phys. Rev. Lett. **56** (1986) 1972.

[14] P. Horowitz and W. Hill. *The Art of Electronics*. (Cambridge University Press, Cambridge, 1989).

[15] A.M. Baro, G. Binnig, H. Rohrer, C. Gerber, E. Stoll, A. Baratoff and F. Salvan, Phys. Rev. Lett. **52** (1984) 1304.

[16] H. Ohtani, R.J. Wilson, S. Chiang and C.M. Mate, Phys. Rev. Lett. **60** (1988) 2398.

[17] T. Wiederholt, H. Brune, J. Wintterlin, R.J. Behm and G. Ertl, Surf. Sci. (1995) 91.

[18] R.Q. Hwang, D.M. Zeglinski, D.F. Ogletree, A.L. Vazquez-de-Parga, G.A. Somorjai and M. Salmeron, Phys. Rev. B **44** (1991) 1914.

[19] B.J. McIntyre, M. Salmeron and G.A. Somorjai, Surf. Sci. **323** (1995) 189.

[20] B.J. McIntyre, P. Sautet, J.C. Dunphy, M. Salmeron and G.A. Somorjai, J. Vac. Sci. Technol. B **12** (1994) 1751.

[21] A.J. Gellman, J.C. Dunphy and M. Salmeron, Langmuir **8** (1992) 534.

[22] L. Ruan, I. Stensgaard, F. Besenbacher and E. Laegsaard, Ultramicroscopy **42-44** (1992) 498.

[23] L. Ruan, I. Stensgaard, E. Laegsgaard and F. Besenbacher, Surf. Sci. **296** (1993) 275.

[24] L. Ruan, I. Stensgaard, F. Besenbacher and E. Laegsgaard, Phys. Rev. Lett. **71** (1993) 2963.

[25] S. Rousset, S. Gauthier, O. Siboulet, W. Sachs, M. Belin and J. Klein, J. Vac. Sci. Technol. A **8** (1990) 302.

[26] S. Rousset, S. Gauthier, O. Siboulet, S.W. Sacks, M. Belin and J. Klein, Phys. Rev. Lett. **63** (1989) 1265.

Chapter 3. EXPERIMENTAL METHODS

3.1 Introduction

The samples studied in this thesis were single crystal metal surfaces covered with adsorbate layers. Metal surfaces are extremely reactive; they become instantly dirty upon exposure to air by adsorbing oxygen, water, and hydrocarbons. Although covering the metal with an adsorbate reduces the reactivity, the surface will still become covered by a water layer when exposed to air. In order to have clean and well characterized surfaces, the experiments described here were carried out in an Ultra-High Vacuum (UHV) environment at pressures in the 10^{-10} Torr range. While even at these pressures the surface eventually becomes dirty, enough time (at least one hour) is available for experiments during which the surface remains moderately clean.

Besides the STM, a number of other surface science techniques and instruments were used to clean and characterize the samples. The apparatus for these techniques, sample preparation, and the STM are all mounted into the UHV chamber. This chapter discusses these instruments and the techniques for fabricating uniform surfaces for study by STM and for characterizing them by other surface sensitive techniques.

3.2 The Ultra-High Vacuum System

A diagram of the UHV chamber used in these experiments is shown in figure 3.1. This chamber is attached to two pumps for producing the vacuum, a turbomolecular pump and an ion pump. The turbomolecular pump is used for initial pumpdown and for pumping an airlock used to transfer the sample into and out of UHV. It is sealed off from the chamber with a gate valve and turned off during STM operation to reduce vibrations. The ion pump maintains the ultra-high vacuum with a base pressure of 1×10^{-10} Torr. The pressure is measured with a standard ionization gauge. A titanium sublimation pump is used occasionally to improve the pumping speed of reactive gasses.

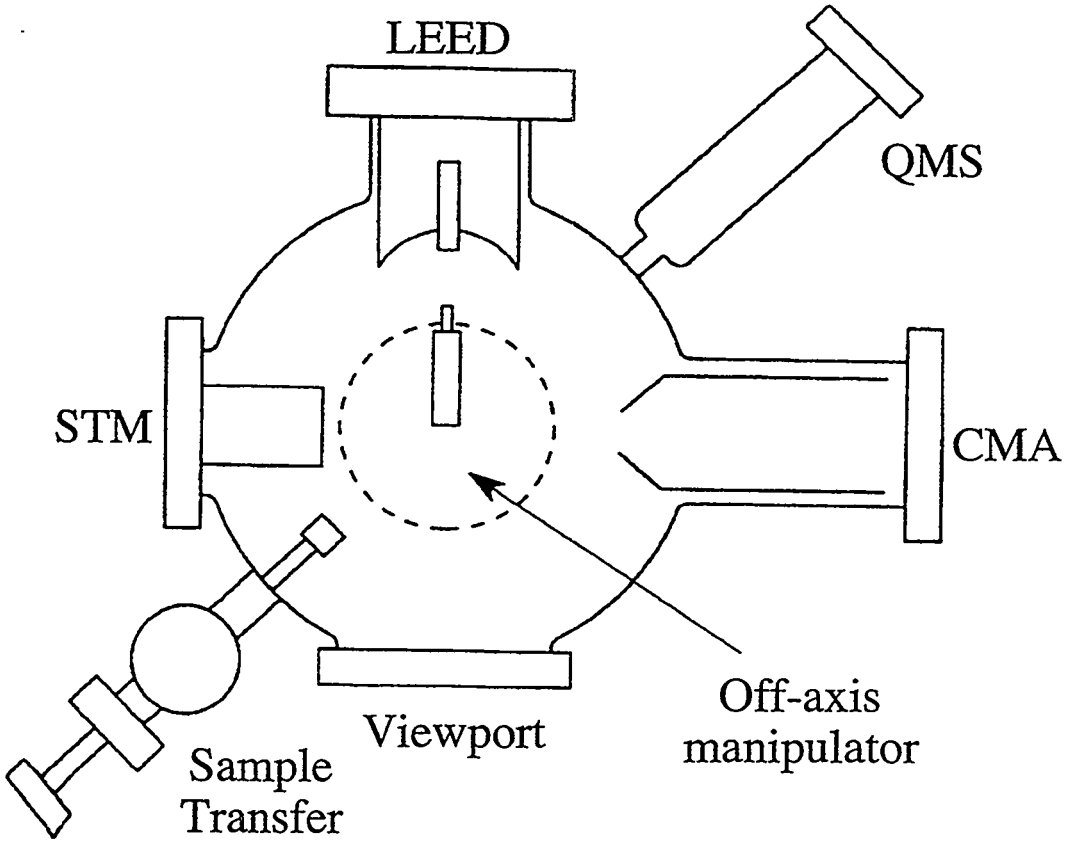

Figure 3.1 A Diagram of the UHV System

This horizontal cross section of the UHV chamber shows the main equipment used to prepare and characterize the adsorbate layers on metal single crystal surfaces. These instruments include a LEED system, a CMA for electron spectroscopy for AES, and a QMS. The sample is held in the center of the chamber by a manipulator with x, y, z, and rotational motion. Samples can be exchanged through an airlock without breaking vacuum. During STM experiments the samples are removed from the manipulator and placed onto the STM stage.

The sample is held within the chamber with a commercial crystal manipulator. This manipulator allows both rotation around a vertical axis and motion in x, y, and z for aligning the crystal face with the instruments. The samples are mechanically attached to the front of a Mo block, shown in figure 3.2, by pressing 0.006" thick Ta foil strips over the edge of the sample and spotwelding them to the block. This Mo block serves as a sample cart which carries the sample into the STM as described later. The Mo block has a hole drilled through it perpendicular to the face on which the sample is mounted. A cylinder on the manipulator containing an electron bombardment heater fits inside this hole, and a clamp above it holds the sample holder onto the manipulator. This clamp may be activated or released from outside the chamber. A thermocouple, attached to the clamp, measures the sample temperature. Up to 3000 volts can be applied to the electron bombardment heater filament while the sample potential is held fixed at ground. With a controlled emission current of up to 40 mA the sample can be heated to temperatures of up to 2000 C.

The manipulator can position the sample in front of several instruments for cleaning or characterization. These include the LEED and AES system described shortly, an ion gun for sputtering the surface of the sample, and deposition sources. The sample can be cooled by placing the sample holder in contact with a liquid nitrogen cooled Cu block.

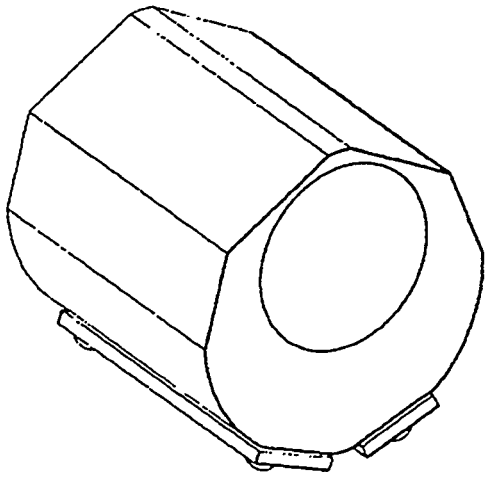

The sample is attached over the hole in the front of a Mo block by spotwelding strips of Ta foil over its edges. An electron bombardment heater on the manipulator fits into the hole in the sample holder.

Figure 3.2 Sample Holder

Low pressures (usually < 1 x10^{-6} Torr) of gasses including Ar, O_2, H_2S, and CO can be introduced into the chamber through several variable leak valves. These gasses are used in sample cleaning and to deposit adsorbates on the surface. A quadrupole mass spectrometer (QMS) is used to monitor the residual gasses in the vacuum and to check the purity of gasses introduced into the vacuum during sample preparation.

Two deposition sources are used in preparing some of the samples. A solid state electrochemical sulfur source[1] is used to deposit sulfur the surface. This device contained a silver sulfide sample which decomposes and emitted S_2 and S_6 when a current is passed through it while it is heated to 150 C. The chamber also contains a gold deposition source consisting of a tungsten wire heater wrapped with gold wire. A tantalum foil shield surrounding the source prevents gold from being deposited anywhere in the chamber except for the sample surface.

3.3 Ultra-High Vacuum STM

3.3.1 Microscope Head Design

The STM is a homemade system which existed at the beginning of this thesis work, but which was substantially modified during the work to improve its performance. Only its final state is described here. The design of the STM[2, 3] is based on a previous successful design of Lyding.[4]

The STM is attached to an eight inch UHV flange on the chamber. The STM head is a "double tube" design as shown in figure 3.3. Two concentric piezoelectric tubes position the sample relative to the tip. The concentric tube design provides first order thermal compensation, reducing thermal drift of the tip relative to the sample during imaging. The tube electrodes are cut into sectors as described in chapter 2, such that the position of the end of each may be controlled in three dimensions. Both tubes are fixed on one end. The other end of the inner tube holds the STM tip. The tip wire is pressed into a tip holder which is held into a fixture on the end of the piezoelectric tube with a Cu-Be

spring as shown in figure 3.4. The outer piezoelectric tube is attached to the sample holder tube. The Mo sample holder block may be deposited onto this anodized aluminum tube from the manipulator.

The sample holder block sits on 0.125" sapphire balls attached to its bottom, as shown in figure 3.5. An asymmetric axial vibration applied by the piezoelectric tube is used to move the sample holder along this tube. When the tube is moved rapidly during one half of the waveform, the sample holder slips relative to the tube, while it follows the slower motion of the tube during the other half. Once the sample is brought within tunneling range of the tip, the outer piezoelectric tube is used to offset the STM image center position.

The tunneling gap bias voltage is applied to the sample through a gold foil in contact with the top of the sample holder block. The tip potential is held at virtual ground.

A cartridge behind the head holds spare STM tips in tip carriers. The tips are changed while the microscope is in vacuum with a "wobble stick" manipulator. This apparatus has jaws on one end which fit the back end of the tip carriers. Tips are extracted and introduced through the inner piezoelectric tube of the microscope.

3.3.2 Vibration Isolation

The STM is isolated from the vibrations in the surrounding environment by several damping stages. The double tube head sits on several heavy metal plates. A vacuum compatible silicone rubber is placed between these plates. The bottom plate is supported with four springs. Viton rubber gasket material is wound around these springs to damp oscillations and acoustic noise. These systems decoupled the microscope from acoustic noise and vibrations above approximately 10-20 Hz.

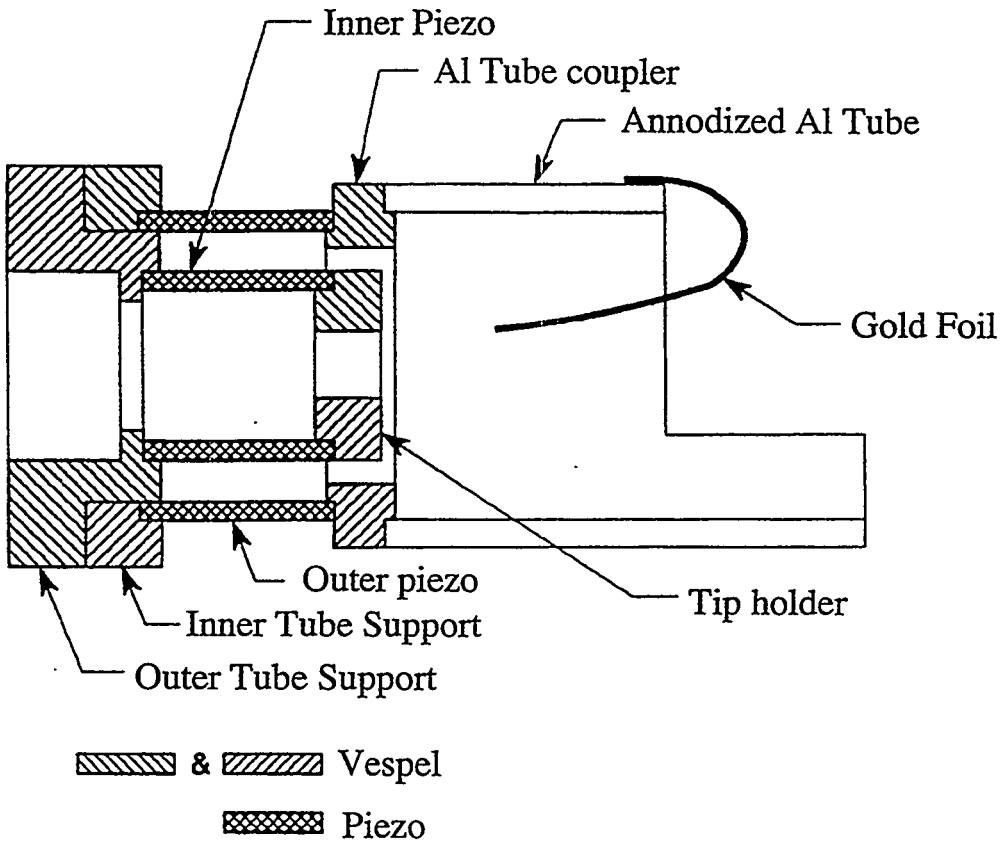

Figure 3.3 Drawing of the STM Head

The left edge of the STM head is fixed to a vibration isolation stage. The inner piezoelectric tube controls the position of the tip and is used to scan the tip during imaging. The outer piezoelectric tube controls the sample position. The sample holder block sits on an anodized aluminum tube connected to this piezoelectric tube. For small offset displacements the range of the piezoelectric is adequate. The "inertial approach" technique is used to produce the macroscopic motion required to bring the sample within tunneling range. The sample is translated toward the tip by applying an asymmetric ramp waveform causing the piezoelectric to change length rapidly in one direction and the sample holder block to slip along the tube, while it sticks when the tube moves more slowly in the opposite direction.

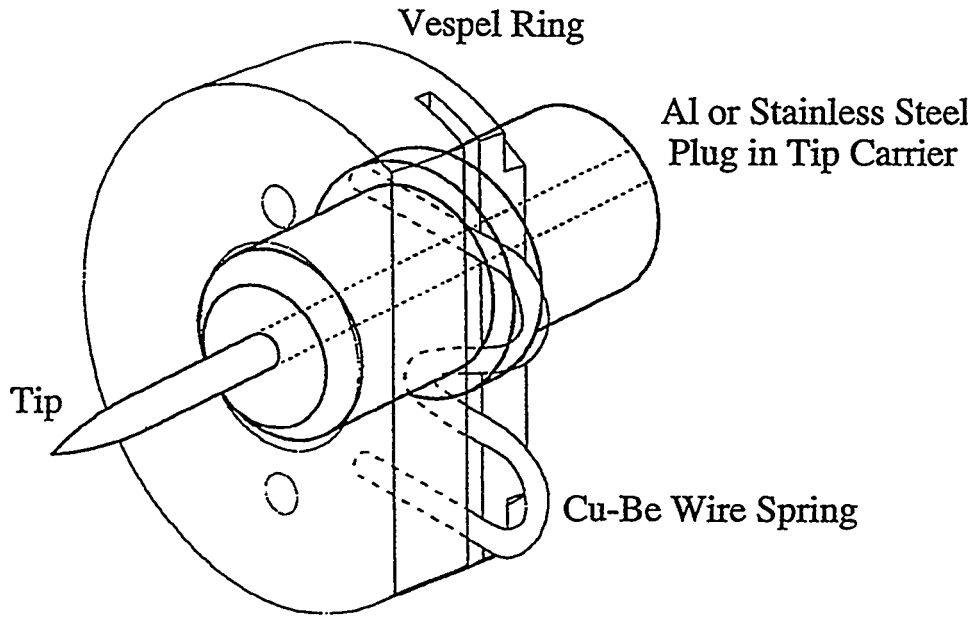

Figure 3.4 Drawing of the Tip Attachment

A vespel ring and Cu-Be spring wire hold the tip carrier on the end of the inner piezoelectric tube.

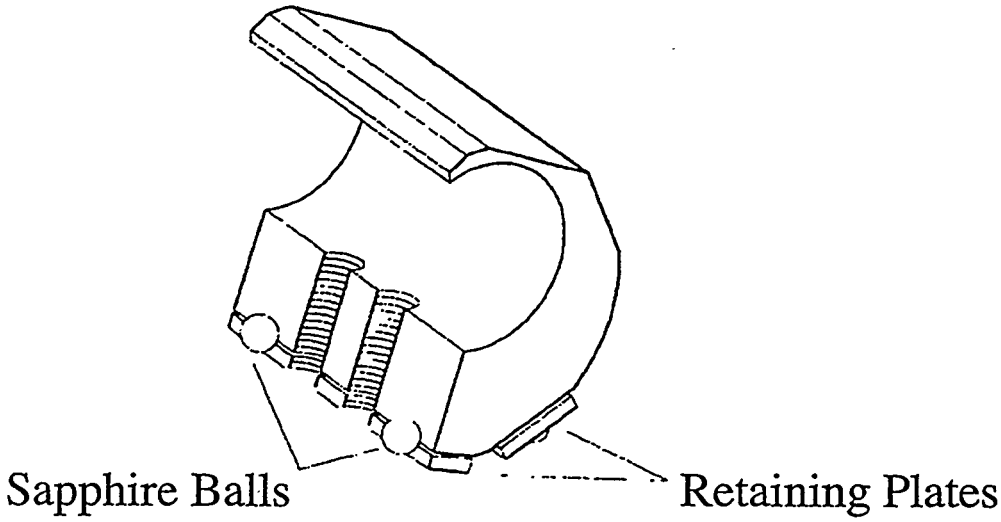

Figure 3.5 Cross Section of the Sample Holder

When in the microscope, the sample holder sits on four sapphire balls fixed to its bottom by two retaining plates. These balls slide on the anodized aluminum tube in 1000-6000 Å steps during the large scale sample translation.

Besides these systems inside the chamber, the entire vacuum chamber is supported on commercial air damper legs which decoupled the chamber from building vibrations above 1-2 Hz. During operation of the STM, unnecessary electronics cables are disconnected from the chamber to prevent them from conducting vibrations to it.

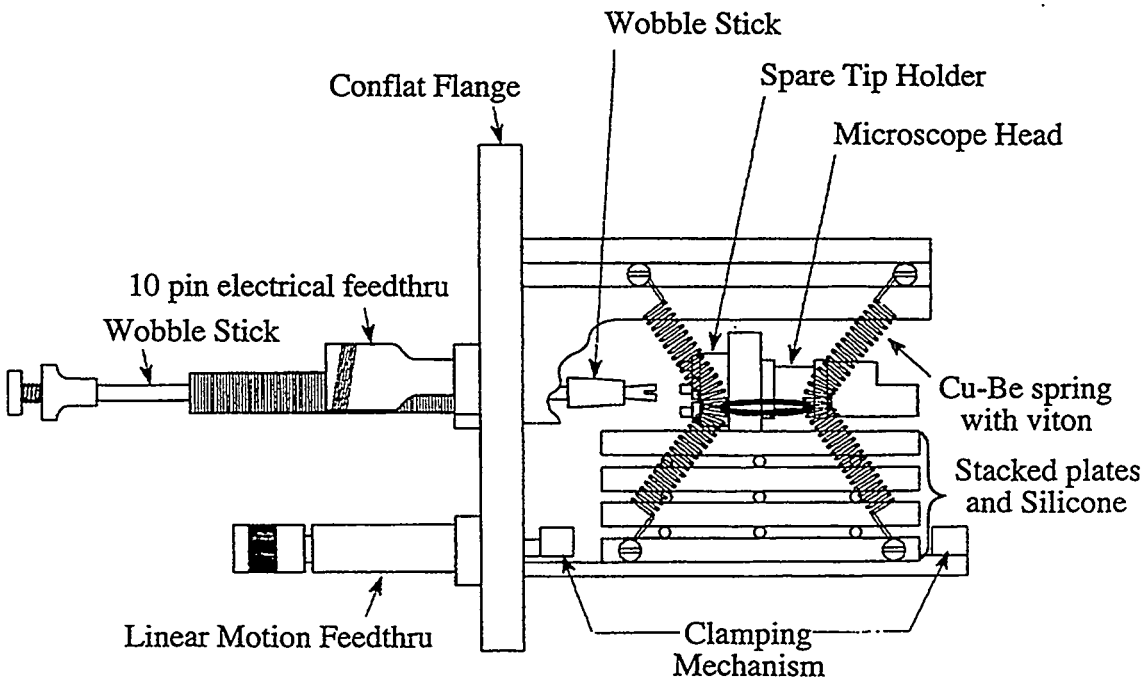

Figure 3.6 A Complete Drawing of the STM

The entire STM is attached to an 8" UHV flange. The STM head sits on a vibration isolation stage consisting of stacked plates with silicone rubber between them and hung from Cu-Be springs. Viton rubber is wound within the springs and between them to provide damping. Tips are changed with a wobble stick manipulator. Spare tips are stored in a cartridge behind the microscope head. A linear motion feedthru controls a clamp which locks the stacked plates and head in place during tip exchange.

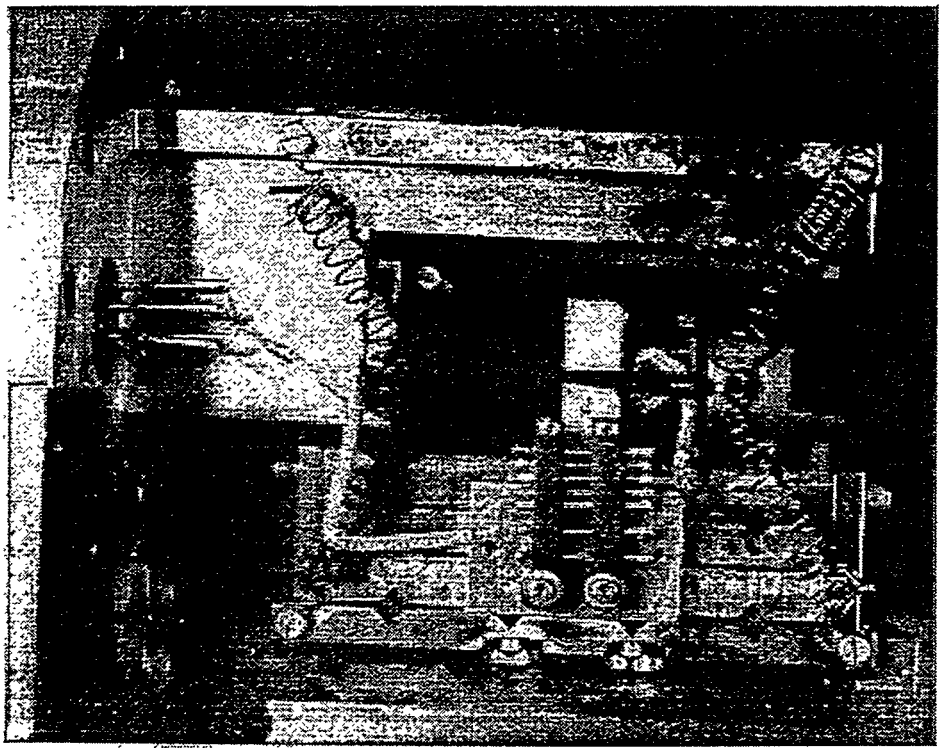

Figure 3.7 A Picture of the STM

This photograph of the STM shows the vibrational isolation components inside the chamber and the STM head. At the left is the 8" conflat flange with electrical feedthrus. On the lower right is the stack of metal plates with elastomer in between with are supported by springs. The head is sitting on top of the upper plate. The piezoelectric tube is partially hidden by the wiring, but the aluminum sample holder tube (with a hole cut through the side for viewing the tip) is clearly visible.

3.3.3 Tip Preparation

Two types of STM tips, platinum alloy and tungsten, were used in these studies. The Pt alloy tips are produced by mechanically cutting 1mm diameter Pt / 40% Rh alloy thermocouple wire. The Pt tips were not cleaned prior to use. Tungsten tips are made by electrochemically etching the end of a 0.25 mm wire in a solution of KOH or NaOH. This treatment produces tips with a termination smaller than the resolution of a standard optical microscope. The tungsten tips are oxidized by exposure to water and air. They were found to perform poorly unless cleaned in vacuum. Both types of tips are mounted in stainless steel or aluminum tip carriers for use in the microscope.

The tungsten tips were cleaned in vacuum by resistive heating the tips. A 1 mm diameter tantalum wire is suspended above the spare tip holder at the back of the microscope. Using the wobble stick to position the tip holder, the tip wire is brought into contact with the tantalum wire. The back end of the tip wire is grounded through the tip holder and wobble stick manipulator. A current of 5 to 8 A is passed through the tip, heating it red to white hot. This procedure removes thick oxide layers from the tungsten tips.

The tips were sharpened using a procedure derived from Field Ion Microscopy techniques.[5] The tips were heated until they glowed red-orange for approximately one minute in a pressure of 10^{-4} Torr O_2. Besides oxidizing and removing contaminants on the tip, oxygen adsorption removes [110] facets on tungsten. Therefore, the tip termination is likely to become rougher and the tip sharper from exposure to oxygen. After this treatment the tip was heated briefly to white hot in order to remove any thick oxide layer which might have formed. This tungsten cleaning procedure was very successful and produced tips which were more likely to have good results and last longer than the uncleaned Pt tips.

3.3.4 Electronic Control

The electronic control for the STM is homemade. It is made up of three components. The first is a ±200 V power supply which produces the control voltages for the outer piezoelectric which moved the sample holder. A second component produces the voltage ramps for rastering the tip over the surface. Both the scan size in x and y and the rate of the scan can be independently controlled. The third component contains the current integrator which controls the z position of the tip and the tunneling bias voltage supply. This unit is connected to the tunneling current preamplifier which is located directly outside of the UHV chamber. STM tunneling current, topography, or other data were digitized by analog to digital converters and recorded by a PC.

The tunneling current preamplifier was calibrated by measuring the current produced by a low voltage applied across a 10^8 Ohm 1% accuracy resistor. The physical response of the piezoelectric tubes per applied volt was calibrated by measurements of the periodicity of known surface lattices and monatomic step heights on the sample surfaces.

The PC used for data acquisition is also used for data analysis, imaging filtering, and measurements. Initial image processing consisted of fitting a plane or parabola to a flat section of the image and subtracting this plane. This procedure corrects for thermal drift, piezoelectric hysteresis, and physical tilt of the sample. Often the images were also corrected by applying a median filter to remove noise spikes (especially effective for current mode images) and by applying a two dimensional Fourier filter to remove spatial frequencies higher than those representing real data.

3.4 Surface Characterization Methods

Besides the STM, two other surface sensitive techniques were used to characterize the crystal surfaces. These techniques, which both operate at a much larger scale than the STM, are complementary to STM in that they provide information on the surface which STM cannot.

3.4.1 Auger Electron Spectroscopy

Auger Electron Spectroscopy (AES)[6, 7] is a surface sensitive technique which provides the chemical composition of a sample. It is based on the Auger process, or the self-ionization of an atom after an excitation has produced a core hole. In this process, an outer shell electron fills the core hole while simultaneously a second electron is ejected into the continuum. Energy conservation requires that the kinetic energy of the free electron be equal to the energy gained by filling the core hole minus the ionization energy of the free electron. These energies depend on the chemical identity of the ionized atom. Each element has its own characteristic spectrum. Thus, the spectrum of these electrons from a material indicate its chemical composition.

In an AES apparatus, sample atoms are ionized by a high energy electron beam creating atoms with core holes. These excited atoms may decay through either Auger processes or X-ray emission. The energy spectrum of electrons emitted from the sample is determined with an electron spectrometer. Besides the Auger electrons, a high background is present in the spectrum from inelastically scattered incident electrons and other secondary processes. Therefore, the first derivative of the spectrum is acquired to highlight the narrow peaks corresponding to Auger transitions. Because the mean free path of high energy electrons in a solid is short (~ 1 nm), AES is sensitive to only the first few layers of the surface.

In the present experiments, the sample was bombarded with a current of 4 to 20 μA of 1500 eV electrons incident at 70° to the surface normal. The emitted electron spectrum was energy filtered by a Cylindrical Mirror Analyzer (CMA) and detected with an electron multiplier. The CMA pass energy was modulated by approximately the AES peak widths or ~4 eV and the modulation in the detector was detected with a lockin to produce a first derivative spectral signal. The signal was recorded either with a chart recorded or a PC. A complete spectrum from 50 to 500 eV including peaks corresponding to the substrate and the common contaminants, sulfur, oxygen, and carbon, was collected in approximately 90

seconds. Because of variations in sensitivity with the precise sample position, adsorbate peaks were normalized to the height of the substrate peaks for semi-quantitative composition analysis. The instrument was capable of detecting as little as one percent of a monolayer of the common surface contaminants. Longer acquisition times were necessary for detection of small amounts of oxygen as it has a small Auger cross section.

3.4.2 Low Energy Electron Diffraction

In a Low Energy Electron Diffraction (LEED)[8, 9] experiment, a monoenergetic beam of electrons with an energy of 20 to 500 eV are diffracted by the surface of a single

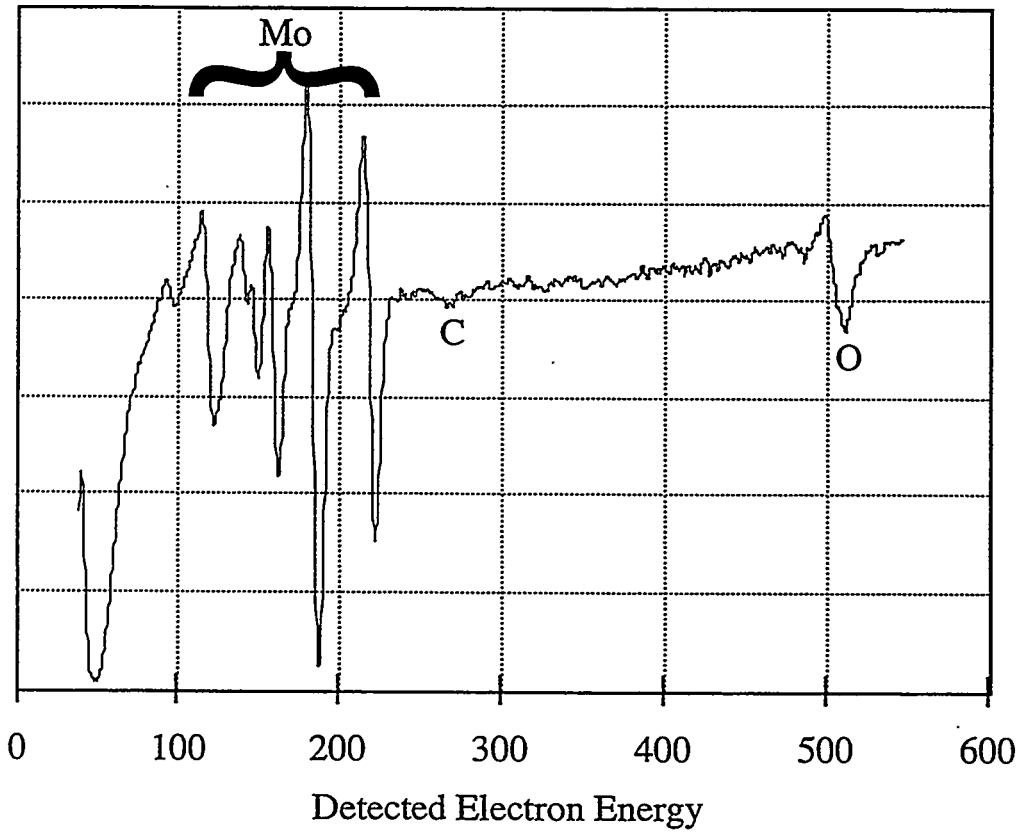

Figure 3.8 Example of an AES spectrum

An AES spectrum for a Mo(100) surface with approximately one monolayer of oxygen and a lesser amount of carbon adsorbed on it. The peaks are labeled with the element to which they correspond.

crystal sample. The angular distribution of elastically scattered electrons is detected. Electrons in this energy range have a deBroglie wavelength in the range of the separation of atoms (~3 Å) in a crystal. Therefore, the scattered electrons have an angular distribution consisting of the diffraction peaks of the Fourier transform of the two dimensional surface periodicity. In addition, the intensity of these diffraction peaks as a function of electron energy contains information on the three dimensional structure of the first few layers of the surface. Because of the limited mean free path for electrons, the technique is sensitive to the top surface layers only.

In this work a LEED apparatus made commercially by Varian was used. The electron beam is produced by an electron gun aimed along the crystal surface normal. Elastically diffracted electrons are filtered from inelastically scattered ones with several electrostatic grids. The elastically diffracted electrons are detected by accelerating them into a fluorescent screen. This apparatus was used to determine the average order of the surface. A high background between the diffraction spots indicates a poorly ordered surface with many defects. The presence of extra spots besides those representing the bulk crystal lattice indicates a reconstruction of the crystal surface or the presence of a superstructure formed by an adsorbate on the surface.

3.5 Crystal Preparation and Cleaning

The experiments described in this thesis were conducted on single crystal metal samples, Re(0001) and Mo(100). These crystals are grown commercially from molten high purity metals. The single crystals are oriented by Laue X-ray back diffraction. They are cut along the desired orientation with a diamond saw or spark cutter into disks approximately 5 to 10 mm in diameter and 1-2 mm thick. The crystals are polished to nearly atomically flat surfaces in many stages, starting with fine sandpaper and working down to fine 0.03 micron diamond or alumina paste. The final surface appears as a flat, nearly scratch free mirror. The orientation of the crystal surface was generally within 1° of

the desired crystallographic face. Final cleaning and preparation of the surface is done in UHV.

Final smoothing of the crystal surface was performed by annealing in UHV during cleaning. In thermal equilibrium at temperatures below the melting point the surface of these crystals are nearly atomically flat. Despite the high purity bulk crystals, further cleaning in UHV was always required. Bulk contaminants segregate to the surface, enhancing their concentration in this region well above the bulk values. In addition, the surface region became contaminated by contact with air, adsorbing hydrocarbons onto the surface. Prior to cleaning, the surface of these crystals was contaminated with a mixture of carbon, sulfur, and oxygen.

The cleaning procedure varies somewhat between different materials, but the basic procedure is invariable. It consists of cycles of annealing followed by reacting or ion sputtering to remove impurities. During the annealing periods the crystal is heated from 1-10 minutes to 500-1000 to allow impurities to segregate at the surface. The impurities are then removed by reaction with O_2 gas in the range of $5x10^{-7}$ Torr while the crystal is heated to around 600° C. This treatment removed sulfur and carbon. The remaining oxygen is removed by flashing the crystals to very high temperature (several hundred degrees below their melting point) for several seconds. Other impurities are removed by sputtering the crystal with ~1000 eV Ar ions produced by the ion gun. This treatment removes impurities which will not react with oxygen. The crystal cleanliness is monitored by AES in between cleaning cycles.

After cleaning the crystal, an overlayer was chemisorbed onto it by exposing the surface to a low (10-7 Torr) pressure of gas or with the sulfur or gold deposition sources. The specific preparations in the experiments are described in the following chapters. The periodicity of the surface was characterized by LEED, and the sample was imaged with the STM.

Chapter 3 References

[1] C. Wagner, J. Chem. Phys. **21** (1953) 1819.

[2] D.M. Zeglinski, D.F. Ogletree, J. T. P. Beebe, R.Q. Hwang, G.A. Somorjai and M. Salmeron, Rev. Sci. Instr. **61** (1990) 3769.

[3] R.Q. Hwang, D.M. Zeglinski, D.F. Ogletree, A.L. Vazquez-de-Parga, G.A. Somorjai and M. Salmeron, Phys. Rev. B **44** (1991) 1914.

[4] J.W. Lyding, S. Skala, R. Brockenbrough, J.S. Hubacek and G. Gammie, J. Microsc. **152** (1988) 371.

[5] H. Wengelnik and H. Neddermeyer, J. Vac. Sci. Technol. A **8** (1989) 438.

[6] G.A. Somorjai. *Chemistry in Two Dimensions: Surfaces*. (Cornell University Press, Ithaca, 1981).

[7] A. Zangwill. (Cambridge University Press, New York, 1988).

[8] M.A. VanHove and S.Y. Tong. *Surface Crystallography by LEED: Theory, Computation, and Structural Results*. (Springer-Verlag, Berlin, Heidelberg, 1979).

[9] G. Ertl and J. Kuppers. *Low Energy Electrons and Surface Chemistry*. (Verlag-Chemie, Germany, 1974).

Chapter 4. STM THEORY

4.1 Overview of STM Theory

The interpretation of the atomic scale features in STM images is not straightforward. The images contain both topographic and electronic structure information about the surface. In general it is difficult to separate these two components. For large scale images the electronic component is often ignored, but with atomic resolution images it is of approximately equal magnitude with the physical structure and cannot be neglected.

Some information on atomic scale surface structure can be immediately determined by inspection of images. It is simple to measure the distance between equivalent points on the surface, both laterally and in height. These measurements provide the periodicity of the surface and the separation of atomic layers (step height). Additionally, the binding site of adsorbate atoms (top, hollow, or bridge) may often be determined from an analysis of the symmetry of the images, especially at defect sites and antiphase boundaries.[1, 2] In contrast, STM does not directly yield information on the relative positions of inequivalent atoms, such as the bond length between adsorbate and substrate atoms or the distance between adsorbate atoms bound at different surface sites. This is because the STM does not produce a simple image of a hard sphere model of the surface, but an approximate map of electron density which is a combination of physical and electronic structure. Other factors besides the surface structure may influence the image contrast, including the tunneling conditions (bias voltage and tunneling current) and the morphology of the tip termination.[2-6] A theoretical approach is needed to separate this electronic structure influence on the image from the physical structure of the surface.

Considerable effort has been focused on developing an accurate theoretical description of electron tunneling with which STM images can be calculated. [7-17] Most early models of tunneling describe the tip and surface with free-electron models which do not have atomic structure.[8-11] Other approaches use more accurate descriptions of the

surface and tip physical and electronic structure, but most use Bardeen's approximation[18], a perturbation approach, to calculate the tunneling current. One such approach, that of Tersoff and Hamann, indicates that STM images may be approximated by the surface electron density at the Fermi level at the center of a tip modeled by a single s-wavefunction.[13] Lang improved the description of the tip, modeling the tip and surface as atoms embedded in jellium and calculating the electronic states with the Local Density Approximation (LDA).[14, 15] Tsudaka et al. have developed a model using a Linear Combination of Atomic Orbitals (LCAO) description of the wavefunction of the surface and a tip cluster coupled to a specialized model of the vacuum tail. Other theories avoid Bardeen's approximation, taking the tip-surface interactions into account which is important for accurate modeling of tunneling with a small tip-surface separation. These include the theories of Doyen et al.[12] and Sautet and Joachim[16, 17] which accurately include the influence of the tip-surface electronic interaction by modeling the surface and tip with atomic orbitals and treating the electron tunneling between them with a scattering theory. All these theories are summarized in table 4.1. Several of them are discussed in detail in the remainder of this chapter.

Authors	Sample	Tip	Barrier	Current
Tersoff and Hamann[13]	Atomic structure (various models for LDOS)	Spherical (s-wave)	N/A	Perturbation
Garcia et al.[9]	1D periodic	1D periodic	Trapezoidal	Scattering
Nguyen et al.[10]	Free electron	Free electron, flat	Image potential	Scattering
Lang[14, 15, 19]	Jellium & single atom	Jellium & single atom	Surface double layer & exchange correlation	Perturbation
Das and Mahanty[11]	Free electron	Hemisphere & free electron	Image potential	WKB
Tsudaka et al.[7]	LCAO with a special description of wavefunction tail	Cluster	Surface double layer & exchange correlation	Perturbation
Sautet and Joachim[16, 17]	LCAO	Cluster LCAO	Calculated Fermi level below vacuum	Scattering
Lucas et al.[8]	Free electron	Hemisphere & free electron		Scattering
Doyen et al.[12]	Muffin tip potential atomic orbitals	Jellium & single atom	work function	Scattering

Table 4.1 Summary of STM Theories

The approach to STM calculations used in a number of papers are listed. Each theoretical approach is divided into four parts: The representation of the sample and tip, the tunneling barrier, and the method used for computation of the tunneling current.

4.2 Tersoff and Hamann

The simple potential barrier model of tunneling described in section 2.1 shows the basic form of the equations for electron tunneling and describes the correct behavior with tip-surface separation, but it does not provide a basis for the interpretation of atomic corrugation commonly seen in STM images. A theory developed by Tersoff and Hamann[13, 20] describes the tunneling more accurately and provides a simple interpretation for the images. However, this theory still makes several approximations which prevent it from making quantitative predictions about image contrast.

Tersoff and Hamann begin with a perturbation theory expression for the tunneling current using Fermi's golden rule. The transition rate between states on opposite sides of the gap is equal to $\frac{2\pi}{\hbar}$ times the sum of the square of all allowed matrix elements of the wavefunction overlap. In this formalism, all interactions between the surface and tip, i.e. the influence of one on the electron wavefunctions of the other, are completely ignored. The tunneling current is

$$I = \frac{2\pi e}{\hbar} \sum_{\mu\nu} f(E_\mu)\left[1 - f(E_\nu + eV)\right] \left|M_{\mu\nu}\right|^2 \delta(E_\mu - E_\nu) \ , \tag{4.1}$$

where $M_{\mu\nu}$ are the overlap matrix elements, and f is the Fermi distribution. The inclusion of the Fermi functions insure that electron may only tunnel from a full state to an empty one.

In the limit of small bias voltage and temperature the Fermi distribution becomes a step function and only electrons extremely close to the Fermi level are able to tunnel across the gap. The expression reduces to

$$I = \frac{2\pi}{\hbar} e^2 V \sum_{\mu\nu} \left|M_{\mu\nu}\right|^2 \delta(E_\mu - E_F)\delta(E_\nu - E_F) \ . \tag{4.2}$$

This expression shows that only states of the sample and tip with the Fermi energy play a role in tunneling. Bardeen[18] has shown that the matrix elements can be calculated by the integral of the current operator over any potential free surface between the tip and sample by

$$M_{\mu\nu} = \frac{-\hbar^2}{2m} \int d\vec{S} \cdot \left(\psi_\mu^* \nabla \psi_\nu - \psi_\nu \nabla \psi_\mu^* \right) . \tag{4.3}$$

Tersoff and Hamann calculate these matrix elements for a special case, a completely spherically symmetric tip described as an s-wave function within the tunneling gap. The wavefunction of the periodic surface can be generally expanded into a plane wave basis set. By expanding the s-wave tip in this basis, the tip structure is shown to drop out of the expression completely. The matrix elements are simply proportional to the surface wavefunction at the center of the spherical tip,

$$M_{\mu\nu} \propto \psi_\nu(\vec{r}_o) . \tag{4.4}$$

Placing this result back into (2.13), one finds that the tunneling current is proportional to the surface local density of states at the Fermi level at the location of the center of curvature of the tunneling tip, $\vec{r}_o$. This local density of states is defined by

$$\rho(\vec{r}_o) \equiv \sum_\nu \left| \psi_\nu(\vec{r}_o) \right|^2 \delta(E_\nu - E_F) . \tag{4.5}$$

Thus topographic mode STM images can be interpreted as a map of constant local density of states at the Fermi level at some distance of order ten Ångstroms from the surface.

Some of the approximations that went into this theory are overly simplistic, particularly the lack of interaction between the tip and surface and a model of the tip so simple that its structure effectively plays no role in the amplitude of tunneling. If fact, this theory predicts that a single s-wave tip will produce the same results as a delta function tip which exists only at a single point. However, it still provides a good starting point for image interpretation as a map of the local density of states. In this interpretation, the corrugation of an adsorbate is related to how much it enhances the Fermi level electron density above the surface.

Using this theory, the ability of STM to resolve periodic features on surfaces may be estimated. The surface wavefunction is expanded into Bloch waves decaying in the vacuum region outside the surface. The corrugation in the density of states from this wavefunction decays with increased distance from the surface. The decay rate is faster for

shorter surface periodicity. In fact, the theory predicts that with a z resolution of 0.01 Ångstroms, common for most STMs, lateral periodicity shorter than 6 Ångstroms should not be resolved under normal tunneling conditions. This is in conflict with experiments which commonly resolve the structure of metals surfaces with a periodicity of approximately 2.5 Ångstroms.

4.3 Jellium Model

A different approach to STM theory was taken by N. Lang based on the jellium model of solids.[14, 15] The goal of this theory was to understand chemisorption systems, especially how the atomic identity of an adsorbate atom and tip termination atom effects the corrugation and shape of the adsorbate in the image. This theory also includes a finite bias voltage and has the capability of predicting spectroscopic measurements.

In Lang's theory, the tip and substrate are equivalent. They are both described as a single atom attached to a jellium[21] model base. Unlike Tersoff and Hamann theory, the tip was not restricted to an s orbital, but included the complete orbital basis set of the atom. The jellium model represents the atomic cores as a uniform positive charge. Hence, it has the drawback of neglecting the different adsorption sites available on a real metal lattice.

The equilibrium distance between the adsorbed atom and the jellium is determined self-consistently, and the exact wavefunction of the surface and tip systems are solved completely. Through its interaction with the surface, each state of the adsorbed atoms is broadened into a resonance. Charge transfer between the atoms and the jellium substrate may take place.

As in the Tersoff-Hamann approach, the tunneling current is calculated using Bardeen's approximation (perturbation theory). By modifying Bardeen's theory, Lang was able to calculate the spatial distribution of tunneling current between the tip and sample. This theory predicts reasonable values of current as a function of tip-sample separation. The tunneling current was found to be approximately proportional to the Fermi level density of states, in agreement with the Tersoff-Hamann approach.

Lang found that the corrugation and size of the maximum of an adsorbate was dependent on the atomic identity of both the tip atom and adsorbate atom. When imaged with a sodium terminated tip, sulfur and sodium were found to have positive corrugation, while helium produced a depression. Most of the tunneling current in the images was found to be a result of the coupling of s orbitals of the sample and tip with much smaller contributions from the d orbitals.

Lang also used this model to calculate the effective work function of the surface defined in the simple trapezoidal barrier model of section 2.1.[19] In order to properly treat small tip-surface distances, perturbation theory was abandoned, and tip and surface were treated as a single quantum mechanical system. With this approach the work function was found to decrease from its asymptotic value as the sample-tip distance is reduced below about 6 Ångstroms. At a distance of 2.5 Ångstroms the effective barrier is reduced to zero. At this point the electron conduction across the gap enters a new regime in which the current is limited by the uncertainty principle limit on the transverse momentum of electrons passing through the small tip-surface contact.

4.4 ESQC Theory

While the two previously discussed theories provide much insight into the electron tunneling which controls the form of an STM image, the do not allow an accurate description of a real experimental system. Because of its complexity and lack of symmetry, the STM problem cannot be solved using an *ab initio* approach with a realistic description of surface and tip structure with the computational capability available today. However, a semi-empirical approach can provide a solution to the problem with a reasonable amount of computer time while including a good representation of the physical and electronic structure of a real surface and tip system. Such an approach was used for the calculations described later in this thesis.

The STM theory calculations applied to the systems discussed here were made using Electron Scattering Quantum Chemistry (ESQC) theory. This method of calculating

STM images was developed by Sautet and Joachim[16, 17] and grew out of a theory of conduction through defects in polymers. The calculations were performed with a computer code developed by P. Sautet.

Compared to the two previously described theories, ESQC theory is less analytical. However, it is capable of describing more complicated and realistic surfaces and tips. Unlike the approaches to calculating STM images outlined above, ESQC accurately models the surface and the tip with an atom by atom description of the bulk, surface, and tip geometry. Besides the work described here, it has been applied to a number of chemisorption on metal systems with good results. For instance, the theory correctly predicts the shape of benzene[22] and CO[23] molecules adsorbed at different sites on the Pt(111) surface.

The basic feature of this theory is the description of electron tunneling as a scattering process. The calculation is done on a three dimensional system and includes the atomic orbitals of the sample and tip. The tunneling junction, that is the surface, the adsorbates, and the tip apex can be viewed as a defect in an otherwise periodic solid bulk. Each tunneling electron has a probability to get through the gap and be transmitted to the tip (sample) bulk, or to be reflected back towards the sample (tip). This probability is expressed by a scattering matrix S that describes how the gap couples the bulk electronic wavefunctions on each side. It is clear that this scattering matrix is a function of the x, y, and z position of the tip with respect to the surface. The conductance of the system is calculated from the scattering matrix by the generalized Landauer formula.[18] This formula relates the conductance to the elements of the scattering matrix which couple states across the gap. The tunneling current for a given voltage is derived from the gap conductance by a linear low voltage approximation.

In order to calculate the scattering matrix, the surface, the adsorbate, and the tip have to be considered simultaneously. The system used in the calculation, modeled in figure 4.2, is infinite in the z direction and finite in the xy plane with cyclic boundary

conditions at the edges. Each part of the system is described atom-by-atom and each atomic center is associated with an orbital basis set made up of the outermost orbital shells of the atoms. The wavefunctions of these orbitals are described by their spherical harmonic radial character (s, p, d, etc.) and radial decay. The radial decay is described by either one or the linear combination of two decaying exponentials. The Extended Hückel theory is used for the calculation of the Hamiltonian matrix elements. In this theory the off-diagonal elements of the Hamiltonian are approximated by the overlap integral of the associated orbitals. These overlap matrix elements may be expressed analytically in terms of the parameters describing the orbitals (s, p, d angular character and radial decay constants). They are exactly calculated. By projection on the atomic basis, the Schrödinger equation is transformed into an infinite matrix, general eigenvalue equation. An important feature of the method is that the complete wavefunction of this infinite non-periodic system is not needed to obtain the scattering matrix. Instead it is calculated by a recursion technique. Propagators, which are transfer operators of the wavefunction in the z direction, are built for both the periodic bulk regions and for the entire STM gap junction. The scattering matrix is derived from these propagators. It should be noted that this calculation of the scattering matrix from the Hamiltonian and overlap matrix elements is exact. The only approximation is in the calculation of these matrix elements. Therefore, electronic multiple scattering in the tunnel gap is completely taken into account on the basis of an approximate wave-function. This contrasts with the Tersoff-Hamann approach[13] where Bardeen's approximation is used to calculate the tunneling current.

In the complete model system used in the calculations, two semi-infinite crystals are generated by repetition of a cell slab and terminated by a surface layer. The adsorbates and the tip, consisting of a cluster of atoms, are inserted between them. The substrate surface is assumed to be in its bulk termination. The system is finite in the lateral directions (a 3x3 to 8x8 cell) with cyclic boundary conditions. The tunneling tip is therefore formally

repeated in x and y but the translation vectors are long enough (at least 10 Ångstroms) that tip-tip interactions are not significant.

Due to the exponential decay of the tunneling current with distance, direct tunneling between bulk tip and surface states should not make a significant contribution to the tunneling current. Therefore, except for the calculations of the bulk Fermi level, the description of the atoms in the bulk has been limited to the outermost s atomic orbital for simplicity. A full spd basis set is used in the surface-adsorbate-tip region where scattering takes place and for bulk atoms in the calculation of the Fermi level. In order to obtain a better description of the long range interactions between the tip and surface, the adsorbed sulfur atoms and the atoms at the end of the tip have a double zeta (linear combination of two radial decaying exponentials) Slater orbital set.[24] This produces a decay of the tunnel current of approximately one order of magnitude per Ångstrom, as found experimentally.[25]

The tip is modeled as a cluster of atoms of a given composition and structure in which the constituent atoms are separated by the sum of their covalent radii. Due to the exponential decay of the tunneling current with the distance to the surface, only the last few atoms at the tip apex contribute significantly to the current. Therefore, the model tips are limited to those with different terminal structures. Both clusters terminating in a single atom and clusters terminated in a group of atoms at the same distance from the surface were used. The cluster was primarily made up of the platinum or tungsten tip material, although various likely tip termination chemical identities were tried. These include likely contamination atoms such as S, C, O, and the bulk sample material.

This theory was used to calculate STM images of the sulfur overlayer on Re(0001) and Mo(100). The details and results of the application of this theory to the experimental systems are described in later chapters of the thesis.

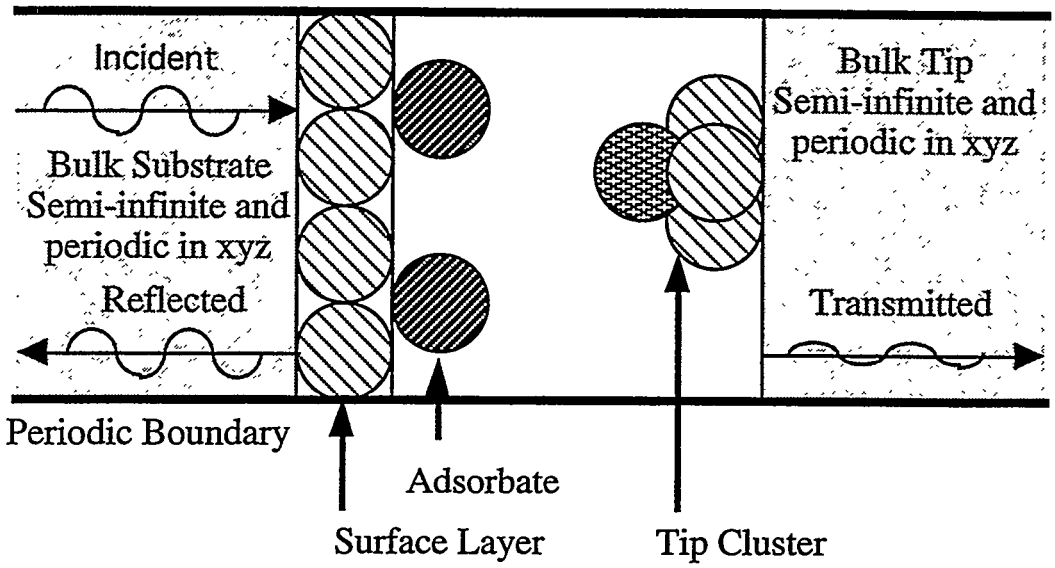

Figure 4.1 The Model System in ESQC Theory

In ESQC theory the sample, tunneling region, and bulk tip are all described atom by atom. Each atom is represented by an orbital basis set of its outermost orbitals. The system is completely periodic in the xy plane, with periodic boundary conditions. The bulk sample and tip are semi-infinite regions with periodic boundary conditions in all three dimensions. A sample-adsorbate-tip region is placed between these two semi-infinite bulks. The sample surface, adsorbate layer, and a cluster model of the tip make up this region. The tunneling current is calculated as a function of the relative position of the tip side of the system to the sample side.

Chapter 4 References

[1] R.J. Wilson and S. Chiang, Phys. Rev. Lett. **59** (1987) 2329.

[2] J.C. Dunphy, P. Sautet, D.F. Ogletree and M.B. Salmeron, J. Vac. Sci. Technol. A (1993) 1975.

[3] M. Tsukada, K. Kobayashi and N. Isshiki, Surf. Sci. **242** (1991) 12.

[4] B.J. McIntyre, P. Sautet, J.C. Dunphy, M. Salmeron and G.A. Somorjai, J. Vac. Sci. Technol. B **12** (1994) 1751.

[5] S. Rousset, S. Gauthier, O. Siboulet, S.W. Sacks, M. Belin and J. Klein, Phys. Rev. Lett. **63** (1989) 1265.

[6] L. Ruan, F. Besenbacher, I. Stensgaard and E. Laegsaard, Phys. Rev. Lett. **70** (1993) 4079.

[7] M. Tsukada, K. Kobayashi, N. Isshiki and H. Kageshima, Surf. Sci. Rep. **13** (1991) 265.

[8] A.A. Lucas, H. Morawitz, G.R. Henry, J.-P. Vigneron, P. Lambin, P.H. Cutler and T.E. Feuchtwang, Phys. Rev. B **37** (1988) 10708.

[9] N. Garcia, C. Ocal and F. Flores, Phys. Rev. Lett. **50** (1983) 2002.

[10] H.Q. Nguyen, P.H. Cutler, T.E. Feuchtwang, T. Miskovski and A.A. Lucas, Surf. Sci. **160** (1985) 331.

[11] B. Das and J. Mahanty, Phys. Rev. B **36** (1987) 898.

[12] G. Doyen, D. Drakova and M. Scheffler, Phys. Rev. B **47** (1993) 9778.

[13] J. Tersoff and D.R. Hamann, Phys. Rev. Lett. **50** (1983) 1998.

[14] N.D. Lang, Phys. Rev. Lett. **56** (1986) 1164.

[15] N.D. Lang, Phys. Rev. Lett. **58** (1987) 45.

[16] P. Sautet and C. Joachim, Chem. Phys. Lett. **185** (1991) 23.

[17] P. Sautet and C. Joachim, Ultramicroscopy **42-44** (1992) 115.

[18] J. Bardeen, Phys. Rev. Lett. **6** (1961) 57.

[19] N.D. Lang, Phys. Rev. B **47** (1988) 9778.

[20] J. Tersoff and D.R. Hamann, Phys. Rev. B **31** (1985) 805.

[21] N.D. Lang. in *Theory of the Inhomogenius Electron Gas* (eds. Lundqvist, S. & March, N.H.) p. 309 (Plenum Press, New York, 1983).

[22] P. Sautet and M.L. Bocquet, Surf. Sci. **304** (1994) L445.

[23] M.L. Bocquet and P. Sautet, in preparation

[24] E. Clementi and C. Roetti, At. Data Nucl. Data Tables **14** (1974) 177.

[25] Y. Kuk and P.J. Silverman, J. Vac. Sci. Technol. A **8** (1990) 289.

Chapter 5. STRUCTURES OF SULFUR ON Re(0001)

5.1 Previous Results

Sulfur adsorption has been studied on a large number of metal surfaces.[1-6] At low coverage sulfur generally forms lattices of single atoms with $c(2x2)$ symmetry on (100) surfaces of bcc and fcc metals and $p(2x2)$ or $\left(\sqrt{3}x\sqrt{3}\right)R30°$ on the hexagonal symmetry surfaces hcp (0001) and fcc (111).[7] Sulfur adsorbs strongly to metal surfaces; the Re(0001) surface must be heated above 1600 K for sulfur to desorb. The binding energy decreases with increasing sulfur coverage, indicating the existence of repulsive interactions between closely packed sulfur atoms.[8]

Rhenium is a transition metal with a hcp crystal structure. Sulfur adsorption on the Re(0001) surface is particularly interesting because a large family of surface structures is formed as a function of sulfur coverage. Studies by LEED[9, 10] have shown that sulfur forms four different ordered structures on this surface as the coverage is increased to the saturation value of approximately half a monolayer. Table 5.1 indicates the symmetry of these structures and the sulfur coverage at which they are observed. The first three structures may coexist on the surface. The $\left(2\sqrt{3}x2\sqrt{3}\right)R30°$ overlayer is produced by annealing the surface and does not form at the same time as any of the other three.

Dynamical LEED calculations of sulfur on metal surfaces[11] have shown that at low coverage sulfur bonds at the highest coordination site. On rhenium, a dynamical LEED analysis of the $p(2x2)$ structure[10] has shown that the binding site is the three-fold hcp hollow site.

Prior to the work described here, all of the structures listed in table 5.1 had been imaged by STM[8, 12], but the work at lower coverage values of sulfur, below one quarter monolayer, was incomplete. Examples of the images of the four structures are shown in figure 5.1.

Sulfur Coverage (Monolayers)	LEED Pattern Symmetry
0.16-0.30	$p(2x2)$
0.30-0.39	$\left(3\sqrt{3}x3\sqrt{3}\right)R30°$
0.39-0.44	$\begin{bmatrix} 3 & 1 \\ 1 & 3 \end{bmatrix}$
0..44-0.59	$\left(2\sqrt{3}x2\sqrt{3}\right)R30°$

Table 5.1 Ordered Structures of Sulfur on Re(0001)

At a coverage of one quarter monolayer the STM produced images of the surface showing an array of maxima such as figure 5.1A. The maxima in this image are spaced by twice the Re surface lattice distance, consistent with the $p(2x2)$ LEED pattern symmetry observed at this coverage. No sign of the underlying Re(0001) $(1x1)$ lattice was observed. Each of the maxima in the image is clearly associated with one adsorbed sulfur atom.

When the sulfur coverage is increased above one quarter monolayer, a dramatic change takes place in the sulfur adatom arrangement. Many of the sulfur atoms group together into trimers of three atoms each. Within these trimers they are spaced by one Re lattice spacing. The formation of trimers indicates that three or more body interactions between adsorbates, usually considered a second order correction in Monte Carlo simulations, are significant in controlling the ordering of the overlayer. In images these trimers generally appear as bright triangles, although sometimes the individual atoms making them up are resolved. At first only one orientation of trimer is present on the surface, but as the coverage is increased a different type, rotated 180°, is also observed. Structurally these two trimers differ in that one has a hollow site directly under its center while the other has a metal atom there. The trimers coexist with the $p(2x2)$ sulfur layer until the coverage reaches approximately 0.45 monolayers. At this point the trimers have been compressed together to form an ordered array with the $\left(3\sqrt{3}x3\sqrt{3}\right)R30°$ symmetry observed by LEED. The first type of trimer to appear on the surface is clearly more stable,

and it makes up 75% of the trimers in a complete overlayer. An STM image of this surface is shown in figure 5.1B.

As the sulfur coverage approaches half a monolayer, a new structure of sulfur is observed by STM, shown in figure 5.1C. This structure has $\begin{bmatrix} 3 & 1 \\ 1 & 3 \end{bmatrix}$ symmetry consistent with the observed LEED pattern. Here the sulfur has formed separate trapezoidal clusters of four atoms each.

Heating the surface while it was exposed to H_2S gas produces a fourth structure of sulfur shown in the STM image in figure 5.1D. In this structure the sulfur was distributed into hexagonal rings of six atoms. This is the saturation coverage of sulfur on this surface; additional sulfur is not adsorbed.

The STM images of sulfur can be directly interpreted. Observations of defects and the symmetry of the images indicates that at all coverage values the sulfur adsorbate atoms appear as a maximum to the STM. If sulfur is assumed to bond only at one of the two three-fold hollow sites, as would be expected from the studies of sulfur adsorption on other metals, then determining the basic structure from the STM images is straightforward. The ordered filling of the hollow sites in each of these structures is shown in figure 5.2.

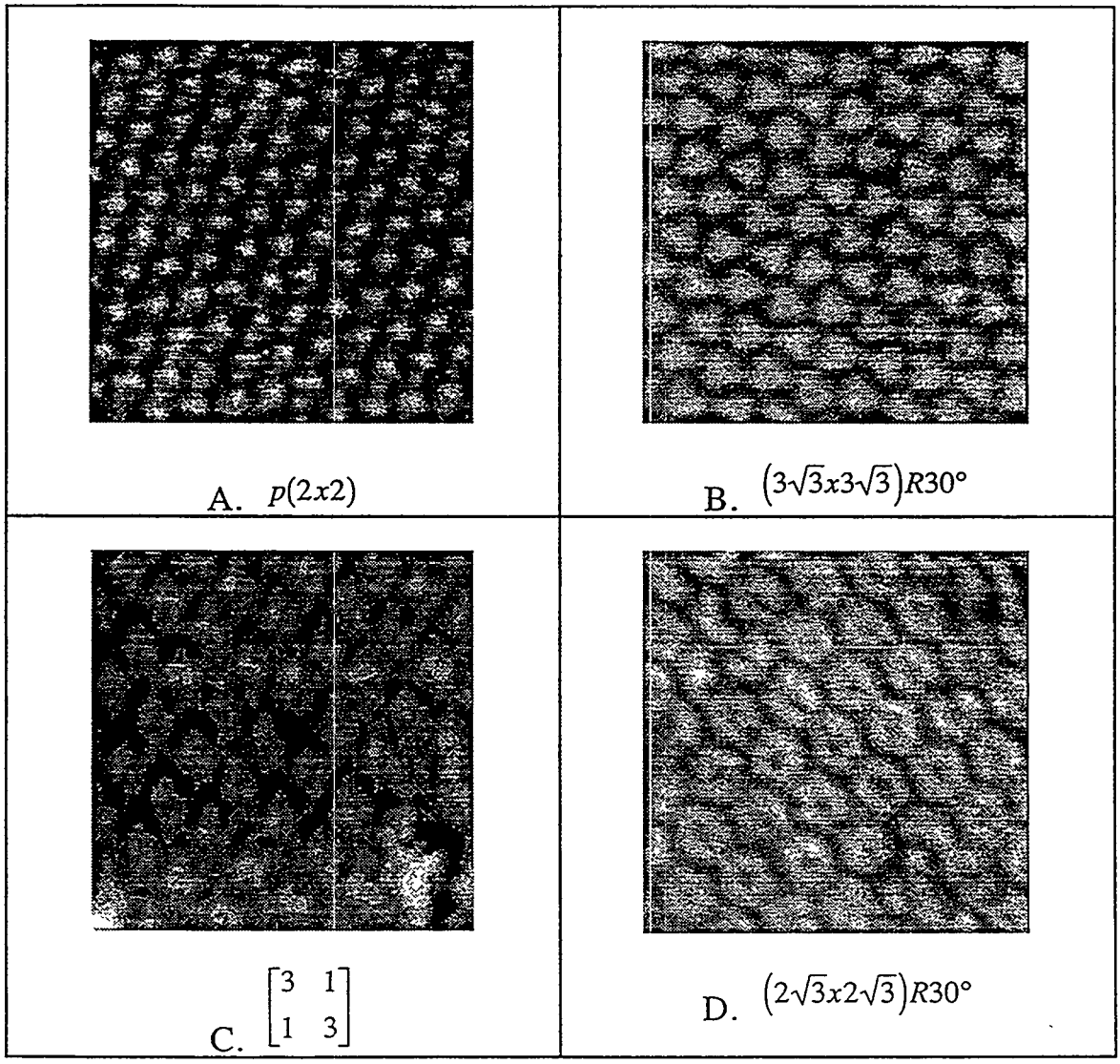

Figure 5.1 STM Images of Sulfur on Re(0001)

Each image is approximately 55 Å square. The symmetry of the LEED pattern corresponding to each structure is labeled below each image. In A the sulfur atoms are separated by twice the Re surface lattice spacing. In B the sulfur has grouped together into trimers of three atoms. Two different types of trimers are present on the surface, but one is more stable than the other and makes up 75% of those in the image. In C the sulfur has grouped into tetramers of four atoms. At saturation, in D, the sulfur has formed hexagons of six atoms.

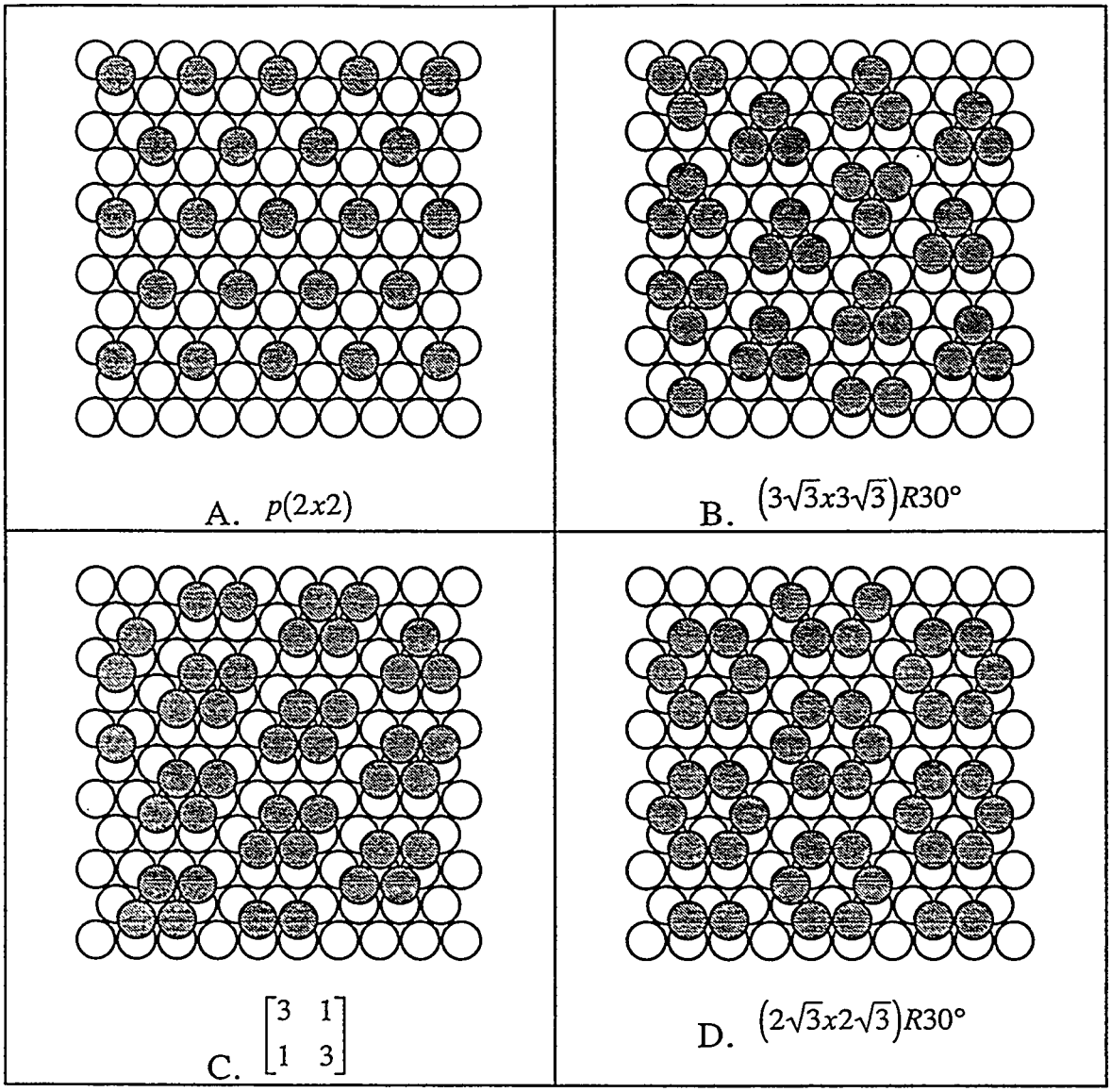

Figure 5.2 Models of the Sulfur on Re(0001) Structures

The Re lattice is shown as white circles. Sulfur, shown as shaded circles, bonds exclusively at hcp hollow sites. Initially the sulfur atoms are separate, but as the coverage is increased they form clusters of 3 and 4 atoms, and finally rings of 6 atoms.

5.2 Sulfur Overlayers at one Quarter Monolayers and Below

The experiments described in this thesis focused on sulfur coverage values of one quarter of a monolayer and below, a regime which had not fully been explored in the previous work. Imaging sulfur at low coverage on this surface is difficult, perhaps because the cleaner Re surface is more reactive and thus more likely to become contaminated or interact with the tip.

The rhenium crystal was prepared using the procedures described in chapter 3. It was cleaned in UHV by Ar+ bombardment and cycles of heating to 1000° C in the presence of 5 X 10^{-7} Torr of oxygen. This treatment removed sulfur and carbon contamination. The oxygen was removed by heating the crystal to approximately 1800° C. Once the crystal was clean as verified by AES, it was exposed to H_2S at 5 X 10^{-8} Torr for two to ten minutes while heating to approximately 700° C. H_2S gas decomposes on the surface, leaving behind sulfur. The crystal was then cooled to room temperature. The large scale ordering of the sulfur overlayer was determined with LEED, and the sulfur coverage determined with AES. If the coverage was higher than desired, some sulfur could be desorbed from the surface by heating to approximately 1000° C for several seconds. Occasionally, annealing for several seconds at 600° C was necessary to obtain an ordered LEED pattern. At coverage values less than one tenth of a monolayer the LEED pattern was $(1x1)$. As the coverage was increased to one quarter monolayer $p(2x2)$ overlayer spots appeared and became more intense and sharp. Finally, well above one quarter of a monolayer the LEED pattern had $\left(3\sqrt{3}x3\sqrt{3}\right)R30°$ symmetry.

5.2.1 One Quarter Monolayer Coverage

Many atomic resolution images of the $p(2x2)$ S structure were obtained. The resolution of the images and the shape of the maxima in the unit cell varied from minute to minute with abrupt changes between the types. With the exception of a few low symmetry images, three main types of unit cell shapes were repeatedly obtained and examples of each

are shown in figure 5.3. They all correspond to a $(2x2)$ overlayer periodicity. The first type of images shows an hexagonal array of round maxima. In the second type of images the maxima have a triangular shape with overlapping vertices. The third type of images consist of Y shaped features joined together to form a honeycomb lattice.

These different images are not a consequence of a change in the bias voltage or of the gap resistance in the range studied. These parameters only modified the corrugation amplitude of the image and had little effect on the shape of the unit cell. Changes from one type of image to another sometimes happened suddenly during the acquisition of an image or after applying a voltage pulse to the tip. This strongly suggests that these different image shapes are associated with the same surface structure but with different tip termination types. Since all of these image types were repeatedly obtained with different tips and sample preparations, none of them can be considered as resulting from an artifact or a very improbable tip configuration, but, on the contrary, each is likely to be associated with a rather stable tip structure. The observation of point defects clearly shows that the tip has a single apex and that the changes in image contrast do not result from several mini-tips that are of similar height over the surface, as has been suggested for some graphite images.[13]

Each of the experimental images of figure 5.3 show point defects which indicate the position of the adsorbate atoms within the image. In the case of round or triangular unit cells, the defect appears as a missing or modified maximum in the array. This indicates that in both these cases the sulfur atoms are located at the positions of the current maxima in the image. In the case of the honeycomb lattice, one might be tempted to assign the S atom position to that of the hole or dark area in the images, as has been proposed for oxygen on several metal surfaces[14, 15] and some images of S on Cu(11,1,1).[16] However, in the point defects in figure 5.3C the vacancy appears as a missing part of the honeycomb and not as a missing dark spot. As a consequence, it can be inferred that the sulfur atom is imaged as a bright Y-shaped feature. The overall image current corrugation $\Delta I / I$ was

found to be highest in the round maxima type images (~65%), smaller in the triangular shaped ones (~50%), and smallest in images of the overlapping Y-shapes that produce a honeycomb structure (~35%). The mechanism producing these different image contrast types is investigated in the next chapter.

5.2.2 Sulfur Coverage Less than 0.25 Monolayers

Obtaining atomic resolution images of the sulfur covered Re(0001) surface was even more difficult at coverage values less than 0.25 monolayers. Under these conditions the $p(2x2)$ LEED pattern spots decayed over a period of several hours. As a period of at least 30 minutes is required to cool the sample and bring it within tunneling range of the tip in the STM, the surface had usually become disordered before imaging. STM images of the surface appeared noisy. The noise consisted mainly of horizontal dashes within the image. Occasionally, small $p(2x2)$ ordered regions were observed. The origin of the decaying LEED pattern and the noisy STM images will be discussed in detail in chapters 10 and 9, respectively.

A. Balls

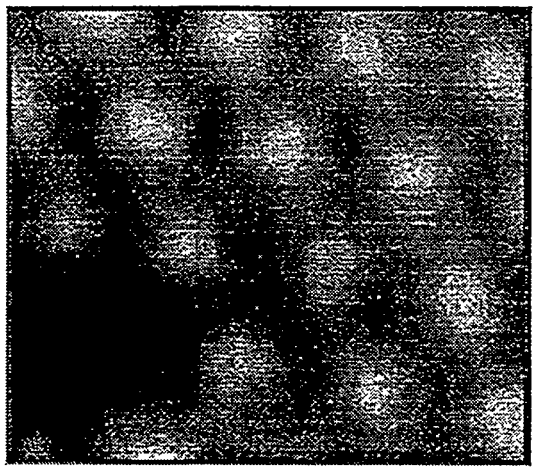

B. Triangles

C. Y's linked into hexagons

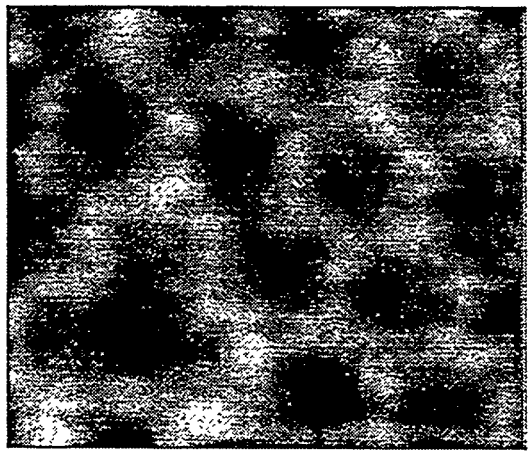

Figure 5.3 Different Contrast in Images of $p(2x2)$ S on Re(0001) Common types of current images of the $p(2x2)$ S structure of selected areas (approximately 22 Å x 19 Å) that contain point defects indicating the location of the adsorbate atoms.

Chapter 5 References

[1] B. Marchon, P. Bernhard, M.E. Bussell, G.A. Somorjai, M. Salmeron and W. Siekhaus, Phys. Rev. Lett. **60** (1988) 1166.

[2] L. Ruan, F. Besenbacher, I. Stensgaard and E. Laegsaard, Phys. Rev. Lett. **69** (1992) 3523.

[3] L. Ruan, I. Stensgaard, F. Besenbacher and E. Laegsaard, Ultramicroscopy **42-44** (1992) 498.

[4] T.M. Gentle, C.T. Tsai, K.P. Walley and A.J. Gellman, Cat. Lett. **2** (1989) 19.

[5] C.C. Knight and G.A. Somorjai, Surf. Sci. **240** (1990) 101.

[6] D.G. Kelley, R.F. Lin, M.A.V. Hove and G.A. Somorjai, Surf. Sci. **224** (1989) 97.

[7] M.A. VanHove and S.Y. Tong. *The Structure of Surfaces* (Springer-Verlag, Berlin, Heielberg, 1985).

[8] D.F. Ogletree, R.Q. Hwang, D.M. Zeglinski, A.L. Vazquez-de-Parga, G.A. Somorjai and M. Salmeron, J. Vac. Sci. Technol. A **9** (1991) 886.

[9] A. Barbieri, D. Jentz, N. Materer, G. Held, J. Dunphy, D.F. Ogletree, P. Sautet, M. Salmeron, M.A. Vanhove and G.A. Somorjai, Surf. Sci. **312** (1994) 10.

[10] D.G. Kelly, A.J. Gellman, M. Salmeron, G.A. Somorjai, V. Maurice, M. Huber and J. Oudar, Surf. Sci. **204** (1988) 1.

[11] J.M. MacLauren, J.B. Pendry, P.J. Rous, D.K. Saldin, G.A. Somorjai, M.A.V. Hove and D.D. Vvedensky. *A Handbook of Surface Structures*. (D. Reidel, Holland, 1987).

[12] R.Q. Hwang, D.M. Zeglinski, D.F. Ogletree, A.L. Vazquez-de-Parga, G.A. Somorjai and M. Salmeron, Phys. Rev. B **44** (1991) 1914.

[13] H.A. Mizes, S. Park and W.A. Harrison, Phys. Rev. B **36** (1987) 4491.

[14] H. Brune, J. Wintterlin, J. Trost, G. Ertl, J. Wiechers and R.J. Behm, J. Chem. Phys. **99** (1988) 2128.

[15] E. Kopatzki and R.J. Behm, Surf. Sci. **245** (1991) 255.

[16] S. Rousset, S. Gauthier, O. Siboulet, S.W. Sacks, M. Belin and J. Klein, Phys. Rev. Lett. **63** (1989) 1265.

Chapter 6. APPLICATION OF ESQC THEORY TO S ON Re

6.1 Introduction

As described in the previous chapter, several different types of image contrast were found for the $p(2x2)$ overlayer of S on Re(0001). An example of each of these images is shown in figure 5.3. While the periodicity of the images always reflects the $p(2x2)$ periodicity of the overlayer, the shape of the current maximum within each unit cell has a great variation between images. This variation in image contrast was found to be independent of the controllable experimental parameters, including the bias voltage, tunneling current, scanning speed, and sample preparation. The contrast appeared to change randomly, sometimes within a single STM image. It is implausible that these changes are a result of some change in the structure of the surface, as the change appeared to occur everywhere on the sample (within the observable scan range of the STM) at once. Therefore, these contrast changes may most reasonably be explained as a result of changes in the structure of the end of the STM tip.

The theory of Tersoff and Hamann[1], described in section 4.2, predicts that tip structure should have no effect on the contrast in STM images, at least at low bias voltages where spectroscopic effects do not play a role. The experimental data showed the changes in contrast even at bias voltages less than 50 mV. Therefore, it is clear, as might be expected, that the Tersoff and Hamann model of the tip as a single s-wavefunction is too simplistic. In order to understand these changes in image contrast, a more detailed theory is necessary. In the ESQC theory the tip is described more accurately as a cluster of atoms of specific chemical composition and structure. Using this theory, images can be calculated as a function of tip structure and surface geometry.

Besides investigating the changes in the image shape found experimentally, ESQC theory was applied in attempt to determine some information on surface structure. While much information on surface structure can be obtained by simple inspection of STM

images, STM does not directly provide other information, such as the chemical identity of surface atoms and the relative position of inequivalent atoms.

For example, in chemisorption systems the most basic structural information is the registry between the adsorbate layer and the substrate (or the binding site of the adsorbate). Unfortunately, it is difficult to determine this registry unambiguously by qualitative inspection of STM images. The corrugation of the substrate is often small, especially on close packed metal surfaces, and it is often not resolved together with the adsorbate. Most images of close packed metals in which the substrate corrugation is resolved are acquired at a small tunneling gap resistance. These conditions are generally incompatible with the imaging of adsorbates[2] due to strong tip-surface forces.[3] Even when atomic resolution images of both the bare surface and the adsorbate are obtained simultaneously, the registry may still be ambiguous. The registry of the STM image may not reflect the registry of the surface because not all adsorbate and substrate atoms appear to the STM as a maximum.[4]

The determination of the height of features above the surface is even more complex. The STM profile is not a simple geometric image of the surface, but includes the electronic structure of the conduction electrons near the Fermi level of the system. Therefore, the corrugation in STM images of an adsorbate layer may differ significantly from the true binding height of the adsorbate atoms.

Since the binding site (xy position) and height (z position) of adsorbate atoms influence the electronic structure of the surface, these parameters may be reflected in STM images in the shape and corrugation of the surface unit cell as a function of tunneling conditions. However, their extraction from this data is far from straightforward, and no general approach has been developed. Towards this goal, ESQC theory has been applied to study how and why surface structure and tunneling conditions affect the shape of the unit cell in the STM images of $p(2x2)$ S on Re(0001).

6.2 Tip Models

The tip is modeled as a cluster of atoms of a given composition and structure in which the constituent atoms are separated by the sum of their covalent radii. Due to the exponential decay of the tunneling current with the distance to the surface, only the last few atoms at the tip apex contribute significantly to the current. Therefore, the model tips are limited to those with different terminal structures. Investigations of the influence of tip structure by making sample calculations show that the number of necessary tip structures can be decreased further without decreasing the number of significantly different simulated images.

Tips terminated in a single atom are modeled by a tetrahedral cluster with the apex pointing toward the surface. Likely single atom tip termination structures consist of non-metallic atoms such as sulfur or carbon, originating from tip contamination or atom transfer from the surface, and metal atoms such as Pt, Rh, and Re, that are present on the tip or substrate. The calculations show that only small differences in corrugation are obtained for different atomic identities within each of these two classes. Likewise, small changes (~0.2 Å) in the binding height of the terminal tip atom are found to produce only small changes in the calculated images. Therefore only two tips, those terminated by a single S or Pt atom, are used to model all single atom terminated tips.

Similarly, the number of model multiple atom terminated tips is limited. The calculations indicate that tips terminating with more than three atoms at nearly the same distance to the surface produce images with an extremely low corrugation which is inconsistent with the experimental results. This is due to the lateral size of the tip apex becoming comparable to or greater than the adsorbate period on the surface. Therefore, the multiple atom terminated tips are restricted to those ending with a dimer or trimer of atoms at the same or nearly the same distance from the surface. For simplicity only one highly symmetric example of multiple atom terminated tips is considered initially. This "3Pt" tip is terminated with a triangle of three Pt atoms parallel to the surface.

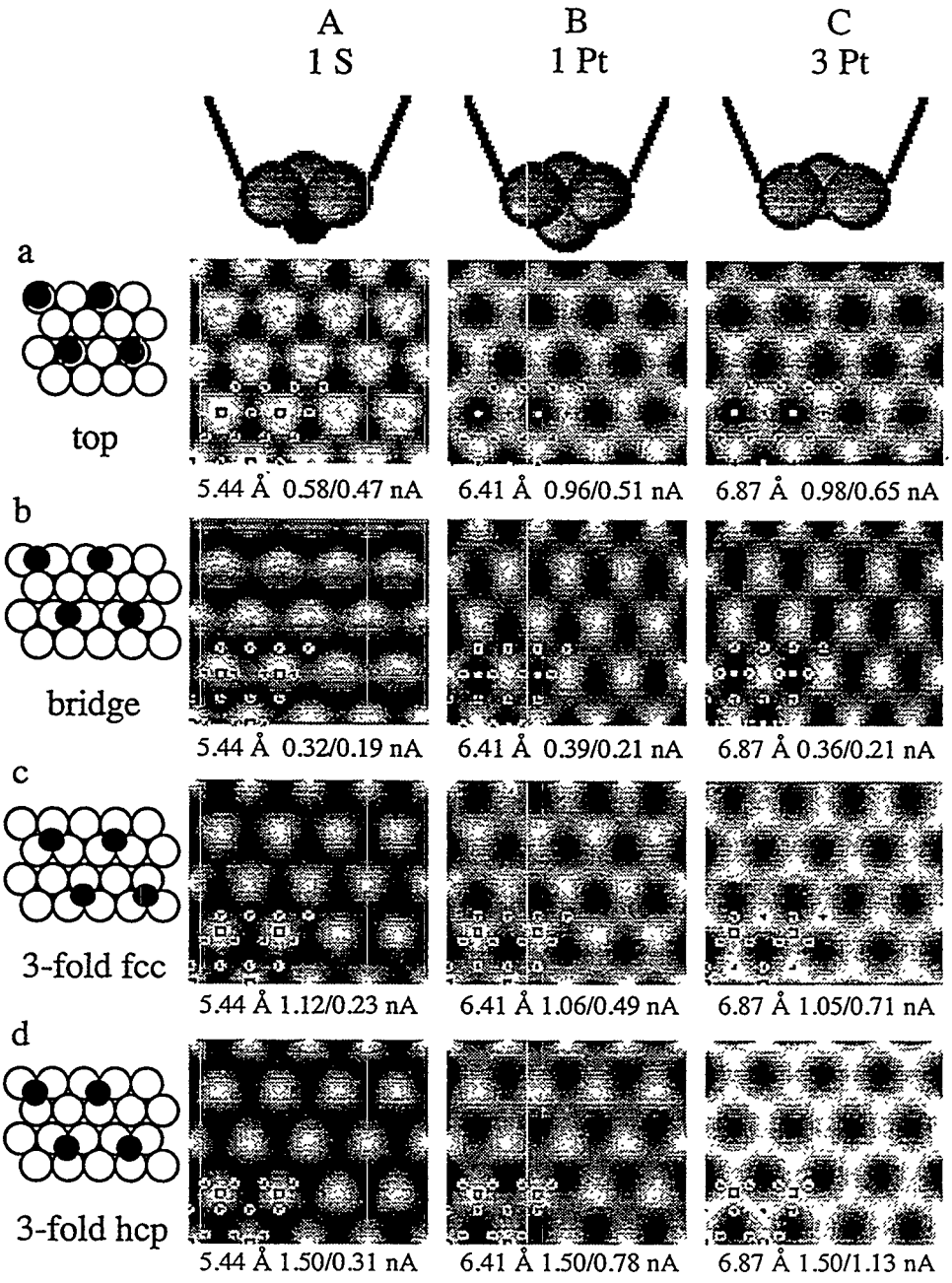

Figure 6.1 Calculated STM Images of $p(2x2)$ S on Re(0001)

Calculated STM current images for $p(2x2)$ S on Re(0001) as a function of adsorbate site: a) top, b) bridge, c) fcc hollow, and d) hcp hollow; and of tip termination: A) 1S tip, B) 1Pt tip, and C) 3Pt tip. At the top of the figure are models of the tip termination structures and on the left are models of the surface for each case. The position of S and Re atoms are indicated in the calculated images by a square and star respectively.

6.3 Dependence of the STM Image on the S Adsorption Site

Using this small set of model tips (S, Pt, and 3Pt terminated), images were calculated for a surface of $p(2x2)$ ordered sulfur atoms bound at the four high symmetry sites on the Re(0001) surface: on top of a Re surface atom, the bridge site between two Re atoms, and the fcc and hcp hollow sites between three Re atoms. These sites are shown in the models of figure 6.1. In order to limit the number of calculations, the height of the sulfur atoms at each binding site is initially set such that the S to nearest Re distance is 2.3 Å. This distance is equal to the sum of the covalent radii, which is consistent with LEED results for many chemisorption systems. The bias voltage used in these calculations was also fixed. It was matched to the experimental bias voltage, 37 mV, used in the acquisition of the images show in figure 5.4. For each tip termination, the tip height over the surface was adjusted to produce for the hcp hollow case a current of 1.5 nA at the maximum, corresponding to a gap resistance of 25 MOhm. The resulting array of calculated images is shown in figure 6.1. Each is labeled with the tip height over the adsorbate and the maximum and minimum value of the tunnel current. The images are clearly dependent on both the adsorption site of the sulfur atom and the nature and structure of the STM tip, with modifications in the image corrugation, the shape, and the position of the current maximum with respect to the sulfur lattice.

6.3.1 On Top Adsorption Site

In the case of on-top adsorption, the maximum of the image does not correspond to the position of the sulfur atom, but a position between them. A tip terminated in a single Pt atom (1Pt tip) and the two symmetric orientations of the tip terminated in a Pt trimer (3Pt tip), produce similar images with clear minima or "holes" at the sulfur positions. These images, shown in panels aB and aC of figure 6.1, have a "honeycomb" appearance, which is one of the three image shapes found experimentally (fig. 1c). However, the position of the sulfur atom at the current minimum is inconsistent with the experimental images of

vacancies or defects in the overlayer. The tip terminated in a single sulfur atom (1S tip), yields a more complicated image (panel aA) with a peculiar 3-lobe structure having a sharp minimum on its center, just above the sulfur atom. This type of image shape was never observed experimentally. The calculated images for the on-top adsorption site, therefore, are not consistent with the experimental data.

6.3.2 Bridge Site

With the same height of the tip relative to the sulfur layer, the bridge adsorption site gives rise to a significantly smaller current (see the current values under each panel of figure 6.1b). Calculation for the 1S tip yields images with asymmetric bumps and maxima that are not on the S atom, but are displaced over to an fcc hollow surface site and elongated in the bridge direction. The image is strongly modified when 1Pt or 3Pt tips are considered: the current maximum is now on a bridge site, but this site is the unoccupied bridge site on the row between the sulfur adsorbates. The image is also asymmetric with a maximum of square shape. These images are again not in agreement with the experimental results.

6.3.3 Three-fold Hollow Sites

Placing the sulfur adsorbate at either the hcp or the fcc 3-fold hollow sites gives rise to similar images with only small differences in the quantitative current values. This is due to the fact that these structures differ only in the second metal layer so their surface electronic structure is quite similar. The average current is higher with sulfur at these positions than for the on-top adsorbate position. The calculations for the 1S tip produce images with an array of round maxima centered on the sulfur atoms. The 1Pt tip produces maxima with a triangular shape with the vertices of the triangles overlapping at a triple saddle point located above a first layer Re atom for both 3-fold hollow sites. The relative current value above this Re-position is increased further in the 3Pt tip case and this position becomes the maximum in the image. The current on the sulfur atom position is still quite

high and almost equal to that of the maximum at the hcp site. The resulting shape of the STM image is a honeycomb lattice with the current nearly uniform over the ring. The main difference between these images (see cC and dC panels in figure 6.1) and the one for the on-top adsorption site (figure 6.1aB) is that the sulfur atom is located at the cross of the Y-shaped fragment of the honeycomb and not in the depression.

Thus, for the 3-fold hollow adsorption sites, the calculated images are in good agreement with the experimental data since the three types of shapes in the experimental images can be reproduced just by changing the tip composition and structure. This adsorption site is in agreement with LEED results[5] and the usual behavior of sulfur on metal surfaces.[6] Based on the STM calculations alone, it is difficult to differentiate between the hcp and the fcc hollow sites. While the tunnel current is 20-25% smaller for the fcc site at the same tip height, an equivalent change in current could be produced by a small (of order of tenths of an Ångstrom) change in tip height, which is not known to this level of accuracy.

6.4 Influence of the Height of the Sulfur Atom on the Surface

The calculations thus far have indicated that the STM images are sensitive to the binding site or xy position of the sulfur adsorbate. Now the assumption of a fixed S-Re bond length is relaxed in order to explore the sensitivity of the STM image to the height z of the adsorbed S atom. In these calculations the sulfur atom is positioned over the 3-fold hcp site. Since the adsorbate-surface distance influences the surface electronic structure, it is expected that a variation of z will modify the STM image. The calculated images in figure 6.2 show that this is indeed the case for a Pt tip. In the calculation of these images the tip distance with respect to the S layer is kept fixed at 6.41 Å. The image in figure 6.2C is for a S atom height of 1.67 Å corresponding to the S-Re bond length of 2.3 Å used in the previous calculations.

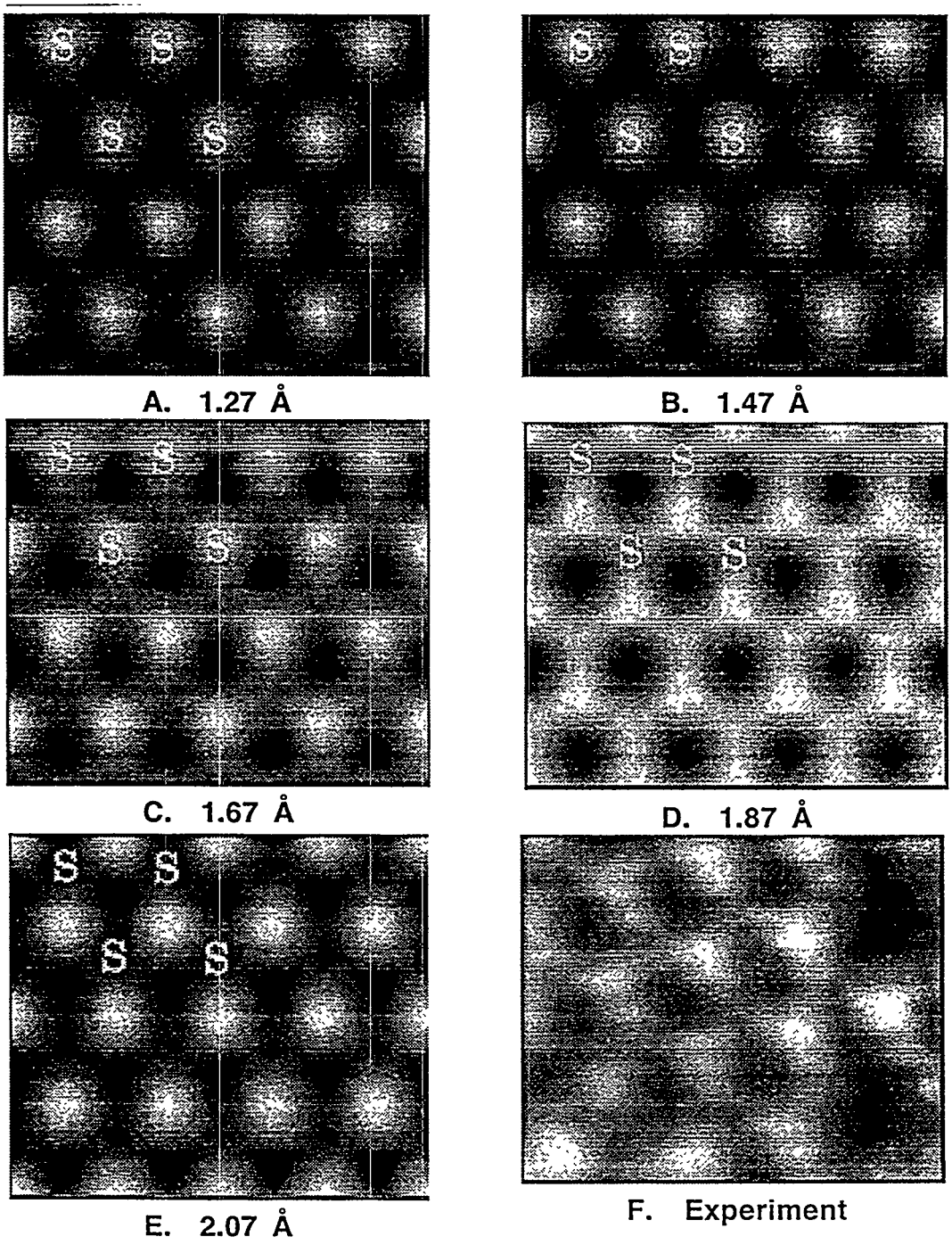

Figure 6.2 Calculated STM Images vs. Adsorbate Height

Images of $p(2x2)$ S on Re(0001) with a 1Pt tip and a five values (A-E) of the height of the S adsorbate relative to the Re surface with a fixed tip height of 6.41 Å. The sulfur atom is at the position marked by the letter S. The triangle type of experimental STM image associated with the 1Pt tip is shown in F.

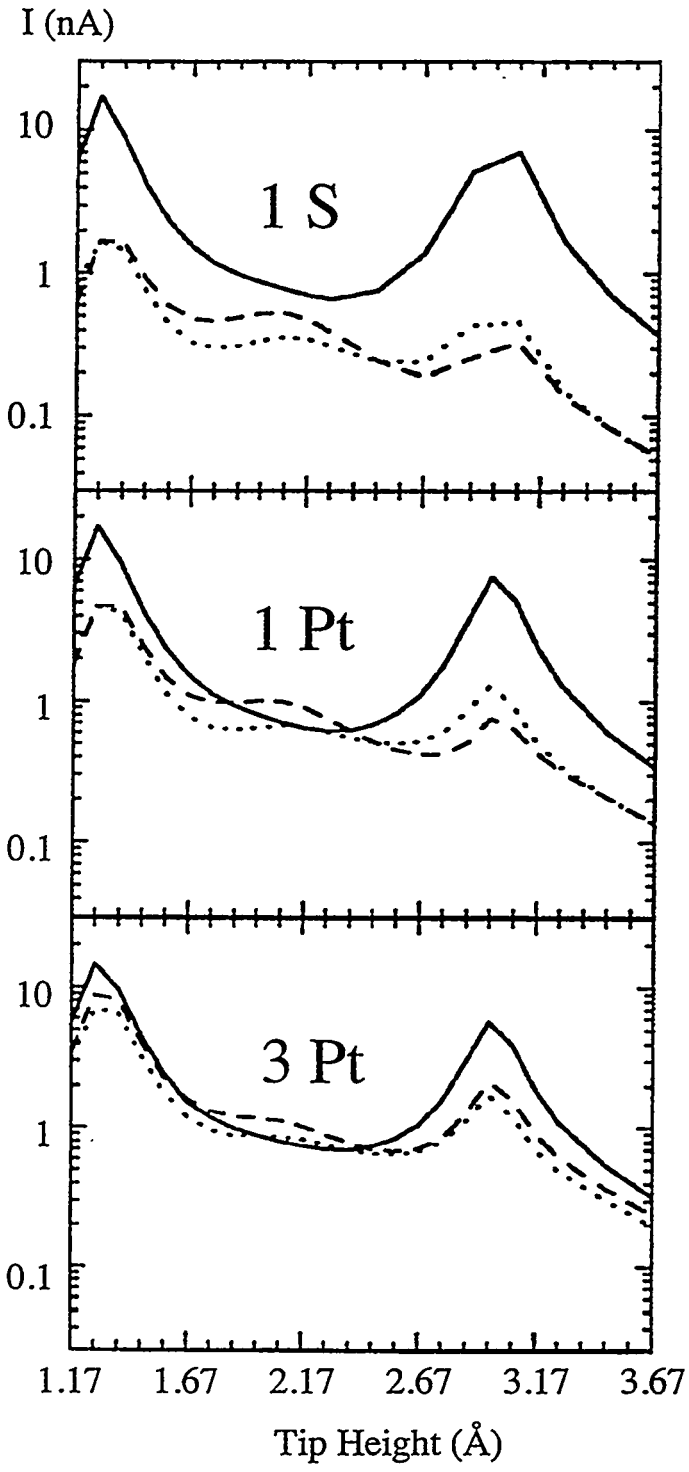

Graphs of the calculated tunneling current (in nA at a bias of 37 mV) vs. the height of the S adsorbate for three tips. The individual curves in each graph correspond to the current at three high symmetry points on the surface shown in the model below. The S position (solid line in the graph) is above a sulfur adsorbate atom, the A position (dashed line) is centered over a Re metal atom between three sulfur atoms, and the B position (dotted line) is centered between three sulfur atoms over a second layer metal atom.

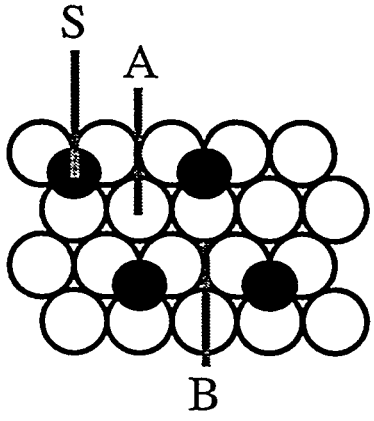

Figure 6.3 Tunneling Current vs. S Adsorbate Height

If z is reduced relative to the starting value of 1.67 Å, the triangular shape of the unit cell is gradually lost and a simple round shape is obtained (images A and B in figure 6.2). A buildup of current intensity between S atoms occurs as the S height increases, producing first images with a triangular shape, then a honeycomb image (figure 6.2D), and finally an image with round maxima (figure 6.2E) which are located between S atoms. Only for a sulfur height of 1.67 Å does the calculated image match the experimental STM image shown in figure 6.2F which is associated with the 1Pt tip. This series of images indicates that the STM is sensitive to changes in adsorbate height of approximately 0.1 Å.

Changes in the S adsorbate height also influence the image shape when the other model tips are considered. Instead of a series of images as in figure 6.2, this dependence of the image shape on z is shown in figure 6.3 as graphs of the values of the tunnel current versus z at a few high symmetry positions on the surface. These positions are on top of the adsorbed sulfur atom (S) and at the center of the triangles between the adsorbate atoms (A and B). Positions A and B are inequivalent with respect to the metal surface; position A corresponds to the site over a Re atom, while B is located over the empty 3-fold fcc site. In these calculations the tip height was individually adjusted for each tip class (1S, 1Pt, and 3Pt) such that the same current is obtained over an adsorbed sulfur atom at its nominal height (z = 1.67 Å). The graphs show complex variations in the current as a function of the adsorbate height z with at least two maxima and a general trend to decrease with z. Two competing effects lead to this behavior: As z increases, the adsorbate-tip interaction becomes larger which should increase the tunnel current. However, this increase is more than counterbalanced by a strong decrease of the coupling between the S atom and the surface. Hence STM images are strongly dependent on the height as well as the binding site of an adsorbate.

The shape of the image is readily obtained from these plots. When the current at one point dominates over that at the others, the shape is more or less round. This is the case for the 1S tip over most of the tip height range. When the current at one point is

somewhat higher than that at a second, and they dominate over the third point, the shape is a triangle. When the current at two points is nearly equal, the shape is a honeycomb. A careful analysis of the shape of the image versus the sulfur adsorbate height indicates that the experimentally observed image contrast types are only in agreement with the calculations for sulfur height in the range 1.67±0.07 Å.

6.5 Orientation and Symmetry Effects for Polyatomic Tips

The previous calculations show that the structure of the STM tip termination plays an important role in determining the image contrast. However, thus far only a very simple symmetric multiple atom tip termination has been considered as representative of all dimer and trimer tip terminations. To determine the effect of less symmetric tips on the image contrast, calculations were made with various orientations of dimer and trimer tips for sulfur bound at the hcp hollow site at the nominal height of 1.67 Å for the same gap resistance as the experiment.

Two additional parameters besides height are necessary to specify the tip-surface geometry of a trimer tip: the azimuthal angle θ around the tip axis, and the tilt angle ϕ between the plane of the Pt triangle and the surface plane. The influence of the azimuthal orientation of the 3Pt tip on the STM image is shown in figure 6.4 by plotting a shape parameter vs. the tip azimuthal angle θ. This shape parameter, $\frac{I_A - I_B}{|I_S - I_B|}$, is the ratio the tunneling current difference at the previously defined high symmetry points S, A and B. A value greater than 2/3 corresponds to a unit cell with a honeycomb shape, while the shape resembles a triangle for values between 2/3 and 1/3. As indicated in the inset, the $\theta = 0°$ value corresponds to an orientation of the 3Pt tip trimer parallel to the triangle formed by adsorbed sulfur atoms in site A and corresponds to the optimum orbital overlap at this site. It gives the highest current and shape ratio, with the current at position A being slightly higher than on the S site. If the trimer is rotated, the overlap is slowly decreased but the honeycomb shape remains until a rotation of ~40° where the shape becomes triangular.

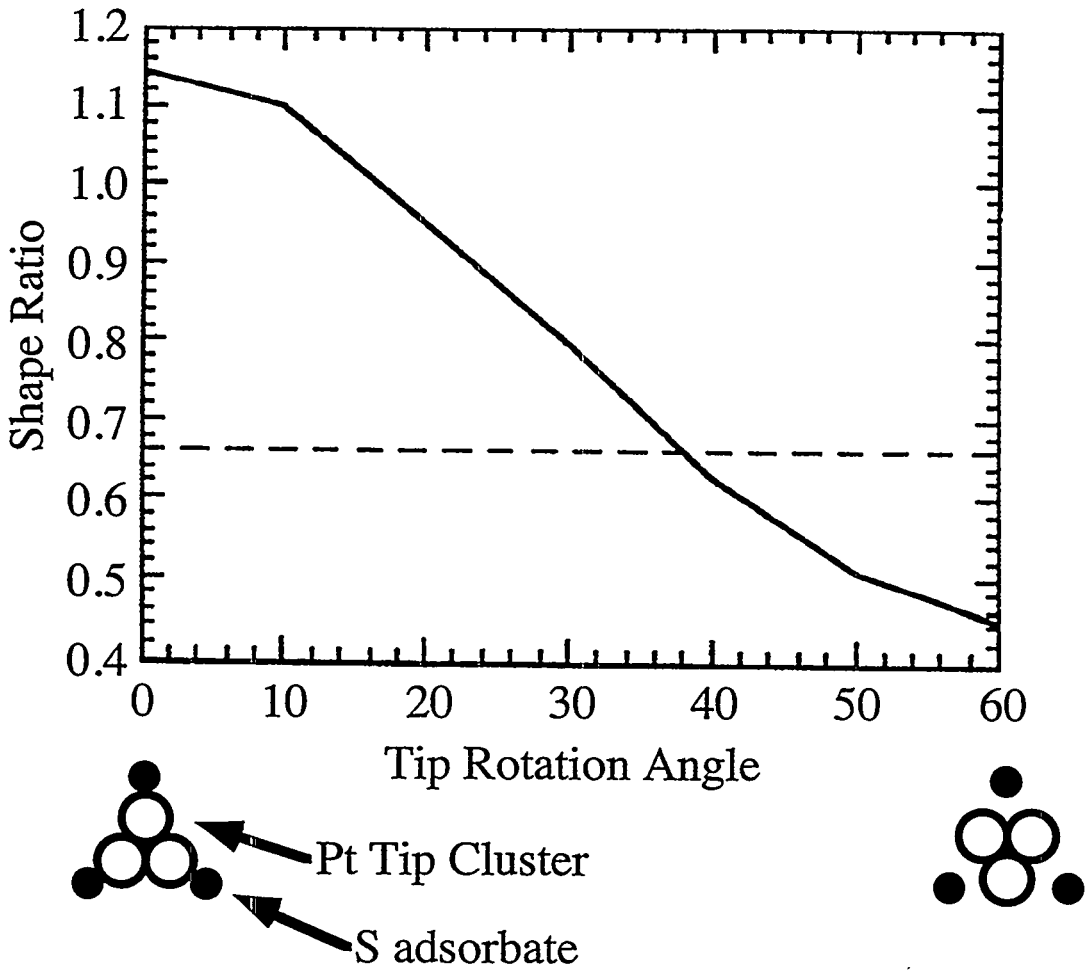

Figure 6.4 Plot of "Shape Ratio" vs. 3Pt Tip Orientation

The shape of the image unit cell is determined by the current value at high symmetry points. A ratio, $\frac{I_A - I_B}{|I_S - I_B|}$, of the tunneling current at the S, A and B positions marked in the diagram in figure 6.3 is used to determine the dependence of the shape on the orientation of the tip, for the 3Pt tip termination. The two different high symmetry orientations corresponding to 0° and 60° are shown in the schematic inset. When the shape ratio is above 2/3 (dashed line) the image has the appearance of a honeycomb. Below 2/3, the image appears as a lattice of triangles. The calculation conditions are identical to those of figure 6.1.

Thus, for 70% of all possible 3Pt tip rotations the image will appear as honeycombs, qualitatively similar to those for the non-rotated 3Pt tip; while for the other 30% of rotations the image will appear as a triangle, similar to that found for the 1Pt tip.

Small tilts ϕ of the 3Pt tip trimer do not affect the image significantly, but large tilts quickly reduce the number of Pt atoms at the apex for tunneling due to the exponential decay of the wavefunction overlap with distance. The tip is then equivalent to a 1Pt or a 2Pt tip, depending on the azimuthal angle. The calculated images for a 2Pt tip are shown in figure 6.5 for two possible orientations. In A the dimer is aligned along the lattice direction, and in B it is rotated by 30°. The corresponding images are asymmetric honeycombs where the sides of the hexagons have slightly different contrasts. As was the case for the 3Pt tip, the 2Pt tip has the same effect of increasing the current between the adsorbates. This effect is not isotropic and yields preferred directions in the image. Such distorted honeycomb images are also often observed in the experiments.

Thus, the calculation of rotated trimer and dimer tips produce results which are qualitatively similar to those for the simple symmetric tips. These results justify the earlier choice of three highly symmetric tips as representative of the tips used in the experiment.

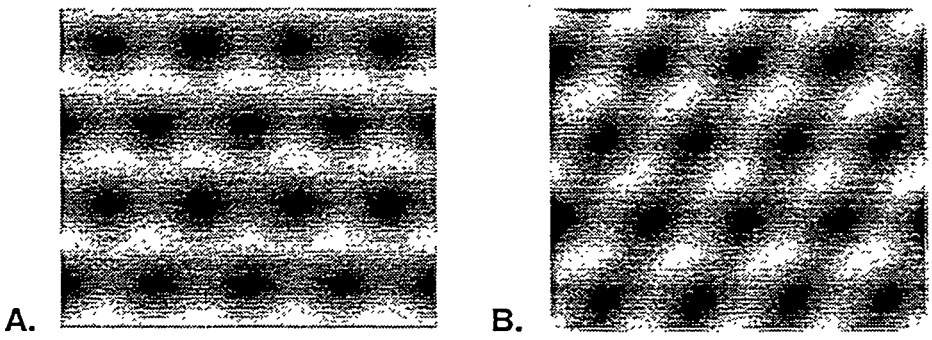

Figure 6.5 Calculated Images With a Dimer Tip

Calculated current images with a dimer 2 Pt tip parallel to the surface. The dimer is aligned (A) and rotated 30 degrees (B) with respect to the Re lattice. The calculation conditions are identical to those of figure 6.1. Distorted honeycomb images are obtained in each case.

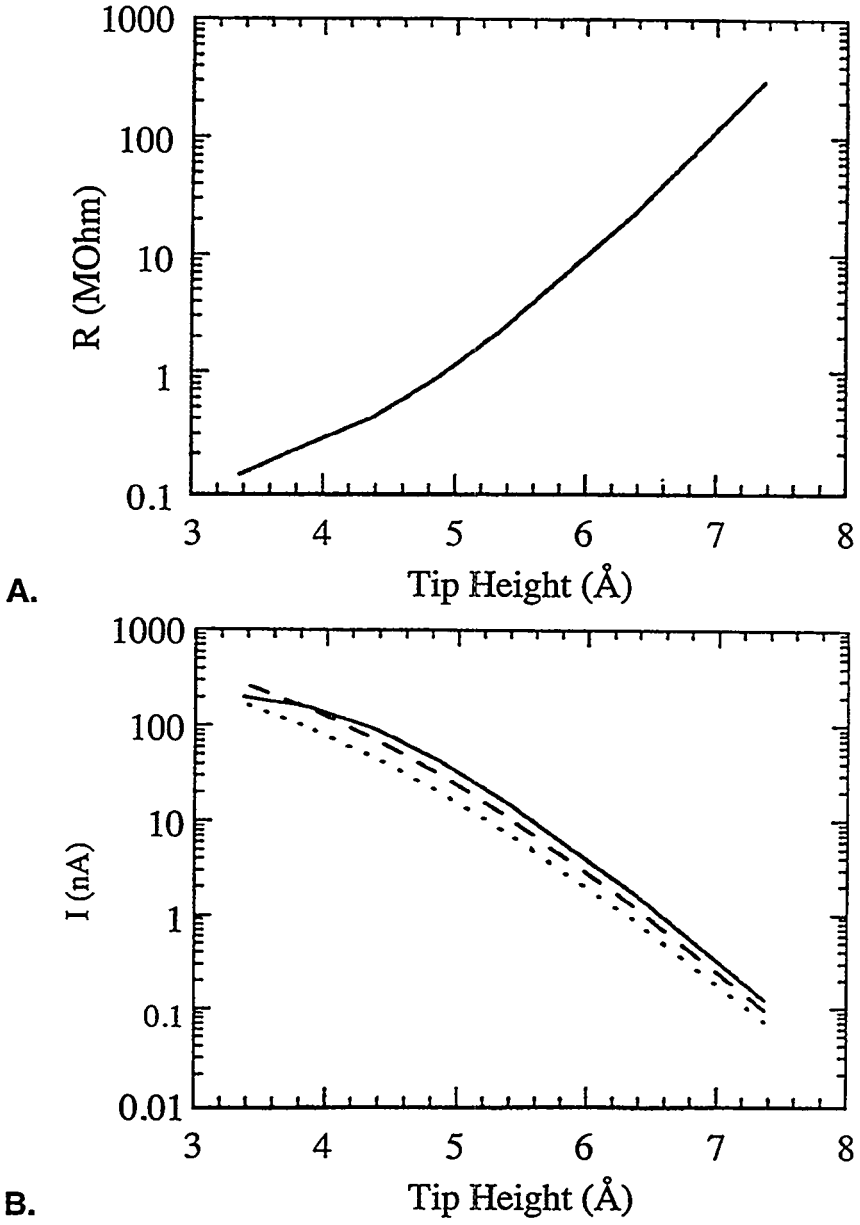

Figure 6.6 Graph of Gap Resistance vs. Tip-Adsorbate Distance

A) Calculated tunnel gap resistance (MOhm) with the tip over a sulfur atom located at an hcp three-fold hollow site as a function of tip-adsorbate distance. An ideal exponential increase is observed above 5 Å. B) The tunnel current (nA) at a bias of 37 mV as a function of tip-adsorbate distance with the tip located at the S (solid line), A (dashed line), and B (dotted line) high symmetry positions. These positions are defined in the model in figure 6.3.

6.6 Influence Of The Tunnel Gap Resistance

The images calculated so far were all constant tip height images, which means that the gap resistance and the current change within an image. However, the change in gap resistance within an image is only a factor of 2 or 3 at a gap resistance of 25 MOhm. Because of the exponential dependence of the tunnel current with distance, this 2-3 factor change in gap resistance corresponds to only a small change in the height of the tip over the surface unit cell, of the order of tenths of an Ångstrom. Now the effect of larger changes in tunneling gap resistance or tip height on the shape of the image is investigated.

The 1Pt tip, which yields the triangular unit cell images, was chosen to study the effect of tip height. First, as shown in the plots in figure 6.6A, the gap resistance was calculated as a function of tip height with the tip located over the S atom which is sitting at the three-fold hcp site. The dependence is approximately exponential at large distances with an increase of resistance of ~1 order of magnitude per Å in agreement with experimental observations.[25] A departure from this exponential law occurs for tip heights below 5 Å. The variation of gap resistance with tip height is slower in that region, indicating that the tunnel barrier height is reduced. This effect happens when there is a significant orbital overlap between tip and surface and a strong electronic interaction between the two. Lang[7] predicted a collapse of the tunnel barrier at very short distances due to substantial overlap of tip and substrate wavefunctions. It should be noted that at very short distances, elastic deformations of tip and surface might be important[8] and these are not taken into account in this calculation.

The tunnel current as a function of tip height for the 3 high symmetry positions of the tip (on top of the adsorbate S, and positions A and B between sulfur atoms) is shown in figure 6.6B. The calculated current curves are similar for the three positions and their relative positions are not modified over a large range (down to 5 Å). As a consequence, the shape of the STM image is essentially constant for tip heights larger than 5 Å. As

expected, the corrugation slowly decreases with tip height. The independence of the image shape with the tunneling gap over a wide range is consistent with the experimental results. However, the unit cell shape is modified when the tip height is below 5 Å, because the current on the S atom levels off faster than that between the S atoms. Similar contrast variation and even inversion at small tip-sample distance have been predicted in other theoretical studies.[9] However, this region corresponds to a gap resistance less than 1 MOhm which is not easily reached in the experiments. At room temperature, the tip apex is not stable enough for imaging at such a small gap resistance.

6.7 Analysis and Discussion

The previously described results indicate that tip structure and adsorbate binding position have an effect on STM image contrast. The origin of this shape variation is attributed to interference effects that appear as the result of the overlap of tip orbitals with orbitals of various adsorbate atoms. This interference effect is first directly demonstrated by comparing the cases of isolated adsorbates vs. dense overlayers. Then the contribution of the different orbitals sets to this interference effect is explored.

6.7.1 Dense Layer Versus Isolated Atom

To determine if the STM image of the $p(2x2)$ S structure is made of a simple juxtaposition of individual S-atom images, images of a fictitious $p(4x4)$ S structure were calculated. In this structure the separation between S atoms is large enough that they can be considered to be isolated. As in the previous calculations, the S atoms were placed at the hcp hollow sites. Surprisingly, for all three selected tip termination structures (1S, 1Pt, and 3Pt) the shape of the maximum in the calculated unit cell was round and it was centered over the adsorbed S atom as shown in figure 6.7. This is in striking contrast to the $p(2x2)$ layer. The only difference between the images of the $p(4x4)$ layer produced by different tips is the size of the maximum in each unit cell, which is found to reflect the size of the tip apex. It is small for the (electronically) small 1S tip, larger for the medium size 1Pt tip, and

largest for the 3Pt tip. Therefore, the unit cell shapes found experimentally (figure 5.3), are characteristic of the $p(2x2)$ packing.

This is the first time that the dependence of an STM image on the packing density of the adsorbate layer structure is evidenced. This dependence can be explained by the fact that the tip (if large enough) can interact simultaneously with 3 adsorbate atoms when located between them in the $p(2x2)$ overlayer. For the $p(4x4)$ structure the S-S distance is doubled and the single atom and 3 atoms tips cannot "feel" several adatoms simultaneously. The tunnel current on top of the S atom in the $p(4x4)$ structure is found to be about half the one for the $p(2x2)$ case at the same tip height. Apparently the six S neighbors of the S atom under the tip make a significant contribution to the tunneling current for the $p(2x2)$ which is absent in the $p(4x4)$ case. Also, the tunnel current minimum between the sulfur atoms is very low in the $p(4x4)$ structure. Thus the interference effects arising from tunneling pathways through the adsorbate and directly from the metal substrate are negligible.

The image of a dense layer can therefore be substantially different from the sum of images of isolated adsorbates due to interference effects. In certain cases the effect is even strong enough to cause a contrast reversal. For example, in the case of a hypothetical on top adsorption of the S atom, the isolated atom appears like a round maximum with a 1Pt tip as shown in figure 6.8, while in the $p(2x2)$ layer it appears as minimum (figure 6.1) (the atoms appear as "holes").

6.7.2 Analysis of the Influence of Different Adsorbate Orbitals

Since the calculation uses a basis set of atomic orbitals, it is possible to analyze the effect of each S atomic orbital in the STM image. The valence orbitals 3s, $3p_x$, $3p_y$, and $3p_z$ at each S atom can be combined to form two sets according to the C_{3v} symmetry of the hcp hollow site. The first set, of a_1 symmetry, includes s and p_z orbitals while the second set, of e symmetry, contains the p_x and p_y orbitals. In order to analyze the

influence of these orbital sets, images were calculated in which the 1Pt atom tip was allowed to electronically couple with only the orbitals of a given set on each adsorbate. More precisely, overlap and Hamiltonian matrix elements between all tip orbitals and the other orbital set on the adsorbed sulfur were set to zero, and therefore did not contribute to the current.

Figure 6.9 summarizes the results of these calculations. The main component of the current comes from the a_1 symmetry set, since it contains the p_z orbital, which extends perpendicular to the surface and can then have a substantial overlap with the tip apex. However the ($s+p_z$) orbital set alone yields an image with a "symmetric" unit cell with round maxima as seen in figure 6.9B and does not show the triangular shape characteristic of the 1Pt tip (figure 6.9A). There is only an insignificantly small intensity difference between the A and B sites. The p_x and p_y orbitals are parallel to the surface and have a nodal plane above the S atom. Therefore, they are not well suited for a large overlap with the tip. Their contribution is, however, not negligible, with a maximum value of 0.3 nA between the adsorbates and a depression at the S atom position. The associated image has also a "symmetric" unit cell and is therefore incompatible with the experimental triangular shaped unit cell.

The simple addition of the images obtained by tunneling through ($s+p_z$) and (p_x+p_y) separately is, of course, still "symmetric" as shown in figure 6.9D. It clearly follows that there is an important interference effect between these two contributions that creates the asymmetry and yields the triangular shaped image. This interference effect is displayed in figure 6.9E where the difference between the total image (figure 6.9A) and the sum of a_1 and e contribution (figure 6.9D) is shown. On the S atom the current is entirely originating from the ($s+p_z$) set. Therefore, the difference is exactly zero. On site A a constructive interference occurs between tunneling channels through the two sets of orbitals giving rise to a current that is ~0.2 nA higher than the sum of the two a_1 and e components. On the contrary, at site B the interference is destructive with a decrease of ~0.2 nA of the

tunneling current. This interference effect strongly differentiates the A and B sites on the image, thereby creating the triangular shape. The strength of these interference effects varies depending on the tip termination due to the different spatial extent of the orbital overlaps. It is small for the 1S terminated tip, quite significant for the 1Pt terminated tip (figure 6.9), and large for the 3Pt tip.

A similar orbital decomposition has been done for the hypothetical on top adsorption site. As has been shown, the calculated images for the 1Pt tip show an inverted contrast image (figure 6.10A and 6.1aB). The a_1 set alone gives a simple array of round maxima centered at the S position (figure 6.10B), and the e set yields an image of holes (figure 6.10C). However the current for the e set is now higher than for the a_1 set. This is due to the fact that there is a resonance for tunneling through the (p_x+p_y) orbitals which is closer to the Fermi level for the on top adsorption site. This makes the current higher despite the fact that the orbital overlap is still not as favorable (due to the energy level dependence of the electronic coupling). Thus the "inverted contrast" (p_x+p_y) contribution dominates and imposes its shape. In the case of the on top adsorption, the adatom layer plus the first metal layer has 6-fold symmetry, the symmetry being reduced to 3-fold only when the second layer metal atoms are included. As a consequence, the interference effect is small (4 times smaller than on the hollow site) and the simple addition of the two symmetry components is very close to the final image.

In the case of the single isolated atom, as in the (4x4) layer, there is very little interference, as indicated by the round maxima in figure 6.7. This shows that the interference of tunneling channels through the a_1 and e orbitals of the same atom is very small. Thus, it is only the overlap of $(s+p_z)$ and (p_x+p_y) orbitals at neighboring atoms in the dense layer that makes the interference effect significant.

A. 1S tip

5.44 A

0.78/0.003 nA

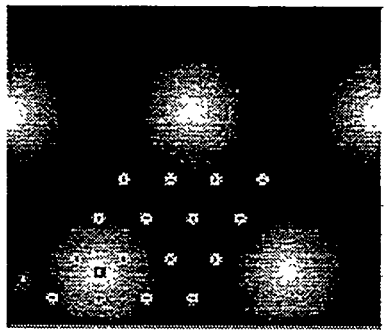

B. 1 Pt tip

6.41 Å

0.68/0.015 nA

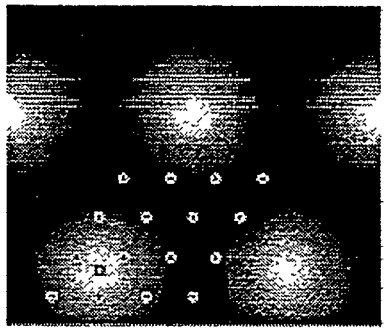

C. 3 Pt tip

6.87 Å

0.57/0.012 nA

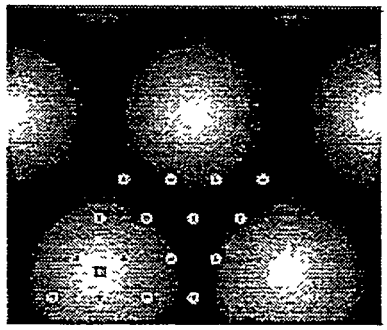

Figure 6.7 Calculated Images of a Fictitious $p(4x4)$ Layer

Current images of a fictitious $p(4x4)$ layer of sulfur in hcp hollow sites on Re(0001) calculated to simulate isolated adsorbate atoms. The same conditions are used in this calculation as in figure 6.1 The tip termination structure, height of the tip apex relative to the adsorbate, and the maximum/minimum current values are given for each image. This result shows that the differences is shape seen in figure 6.1 disappear when simultaneous overlap of more than one sulfur atom with the tip becomes negligible.

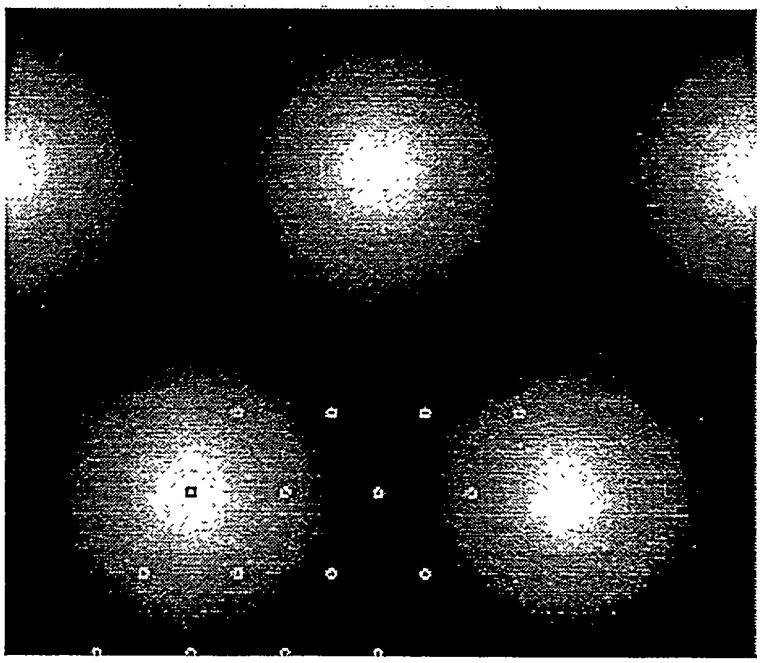

Figure 6.8 Calculated Images of a Fictitious $p(4x4)$ Layer of Sulfur in Top Sites

Calculated current STM images of a fictitious $p(4x4)$ layer of sulfur in top sites on Re(0001) with a 1Pt tip. The same calculation conditions are used as in figure 6.1. The contrast reversal of figure 6.1aB disappears, indicating that the origin is due to interferences that appear as a result of S-S orbital overlap.

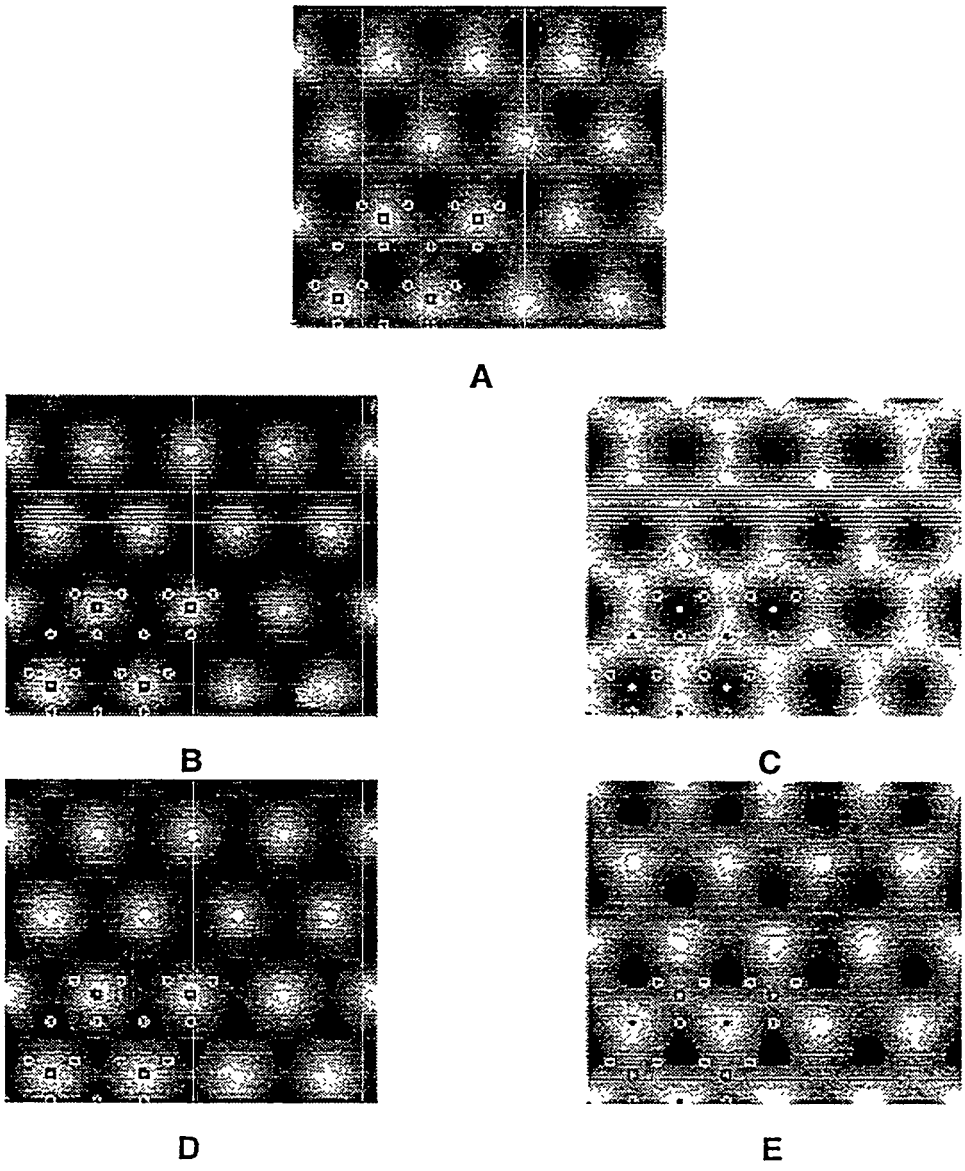

Figure 6.9 Orbital Decomposition of the Image of S on Re(0001)

The S sits on the three-fold hcp site and the tip terminates in one Pt atom. A) Calculated images with all sulfur orbitals included. B) Only the sulfur atomic orbitals of a_1 symmetry are used (s and p_z). C) Only the orbitals of e symmetry (p_x and p_y). D) The composite image formed by the sum of B and C. The triangular symmetry shape of the complete image A is not reproduced. E) Difference image A minus D showing the contribution of interference effects to the image. The tip height is 6.41 Å.

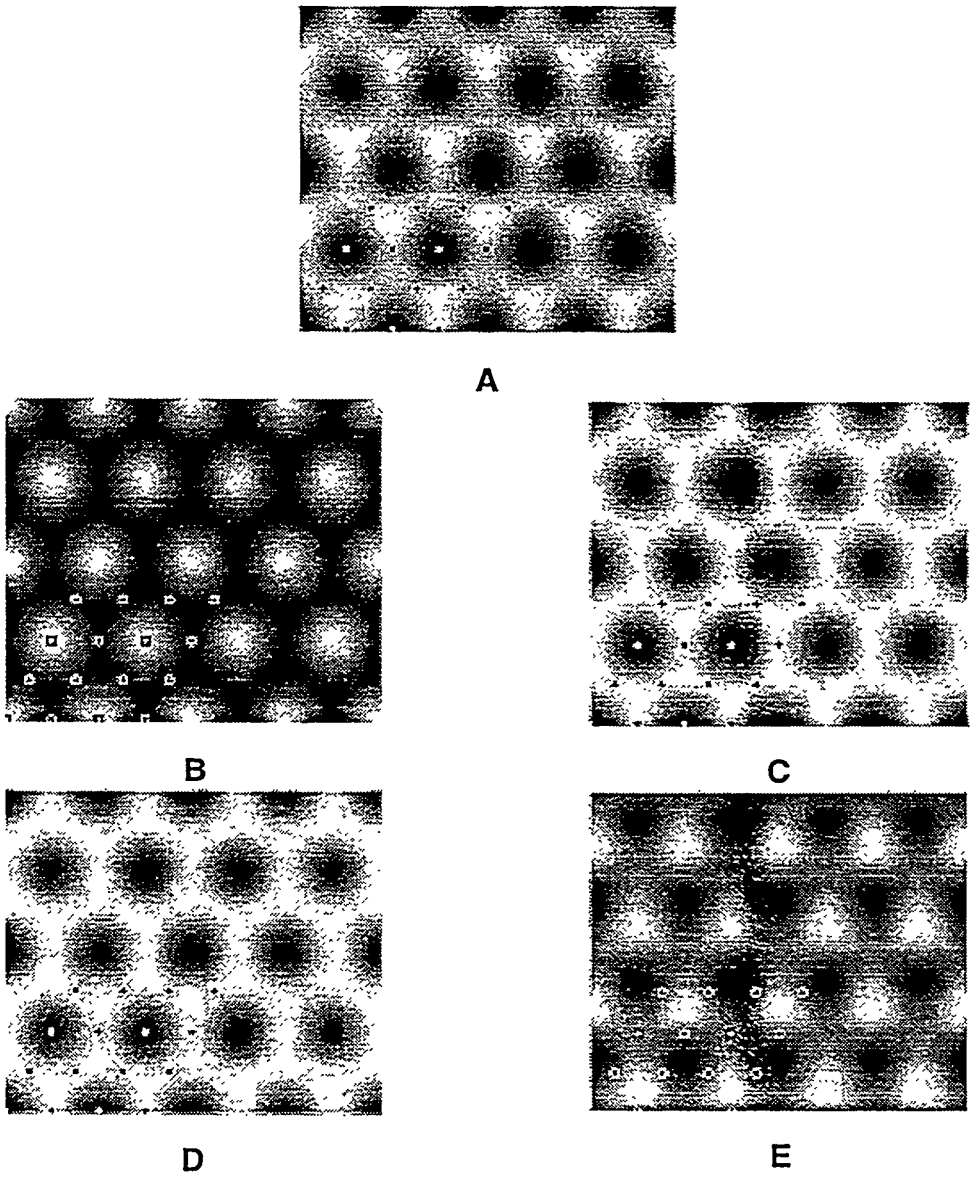

Figure 6.10 Orbital Decomposition for a Hypothetical Top Site Adsorption

Orbital decomposition of the $p(2x2)$ S on Re(0001) for a hypothetical on top adsorption site and a 1 Pt tip: A) total image. B) only a_1 sulfur orbitals are used. C) only e orbitals are used. D) sum of B and C E) the difference of A and D showing the contribution of the interference term in the tunneling current.

The fact that image shape comes about through this interference effect explains why changing the height of the adsorbate on the surface produces a large change in the image, while small changes in the composition (Pt, Rh, or Re) and binding height of the atom on the tip end have only a small effect on the image. Since the atoms on the surface are part of a dense layer, changing their binding site or height modifies the interference effect by changing their overlap with the tip. However, since the tip termination is not part of a dense layer, changing the precise termination structure has little effect on the interferences which control the image shape.

6.8 Conclusion

The ESQC theoretical approach has shown great potential in predicting the shape of STM images. The calculations are able to accurately predict the different experimental images and explain them as being a result of imaging with several different simple STM tip terminations. Additionally, the theory is able to answer questions as to what parameters affect the contrast of STM images. Both the binding site and height of the S adsorbate over the surface was shown to strongly influence the image contrast, while the tunneling gap resistance had little effect over a wide range. This indicates that it potentially possible to extract information on the atomic position of adsorbate atoms from the contrast within the unit cell of STM images.

The ESQC theory is also able to explain how the shape of the images comes about. The shape is a result of the complex interactions between the tip orbitals and the orbitals from the surface atoms that involve interference effects when these orbitals couple through nearest neighbor interactions. The variation in the image with the tip structure is a result of changes in the "electronic size" of the tip, where "small" atoms (S and C) overlap less efficiently with several adsorbate atoms than larger tips (Pt and 3Pt), producing different interferences. Therefore, these interference effects are absent in the case of well separated adsorbates where the tip orbitals only overlap with one adsorbate atom at a time. Changes in the surface structure (binding height and site of the adsorbate atom) also modify these

interferences. Additionally, the surface structure influences the electronic spectrum of the surface and the energy position relative to the Fermi level of the tunneling current resonances through the gap.

Because all the multiple scattering contributions are included in the calculation, as well as all the symmetry elements of the tip and surface structure, the ESQC method shows a great promise for site determination and perhaps also for binding height determination. It is important to ascertain the degree of numerical accuracy of the method by testing it on surfaces of well known geometry, determined by well proven diffraction techniques (e.g. LEED). Some work in this area is discussed in chapter 8.

Chapter 6 References

[1] J. Tersoff and D.R. Hamann, Phys. Rev. Lett. **50** (1983) 1998.

[2] J.A. Stroscio and D.M. Eigler, Science **254** (1991) 1319.

[3] M. Salmeron, D.F. Ogletree, H.-C. Wang, G. Neubauer, W. Kolbe and G. Meyers, J. Vac. Sci. Technol. B **9** (1991) 1347.

[4] L. Ruan, F. Besenbacher, I. Stensgaard and E. Laegsaard, Phys. Rev. Lett. **70** (1993) 4079.

[5] A. Barbieri, D. Jentz, N. Materer, G. Held, J. Dunphy, D.F. Ogletree, P. Sautet, M. Salmeron, M.A. Vanhove and G.A. Somorjai, Surf. Sci. **312** (1994) 10.

[6] J.M. MacLauren, J.B. Pendry, P.J. Rous, D.K. Saldin, G.A. Somorjai, M.A.V. Hove and D.D. Vvedensky. *A Handbook of Surface Structures*. (D. Reidel, Holland, 1987).

[7] N.D. Lang, Phys. Rev. B **47** (1988) 9778.

[8] M. Salmeron, D.F. Ogletree, C. Ocal, H.-C. Wang, G. Neubauer, W. Kolbe and G. Meyers, J. Vac. Sci. Technol. B **9** (1991) 1347.

[9] G. Doyen, D. Drakova and M. Scheffler, Phys. Rev. B **47** (1993) 9778.

Chapter 7. SURFACE CRYSTALLOGRAPHY OF S ON Mo(100)

7.1 Introduction

Molybdenum single crystals surfaces are of interest as a model for industrial molybdenum sulfide catalysts.[1, 2] A number of studies[1-10] have been published on the sulfided Mo(100) surface. These studies have determined that sulfur forms several ordered structures as a function of coverage. While early reports[4-7] conflicted over the order and number of distinct LEED patterns, more recent results[3, 8-10] agree on four LEED patterns and the sulfur coverage at which they appear. However, except for the $c(2x2)$ ordered overlayer, the structures of the unit cells which produce these LEED patterns are unknown. Several models have been proposed[4-6] for each of the other overlayers. STM, by providing information complimentary to the LEED results, should be of help in determining which of the proposed models is correct.

The most recently published studies[3, 8-10] of S on Mo(100) agree on four ordered structures. At a coverage of approximately 0.5, 0.67, 0.75 and 1 monolayer of sulfur the reported LEED patterns have $c(2x2)$, $\begin{bmatrix} 2 & \bar{1} \\ 1 & 1 \end{bmatrix}$, $c(4x2)$, and $p(2x1)$ symmetry. These coverage values correspond to one, two, three, and two atoms per unit cell respectively. A LEED calculation performed on the $c(2x2)$ structure determined that the sulfur atoms reside at four-fold hollow sites.[6] Later a dynamical LEED[11] and tensor LEED[12, 13] calculations determined the precise position of the sulfur adatoms and the displacements of the substrate Mo surface atoms in this structure. Dynamical LEED calculations have also been attempted for the $p(2x1)$ overlayer, but an adequate fit between the calculation and experimental I(V) curves has not been obtained.[14] A previous STM study[15] of this structure in air favored a model with all sulfur atoms occupying an asymmetric site between hollow and bridge. However the symmetry of this structure would cause the extinction of some spots in the LEED pattern which is not observed

experimentally. A total energy calculation favored a model with half the sulfur atoms in hollow sites and the other half in bridge sites.[16]

The four structures were prepared and imaged by STM. Models with sulfur atoms adsorbed at bridge and hollow sites were considered in the analysis of the STM images. Unfortunately, it is not possible to directly determine which of these structures is correct. Although the unit cell periodicity is resolved by the STM, the constituent atoms are not always resolved individually except in the simple $c(2x2)$ structure. However, proposed structures could be eliminated from consideration by showing them to be incompatible with observations of the symmetry of the overlayer and of point defects and domain boundaries.

7.2 Mo Sample Preparation

The single crystal sample was prepared using the methods generally described in chapter 3. It was approximately one centimeter in diameter and less than one millimeter thick. After orientation to within less than 1.5° of the [100] direction and polishing, it was cleaned in UHV. Carbon and other impurities were removed by sputtering while heating to approximately 600 K. The carbon remaining after this treatment was removed by repeated heating in oxygen (5×10^{-7} Torr at 1600 K). The remaining oxygen was removed by heating the crystals in UHV above 1900 K. Careful cleaning of the crystal was important to insure that only sulfur structures were imaged with the STM. Carbon and oxygen, the most common impurities on the surface, form ordered structures with some of the same LEED patterns as sulfur. Unless the bulk is depleted of these impurities to a sufficient degree, they will segregate back to the surface while the crystal is cooled.

Sulfur was deposited on the clean surface immediately after cleaning to reduce the adsorption of the residual gasses in UHV. While the lower coverage structures could be produced easily by H_2S exposure, the solid-state electrochemical source[17] was necessary to cover the surface with enough sulfur to produce the highest coverage $p(2x1)$ overlayer. The crystal was heated during exposure to H_2S gas, while it was kept at room temperature during exposure to sulfur from the electrochemical source.

Prior to imaging of the sulfur overlayer, AES was used to determine the sulfur coverage on the surface. The sample was annealed to produce an ordered LEED pattern. STM images of the surface were obtained using several different tips and preparations of each structure. A total of several hundred STM images of the overlayer structures were obtained.

The surface was imaged in both constant current (topographic) and constant height mode. In most of the images the sample was biased negative relative to the tip. Changing the polarity of the bias was found to have no effect on the images. The tunneling current was set at between 1 and 3 nA and the bias voltage between 10 and 100 mV. Decreasing the gap resistance tended to increase the corrugation of the sulfur structures. Changing the bias had little effect on the image as long as the tunneling gap resistance was kept constant.

7.3 Thermal Drift Correction

Thermally induced drifts of the sample during imaging significantly distorted the images, particularly the topographic mode images that require longer acquisition time. This distortion made determination from the raw data of the registry between different domains of the sulfur overlayer difficult. The correct shape and size of the images was determined from current mode images acquired quickly enough so that the drift had little effect on them. Using this information, the topographic images were replotted with the correct shape using a two dimensional second order fit of the lattice.

The thermal drift correction procedure was performed on an IBM RS6000 workstation using a custom image processing code. First, the equivalent points on the image were located by finding the maxima in an autocorrelation map calculated from the image data. The autocorrelation image is calculated with

$$C(\vec{r}) = \sum_i \left(Z(\vec{r}_i - \vec{r}_o) - Z(\vec{r}_i - \vec{r}) \right)^2 \quad (7.1)$$

Here, $Z(\vec{r})$ is the topographic image data and the sum is over a small set of vectors $\vec{r}_i$ making up an area of one to four unit cells of the overlayer. This formula expresses the

correlation between a small region surrounding each pixel of the image and an equivalent region of the image selected as representative of the overlayer. This representative area, the pixels at $\vec{r}_i + \vec{r}_o$ surrounding $\vec{r}_o$, consisted of one to four unit cells of the overlayer which did not include any defects or noise spikes. The resulting correlation map is a representation of how similar is the region surrounding any point on the image to the selected representative area. The maxima of this representation form a lattice with the periodicity of the overlayer as the image is self-similar with this periodicity. These points were located and their positions in the data-space of the image (pixel location) was recorded.

The relative positions of the maxima in real space is determined by estimating the size of the lattice in pixels, and this estimate is used to calculate the distance in real space between near neighbors in the lattice of correlation image maxima. As shown in figure 7.1, if sulfur atoms are only located at bridge, hollow, and top sites, the distance between equivalent points in the image must be a linear combination of an integer number of half of the two Mo surface lattice vectors. The real space separation between maxima was rounded off to the nearest such vector. Having identified the locations of the maxima in both real space and pixel space, a twelve parameter second order two dimensional least squares fit was made for the transform between these spaces. The transform between the two spaces is described by

$$\begin{aligned} X &= P_0 + P_1 x + P_2 y + P_3 x^2 + P_4 y^2 + P_5 xy \\ Y &= P_6 + P_7 x + P_8 y + P_{10} x^2 + P_{11} y^2 + P_{12} xy \end{aligned} \qquad (7.2)$$

This fit was then used to remap the image into real space correcting for the non constant thermal drift and piezoelectric hysteresis. The resulting images are completely square with the Mo lattice [001] directions aligned along the x and y directions of the image. On the corrected images the distances between points and registry between lattices in the corrected images can be accurately determined. The images shown in this chapter have all been remapped with this technique.

7.4 Structures of S on Mo(100)

7.4.1 The $c(2x2)$ Structure

Images of the Mo(100) surface with half a monolayer of sulfur and a $c(2x2)$ LEED pattern show ordered regions with an atomic corrugation of approximately 0.2 Å which are approximately 20 - 50 Å across separated by partially ordered regions. The boundaries between these regions run in the [010] directions of the substrate. The partially ordered regions contained maxima with approximately 0.8 Å corrugation which were commonly, but not always, spaced by twice the Mo lattice constant a of 3.15 Å. As the AES spectrum showed little carbon or oxygen contamination and the disordered regions were common on the surface, it is likely that these areas are covered by a different structure of sulfur and not an impurity. They probably consist of sulfur which has not ordered into the $c(2x2)$ structure due to insufficient annealing or too low a sulfur coverage. These regions may produce the $p(2x2)$ and $c(4x4)$ LEED patterns which have been reported by some

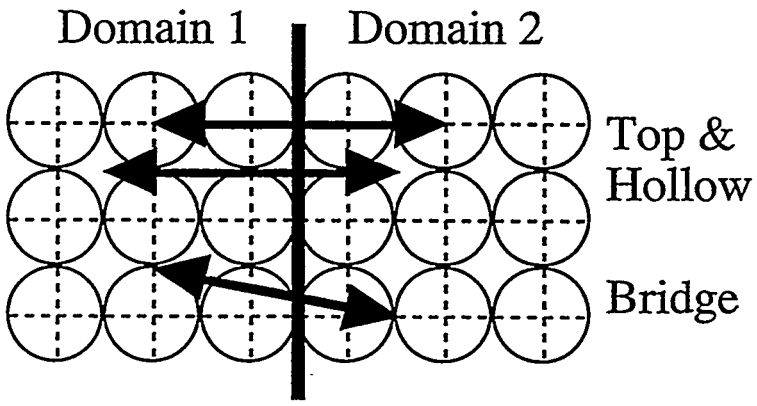

Figure 7.1 Separation of High Symmetry Sites

A model of the Mo(100) surface showing the separation between high symmetry sites in two domains rotated by 90° relative to each other. A $(1x1)$ lattice aligned on the four-fold symmetric top or hollow sites remains on the same points after a rotation through 90°. Conversely, a lattice aligned on bridge sites is displaced by a lattice vector of $\left[0,\pm\frac{a}{2},\pm\frac{a}{2}\right]$ after a 90° rotation.

authors[6-8] at a coverage well under half a monolayer.

An example of an image of an ordered region of this surface is shown in figure 7.2. The structure in the image is consistent with the observed LEED pattern. Rows of nearest neighbor maxima run at 45° to the lattice directions of the substrate. Also the measured spacing between the maxima is within 10% of the 4.7 Å nearest neighbor distance of a $c(2x2)$ overlayer. The corrugation of the maxima in this image is 0.22 Å. Occasionally images of the $c(2x2)$ structure were obtained which contained a smaller secondary maximum at the center of four primary maxima. We believe that these images were produced by a different tip end structure and/or composition. Point defects in the images always appeared as a missing maximum. This demonstrates that the primary maxima in the image corresponds to the location of the sulfur atoms, in agreement with the positive corrugation observed for sulfur on other metal surfaces.[18-21]

As described previously, several LEED studies [3, 11, 12] of this surface placed the sulfur atom in each unit cell at a four-fold hollow site as shown in figure 7.3. The STM images are consistent with this result. The maxima in the images have four-fold symmetry, which is inconsistent with any sulfur bonding sites except the hollow and top. Additionally, if the sulfur atoms reside at any site other than the hollow or the top site there would be at least two domains of this structure inequivalent except by a rotation by 90°. Sulfur atoms in these two domains should be separated across the boundary by half-integer lattice vectors as shown in figure 7.1. While many domain boundaries were observed in images of the $c(2x2)$ structure, the maxima in the image were always found to be separated by an integer number of lattice vectors across these boundaries. While the top site is consistent with the symmetry of the images, sulfur has never been found to bind at these sites on any metal surfaces,[22] so we consider this site unlikely.

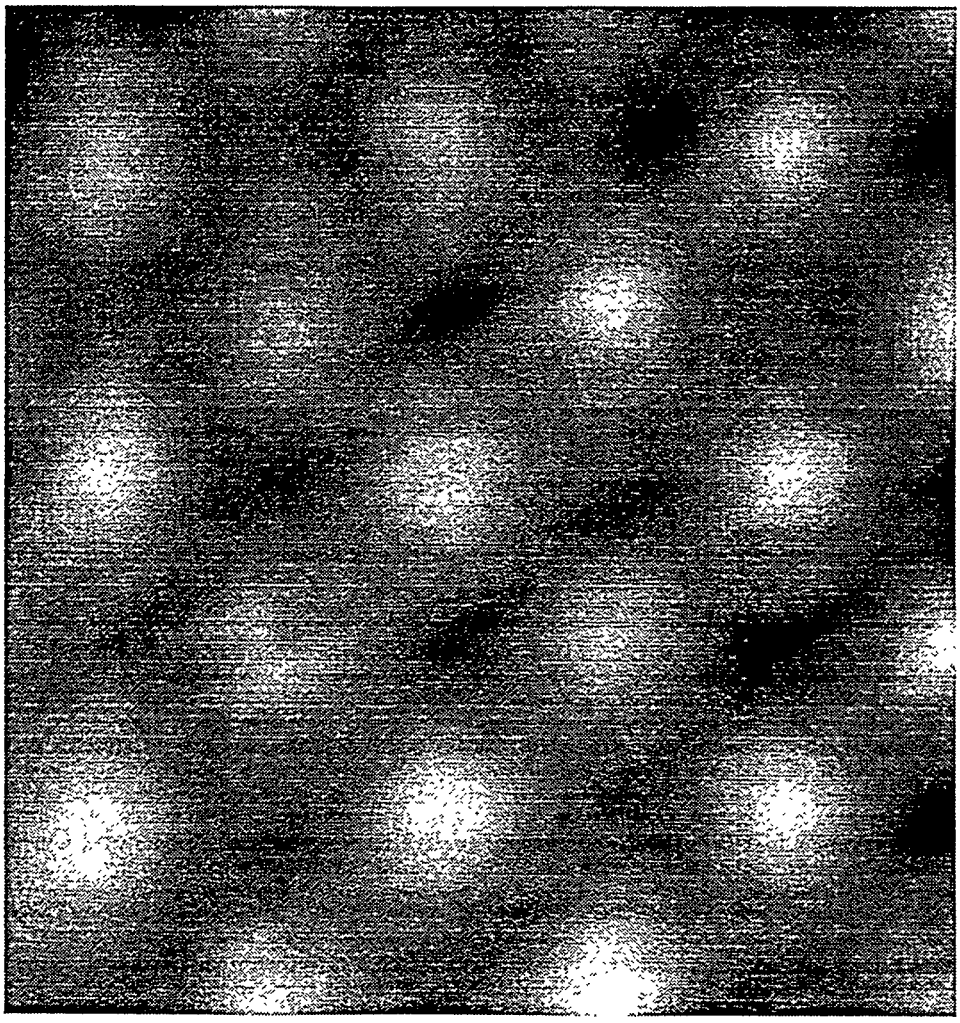

Figure 7.2 A Topographic STM Image of the $c(2x2)$ Structure An 18 Å X 19 Å topographic STM image of the $c(2x2)$ structure of S on Mo(100). The lattice directions of the Mo substrate are the horizontal and vertical directions in the image. The bright maxima in the image are 0.22Å in height. Point defects appear as missing maxima in STM images indicating that these maxima correspond to the position of sulfur atoms on the surface. Bias = 15mV, I = 1.0nA.

7.4.2 The $\begin{bmatrix} 2 & \bar{1} \\ 1 & 1 \end{bmatrix}$ Structure

It was difficult to obtain the proper sulfur coverage to produce a surface with a LEED pattern with only the spots of the $\begin{bmatrix} 2 & \bar{1} \\ 1 & 1 \end{bmatrix}$ structure and no spots from either the $c(2x2)$ or $c(4x2)$ structures. In STM images the surface was always covered with domains of the $\begin{bmatrix} 2 & \bar{1} \\ 1 & 1 \end{bmatrix}$ structure intermixed with areas of $c(2x2)$ or $c(4x2)$ ordered sulfur. An image of an area with the $\begin{bmatrix} 2 & \bar{1} \\ 1 & 1 \end{bmatrix}$ structure is shown in figure 7.4. The rows of maxima in this image run in the [011] direction and are separated by three Mo lattice spacing distances a in the [001] directions, as expected from the symmetry. The rows' appearance was dependent on the STM tip. Sometimes individual atoms within the rows were not resolved and they appeared instead as a bright bar. On other occasions, the rows contained half as many maxima as there are atoms in the overlayer. In contrast, the image shown in figure 7.4 contains one maxima for each atom of the overlayer.

There are three possible high symmetry models for the $\begin{bmatrix} 2 & \bar{1} \\ 1 & 1 \end{bmatrix}$ structure consisting of bridge and hollow sites. These are shown in figure 7.5. Without knowing the contrast of atoms in the overlayer it is impossible to determine which of these models is correct. If we assume that, as in the $c(2x2)$ structure, the sulfur atoms have positive corrugation, the

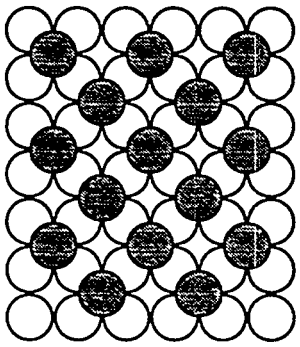

The white circles represent the surface layer of Mo. The sulfur atoms, indicated by shaded circles fill one half of the four-fold hollow sites.

Figure 7.3 A Model of the Hollow Site $c(2x2)$ Overlayer

rows of sulfur atoms in figure 7.5A and 7.5C could correspond to the rows in the image. However, the rows of bridge sites in model B could also produce the rows in the image due to an asymmetric STM tip termination. The observed variations in the experimental shape of the rows can be explained in all cases as the effect of a particular tip structure and are not helpful in determining the correct unit cell structure.

Since the $\begin{bmatrix} 2 & \bar{1} \\ 1 & 1 \end{bmatrix}$ structure coexisted on the surface with the $c(2x2)$ and $c(4x2)$ structures it was possible to determine the relative position of the rows and the maxima of the $c(2x2)$ overlayer in the STM images. Figure 7.6 shows an image of the boundary region between both structures. In this image the $c(2x2)$ domain occupies the upper left hand side and its maxima have a low average intensity. A single row of the $\begin{bmatrix} 2 & \bar{1} \\ 1 & 1 \end{bmatrix}$ structure appears running diagonally up on the right hand side. The intensity is higher in this region. A $(1x1)$ grid is drawn over the image aligned to the maxima in the $c(2x2)$ domain. If the hollow site $c(2x2)$ model is correct, the top Mo substrate atoms are located at the center of the squares of the grid. The maxima in the rows of the $\begin{bmatrix} 2 & \bar{1} \\ 1 & 1 \end{bmatrix}$ structure appear to be centered over hollow sites of this lattice. This position is consistent with model A. However as we have not yet ascertained that sulfur atoms have positive corrugation in this structure, the result is not completely conclusive.

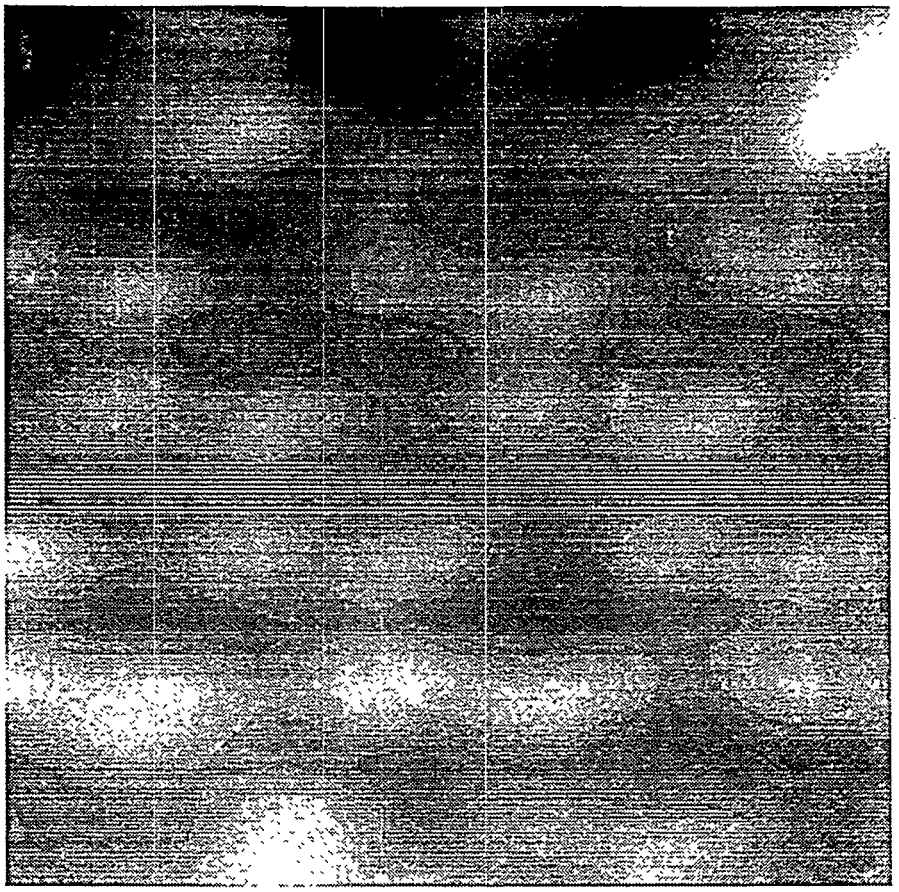

Figure 7.4 A Topographic Image of the $\begin{bmatrix} 2 & \bar{1} \\ 1 & 1 \end{bmatrix}$ Structure

A 20 Å square STM topographic image of the $\begin{bmatrix} 2 & \bar{1} \\ 1 & 1 \end{bmatrix}$ structure of S on Mo(100). One maximum is visible in the image for each adsorbed sulfur atom on the surface.

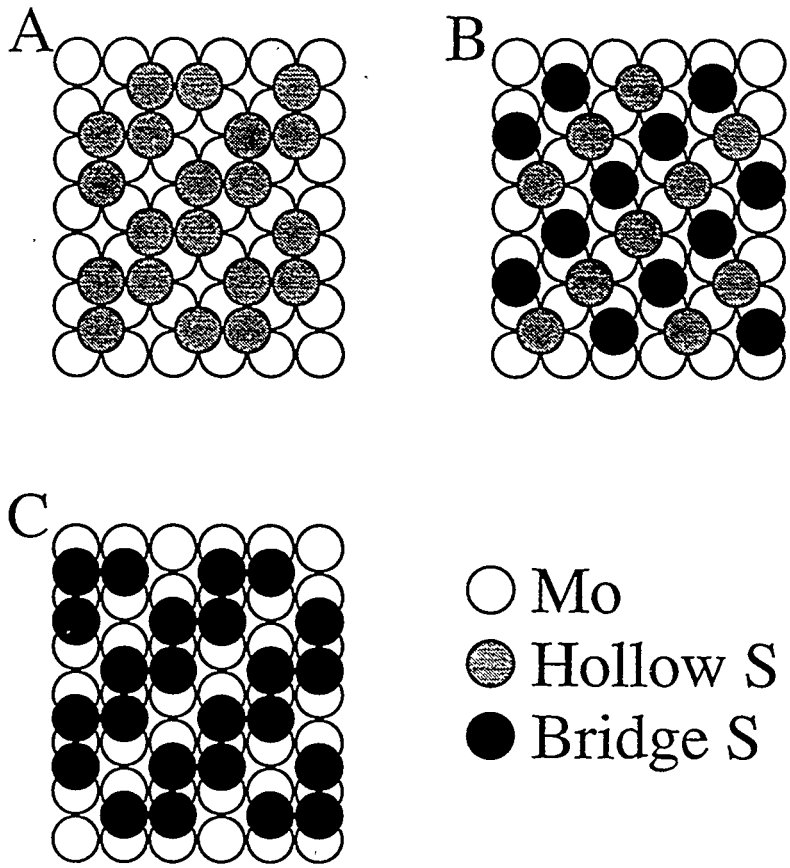

Figure 7.5 Three Models of the $\begin{bmatrix} 2 & \bar{1} \\ 1 & 1 \end{bmatrix}$ Structure

Three models of the $\begin{bmatrix} 2 & \bar{1} \\ 1 & 1 \end{bmatrix}$ structure with sulfur atoms at bridge and hollow sites. A) All sulfur atoms at hollow site. B) A mixture of hollow and bridge sites. C) All sulfur atoms at bridge sites.

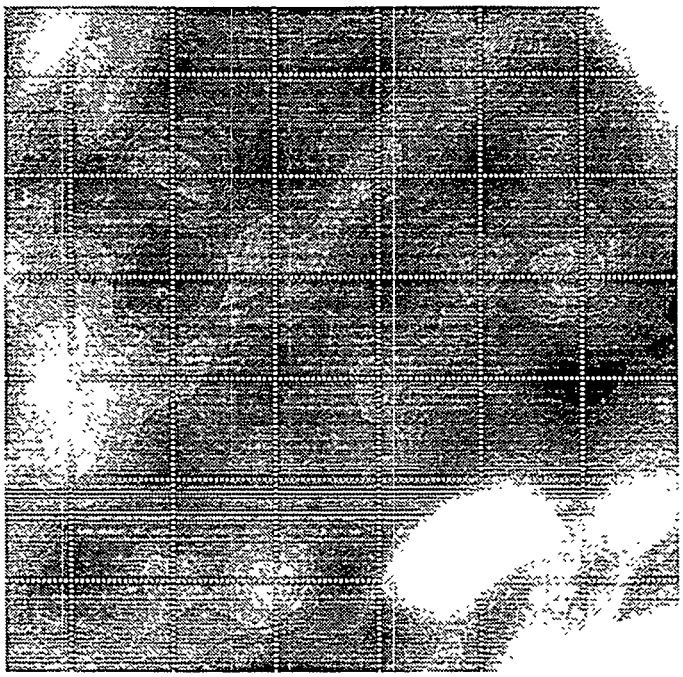

Figure 7.6 A Boundary of Two Domains of the $\begin{bmatrix} 2 & \bar{1} \\ 1 & 1 \end{bmatrix}$ Structure

A 20 Å square topographic STM image showing a single row of the $\begin{bmatrix} 2 & \bar{1} \\ 1 & 1 \end{bmatrix}$ structure (on the right) adjacent to a $c(2x2)$ ordered region (upper left). A $(1x1)$ grid is drawn over the image and aligned to maxima of the $c(2x2)$ overlayer. The cross marks on the grid are therefore positioned over four-fold hollow sites of the substrate. The grid shows that the maxima of the $\begin{bmatrix} 2 & \bar{1} \\ 1 & 1 \end{bmatrix}$ structure appear to be centered over hollow sites. The bright spots on the right side of the image are defects in the overlayer.

7.4.3 The $c(4x2)$ Structure

At a coverage of approximately three quarters of a monolayer a sharp $c(4x2)$ LEED pattern was obtained. STM images of the surface showed it was covered with ordered domains of approximately 100 Å in size. An example of an image of a single domain is shown in figure 7.7. The staggered vertical rows of maxima in the figure are separated by twice the Mo lattice vectors. The maxima along the rows are also separated by this distance. The symmetry of the maxima in this images is $c(4x2)$, consistent with the LEED pattern. There are two perpendicular mirror planes in each unit cell of the STM image which run through the maxima in the unit cells. Six possible model structures, shown in figure 7.8, have these two mirror planes and contain the three atoms per unit cell required to have 0.75 monolayers coverage. In models A-C the perpendicular mirror planes cross at hollow sites while in models D-F they cross at bridge sites.

Half of these models can be discarded by observing the symmetry of domain boundaries in this structure. An image of the boundary between two domains of $c(4x2)$ ordered sulfur rotated by 90° relative to each other ($c(4x2)$ and $c(2x4)$) is shown in figure 7.9. A $(1x1)$ lattice is plotted over this image and lined up with the maxima of one domain. In the rotated domain the same lattice is found to line up with the maxima. This indicates that the maxima must be located at four-fold (hollow and top) sites on the lattice. If they were located over two-fold (bridge) sites one domain would be shifted by $\left[0,\pm\frac{a}{2},\pm\frac{a}{2}\right]$ relative to the other domain as shown in figure 7.1. The lack of this registry shift was observed on all of images of domain boundaries. The maxima are at points in the image where the two perpendicular mirror planes cross. Therefore, the mirror planes cross over hollow sites, and models D-F must be discarded.

Observations of other domain boundaries support only one of the remaining models. Figures 7.10A shows an antiphase boundary in which one domain is shifted by one substrate lattice distance a relative to the other. Figure 7.10B is an image of a domain

boundary region between two perpendicular domains in which the domains appear to "mix" into a $(2x2)$ structure. The structure in this area can be explained as a periodic array of antiphase boundaries like that shown in figure 7.10A. This region appears to have a four fold symmetry, and extends away from both the $c(4x2)$ and $c(2x4)$ domains symmetrically. As two domains of models B and C contain two different orientations of bridge sites, these models may not extend symmetrically into a $(2x2)$ region. A periodic array of antiphase boundaries in the structure of model A would have four fold symmetry. Therefore model A, in which all sulfur atoms are located at hollow sites, is the most consistent with the STM images.

7.4.4 The "$p(2x1)$" Structure

Producing a sample with a sharp $p(2x1)$ LEED pattern proved to be difficult. As it is not possible to produce the required saturation coverage of sulfur by exposure to low pressures of H_2S, the electrochemical sulfur source was used to deposit sulfur on the surface. Annealing of the surface was necessary to obtain an ordered LEED pattern. Excessive annealing produced the $c(4x2)$pattern while insufficient annealing left the LEED pattern diffuse. Previous reports[5, 6] of this structure have stated that the LEED pattern was often streaked, at least at some values of sulfur coverage. In the present experiment the overlayer spots of the LEED pattern were streaked in the direction of the quarter order spots of the $c(4x2)$ LEED pattern at some electron energies. Adjusting the electron energy changed the intensity of the streaking; at some energies it was nearly invisible.

Unlike the previous lower coverage structures, we were unable to obtain STM images of a surface structure consistent with the symmetry of the LEED pattern. This result is different from our previous STM study of this surface in air in which images of a surface with apparent $p(2x1)$ symmetry were obtained.[15] Because of the air environment, the observed $p(2x1)$ ordering may be due to some impurity which was absent in our UHV experiment.

A representative image of the surface with a $p(2x1)$ LEED pattern is shown in figure 7.11. It consists of very small domains of $c(4x2)$ ordered sulfur. This image is not actually inconsistent with the LEED pattern, but only with its apparent $p(2x1)$ symmetry. The $p(2x1)$ LEED pattern contains all the spots of the $c(4x2)$ pattern and additional quarter order spots. The streaking we observed in the $p(2x1)$ LEED pattern was in the direction of these spots. The lack of large domains on the surface would cause streaking of the higher order spots as they correspond to longer range order on the surface. The higher coverage of sulfur on this surface relative to the ordered $c(4x2)$ overlayer may be explained by the large number of antiphase defects present which have a local coverage of one monolayer. As others authors have also reported, streaking of the $p(2x1)$ overlayer LEED spots, it is possible that all reports of the $p(2x1)$ LEED pattern were obtained from surfaces with small $c(4x2)$ domains. It also may be that some impurity is required to induce $p(2x1)$ ordering of the sulfur.

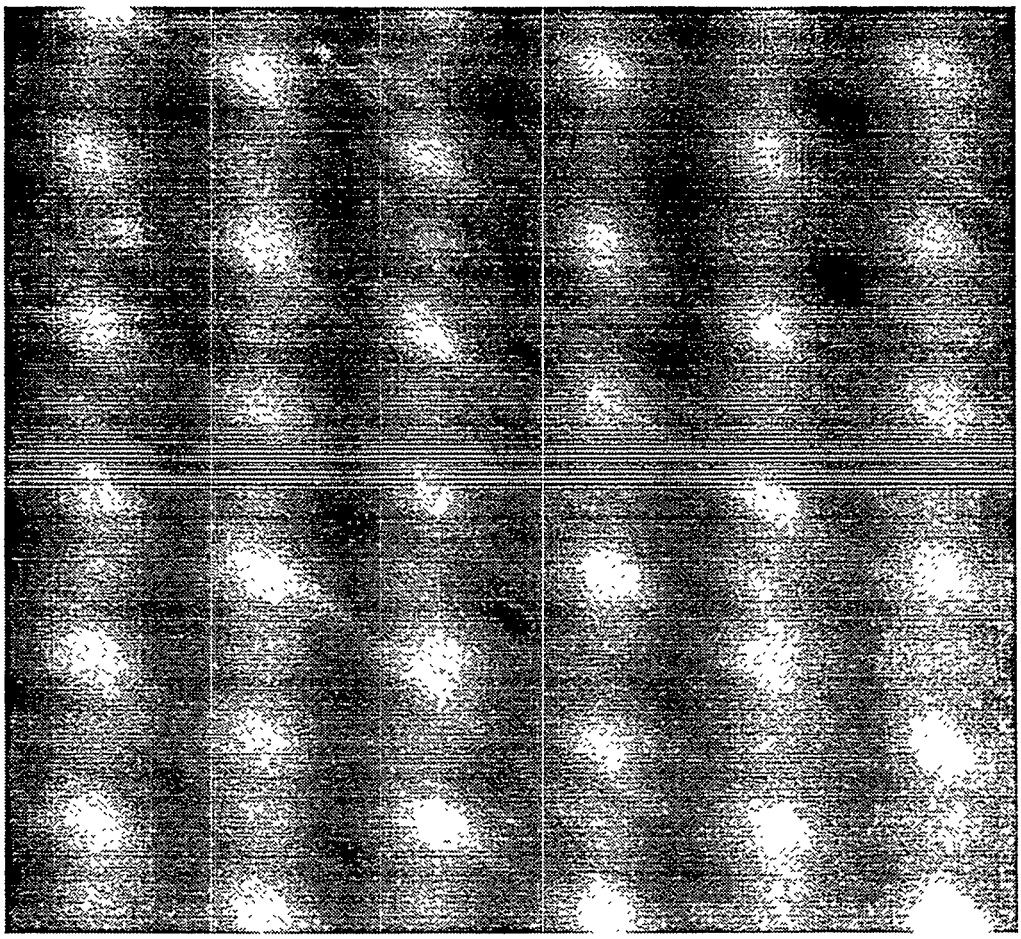

Figure 7.7 An STM topographic image of the $c(4x2)$ structure

The long direction of the unit cell runs in the horizontal direction in this image. Each unit cell contains one bright maxima which is joined by a dimmer region to other maxima along the short direction of the unit cell. There are two perpendicular mirror planes in each unit cell which cross at the maxima. The maximum corrugation between the rows is 0.45 Å. Bias = 50 mV, I = 2.8 nA.

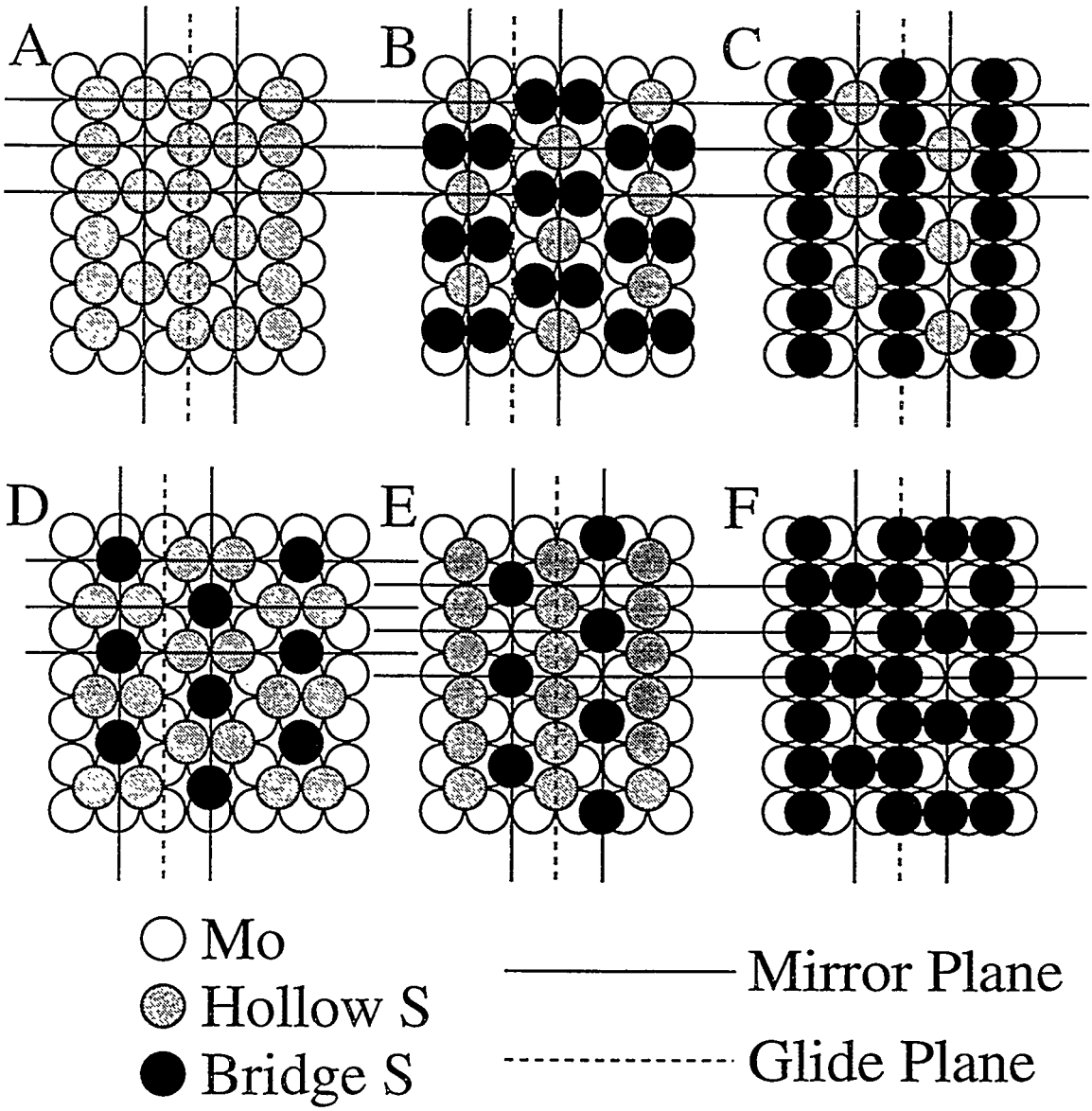

Figure 7.8 Potential Models of the $c(4x2)$ Structure of S on Mo(100) Models of the possible $c(4x2)$ unit cells which contain three sulfur atoms and have the two perpendicular mirror planes (continuous lines) apparent in the STM images. The mirror planes in models A-C cross over hollow sites. In models D-F they cross over bridge sites. Glide planes are shown as dashed lines.

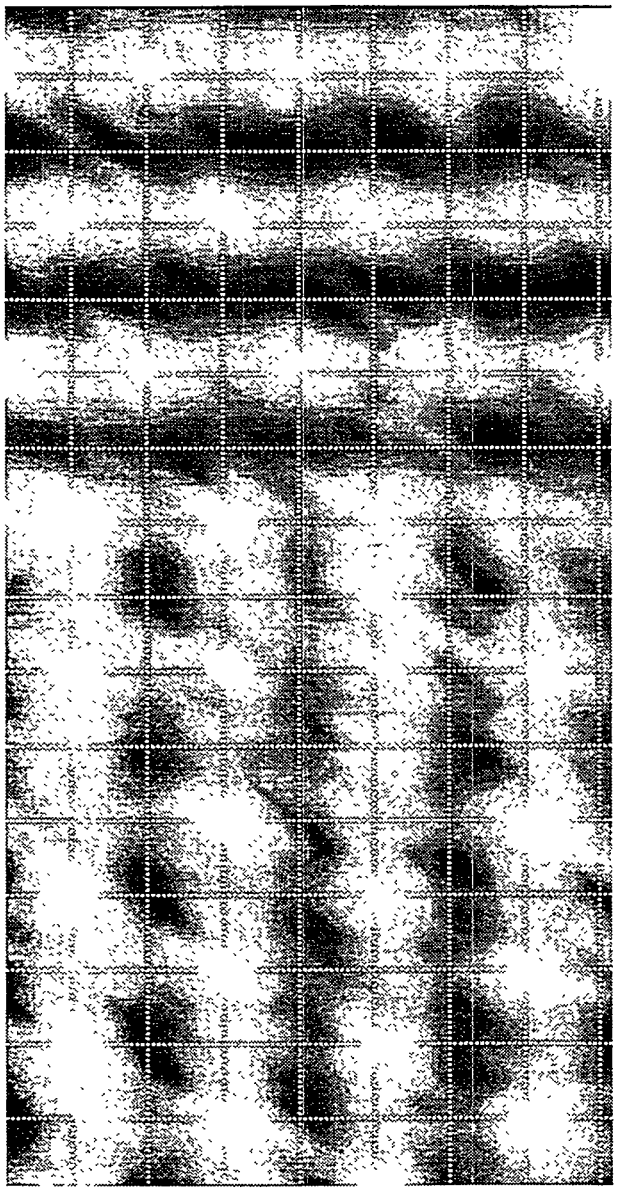

A 25Å X 50Å STM topographic image showing two domains of the $c(4x2)$ structure. The domain on the top is rotated 90° relative to the domain on the bottom. A $(1x1)$ grid is drawn over the image and aligned to the maxima of one domain. It is also found to be aligned with the maxima of the second domain. This indicates that the maxima in the image reside on four-fold symmetric sites.

Figure 7.9 An STM Image of Two Domains of the $c(4x2)$ Structure

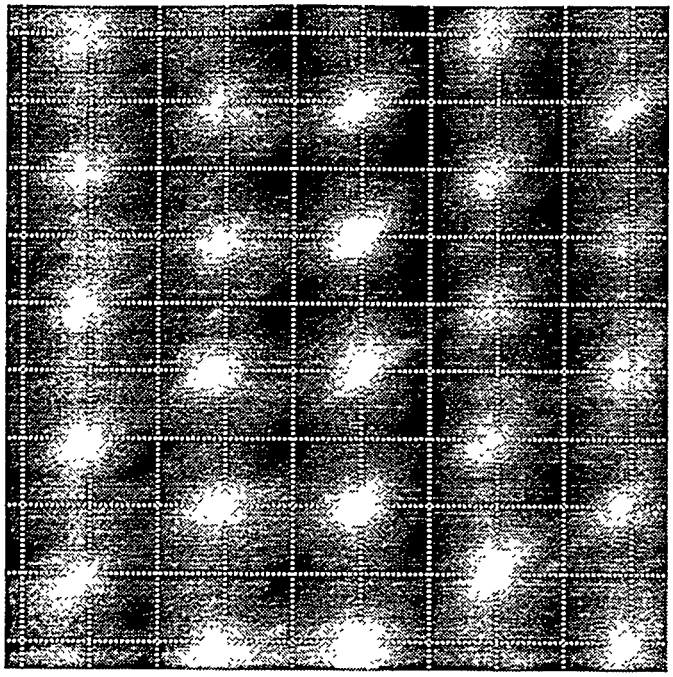

A) A 31 Å square image of an antiphase boundary in which one domain is shifted by one Mo lattice spacing a relative the other.

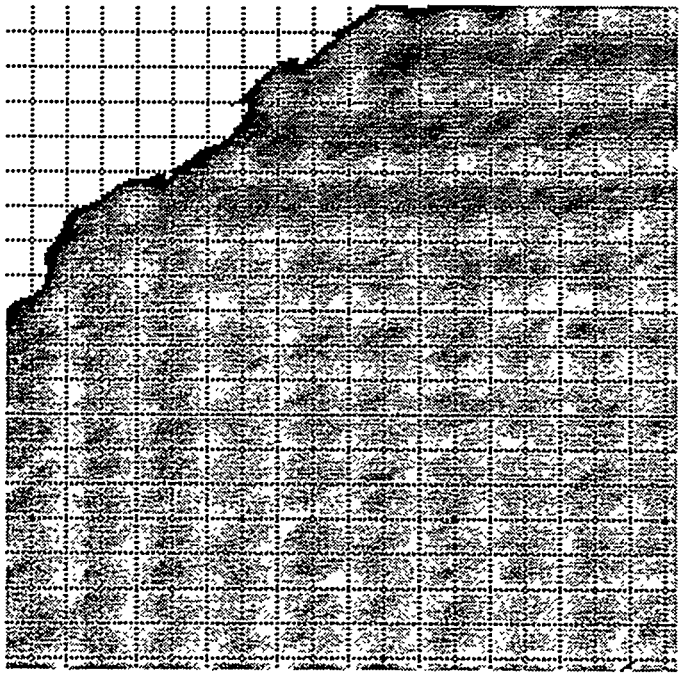

B) A 60 Å square image of an area in which two perpendicular domains of the $c(4x2)$ overlayer appear to mix into a $(2x2)$ structure. The four-fold symmetry of this structure is only compatible with the all hollow site sulfur $c(4x2)$ model.

Figure 7.10 Defects in the $c(4x2)$ Overlayer

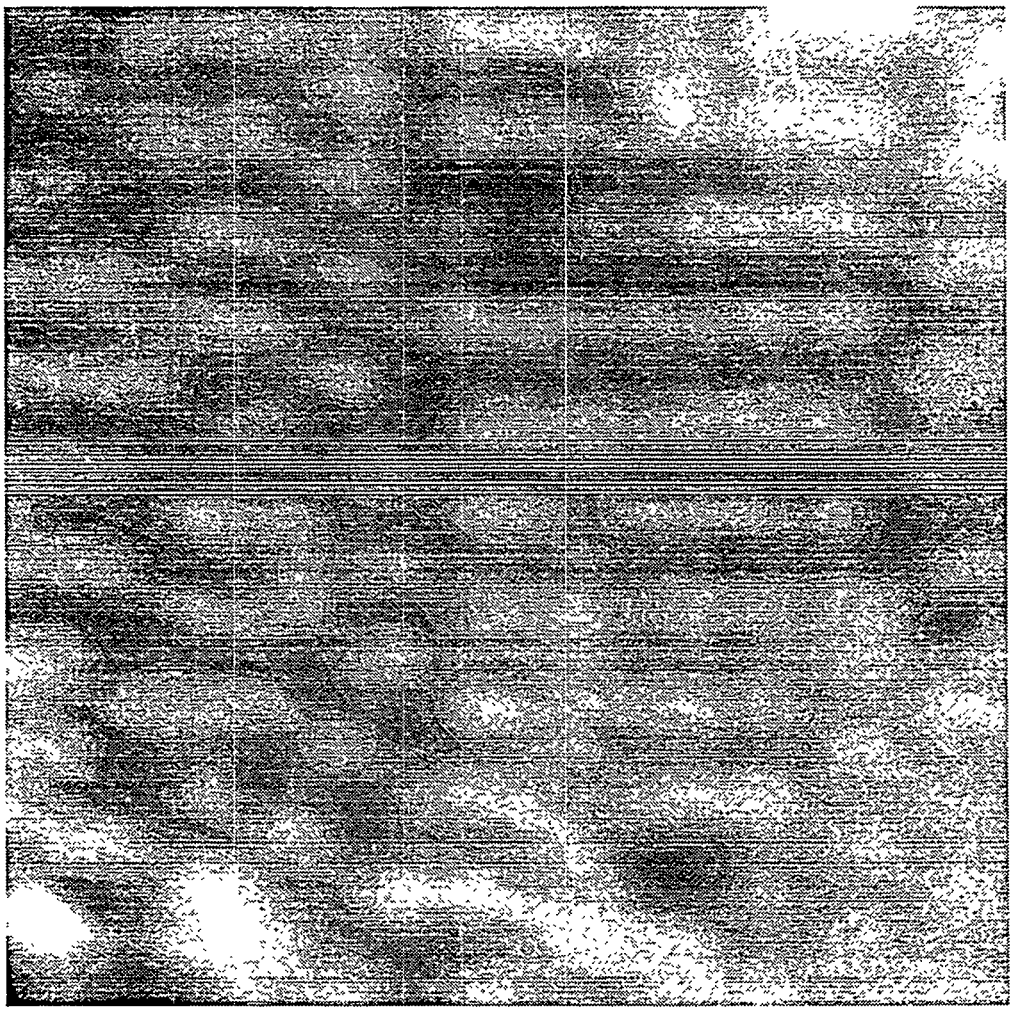

Figure 7.11 An Image of Sulfided Mo(100) with a $p(2x1)$ LEED Pattern

The symmetry is not the expected $p(2x1)$. The surface is instead covered by small domains of one to three unit cells with $c(4x2)$ symmetry. Extra sulfur atoms at the domain boundaries increase the average sulfur coverage above that of the ordered $c(4x2)$ overlayer.

7.5 Conclusions

The structures of the four ordered overlayers of sulfur on the Mo(100) surface were investigated by scanning tunneling microscopy. In order of increasing sulfur coverage, the overlayers have $c(2x2)$, $\begin{bmatrix} 2 & \bar{1} \\ 1 & 1 \end{bmatrix}$, $c(4x2)$, and $p(2x1)$ low energy electron diffraction patterns. Only the $c(2x2)$ overlayer geometry has previously been determined from LEED I(V) analysis. An examination of point and line defects and domain boundaries in STM images provides information beyond that known from LEED on the required symmetries of the ordered overlayers. Several proposed structures were shown to be incompatible with these symmetries and therefore discarded. Only one model of the $c(4x2)$ structure was found to be consistent with the symmetry of the STM images. This structure contains sulfur atoms occupying exclusively four-fold hollow sites. Unexpectedly, STM images of the surface with the $p(2x1)$ LEED pattern did not have $p(2x1)$ symmetry, but consisted of small domains of the $c(4x2)$ structure.

Chapter 7 References

[1] M.E. Bussell and G.A. Somorjai, J. Cat. **106** (1987) 93.

[2] M.E. Bussell, A.J. Gellman and G.A. Somorjai, Cat. Lett. **1** (1988) 195.

[3] C.C. Knight and G.A. Somorjai, Surf. Sci. **240** (1990) 101.

[4] M. Salmeron, G.A. Somorjai and R.R. Chianelli, Surf. Sci. **127** (1983) 526.

[5] V. Maurice, L. Peralta, Y. Berthier and J. Oudar, Surf. Sci. **148** (1984) 623.

[6] L.J. Clarke, Surf. Sci. **102** (1981) 331.

[7] F. Zaera, E.B. Kollin and J.L. Gland, Surf. Sci. Lett. **166** (1986) L149.

[8] M.H. Farias, A.J. Gellman, G.A. Somorjai, R.R. Chianelli and K.S. Liang, Surf. Sci. **140** (1984) 181.

[9] C.C. Knight and G.A. Somorjai, Surf. Sci. **272** (1992) 326.

[10] J.C. Dunphy, C. Knight, P. Sautet, D.F. Ogletree, M. Salmeron and G.A. Somorjai, Surf. Sci. **280** (1993) 313.

[11] D.G. Kelley, R.F. Lin, M.A.V. Hove and G.A. Somorjai, Surf. Sci. **224** (1989) 97.

[12] D. Jentz, S. Rizzi, A. Barbieri, D. Kelly, M.A. VanHove and G.A. Somorjai, submitted to Surface Science (1994)

[13] P.J. Rous, D. Jentz, D.G. Kelley, R.Q. Hwang, M.A.V. Hove and G.A. Somorjai. in *The Structure of Surfaces III, Procedings of the 3rd International Conference on the Structure of Surfaces (ICSOS-III)* (eds. Tong, S.Y., Hove, M.A.V., Takayanagi, K. & Xie, X.D.) p. 432 (Springer-Verlag, 1991).

[14] D. Jentz and M.A. VanHove, private communication

[15] B. Marchon, P. Bernhard, M.E. Bussell, G.A. Somorjai, M. Salmeron and W. Siekhaus, Phys. Rev. Lett. **60** (1988) 1166.

[16] X.W. Wang and S.G. Louie, Surf. Sci. **226** (1990) 257.

[17] C. Wagner, J. Chem. Phys. **21** (1953) 1819.

[18] S. Rousset, S. Gauthier, O. Siboulet, W. Sachs, M. Belin and J. Klein, J. Vac. Sci. Technol. A **8** (1990) 302.

[19] A.J. Gellman, J.C. Dunphy and M. Salmeron, Langmuir **8** (1992) 534.

[20] V. Maurice and P. Marcus, Surf. Sci. **262** (1992) L59.

[21] J.C. Dunphy, D.F. Ogletree, M.B. Salmeron, P. Sautet, M.L. Bocquet and C. Joachim, Ultramicroscopy **42** (1992) 490.

[22] J.M. MacLauren, J.B. Pendry, P.J. Rous, D.K. Saldin, G.A. Somorjai, M.A.V. Hove and D.D. Vvedensky. *A Handbook of Surface Structures*. (D. Reidel, Holland, 1987).

Chapter 8. QUANTITATIVE STRUCTURE FROM STM

8.1 Introduction

The understanding of the electronic, physical, and chemical properties of surfaces requires an accurate knowledge of their atomic level structure. A number of methods are now routinely used to determine the adsorption sites and bond lengths of adsorbates on metal surfaces. These include Low Energy Electron Diffraction (LEED),[1] Ion Scattering,[2] X-ray Photoelectron Diffraction (XPD),[3] and Surface Extended X-ray Absorption Fine Structure (SEXAFS).[4] When coupled with appropriate theoretical modeling, these methods provide information on either the average surface structure or the structure of well ordered portions of the surface. However, it is generally believed that many of the properties of surfaces are a consequence of defect sites which may be present in low concentration and randomly distributed. As a real space technique, Scanning Tunneling Microscopy (STM) has the ability to focus on a specific region of the surface, such as a defect site, isolated adsorbate atom, or antiphase boundary. The ability to study non-periodic surface features gives this technique the potential to provide structural information unavailable by other methods. However, no general technique of deriving the complete surface structure from STM images has been developed.

Some information on surface structure can be immediately determined by inspection of STM images. It is simple to measure the distance between equivalent points on the surface, both laterally and in height. These measurements provide the periodicity of the surface and the separation of atomic layers (step height). As is described in chapter 7, the binding site of adsorbate atoms (top, hollow, or bridge) may often be determined from an analysis of the symmetry of the images, especially at defect sites and antiphase boundaries.[5] In contrast, STM does not directly yield information on the relative positions of inequivalent atoms, such as the bond length between adsorbate and substrate atoms or the distance between adsorbate atoms bound at different surface sites. This is

because the STM does not produce a simple image of a hard sphere model of the surface, but a map of tip-surface conductance which is a combination of physical and electronic structure. Other factors besides the surface structure may influence the image contrast, including the tunneling conditions (bias voltage and tunneling current) and the morphology of the tip termination.[5-9] A theoretical approach is needed to separate this electronic structure influence on the image from the physical structure of the surface. As discussed in chapter 4, considerable effort has been focused on developing an accurate theoretical description of electron tunneling with which STM images can be calculated.[10-20]

Despite the development of these theoretical methods, STM theory has only rarely been applied to deduce surface structure from STM images. Feenstra et al. used the Tersoff and Hamann[16] approach to determine the buckling angle of bonds on the GaAs surface.[10] STM images acquired with positive and negative bias voltage were compared to calculations of the surface density of states as a function of the bond angle. In chapter 6 a partial structural determination for the $p(2x2)$ S on Re(0001) chemisorption system is described.[11, 12] The experimental images of this system were consistent with calculated images only for a small range of trial surface structures. From the comparison of the experimental and calculated images, the binding site of the adsorbed sulfur atom was determined to be the three-fold hollow site. The height of the sulfur over the surface was limited to within the small range 1.67 ± 0.07 Å above the first Re layer. The results agree closely with those of a dynamical LEED structure determination.[13]

An important result of this theoretical work has been the improved understanding of the mechanisms of contrast in STM images.[11] The contrast was found to be modified by electronic interferences among several tunneling paths between the surface and the tip. In general, atomic orbitals of more than one surface atom overlap significantly with the atomic orbitals of the tip termination atom. The tunneling amplitudes of electrons for these paths are complex quantities which may interfere, significantly enhancing or reducing the tunneling current compared to the sum of the individual paths. This electronic interference

of states with approximately the Fermi wavelength (~ 1 Å) makes STM contrast sensitive to the geometry of the tunneling gap region with a resolution of a fraction of this wavelength, of order 0.1 Å. In principle, this fact allows quantitative information on the structure of the surface to be obtained from the contrast in STM images.

Here, a comparison of experimental STM images with those calculated by a electron scattering theory is used to quantitatively determine the structure of the $c(2x2)$ S on Mo(100) system. We begin with a model structure assuming that S is bound at the 4-fold hollow site as it was shown to be in chapter 7. Sulfur has been found to bind at the highest coordination site on nearly all metal surfaces studied to date.[14] Two parameters of the structure are optimized by fitting the STM data: the height of the bound sulfur and the buckling of the second Mo layer. Unlike the previous work on the S on Re system, a quantitative approach is used for the comparison of theoretical images with calculated ones. In addition, the images are obtained at more than one tunneling condition, enlarging the experimental data set.

8.2 Approach

Our approach to STM structure determination is analogous to that of dynamical LEED. As with STM image data, there is no way to directly invert LEED I(V) curves to real-space surface structure. Instead, a multiple-scattering theory is used to calculate I(V) curves for each of a large set of trial structures. Each of these curves is numerically compared to the experimental one by calculating an "R" factor representing the quality of the fit. The trial structure which has the best "R" factor is presumed to be the correct structure.

In the STM approach, images are calculated as a function of surface structure, tip structure, and tunneling conditions for a set of trial structures. The surface structure is determined from the best fit between these calculations and the experimental STM data. As a single unit cell of an STM image has few distinct features, we enlarge the data set by

obtaining simultaneously a set of images with different tunneling conditions. The complete set of images is fit to an equivalent set of calculated images.

Two tunneling parameters can be controlled by the experimenter: the bias voltage and the tunneling current (or gap resistance). Changing the bias voltage modifies the energy overlap of the states of the surface and tip. In systems, such as semiconductors, in which the density of states or their wavefunctions vary rapidly with energy, changes in the bias voltage will have a pronounced effect on the image contrast. However, metals have a relatively flat density of states near the Fermi level, and hence changing the bias voltage has little effect on the image. Experimentally, this was verified for the S on Mo system. Inverting the bias voltage from +0.2 to -0.2 volts produced almost no measurable change in the image contrast.

On the other hand, changing the gap resistance (through variation of the tunneling current), does have an effect on the image contrast of adsorbates on metals. Changes in the gap resistance results in a shift in tip-surface separation. The separation varies approximately linearly with the logarithm of the gap resistance. Changing the distance between the tip and surface modifies the interference between different tunneling paths, resulting in image contrast variations. Different surface structures will have different degrees and forms of interference change with tip height. Therefore, acquiring data at multiple tunneling gaps provides additional information on surface structure beyond what an image at a single tunneling gap can provide.

In order to maximize the amount of experimental data, images were acquired over a wide range of tunneling gap resistance values at a low fixed bias voltage. The gap resistance was modified by changing the tunneling current setpoint of the feedback loop controlling the tip z position. A special parallel image acquisition mode was implemented which preserves information on the relative z separation and registry of images acquired at different tunneling gap resistance values.

An additional factor which may vary in the STM experiment is the structure of the STM tip termination. Unfortunately this structure is currently beyond the control and knowledge of the experimenter. Therefore, a number of likely model tip termination structures must be used in the theoretical image simulation. The fit between the experiment and theory must simultaneously determine the surface structure and at least part of the structure of the tip.

8.3 Theory Results

The simulated STM images were calculated using Electron Scattering Quantum Chemistry (ESQC) theory[15, 16] which was described in section 4.4. This theory has been employed to calculate STM images on a wide range on systems with a high degree of success. As previously discussed, this theory was successfully applied to the $p(2x2)$ S on Re(0001) system. The theory has also correctly predicted the shape of benzene[17] and CO[18] molecules adsorbed at different sites on the Pt(111) surface. While it has proven to be highly accurate, ESQC theory is capable of simulating STM images of a simple surface structure in less than one hour of computer time on a standard workstation. This computational efficiency is required for application to structural determination, where it is necessary to calculate the STM images of large number of possible structures. In addition, unlike in some of the approaches to calculating STM images outlined above, ESQC theory accurately models the surface and the tip with an atom by atom description of the bulk, surface, and tip geometries.

The model of the $c(2x2)$ S on Mo(100) surface which is input into the theory is shown in figure 8.1. The $c(2x2)$ structure has the lowest S coverage of the three ordered structures formed by S on the Mo(100) surface. The models considered all have the S adsorbate atoms placed at the 4-fold hollow site, consistent with a dynamical LEED structure determination of this surface.[19] The Mo surface interlayer spacing is taken from the LEED structural determination. The value of this spacing is quite close to the bulk value of 1.575 Å so that using the bulk value would not have a significant effect on the

results. Two parameters in the model are left free: the height of the sulfur adsorbate and the buckling of the second Mo layer. As half of the atoms in the second Mo layer are nearest neighbors with the sulfur adsorbate atoms while the other half are not, buckling of the second layer is expected. These two free parameters were independently varied over a likely range of values. The sulfur height over the surface was set to one of five values from 0.8 to 1.2 Å while the second layer buckling was picked from five values between -0.4 and +0.4 Å. Hence, a total of twenty five trial surface structures were considered.

Besides the structure of the surface, the tip structure must be input into the theory calculation. The tip is modeled as a cluster of atoms of a given composition and structure. Due to the exponential decay of the tunneling current with the distance to the surface, only the last few atoms at the tip apex contribute significantly to the tunneling current and thus to the image contrast. Therefore, the completely set of possible tips may be modeled by a smaller set of tip termination structures. The number of trial tips can be further reduced by considering only symmetrical tips terminating in one atom. Theoretical work has shown that slightly asymmetric or tilted tips produce nearly the same image contrast as completely symmetric ones.[6] Experimental data with low corrugation or which does not have the complete symmetry of the surface, known from LEED, must be a result of a more complex tip termination or multiple termination tip and can be excluded, making it unnecessary to model these complex tips in the theory.

The model tip we used is shown in figure 8.2. Since the bulk tip composition has no effect on image contrast, it can be modeled as any conductor. For simplicity, the theory uses the same material and crystal structure as the bulk sample, bcc molybdenum. Attached to the end of the bulk tip, near the tunneling gap, is a cluster of Pt which is the predominant atomic species in the experimental tip. (Pt / 40% Rh alloy wire) A single atom is attached to the end of this cluster. The atomic identity is chosen from several likely candidates: Pt from the bulk tip and S, Mo, or C to model contaminated tips. The separation between neighboring atoms in the tip is set to the sum of the covalent radii of the neighbors. Test

calculations have confirmed that small changes in this separation, even at the tip termination, produce very little change in the simulated image contrast.[12]

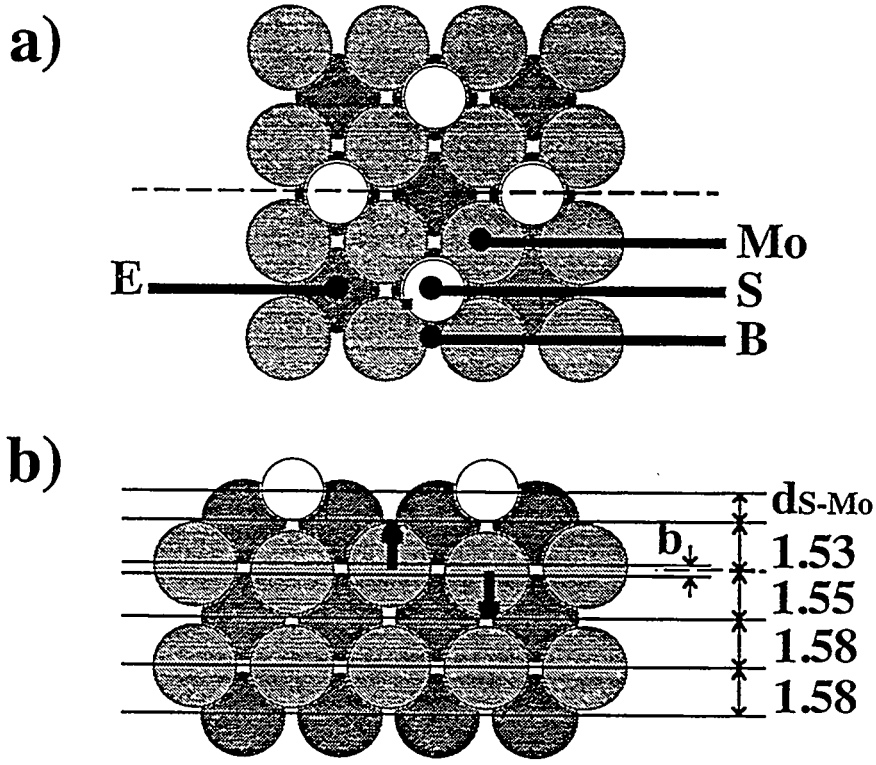

Figure 8.1 A Model of the $c(2x2)$ S on Mo(100) Surface

a) Top view. Every other four-fold hollow site contains a S adsorbate atom, shown in white. There are four high symmetry sites on the surface: the location of the adsorbed sulfur atom (S), the bridge site (B), the empty hollow site (E), and over a Mo substrate atom (Mo). b) Cross section. There are several numerical parameters which describe the surface structure. Two of these are determined by the analysis of the STM image data: the height of the sulfur atom over the surface ($d_{S\text{-}Mo}$) and the second layer Mo buckling (b). The other parameters, which specify the interlayer spacing of the Mo, are set to the values determined by a dynamical LEED study. These values are very close to the bulk layer spacing.

The complete set of image calculations were done on twenty five surface structures and four tip structures for a total of one hundred model systems. Each individual calculation determined the tunneling gap conductivity at four high symmetry points of the surface overlayer unit cell over an approximately 5 Å range of tip-surface separations at 0.5 Å increments. The four high symmetry points chosen, shown in figure 8.1a, are at the sulfur adsorbate (denoted S), the empty four-fold hollow site (E), over a Mo atom (Mo), and at a bridge site (B). Every point on a 1.57 Å $(1/2x1/2)$ mesh covering the surface is

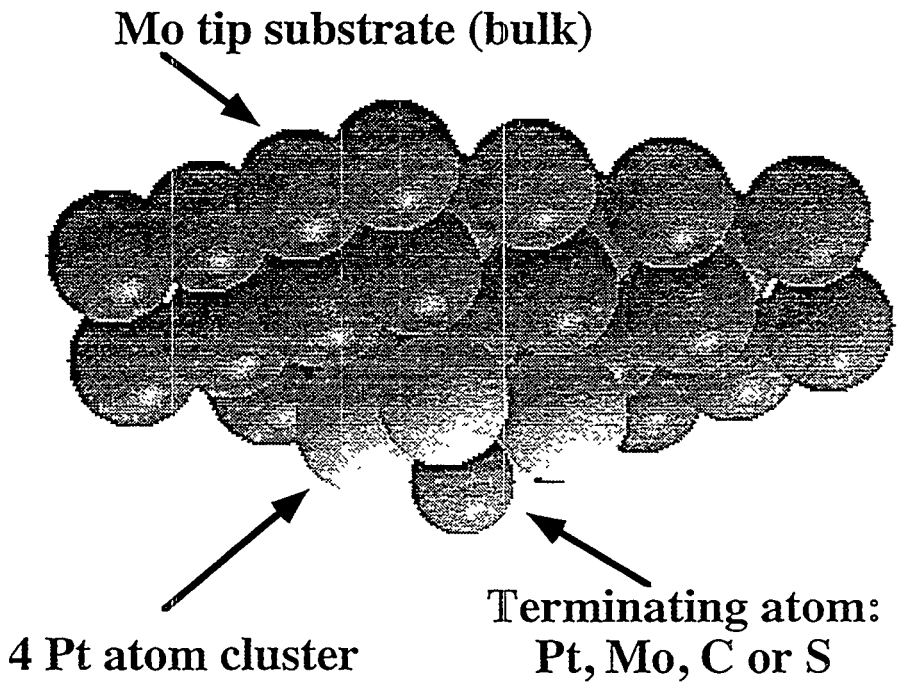

Figure 8.2 Model Tips Used in the Theory

The tip model contains three parts: the bulk, a cluster, and a termination atom. Throughout the tip all nearest neighbor atomic separations are set to the sum of the covalent radii of the two neighbors. The bulk tip consists of Mo (the sample material) for simplicity. A four atom Pt cluster is attached to the bulk to model the Pt alloy tip used in the experiment. A single atom is attached to this cluster. This tip termination atom is chosen from a set of likely experimental tip termination structures: Pt for a clean tip and S, C, or Mo for a contaminated tip.

symmetrically equivalent to one of these points. This distance is approximately the lateral resolution of STM under optimum tunneling conditions. Hence, these four points are sufficient to fully describe the shape of the surface observed by STM at a fixed tunneling gap. The complete set of data for a given tip and surface structure is a three dimensional spatial map of the tunneling current with a resolution of 0.5 Å in z and 1.57 Å in x and y.

Topographic images, over a four order of magnitude range of tunneling gap resistance, may be easily interpolated from this map. However, for comparison with experimental data, a complete set of images is not necessary. Instead, the tip height for a set of experimental gap resistance values was interpolated at each of the high symmetry sites. The result for a single surface model and tip structure (one of the hundred) is shown in figure 8.3. The y-axis of this graph is the tip height, specifically the distance between the center of the tip termination atom and the top Mo layer. On the x-axis are the four high symmetry points on the surface (one is repeated). Each curve represents the tip height over the surface as it follows the triangular path shown below the graph over the four high symmetry points and back to its starting position while maintaining a constant tunneling gap resistance, labeled to the right of the curve. Concave-up curves represent images with a maximum at the location of the sulfur adsorbate while concave-down curves have a minimum at this location. In the example shown, the image contrast changes significantly with the gap resistance, as shown by the simulated images at the highest and lowest gap.

Figure 8.4 displays how the contrast indicated by these curves is affected by surface structure. The results for all of the twenty five surface structures calculated for a Pt terminated tip are displayed simultaneously. Each set of curves is in the same form as the plot of figure 8.3. The outer y-axis represents the sulfur adsorbate height over the Mo surface while the x-axis represents the second layer Mo buckling. As the surface structure is changed along either axis, clear changes appear in both the image shape at different gap resistance values and in the decay of the tunneling current with gap distance (separation of

the curves). These curves can easily be numerically compared to analogous ones derived from our experimental STM data.

8.4 Experiment

The single crystal sample was prepared with the methods described in chapters 3 and 7. In order to prevent contamination, sulfur was deposited on the surface immediately after cleaning by the decomposition of H_2S gas. The sample was heated to approximately 800K and exposed to 10 Langmuir of H_2S. After this treatment, the S coverage on the surface slightly exceeded the 0.5 monolayer required for the $c(2x2)$ structure, as indicated by AES and the LEED. The LEED pattern had $c(2x2)$ symmetry with streaks in the <011> directions from each of the overlayer half-order spots, indicating frequent antiphase boundaries in the overlayer.[1] The crystal was annealed in short cycles to desorb S and reorder the surface until a sharp $c(2x2)$ LEED pattern was observed. After this preparation procedure the AES spectrum showed no trace of carbon or oxygen contamination.

Mechanically cut Pt/Rh (60%/40%) STM tips were used. The tips were cleaned by applying electrical pulses of several volts between a sacrificial area of the sample and the tip when in tunneling range.

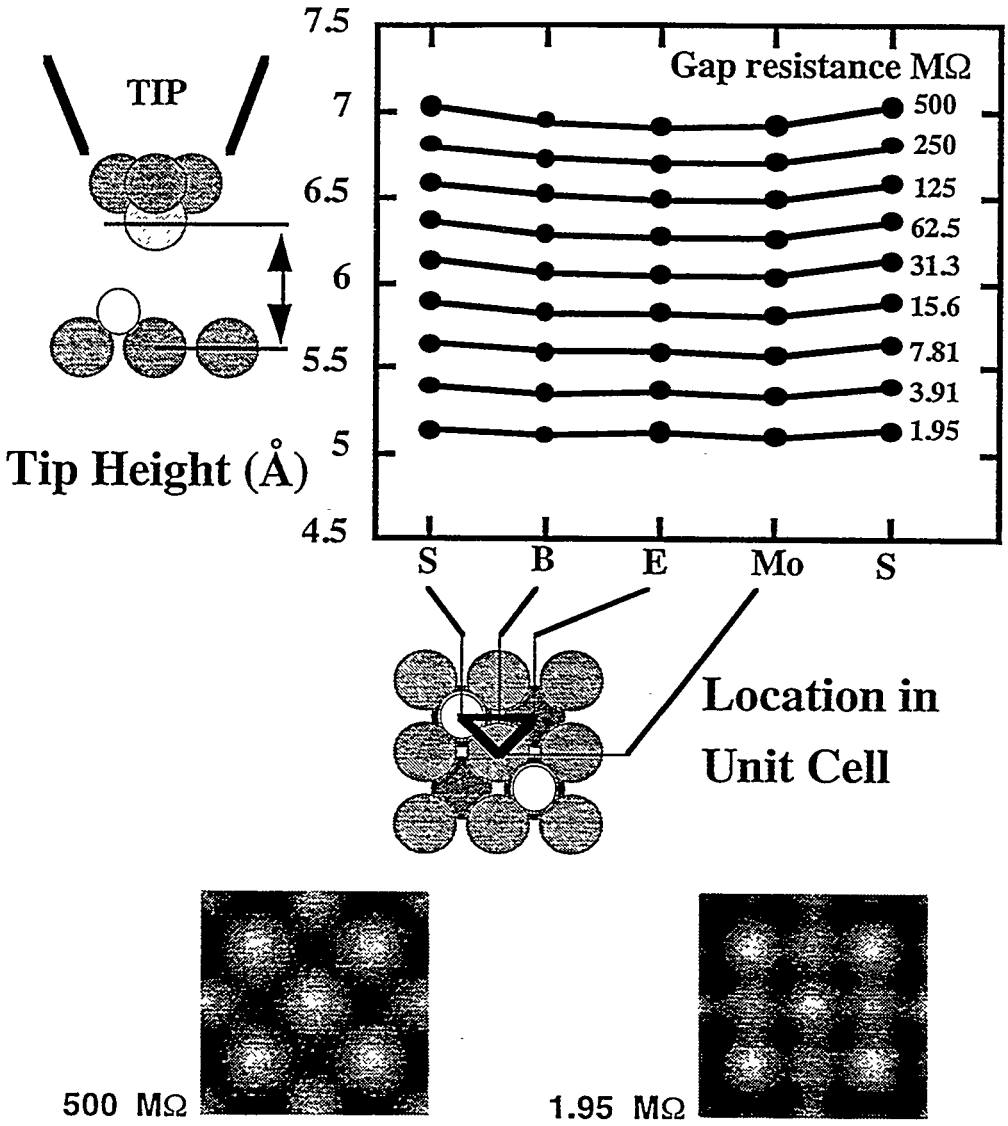

Figure 8.3 Theoretical Image Shape vs. Gap Resistance

Each curve in this graph represents the distance from the tip to the surface at a specific tunneling gap resistance at the four high symmetry sites on the surface, shown in the model below the graph. The distance between the tip and surface is defined as shown in the model to the left of the graph. The tunneling gaps range from 2 to 500 MΩ by factors of 2. Below the plot are simulated images corresponding to the highest and lowest values of the tunneling gap.

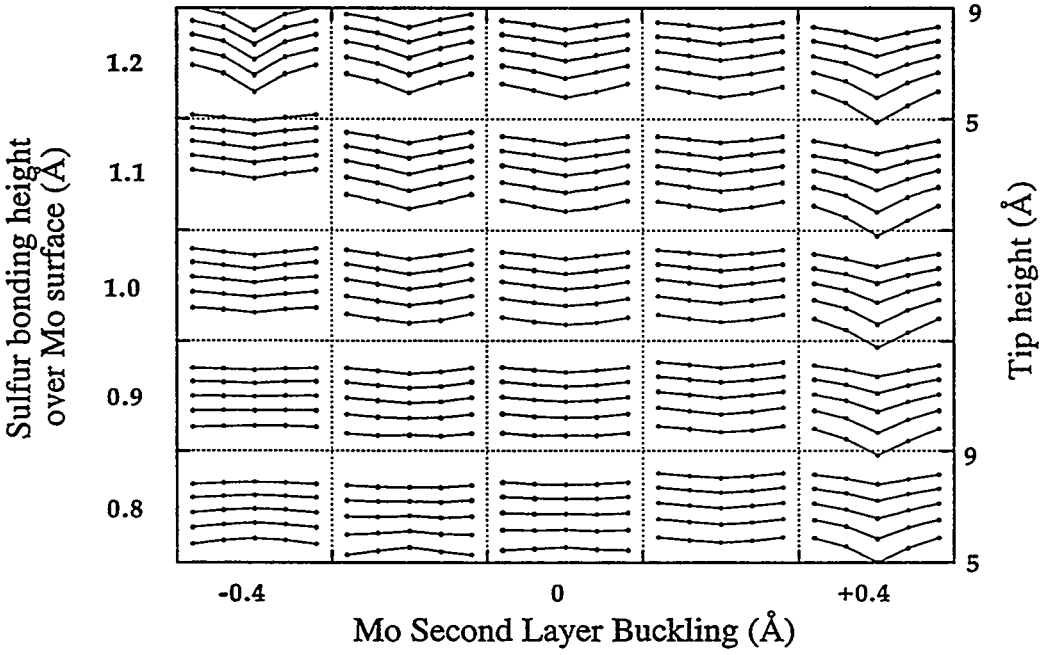

Figure 8.4 Theoretical Image Shape vs. Surface Structure (Pt tip)

Each set of curves in this graph is equivalent to the graph in figure 8.3 for a specific structure of the surface. They indicate the tip height (labeled for several of the groups on the right y-axis) at the four high symmetry points on the surface at five values of tunneling gap resistance. The outer x and y axes represent the two free parameters of surface structure, the S adsorbate height and the buckling of the second Mo layer. The changes in the shape of the groups of curves and the spacing between them indicates that the STM images are sensitive to changes in the structure of the surface. The surface structure is determined by ascertaining which set of these, compared with similar ones for other tip termination structures, best fits the experimental data.

As shown in the example of figure 8.5, STM images of the sample showed an array of maxima spaced by $\sqrt{2}$ of the Mo(100) surface lattice. Each maxima is therefore attributed to one unit cell of the $c(2x2)$ S overlayer, consisting of one S atom and two top layer Mo atoms. As is described in chapter 12, S adsorption on Mo(100) is found to

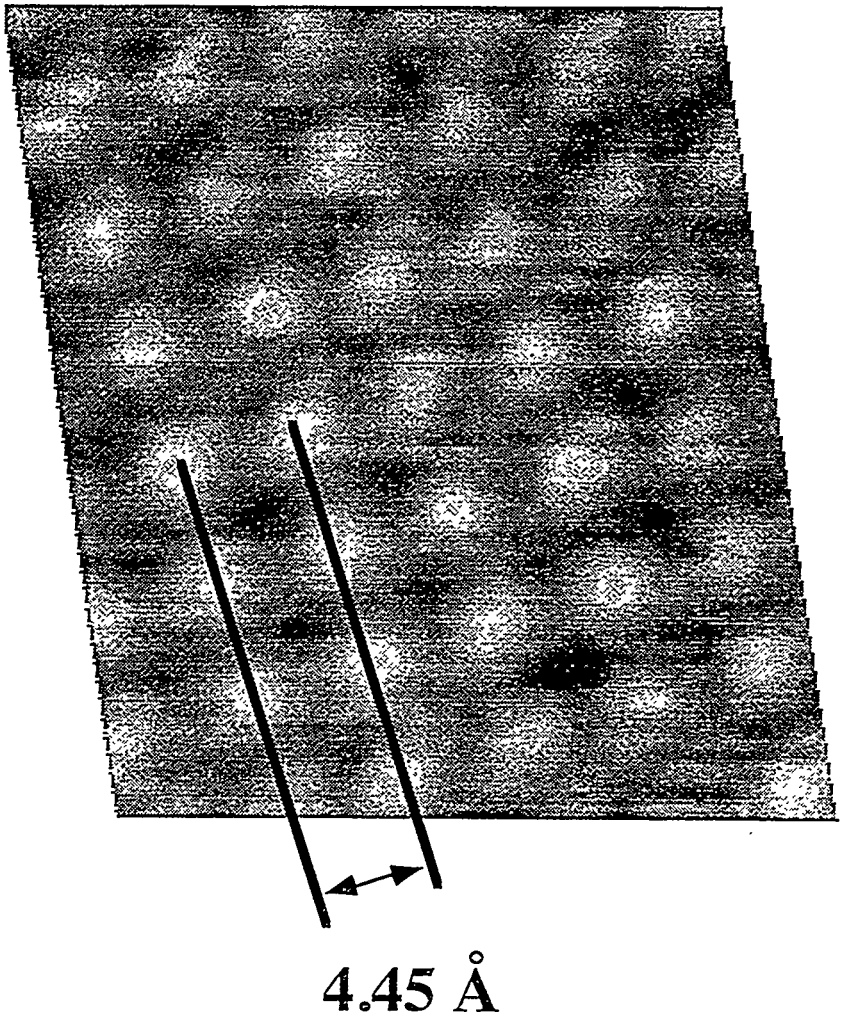

Figure 8.5 A Topographic STM Image of $c(2x2)$ S on Mo(100). The maxima in the image are separated by 4.45 Å or $\sqrt{2}$ Mo(100) lattice constants. This distance corresponds to the separation of the sulfur adsorbates. Therefore, each maxima is associated with one S and two Mo surface atoms. Defect sites in the lattice always appear as a missing maxima, indicating that the maxima correspond to the location of adsorbed S atoms.

promote the clustering of single-atomic height steps, increasing the size of atomically flat terraces. Occasional point defects and antiphase boundaries were observed on these terraces. Point defects always appeared in the image where a current or topographic maximum would otherwise be found, indicating that the sulfur atoms are located at current maxima in the STM images, consistent with observations of sulfur on other metal surfaces.[20-22] Changes in the contrast of the image sometimes occurred during scanning and are attributed to movement of atoms at the tip termination. The z (perpendicular to the surface) calibration of the piezoelectric element was determined by measurements of the height of single atomic steps. The calibration was calculated from the offset in z control voltage between planes fit to the terraces above and below a step. This calibration was reproducible within a single experiment to within 2%. After stable tunneling conditions were obtained with low thermal drift, images containing 30-40 S atoms total were acquired with a tunneling gap bias voltage in the range ±50 to ±150 mV.

8.5 Multiple Gap Imaging

A special mode of image acquisition, "multiple-gap" imaging, was used to acquire STM data over a wide range of tunneling gap resistance values. While in principle this could be accomplished by sequentially obtaining a series of images at different tunneling currents, it is not clear whether such images are generated with the same tunneling tip and are of precisely the same area of the surface. The tip termination may change between images by the diffusion of the atom at the tip end or the movement of an atom between the tip and the surface. Thermal drifting of the sample relative to the tip makes accurate determination of the relative registry and gap distance between images very difficult. These problems may be overcome by taking nearly simultaneous images at multiple tunneling gaps using a multiplexing technique.

A schematic model of this technique is shown in figure 8.6. In the multiple-gap imaging mode the tip is scanned over the surface while maintaining constant tunneling current within each line by means of a feedback loop as in standard STM imaging. The

setpoint of the feedback loop is cycled over a range of exponentially distributed current values, changing at the end of each scan line. In other words, line numbers 0, 8, 16, etc. are acquired with a tunneling current of 0.1 nA, while lines 1, 9, 17, etc. are acquired at 0.2 nA, and lines 2, 10, 18, etc. are acquired at 0.4 nA. Due to the exponential response of the tunneling gap, the gain of the feedback integrator must be changed inversely with the current setpoint in order to maintain a constant feedback loop response. Once an entire image of scan lines has been acquired, the individual lines of data are sorted by their gap resistance (or tunneling current setpoint) into separate images. As all the data is acquired at the same time, any thermal drift in the lateral or z directions is the same for all the images, and a uniform correction may be applied. Therefore, the relative registry and the z displacement between the images are known. Since the images are acquired almost simultaneously (the time difference corresponds to only the time to acquire one scan line) it is certain that the tip termination which produced them is the same. Any change in the tip termination structure will appear as a contrast change at the same point in all the images. In this case the complete set of data was discarded.

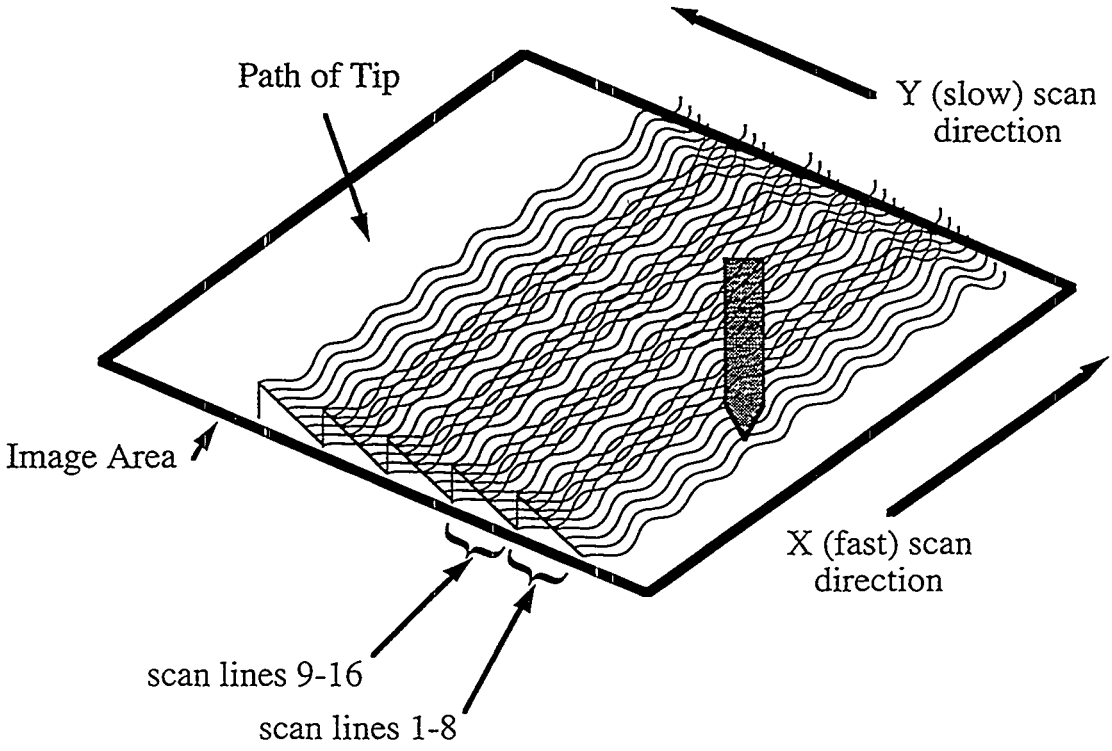

Figure 8.6 A Representation of the Multiple-Gap Technique

In this imaging mode the tunneling current is cycled between a small number of exponentially spaced values, changing between these values at the end of each scan line. This change in current setpoint causes the feedback loop to change the physical distance of the tunneling gap. After an entire image is acquired, the data is sorted into separate images, each corresponding to one tunneling gap resistance. This method of data acquisition has the advantage of preserving the relative position of the images taken at different tunneling gap resistance values. In addition, it prevents discrepancies in the data produced by tip changes occurring between sequential images.

8.6 Experimental Data

Hundreds of experimental multiple-gap images were acquired at eight tunneling gaps exponentially spaced from 2.5 to 500 MΩ. Much of this data was discarded for one of several reasons. Any data showing defects either in the overlayer or due to atomic steps was excluded in order to avoid the complication of possible changes in surface structure in the regions surrounding these defects. Images in which the contrast was extremely low or in which the tip showed signs of instability were also discarded. The decay of the tunneling current with the gap distance was extracted from each of the remaining image sets by simply calculating the average tip height for each of the eight gap resistance values. In many cases the decay rate was found to be far less than the one order of magnitude per Ångstrom expected from the theory and consistent with most other experiments. An example of this result is shown in figure 8.7. Additionally, this data deviated from the expected exponential behavior at small tunneling gap resistance values. Such anomalous data is attributed to tips contaminated with a non-conductive material at the contact point with the surface. During acquisition of these images, the tip was physically pressing against the surface, decreasing its ability to move in response to a voltage change to the piezoelectric element, especially at high current setpoint values.[23] This produced a slow decay of tunneling current with changes in the apparent z position (applied control voltage). Surprisingly, these images were among those which qualitatively looked best, perhaps due to the stabilizing effect a mechanical contact has on the tunneling gap. As the theory assumes a conductive tip and does not include mechanical interactions between the tip and surface, data showing these features were excluded from comparison with the theory results.

The remaining experimental image data was processed into the same form as the theory data shown in figure 8.3. The raw data consists of a multiple images with eight gap resistance values, each of approximately 20 x 20 Å size and containing around 30 unit cells

of the overlayer. In order to correct for the surface slope and piezoelectric element hysteresis, a single parabolic fit is subtracted from all eight of the images, taking into account the one scan line displacement between sequential images. The maxima in the images are connected with the vertices of a $c(2x2)$ square lattice. The images were corrected using a procedure similar to that described in section 7.2. A second order two-dimensional transform mapping the data-space to real-space was determined from a least squares fit between the locations of maxima in the image and their presumed relative locations in real space. This fit precisely corrects for any non-linear thermal drift or piezoelectric hysteresis in the (xy) image plane during data acquisition. The data in the equivalent unit cells of the images were averaged together to make a composite unit cell for each tunneling gap. The composite unit cells was Fourier filtered to remove spatial frequencies higher than those which could represent real data. The resulting average unit cells (repeated 3 times in each direction) are shown in figure 8.8.

Measurements are made of the relative tip height at the four high symmetry points in these unit cells. Unlike the theoretical results, the absolute height of the STM tip over the surface cannot be determined experimentally; only the relative tip height within the set of data is measurable. This numerical image data, in the same form as the theoretical data in figure 8.5, is shown in figure 8.9. Due to the symmetry of the surface, some of the high-symmetry points (B and Mo) are present more than once in each overlayer surface cell. These locations have more than one data point associated with them.

A completely symmetric tip termination should produce images in which all equivalent points are equal. However, in all of the data sets, including that shown in figure 8.9, some asymmetry was observed. In the data of figure 8.9 this asymmetry is most severe in the middle range of gap resistance at the Mo location, and disappears at high and low gaps. Changes in the asymmetry with gap resistance qualitatively shows the changes in image contrast with gap resistance predicted by the theory, albeit for a non-ideal tip. In this case, the tip might have been a tilted dimer. At certain gap distances, the dimer atom

which was further from the surface contributed more significantly to the current than at other gaps, perhaps as a result of interferences between the tunneling paths through the two atoms making up the dimer.

Unfortunately, all of the acquired data showed some degree of asymmetry at least at some range of gap resistance. This indicates the tip structure was in general less ideal than the models used in the theory, as might be expected. Various experimental methods were explored to produce completely symmetric tips, with only partial success. The least asymmetric images were selected for comparison to the theory.

8.7 Structure Fit

Each set of data from the experiment and the results of each trial structure calculations in the theory consists of the tip height at four high symmetry positions in the overlayer unit cell for a set of eight tunneling gap resistance values. The experimental and theoretical data were compared in the simplest possible way. The average RMS difference in tip height between the experiment and theory was calculated for each trial structure and each set of experimental data. Experimental data for symmetrically equivalent points on the surface was averaged together (i.e. 4 B sites and 2 Mo sites). Since the absolute tip height was unknown in the experiment, the average experimental tip height was normalized to the average height in the theory for the entire data set. The complete formula used is,

$$R_{STM} = \sqrt{\left\langle \left(Z_{R;\bar{X}} - \zeta_{R;\bar{X}} - \left\langle Z_{R;\bar{X}} - \zeta_{R;\bar{X}} \right\rangle \right)^2 \right\rangle}, \tag{8.1}$$

where $Z_{R;\bar{X}}$ are the experimental data points and $\zeta_{R;\bar{X}}$ are the theoretical values at location $\bar{X}$ within the unit cell and gap resistance R. The quantities inside $\langle\ \rangle$ are averaged over the entire set of 32 data points. The quantity,

$$\left\langle Z_{R;\bar{X}} - \zeta_{R;\bar{X}} \right\rangle, \tag{8.2}$$

is simply the average difference in tip height, which is subtracted from each difference to normalize the absolute tip height. Theoretical data points were interpolated over a

continuous range of surface structures from the twenty five individual calculations for each of the three tip types.

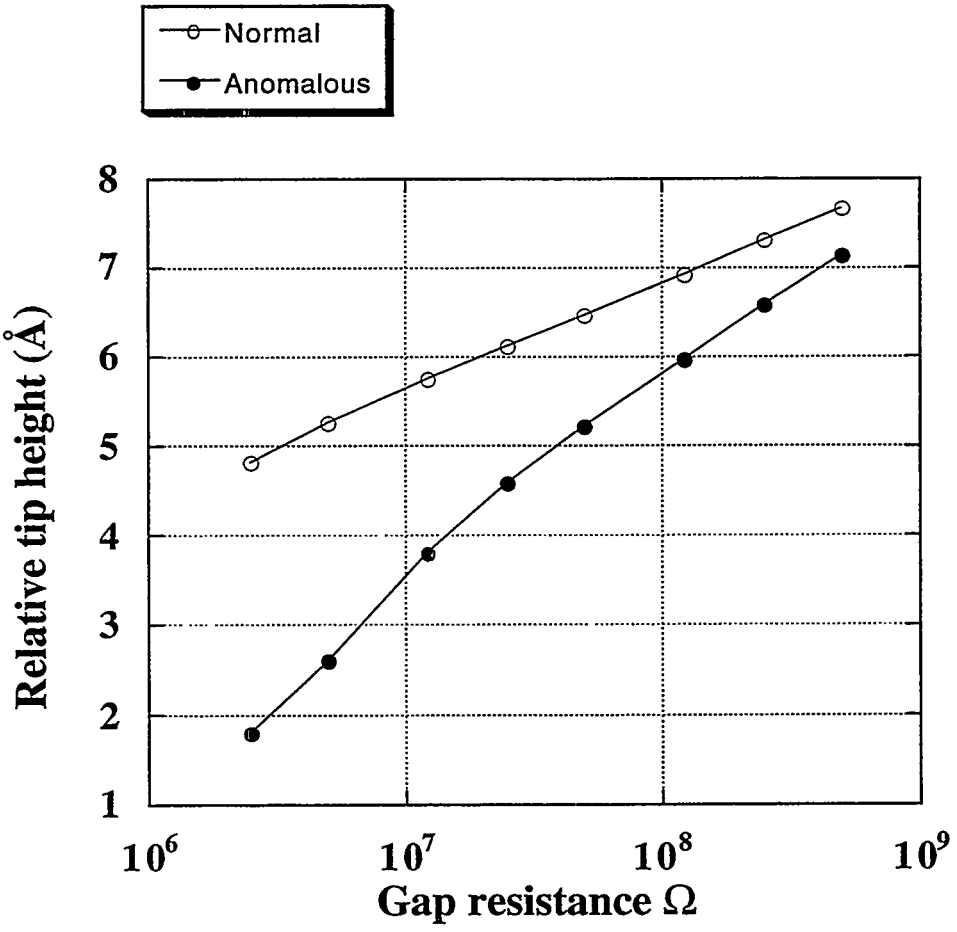

Figure 8.7 Decay Of The Tunneling Current With Gap Size

Theoretical results, even from simple models, indicate that the electron wavefunction and hence tunneling current should decay exponentially away from the surface at a rate of approximately one order of magnitude per Ångstrom. The experimental data in the top curve is consistent with this prediction. Often, however, we found experimental I(z) curves, such as the lower curve, showing anomalous slow decay rates and a non-exponential shape at low tunneling gaps. As is explained in the text, these curves are attributed to tips contaminated with non-conducting material.

A representative set of results of the fit between the experimental data and the calculated images for each of the three model tips is shown in figure 8.10. These models show the R_{STM} factor as a function of the two structure parameters. The y-axis represents the S height above the surface while the x-axis represents the Mo second layer buckling.

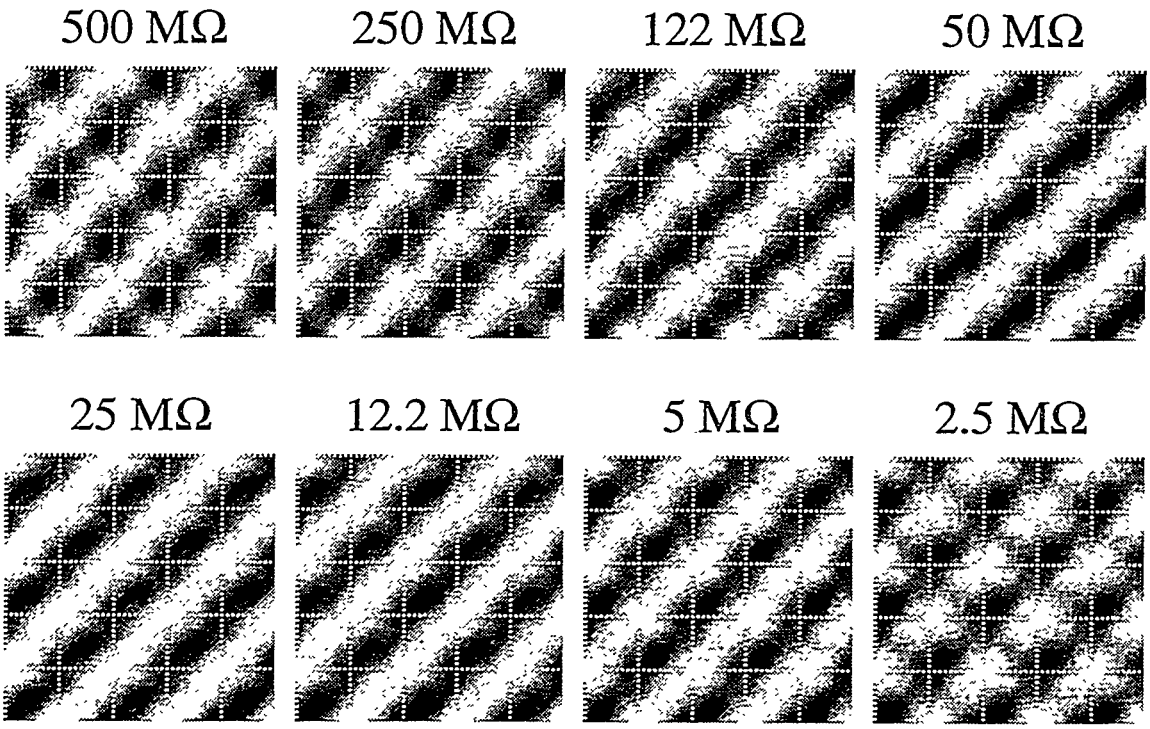

Figure 8.8 Average Unit Cell Contrast vs. Gap Resistance Value

Each image is a 5x5 Mo surface unit cell plot of the composite unit cells derived by averaging approximately 20 unit cells from an image. All the image data was acquired simultaneously with the multiple gap imaging technique. The grid in the plots has vertices over the 4-fold hollow sites of the Mo(100) lattice. While the maximum in the unit cells remain at the same place in all of the images, the contrast surrounding these maxima change with the gap resistance. In particular, this data shows an asymmetry, due to an asymmetric tip, which appears most prominently in the middle range of the tunneling gaps and nearly disappears at high or low tunneling gaps.

The fit for the Pt atom terminated model tip was always found to be much better than for the C, S, and Mo results. This is due to a better match of both the image shape and the rate of decay of tunneling current with tip-surface separation. The Pt fit plot shows a roughly triangular central region with a nearly constant R_{STM} factor. The R_{STM} factor rises quickly outside of this region.

Thus, the fit results indicate that the termination of the tunneling tip in our

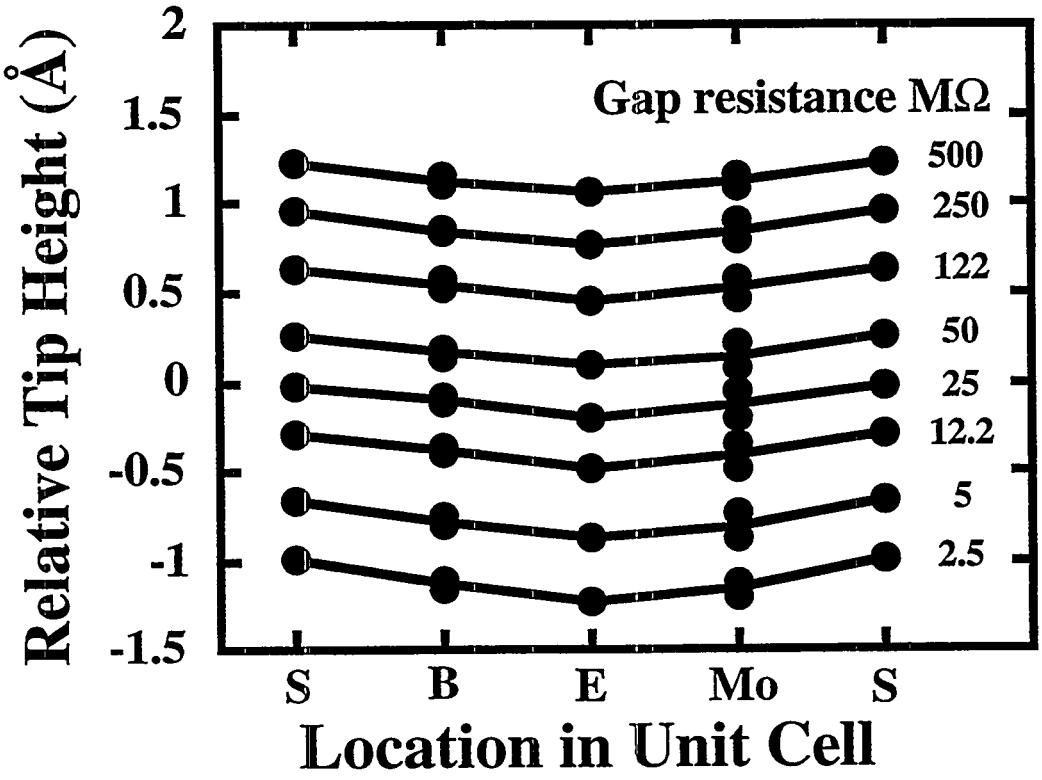

Figure 8.9 Example Of An Experimental Data Set

The data in this graph is extracted from the image data in figure 8.8. The data is in the same form as the theoretical data in figure 8.3 and can be easily compared quantitatively with it. An asymmetry appears at the Mo point in the unit cell in the middle range of tunneling gap resistance images. Two symmetrically equivalent data points have slightly different values.

experiments was always Pt. This is consistent with an uncontaminated predominantly Pt bulk tip. In addition, the results of the fit exclude a range of the possible surface structures. The best fit was for a S adsorbate height of 0.94 Å and a buckling of +0.10 Å. However, a range of about 20% of the selected parameter space produces nearly as good a fit.

The best fit results of the surface structure differ from the dynamic LEED[19] (S adsorbate height of 1.03 Å, buckling of -0.05 Å) results by approximately 0.1 Å. This error is significantly greater than the error expected for the LEED results (~0.03 Å). The most probable causes of the error in the STM results are inadequate modeling of the tip, which the data indicates was always somewhat asymmetric. Additionally, the Extended Hückel approximation of the electronic structure of the surface and tip produces inaccuracies in the theory. Finally, experimental error, such as small inaccuracies in the calibration of the piezoelectric elements moving the tip could have produced some additional error.

Figure 8.10 (NEXT PAGE)

All units in the plots are Ångstroms. These four contour plots show the variation of the fit quality factor, R_{STM}, with surface and tip structure. Each plot is for a different tip termination atom: S, Pt, C, or Mo. The x-axis on each plot represents the buckling of the second Mo layer; the y-axis represents the adsorption height of the S atom over the first Mo layer. The contours show the STM quality of fit factor R_{STM} defined in the text. The best fit is found for the Pt tip termination and a small range (about 20%) of the trial range of surface structures.

8.8 Conclusion

We have demonstrated that the contrast in STM images as a function of the tunneling gap is sensitive to the structure of the surface and that this fact may be utilized to

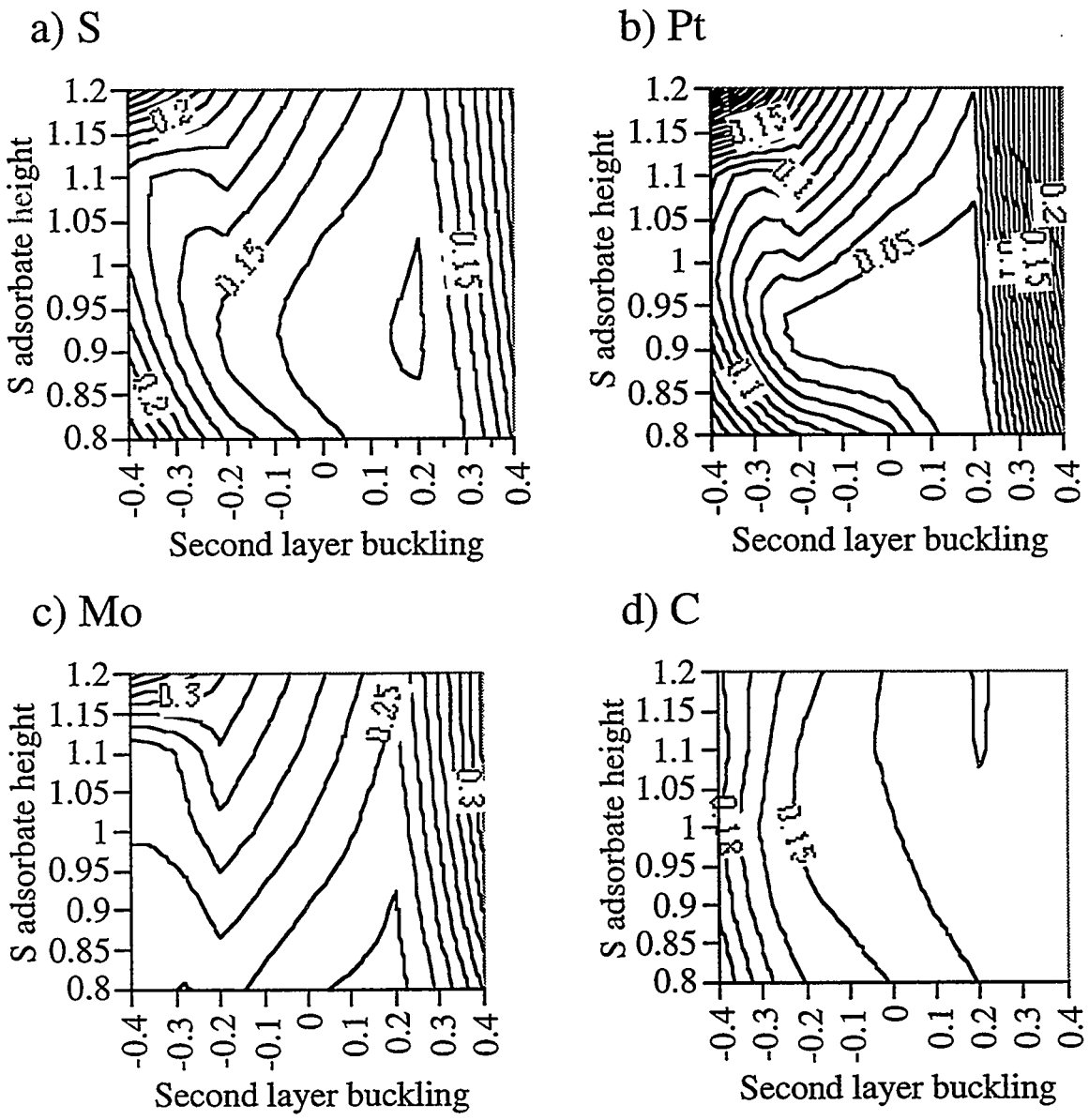

Figure 8.10 Fit Of The Experimental Data To Theory

determine quantitative information on the structure of the surface. By obtaining images over a wide range of tunneling gaps, the structure of the tip termination can be determined

while simultaneously reducing the range of potential surface structures. While STM is never likely to be as sensitive a probe of surface structure as diffraction techniques such as LEED, it can provide information inaccessible to these techniques. While here our technique was applied to a periodic surface to make comparison with LEED results possible, there is no reason why the same techniques cannot be applied to the study of defects on surfaces. In fact, the method may be even more accurate in this case, as images of the periodic areas of the surface may serve as a reference point with which to optimize the model of the tip structure.

There are several areas in which future work may improve the accuracy of the technique. The current definition of R_{STM} may overemphasize the rate of decay of the current with gap distance relative to the shape and corrugation of the images. This definition can be modified to better reflect the important features in the image from a structural point of view. The weakest point in the theory is the calculation of the Hamiltonian matrix elements by extended Hückel theory. In the future this calculation will be replaced with a more accurate method derived from *ab-initio* calculations of the surface electronic structure. In the experiment the greatest gains can be made through better control and characterization of the tip termination structure. It is likely that few methods will provide more accurate information on the tip termination than the analysis of the contrast of STM images produced with the same tip. Therefore, the tip termination will be characterized by imaging a known surface structure before or simultaneously with the imaging of an unknown structure. Tips with more symmetric tip termination structures may be produced by etching single crystal wire.

While a number of challenges remain ahead, we believe that the combination of multiple-gap imaging with theoretical calculations will allow the structure of simple chemisorbed systems on metal and defects in these overlayers to be determined from STM images.

Chapter 8 References

[1] M.A. VanHove and S.Y. Tong. *Surface Crystallography by LEED: Theory, Computation, and Structural Results.* (Springer-Verlag, Berlin, Heidelberg, 1979).

[2] H. Niehus, W. Heiland and E. Taglauer, Surf. Sci. Rep. **17** (1993) 213.

[3] C.S. Fadley. in *Synchrotron Radiation Research : Advances In Surface And Interface Science* (eds. Bachrach, R.Z.) p. (Plenum Press, New York, 1992).

[4] J.E. Rowe. in *Synchrotron Radiation Research : Advances In Surface And Interface Science* (eds. Bachrach, R.Z.) p. (Plenum, New York, 1992).

[5] J.C. Dunphy, P. Sautet, D.F. Ogletree and M.B. Salmeron, J. Vac. Sci. Technol. A (1993) 1975.

[6] M. Tsukada, K. Kobayashi and N. Isshiki, Surf. Sci. **242** (1991) 12.

[7] B.J. McIntyre, P. Sautet, J.C. Dunphy, M. Salmeron and G.A. Somorjai, J. Vac. Sci. Technol. B **12** (1994) 1751.

[8] S. Rousset, S. Gauthier, O. Siboulet, S.W. Sacks, M. Belin and J. Klein, Phys. Rev. Lett. **63** (1989) 1265.

[9] L. Ruan, F. Besenbacher, I. Stensgaard and E. Laegsaard, Phys. Rev. Lett. **70** (1993) 4079.

[10] R.M. Feenstra, J.A. Stroscio, J. Tersoff and A.P. Fein, Phys. Rev. Lett. **58** (1987) 1192.

[11] P. Sautet, J. Dunphy, D.F. Ogletree and M. Salmeron, Surf. Sci. **295** (1993) 347.

[12] P. Sautet, J.C. Dunphy, D.F. Ogletree, C. Joachim and M. Salmeron, Surf. Sci. **315** (1994) 127.

[13] A. Barbieri, D. Jentz, N. Materer, G. Held, J. Dunphy, D.F. Ogletree, P. Sautet, M. Salmeron, M.A. Vanhove and G.A. Somorjai, Surf. Sci. **312** (1994) 10.

[14] J.M. MacLauren, J.B. Pendry, P.J. Rous, D.K. Saldin, G.A. Somorjai, M.A.V. Hove and D.D. Vvedensky. *A Handbook of Surface Structures.* (D. Reidel, Holland, 1987).

[15] P. Sautet and C. Joachim, Ultramicroscopy **42-44** (1992) 115.

[16] P. Sautet and C. Joachim, Chem. Phys. Lett. **185** (1991) 23.

[17] P. Sautet and M.L. Bocquet, Surf. Sci. **304** (1994) L445.

[18] M.L. Bocquet and P. Sautet, in preparation

[19] D. Jentz, S. Rizzi, A. Barbieri, D. Kelly, M.A. VanHove and G.A. Somorjai, submitted to Surface Science (1994)

[20] S. Rousset, S. Gauthier, O. Siboulet, W. Sachs, M. Belin and J. Klein, J. Vac. Sci. Technol. A **8** (1990) 302.

[21] V. Maurice and P. Marcus, Surf. Sci. **262** (1992) L59.

[22] A.J. Gellman, J.C. Dunphy and M. Salmeron, Langmuir **8** (1992) 534.

[23] M. Salmeron, D.F. Ogletree, C. Ocal, H.-C. Wang, G. Neubauer, W. Kolbe and G. Meyers, J. Vac. Sci. Technol. B **9** (1991) 1347.

Chapter 9. DIFFUSION OF S ON Re(0001)

9.1 Imaging Low Coverage S on Re(0001)

Images of less than one quarter monolayer of S on Re(0001) were described briefly in chapter 5. In this chapter the results are described completely and analyzed. When a clean Re surface is exposed to H_2S gas the first observed change in the LEED pattern is from the clean Re(0001) $(1x1)$ pattern to a $p(2x2)$ pattern. Hence, there is no large scale ordering of the sulfur atoms in which they are spaced by a distance greater than twice the Re substrate lattice spacing a of 2.75 Ångstroms. The $p(2x2)$ spots in the LEED pattern do not appear suddenly. They gradually emerge from the background and increase in brightness and sharpness with increasing sulfur coverage. This indicates that some areas of the surface are covered with $p(2x2)$ ordered sulfur before a complete layer is formed.

Figure 9.1 shows an STM image of such a surface, covered with approximately 0.1 monolayers of sulfur. The image shows an island of hexagonally ordered maxima spaced by $2a$ surrounded by apparently clean regions. Such islands were found to vary in size between approximately four to twenty atoms. The presence of $p(2x2)$ islands at very low sulfur coverage indicates the interaction between single sulfur atoms, mediated by the substrate, is attractive at the third nearest neighbor distance of twice the rhenium lattice constant $(2a)$ and less attractive or repulsive at nearest neighbor (a) and second nearest neighbor $(\sqrt{3}a)$ distances. These distances, characteristic of triangular surface lattices, are indicated in figure 9.2. Because of the attractive interaction at $2a$, the sulfur atoms prefer to form $p(2x2)$ islands rather than spreading evenly across the surface while short range repulsive interactions prevent the formation of more densely packed islands.

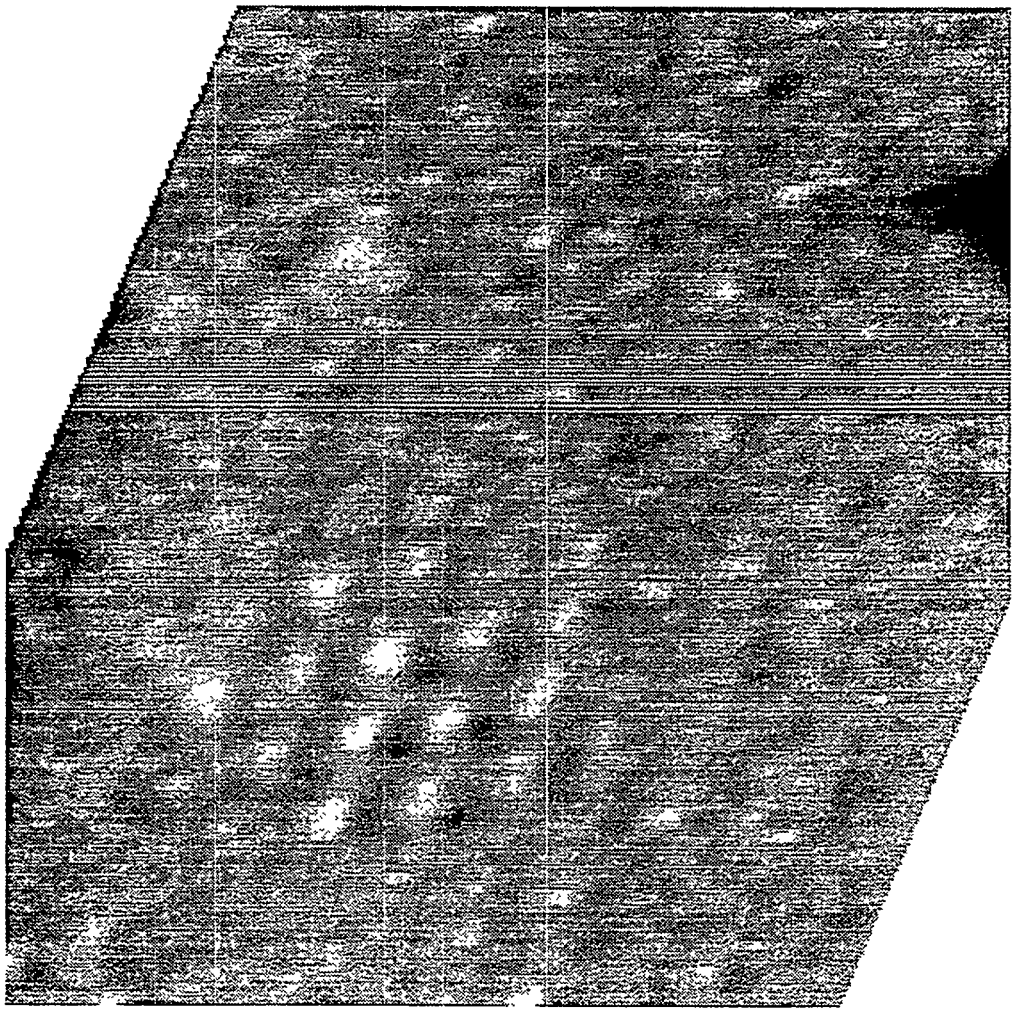

Figure 9.1 STM Image of a $p(2x2)$ Sulfur Island

Fourier filtered STM images of the Re(0001) surface covered with less than one quarter monolayer of sulfur show small sulfur islands. The corrugation of the atoms on the islands is higher at the center than at the edge. The image appears much more "noisy" than images of a complete $p(2x2)$ overlayer. This is explained as being a result of sulfur diffusion on the surface with a reduced residence time of the sulfur atoms at the edge of the island.

There are two unusual features of the STM images of $p(2x2)$ sulfur islands. First, in smoothed images, such as figure 9.1, the corrugation of the sulfur atoms making up the islands is not constant. Atoms near the center of the islands have the highest corrugation, while those near the edge have a smaller corrugation. Secondly, the raw data images such as figure 9.3 contains a large amount of apparent noise in the areas between the islands. This noise is primarily made up of horizontal "frizzes" which extends approximately the width of an atom in the horizontal direction, but only one to three lines in the vertical direction.

These features of such images may be explained as an effect of sulfur atoms moving across the surface at a time scale shorter than that required to produce an STM image. The STM tip rasters across the surface in the horizontal direction of the image while scanning slowly in the vertical direction. Therefore, adjacent pixels in the horizontal direction are acquired much closer together in time than adjacent pixels in the vertical direction. If the diffusion rate is not too rapid, a diffusing atom has much less probability

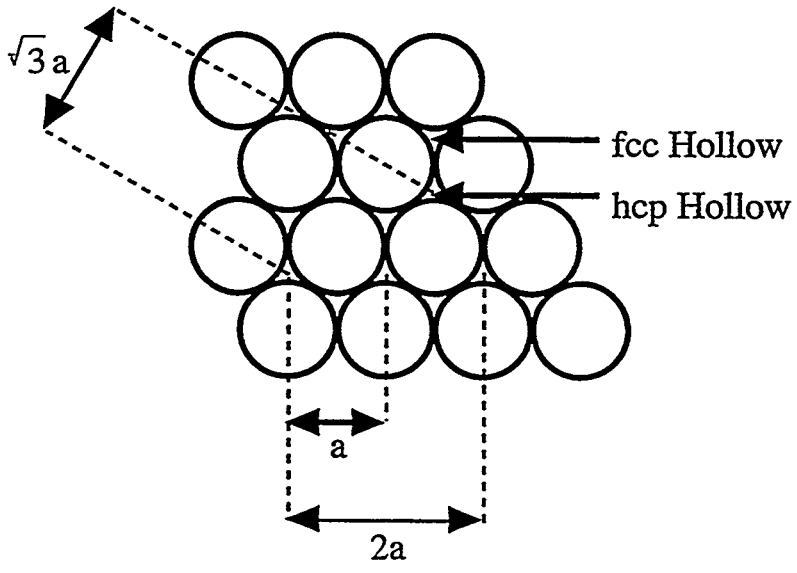

Figure 9.2 Distances Between High Symmetry Points on Re(0001)
This diagram shows the distances between closely neighboring hcp hollow sites on the Re(0001) surface. The fcc and hcp hollow sites are labeled.

to move while it is being scanned over in one line than it does between scan lines. The images of atoms are, therefore, sometimes complete in the horizontal direction, but not in the vertical direction. These incomplete images of atoms are shaped like horizontal dashes. Images with features of this type have been observed before by others,[1-5] and they were also interpreted as diffusing atoms or molecules.

The decrease in the corrugation of the atoms at the edge of islands seen in smoothed

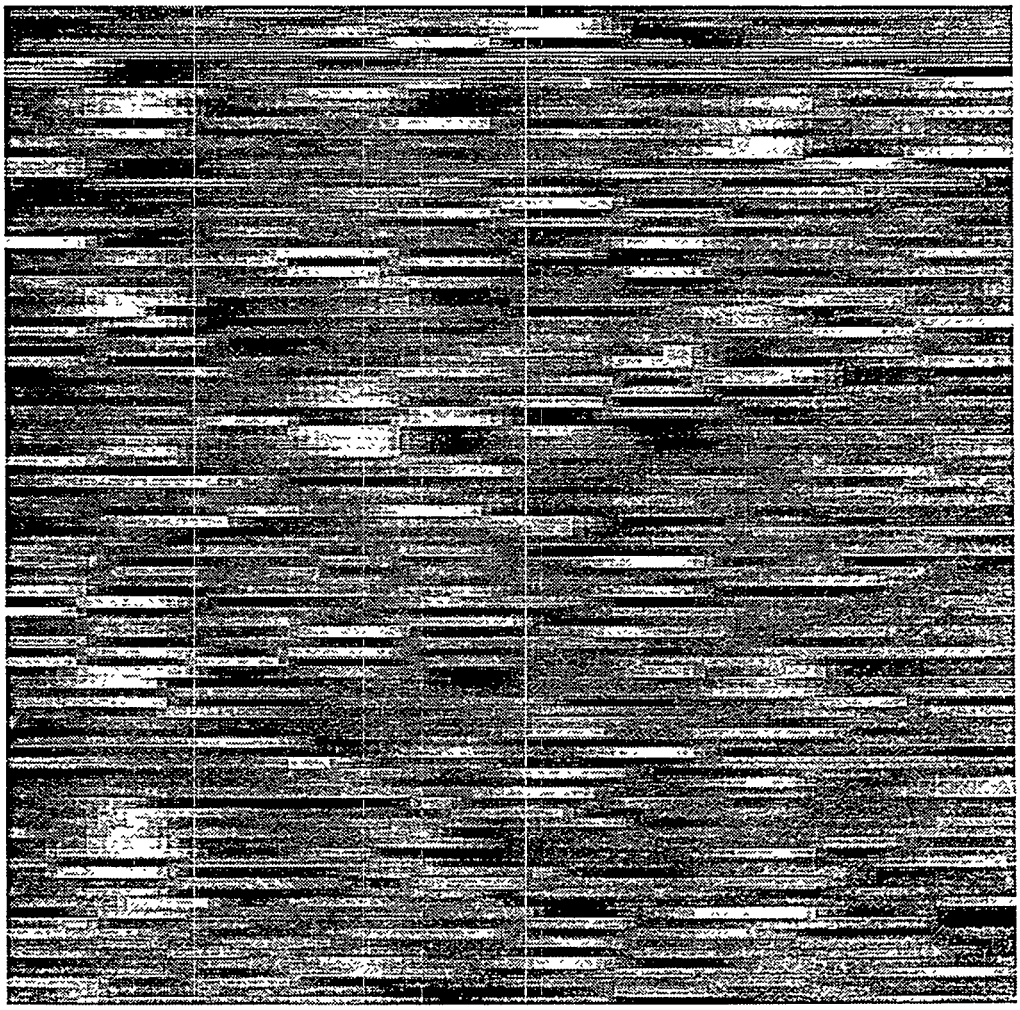

Figure 9.3 Magnified Raw Data Image of Diffusing Sulfur

This image shows a magnified area of the raw data of an STM image of an area between (2x2) islands. The horizontal "frizzes" in the image are the fraction of a sulfur atom which is imaged before it moves to another site.

images can be explained as a result of diffusion. The Fourier filtering used to remove noise from the images spatially smoothes the image, blending each scan line into the adjacent ones. If an atom is only present in half of the lines in the raw data, it will averaged into all nearby lines in the filtered image, but with a lower corrugation. The atoms at the edges of islands are clearly more likely to diffuse than those at the center, and therefore they have a lower corrugation due to a lower percentage occupation of these lattice sites. Atoms at the center of islands are blocked from moving by their neighbors. In contrast, atoms at the edge of islands are free to move away from the island, but weakly attracted to the island by the attractive interaction between the sulfur atoms at the $2a$ distance.

9.2 Surface Diffusion

Before discussing a more detailed analysis of the images of diffusing sulfur, it is worth fitting this work into the context of other studies of surface diffusion. The diffusion of atoms is important in any study of dynamic processes on surfaces. Such processes include chemical reactions in which reactants must be mobile in order to reach each other and react. Diffusion also plays a major role in controlling nucleation and growth on surfaces by controlling the ability of an adsorbed atom to find and attach to an island or a step edge. Because of its importance, surface diffusion of adsorbates has been detected and measured using a variety of techniques on a large number of systems.[6]

Many methods of determining diffusion coefficients on surfaces have been developed, but few of these techniques provide atomic-scale information. One method relies on measuring the change in shape of a feature on a surface that is composed of many atoms. This can be done using SEM or STM imaging.[7, 8] This method does not separate the effects of surface diffusion on terraces from kink and bulk diffusion. Several other methods which do make an independent measurement of surface diffusion are high energy electron diffraction,[9] quasi-elastic helium scattering,[10] and laser-induced thermal desorption.[11] These techniques make a macroscopic average measurement of diffusion,

and the measurement may be affected by the presence of surface defects such as steps. They also do not provide information on the interactions between adsorbed atoms.

Methods which observe diffusion at a more microscopic scale may overcome these limitations. Field electron emission may be used to measure diffusion by direct observation of the diffusion of an overlayer over the end of a tip as a function of temperature.[12] Another approach is to analyze the correlation of field emission current fluctuations generated by atoms or molecules diffusing into and out of a small area of the surface.[13] Field ion microscopy has been extensively used to directly observe the diffusion of single atoms and small clusters on a number of metal surfaces.[14, 15] These observations allow a direct measurement over a wide range of temperatures of anisotropic diffusion, diffusion over barriers such as steps, and cooperative diffusion. In the appropriate temperature range, the Scanning Tunneling Microscope (STM) also allows diffusion of single adatoms to be observed on a variety of systems.

Several methods have been employed for obtaining quantitative measurements of diffusion from STM images. The simplest method is to measure the change in shape of some nanometer-scale feature placed on the surface.[16, 17] Another method is to observe the shape and number of islands formed during deposition of atoms on a surface[17, 18] and after annealing of the surface. These experimental results can be compared with the results of Monte Carlo simulations to determine diffusion parameters.[16] On other systems the diffusion is slow enough so that the hopping of atoms can be observed directly from the changes between images taken sequentially.[1-4] Diffusion occurring at rates faster than the time between two images has been observed in a number of systems,[1, 2, 4, 5, 19] but obtaining a quantitative measurement of diffusion is difficult in this case. Since interpretation of the images is complicated by the possibility that the state of the surface may change between the acquisition of two image pixels, few have tried to derive quantitative information from these images. Binnig et al. have attempted to measure the diffusion constant of oxygen on nickel from "flicker noise" or spikes in the STM tunneling

current which they interpreted as due to atoms diffusing under the tip.[19] M. Poensgen et al. calculated the density and diffusion rate of kinks from the "frizzing" of steps in their STM images caused by step diffusion.[5] A somewhat similar analysis is applied here to the S on Re(0001) system to measure the diffusion rates and interactions of single adsorbate atoms.

9.3 Analysis of Images of Diffusing Atoms

9.3.1 Lattice Gas

Naturally sulfur would not be expected to diffuse smoothly over the surface. Because the hcp hollow sites have a lower energy than other sites, the sulfur will occupy these sites the overwhelming majority of the time and hop between them as a lattice gas.[20] While direct evidence showing that the sulfur diffuses as a lattice gas will be presented later, there is some evidence of this visible in the raw data. In some areas of the images such as figure 9.3 it is possible to observe streaks due to single atoms hopping between hcp hollow sites. Here, the dashes in the image appear at one point in the section of the image lines, but never at more than one.

The results so far indicate that there are sulfur atoms diffusing over the surface as a lattice gas in the areas between islands of $p(2x2)$ ordered sulfur. There are more questions about how this diffusion occurs that may be answered with the STM data: What is the residence time of a sulfur atom per site? What is the energy barrier for diffusion? How do the diffusing sulfur atoms interact with each other?

9.3.2 Correlation Function

In order to answer these questions, a method for interpreting STM images of diffusing atoms needs to be developed. As some of the sulfur adatoms are moving at a rate faster than the STM imaging, it is impossible to know the exact location and motion of all atoms in the image. However, the average positions of atoms relative to each other is

contained in the image data. A spatial pair correlation function was used to extract this information. This function,

$$C(r,t)=\frac{1}{N}\sum_{\vec{r}_o,t_o} I(\vec{r}_o,t_o)I(\vec{r}_o+\vec{r},t_o+t)\ . \tag{9.1}$$

is the average product of the tunnel current value at pixels in an image or part of an image separated by a particular vector. It is quite different from the autocorrelation function used in chapter 7 for finding similar points in images. N is the number of products in the sum, and $I(\vec{r},t)$ is the current value at a pixel in the image at position $\vec{r}$ at time t. In an STM image, t is a function of $\vec{r}$ since it is only possible for the tip to be at one point in the image at a time. The value of this average product or correlation function is a measure of how well pixels at a particular distance and time separation are correlated. On a well ordered surface, pixels separated by vectors close to the lattice vectors of the overlayer should be well correlated, because the overlayer atoms are well correlated at this distance. This spatial correlation function can be represented as a two dimensional map or image which will be called a correlation image.

It is convenient to express the tunneling current as

$$I(r,t)=I_o+I_n(t)+\sum_i n_i(t)f\left(\left|\vec{R}_i-\vec{r}\right|\right) \tag{9.2}$$

where $I_o+I_n(t)$ is an average current and noise, and the sum represents the contribution of the sulfur overlayer. It is over the lattice of hcp hollow sites $\vec{R}_i$, where the occupation $n_i(t)$ is zero or one, depending on whether or not a site is occupied at time t. The function $f(\vec{r})$ describes the shape of sulfur atoms in the image.

Substituting this model for the current into equation (9.1), one finds that only one term besides the noise is not constant. The noise term averages to zero for sufficiently large times t. The remaining term is the average correlation between atoms at two times and places separated by a fixed time and distance,

$$I_{corr}(\vec{r},t)=\sum_{i,j}\left\langle n_i(t_o)n_j(t_o+t)\right\rangle_{t_o}\left\langle f\left(\left|\vec{r}_o\right|\right)f\left(\left|\vec{R}_j-\vec{R}_i-\vec{r}_o-\vec{r}\right|\right)\right\rangle_{\vec{r}_o}\ . \tag{9.3}$$

One would expect that the correlation function has a maximum at each $\vec{r}$ which is a lattice vector separating two hcp hollow sites. The size of this maximum is proportional to the probability of overlayer atoms being separated by this lattice vector. The first term in the sum of equation (9.3) represents the separation in time at which the correlation is determined. For an STM image, one is limited to a given t for each vector $\vec{r}$, but since lattice vectors rotated by 60° are equivalent, several time separations for each lattice vector are available in the data.

In the first part of the analysis, the time correlation in equation (9.3) is neglected and the occupations $n_i(t)$ and $n_j(t)$ are assumed to be constant in time. This is the idealized case in which the STM image is taken quickly enough so that no adsorbate atoms move during the image acquisition. The effect of changes in $n_i(t)$ and $n_j(t)$ with time during imaging, and the information which may be obtained from these changes, will be discussed later.

The correlation function was calculated for a number of experimental images and sections of experimental images. Two representative correlation images, together with the original data, are shown in figures 9.4 and 9.5. When an image with many of the "frizzes" of diffusing atoms is used as input, the correlation image shows that the surface is unexpectedly well ordered. The image shows clearly that the sulfur is diffusing between low energy sites as a lattice gas. The correlation image has maxima on a $p(2x2)$ lattice, not the $(1x1)$ lattice of hcp hollow sites that would be expected if the sulfur atoms were not interacting. The diffusing sulfur atoms are most likely to be separated by lattice vectors of the $p(2x2)$ lattice, even when they are separated by many lattice constants. At small odd multiples of a there are minima in the correlation plot, signifying that it is unlikely to have atoms separated by this distance. The first of these minima is the lowest, due to the repulsive interaction of sulfur atoms at this short distance. Although the atoms are diffusing, they maintain a local $p(2x2)$ order which extends at least several unit cells over

the surface. This order is maintained even on parts of the surface, such as the upper part of figure 9.5, where there appear to be no stationary sulfur atoms.

The size of the maxima in the correlation image, as a function of their position away from the center, is a direct measure of the probability that atoms are spaced by that particular lattice vector. The experimental curve (A) in figure 9.6 shows a cross section through several of the maxima of a correlation image. The central maxima is the correlation of each atom with itself. Each atom of the surface contributes to this peak, and thus its height is proportional to the coverage. Peaks at a distance of $2a$ receive a contribution from each pair of atoms separated by $2a$ in the image. Their height is proportional to the probability of $2a$ neighbors on the overlayer lattice. Peaks at large distances represent the probability of finding two atoms at a large distance from each other at the same time. Since atoms far from each other should not be well correlated, and since the probability of each atom being present is proportional to the coverage, this peak height is proportional to the square of the coverage.

9.3.3 Effect of the STM Tip on Diffusion

In any measurement of diffusion by STM, it is important to consider what effect, if any, the presence of the STM tip may have on the process. Could the presence of the STM tip over the surface be catalyzing or increasing the rate of diffusion? There are several reasons to believe that this is unlikely. First, there is no evidence in the images that the tip is having any direct effect. Two images, one in which the tip is scanning to the right in each image line and one with it scanning left, are acquired simultaneously. They were found to be identical. If the tip were pushing the sulfur atoms in the scan direction, the motion would be apparent from large differences in the position of sulfur atoms in these two images.

A. Raw STM Image

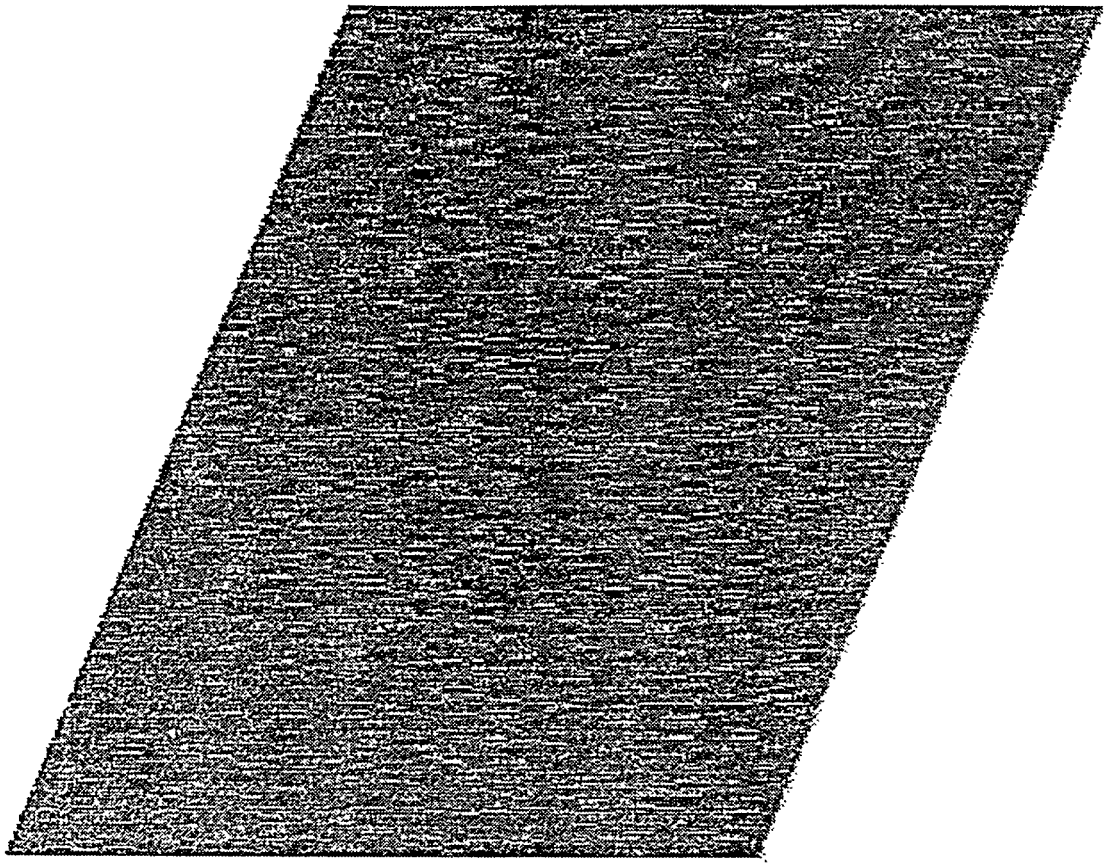

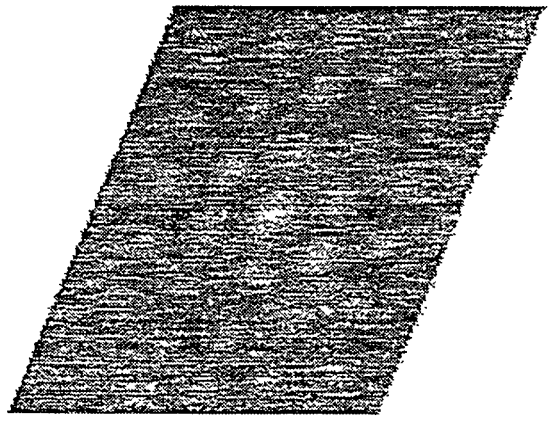

B. Pair Correlation Image

Figure 9.4 An Image of Diffusing Sulfur and its Correlation Image

A 70 X 70 Å STM image (A) of diffusing sulfur atoms and the corresponding correlation image (B). The correlation image shows that the diffusing sulfur is a lattice gas which maintains a local $p(2x2)$ order over several lattice distances.

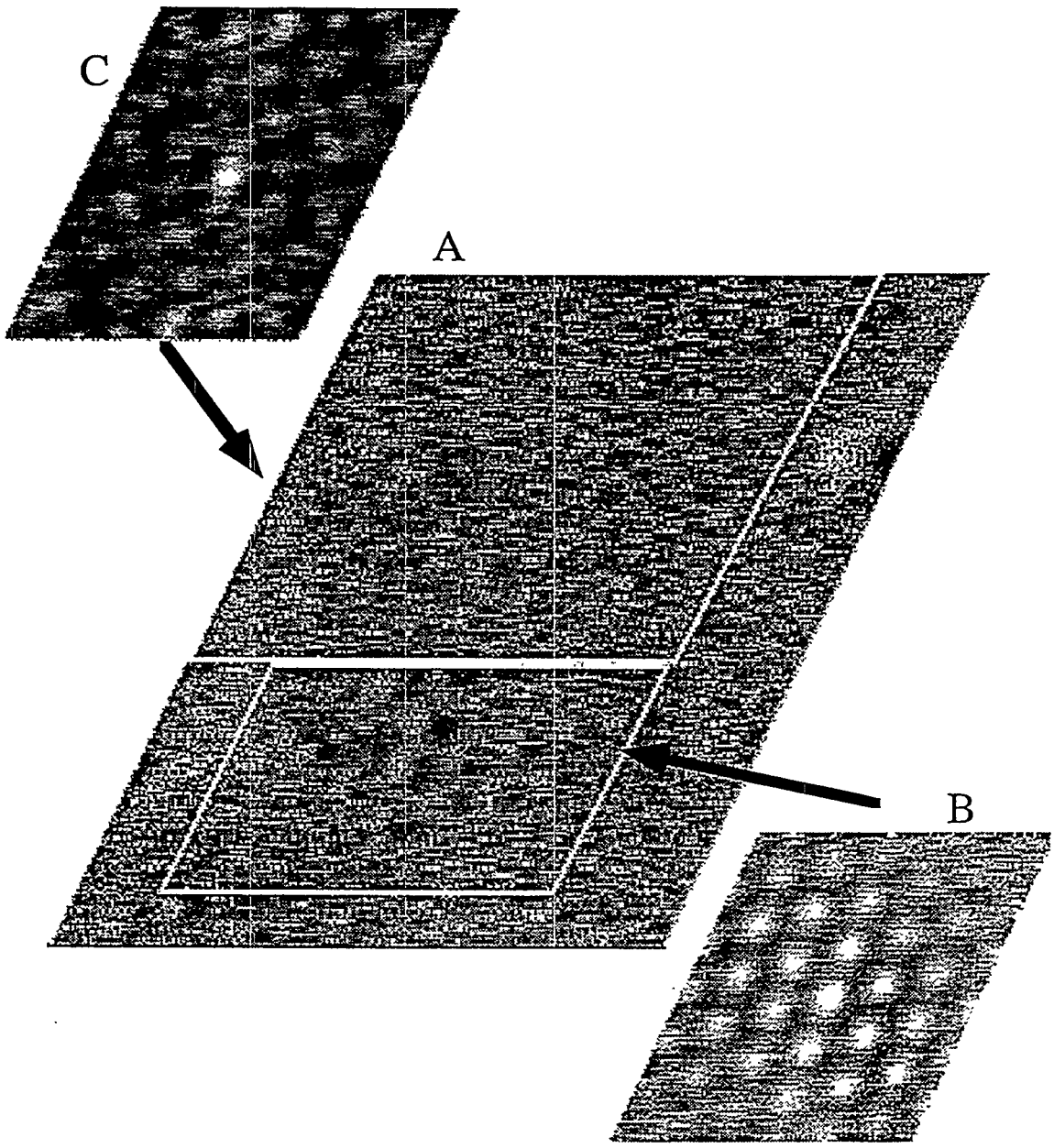

Figure 9.5 Image of Diffusing Sulfur and Partial Correlation Images An STM image (A) of a sulfur island surrounded by an area of diffusing sulfur. In the correlation image (B) of the island area all the peak heights are roughly equal. However, in the correlation image (C) of the diffusing atoms, the center peak is much higher than the surrounding peaks because the coverage in this area is low.

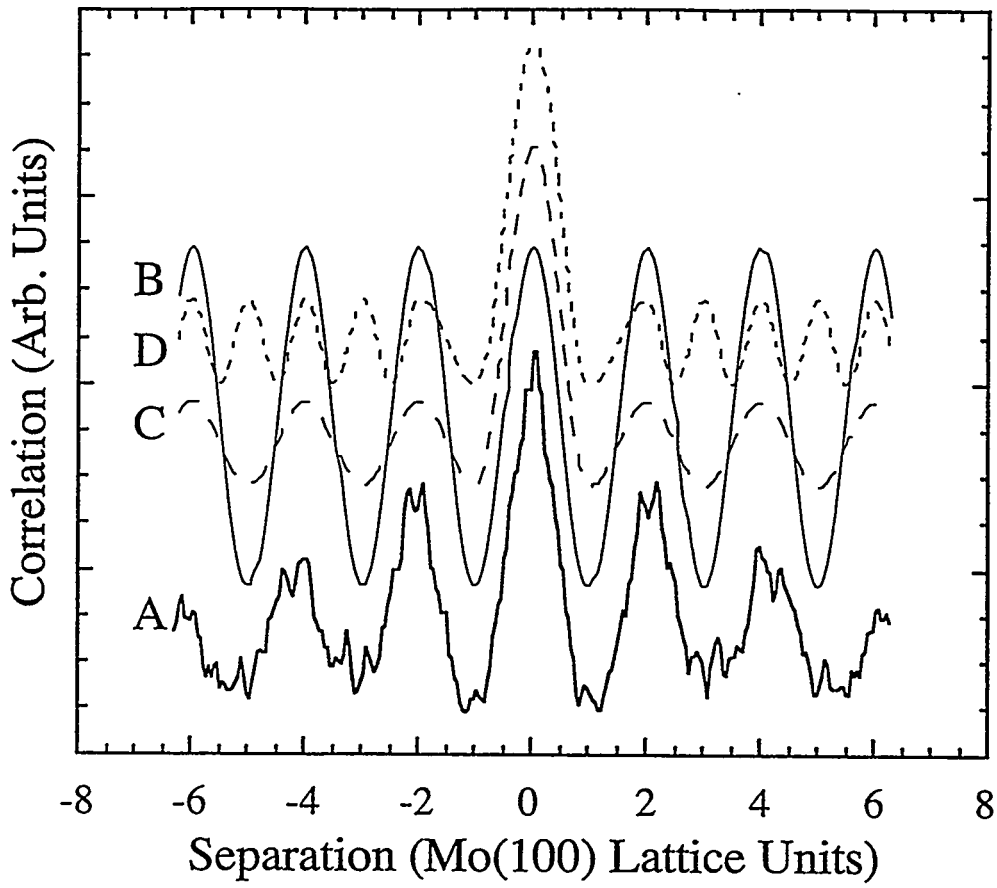

Figure 9.6 Correlation Cross Section Plots

This graph shows the cross section of an experimental correlation image through the center maxima and the expected cross section in the limiting cases of no interaction (C & D) and a large interaction (B) between sulfur atoms. In curve (C) the sulfur atoms have a long range $p(2x2)$ order as observed experimentally despite the lack of interaction, while in curve (D) no long range order is enforced. The experimental cross section (A) is between the limits (B) and (C).

Secondly, at the gap used in imaging, approximately 50 MΩ, the ESQC theoretical calculations of the tunneling gap described in chapter 6 indicate that the tip is six Angstroms from the sulfur atoms on the surface. This distance is too far for any direct chemical bond to exist between the sulfur atoms and the tip end atom. Experimentally, Eigler et al. have shown that a gap resistance ten times as small as the one used here is required to move xenon atoms along the rows on Ni (110) and a gap two hundred and fifty times as small is needed to move platinum atoms on the Pt(111) surface.[21] The binding energy of sulfur to the rhenium surface is more than an order of magnitude stronger than that of xenon on nickel and of the same order of magnitude as platinum on platinum. Therefore, the gap resistance used in imaging is several orders of magnitude larger than that needed to push the sulfur atoms across the surface. The observed sulfur diffusion is not a result of the close proximity of the STM tip.

9.4 Ising Model of Sulfur-Sulfur Interaction

The ability to measure the relative probability of atoms being separated by different distances on the surface allows the interaction of the atoms to be measured by fitting the results to a model. The most basic information available in the correlation function is the sulfur coverage and the probability of pairs of adatoms at the $2a$ distance on the rhenium surface. If there were no interaction between overlayer atoms, the probability of pairing at multiples of $2a$ would be proportional to the square of the coverage for any separation distance, as indicated in cross section curve (D) in figure 9.6. If the diffusing sulfur atoms are forced to order in a $p(2x2)$ lattice, as observed experimentally, the cross section curve would appear as (C) in figure 9.6. If there is an attractive interaction between atoms separated by this distance, one would expect an increased number of pairs. In the limiting case in which the attraction is so strong that all the sulfur atoms are on islands, a cross section of the correlation image would appear like curve (B) in figure 9.6. The actual experimental data in curve (A) is in between these limits.

The number of pairs can be calculated in a simple model. We chose to use the simplest possible model for the interaction between the diffusing sulfur atoms, an Ising model,[22] since it can be solved analytically. In this model, atoms are only allowed to be on the sites of a lattice, in this case the $p(2x2)$ overlayer lattice. This accurately reflects the experimental finding that repulsive interactions prevent sulfur atoms from coming closer together than $2a$ at the low sulfur coverage of the experiment. The model only includes the interaction between pairs of atoms separated by $2a$. However, this interaction appears to dominate the long range adsorbate-adsorbate interactions. The lack of ordered structures with sulfur atoms separated by more than $2a$ is evidence that longer range interactions are weaker than the $2a$ separated pair interaction. While, at higher coverage, many body interactions must be considered to explain the variety of structures formed by sulfur on rhenium,[23] the atoms are widely separated at the low coverage of the $p(2x2)$ structure so interactions beyond the nearest neighbor are not likely to be significant. Therefore, the Ising model is a reasonable approximation for the experimental system.

In this model the total energy is the sum of a pair interaction energy and a chemical potential energy for each atom. The total pair interaction energy is simply the product of a pair interaction energy E_{12} and the number of pairs separated by a distance of $2a$. The chemical potential energy term controls the equilibrium coverage. The total energy of the system may be written as

$$H = E_{12} \sum_{pairs(i,j)} n_i n_j + E_1 \sum_i n_i \quad , \tag{9.4}$$

where n_i is the occupation of a site i. This model is analogous to the Ising model for ferromagnetism.[24] The first term is equivalent to the exchange interaction between pairs of spins and the second term is equivalent to the interaction between spins and a magnetic field. Equation (9.4) may be rewritten in the usual Ising form by substituting the spin σ_i for the occupation,

$$n_i = \frac{1}{2}(1 + \sigma_i) \quad . \tag{9.5}$$

This model may be solved analytically using the Weiss molecular field approximation.[22] Since the Re(0001) surface is a triangular lattice, the calculation was done on a group of three overlayer nearest neighbor sites. All the other nearest neighbors of these atoms on the overlayer were taken to have the average occupation. The probability of pairs was calculated as a function of average coverage and pair interaction energy E_{12}, and normalized to the non-interacting case where the probability is equal to the square of the coverage.

The results of this model are shown in a contour graph, figure 9.7, of pair interaction energy as a function of coverage and normalized pair probability. The experimental results from the correlation function are indicated by stars. From the fit of the experimental results to the theoretical curves, the pair interaction energy for sulfur atoms is found to be 24 ± 5 meV. The error bars on the data are wide because there are statistical fluctuations due to the limited size of the STM images.

The molecular field approximation assumes that the overlayer is homogeneous which is inaccurate when large islands form. This approximation is valid at low coverage and energy, but causes an underestimate of the probability of pairs at higher energy and coverage. An exact solution of the Ising model[7], which is possible only at a coverage of one eighth of a monolayer, shows that islands will form in the overlayer at a pair interaction energy above 28 meV at room temperature. Since this energy is very close to the interaction energy determined by this experiment, the model is not accurate for this system at a coverage above approximately one eighth of a monolayer. Due to this limitation of the theoretical model, the two highest coverage experimental points do not fit well with the model and were not used in the determination of the interaction energy.

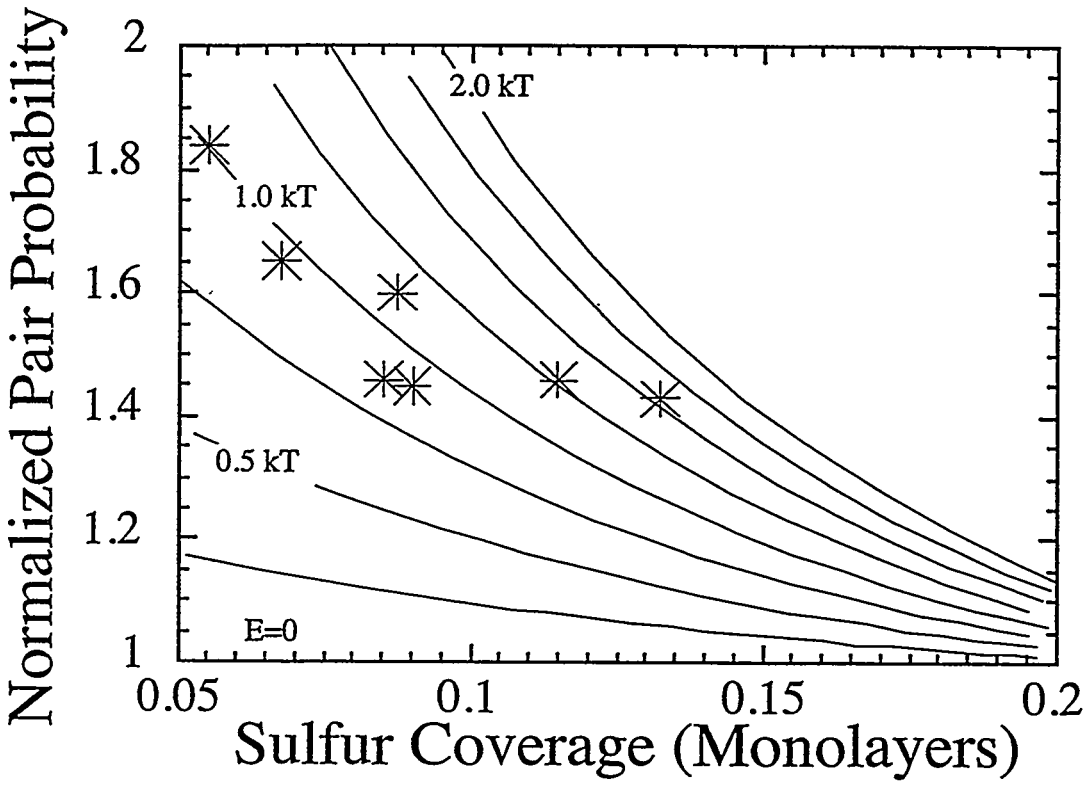

Figure 9.7 Graph of Ising Model Results and Experimental Data

This graph displays the results of the Ising model and experimental data. The horizontal axis represents the sulfur coverage or the ratio of the number of sulfur atoms to first layer rhenium atoms. The vertical axis is the probability of pairs of atoms at the $2a$ distance. This axis is normalized such that the result is 1.0 in the zero interaction energy case in which pairs form randomly. The results of the Ising model are displayed as contours of constant interaction energy spaced at intervals of 0.25 kT. The experimental results are shown as stars. The five experimental points at low coverage follow these contours, but the contours fall below the two higher coverage points due to inaccuracies in the theoretical model at high coverage at which large $p(2x2)$ islands begin to form on the surface. From the fit of the five low coverage experimental points to the Ising model, the attractive interaction energy between sulfur atoms at the $2a$ distance was determined to be 24 ± 5 meV.

The effect of the approximation that the time part of the correlation in equation (9.3) is ignored must be considered. Since atoms are known to be moving at a rate comparable to the scan speed, this term is clearly of some significance. However, its presence does not affect the size of the central maximum or maxima at large distances in the correlation image. At the central maximum, the time difference is nearly zero so the approximation that n_i and n_j are constant is nearly valid. At large distances there is little spatial correlation, so the expected lack of time correlation is unimportant. However, the probability of pairs separated by $2a$ would be affected by this term. If the diffusion rate is too fast, there is a large chance of one or both atoms in a pair moving before the tip scans over them both. This would cause a decrease in the measured probability of pairs. In the limiting case of short residence time, these maxima would be the same size as those at large distances, and proportional to the square of the coverage. However, the amount of the decrease would be dependent on the time separation between the tip scanning over each of the two atoms and so it would be dependent on the angle of the pair relative to the horizontal scan direction. Within the measurement error no such dependence was seen in the experimental results. This may be due to the increase in the residence time caused by the attractive pair interaction. Since none of the correlation maxima in the image is strongly affected, inaccuracies due to the constant $n_i(t)$ approximation are expected to be small.

The time correlation term does have an effect on the shape of the central maximum in areas of the surface with a very low sulfur coverage, such as the upper part of figure 9.5. In these areas, the sulfur atoms appear to move before they are completely imaged. The time correlation in equation (9.3) decays with increasing time separation, as the atoms have an increasing probability of having moved. This causes a decay in the central maximum of the correlation image in the y-scan direction. Comparison of the central maximum in the correlation of the low coverage section of figure 9.5C with that of the island, shows that this asymmetric shape is not due to the STM tip structure.

9.5 Diffusion Energy Barrier Calculation

The residence time for atoms which are not attached to an island can be determined from the shape of the maxima in the correlation image or from the size in the y-scan direction of the dashes in the raw data. This turns out to be approximately two STM scan lines or 100 ms. An estimate of the energy barrier to diffusion can be calculated from this measurement. Since the residence time was measured at only one temperature, the exact pre-exponential term cannot be determined. Using a standard pre-exponential of 10^{14} sec^{-1} the mean number of diffusions per second between two sites is given by the Einstein equation[25],

$$n = 10^{14} \exp\left(-\frac{E}{kT}\right) \quad . \tag{9.6}$$

Taking into account the number of possible sites an atom may diffuse to, this formula gives a diffusion energy barrier of 0.79 ± 0.1 eV. Since the residence time and pre-exponential factor determine E through a logarithmic dependence, errors of one order of magnitude in these parameters imply only a 0.06 eV change in E.

This result compares well with the energy barrier predicted by an Extended Hückel calculation of the relative energy of a sulfur atom at several positions on a rhenium cluster. In this calculation a sulfur atom was placed on the top of a three layer thick seventy atom cluster of rhenium atoms at hcp and fcc hollow sites, the top site, and a bridge site. The height of the sulfur atom was such that its distance to the nearest rhenium atom was set equal to the sum of the covalent radii. A correction was made for the effect of the edges of the cluster.[26] Relative to the hcp hollow site, the fcc hollow had an energy 0.1 eV, the bridge site had an energy 0.74 eV, and the top site energy was 1.6 eV. Therefore, the lowest energy path between two hcp hollow sites is over a bridge site to an fcc hollow and then over a second bridge site. The highest energy along this path is at the bridge sites. The energy of these sites (0.74 eV) compares quite well to the experimentally determined energy barrier.

This result is toward the high end of the range of diffusion barriers which have been measured by field ion microscopy, especially on close packed surfaces. In particular, the energy barrier for diffusion of sulfur on Ni(111) has been measured to be 0.29 to 0.30 eV.[27] However, this discrepancy can be explained by the large binding energy of sulfur on Re(0001). Diffusion barriers roughly scale with adsorption energy. The adsorption energy of sulfur on Re(0001) of 4.3 eV[28] is approximately 65% higher than that of sulfur on Ni of 2.6 eV.[29]

9.6 Monte Carlo Simulation

9.6.1 Motivation

While the mean field approximation solution to the Ising model provides an analytical description of the statistical mechanics of the interactions of adsorbed sulfur, it suffers from several inaccuracies. First, the model allows interactions only between nearest neighbor atoms so the lattice used to represent the substrate must be the $p(2x2)$ overlayer lattice and not the underlying $(1x1)$ lattice formed by hcp hollow sites. This approximation creates inaccuracies at low sulfur coverage at which the overlayer begins to disorder from a partially filled $p(2x2)$ lattice to a randomly filled $(1x1)$. Secondly, the mean field approximation is only valid when the local environment of each sulfur atom can be accurately described as a disordered distribution of filled and unfilled $p(2x2)$ sites. This approximation becomes invalid when islands, such as the one shown in figure 9.1, begin to form on the surface. The poor fit to the experimental results at higher coverage are clearly shown in figure 9.7.

In addition to these inaccuracies of the analytical model, several questions still remain regarding the correlation images. Why is the sulfur well correlated into a $p(2x2)$ lattice even at many lattice spacing distances and low coverage? Why don't the images show a large anisotropy between the x and y directions due to the difference in time scale between these directions?

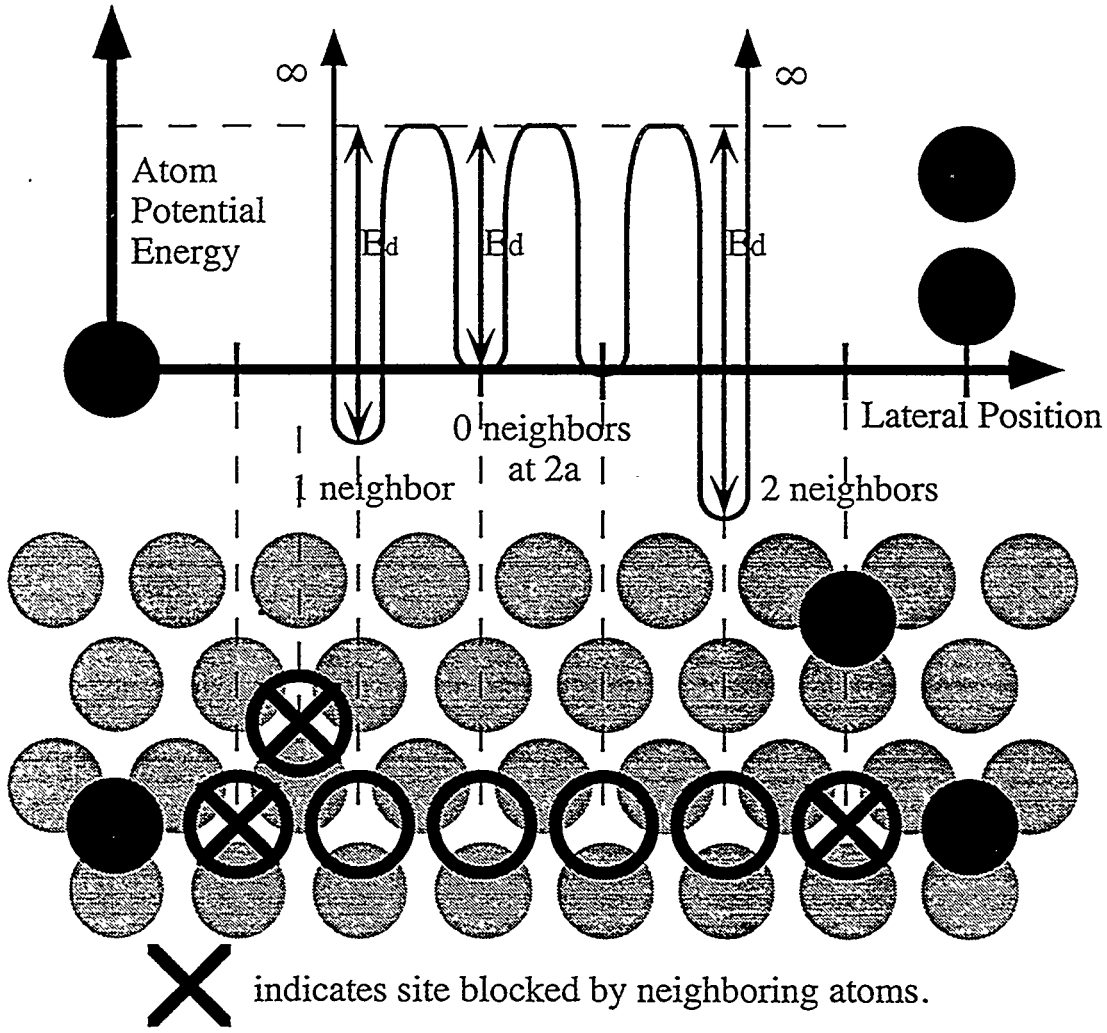

Figure 9.8 Monte Carlo Simulation Energy Diagram

The energy of each adsorbate atom is determined by its surroundings. The graph above shows a potential energy diagram for a sulfur atom at the locations indicated by the open circles on the model of the surface below. Atoms are not allowed to be closer than $2a$ from each other (effectively an infinite energy at distances $<2a$). Each neighbor at a distance of $2a$ reduces the energy of an atom by $\frac{1}{2}E_{12}$, its share of the pair interaction energy. The energy of the transition state for diffusion to another hcp site is kept constant, regardless of the surroundings.

9.6.2 Model

While there is no way to analytically solve the complete statistical mechanical problem of interacting sulfur, the Monte Carlo computer simulation method[20] may be used to accurately model the problem, and statistical information may be derived from the simulation. In addition, the Monte Carlo method includes the time dependence of the surface structure and thus it is possible to simulate the STM images of diffusing sulfur.

The complete model used in the Monte Carlo simulation for the sulfur adsorbate energy as a function of the local configuration is shown in figure 9.8. For each neighbor at $2a$, the energy of a sulfur atom is reduced by $\frac{1}{2}E_{12}$, one atom's share of the pair interaction energy. The atoms are not allowed to move closer than this distance, which is the equivalent of an infinite repulsion at shorter distances. This is an accurate model of the high (relative to kT) repulsive interaction between sulfur atoms at short distances. The energy of the diffusion transition state (presumably sulfur bound at a bridge site) is kept constant regardless of the surroundings. Thus the barrier to diffusion for an atom from a site increases proportionaly with the number of pairs associated with that atom.

In the simulation the surface is represented by a triangular lattice of 128 x 128 sites with periodic boundary conditions. Initially, a specific coverage of sulfur atoms is deposited randomly over these sites. In each time-step (0.1 to 1 ms) of the simulation every sulfur atom is given a chance to diffuse to any of its surrounding 6 neighboring sites. The atoms are blocked from moving to any site at which they would have a neighbor close than $2a$. The probably of diffusion to the remaining sites is determined by equation (9.6). As the diffusion energy barrier is determined by the number of pairs associated with the atom, atoms with fewer neighbors at $2a$ diffuse move more quickly than those with many neighbors.

9.6.3 Phase Transition

The number of pairs is measured as a function of time. With increasing simulation time this value approaches an equilibrium with small fluctuations due to the finite lattice size. After running the simulation for 5-10 times the number of cycles required for the number of pairs to reach an equilibrium, the state of the surface is recorded or an STM image is simulated.

There are two controllable parameters in the simulation: the sulfur coverage and the pair interaction energy. The phase space of the system was partially mapped by comparing the results of simulations with different values of these parameters. The interesting portion of the results is displayed in figure 9.9. Each image is representative of the equilibrium state of the surface with a particular sulfur coverage and pair interaction energy. The figure shows the phase transition from a lattice gas, at low pair energy and coverage, to complete ordered islands in equilibrium with a dilute lattice gas at higher interaction energy and coverage.

The phase transition takes place at approximately the pair interaction energy determined by the fit to the Ising model, 24 meV. This is consistent with the observation of small islands forming at the higher coverage range studied in the experiments.

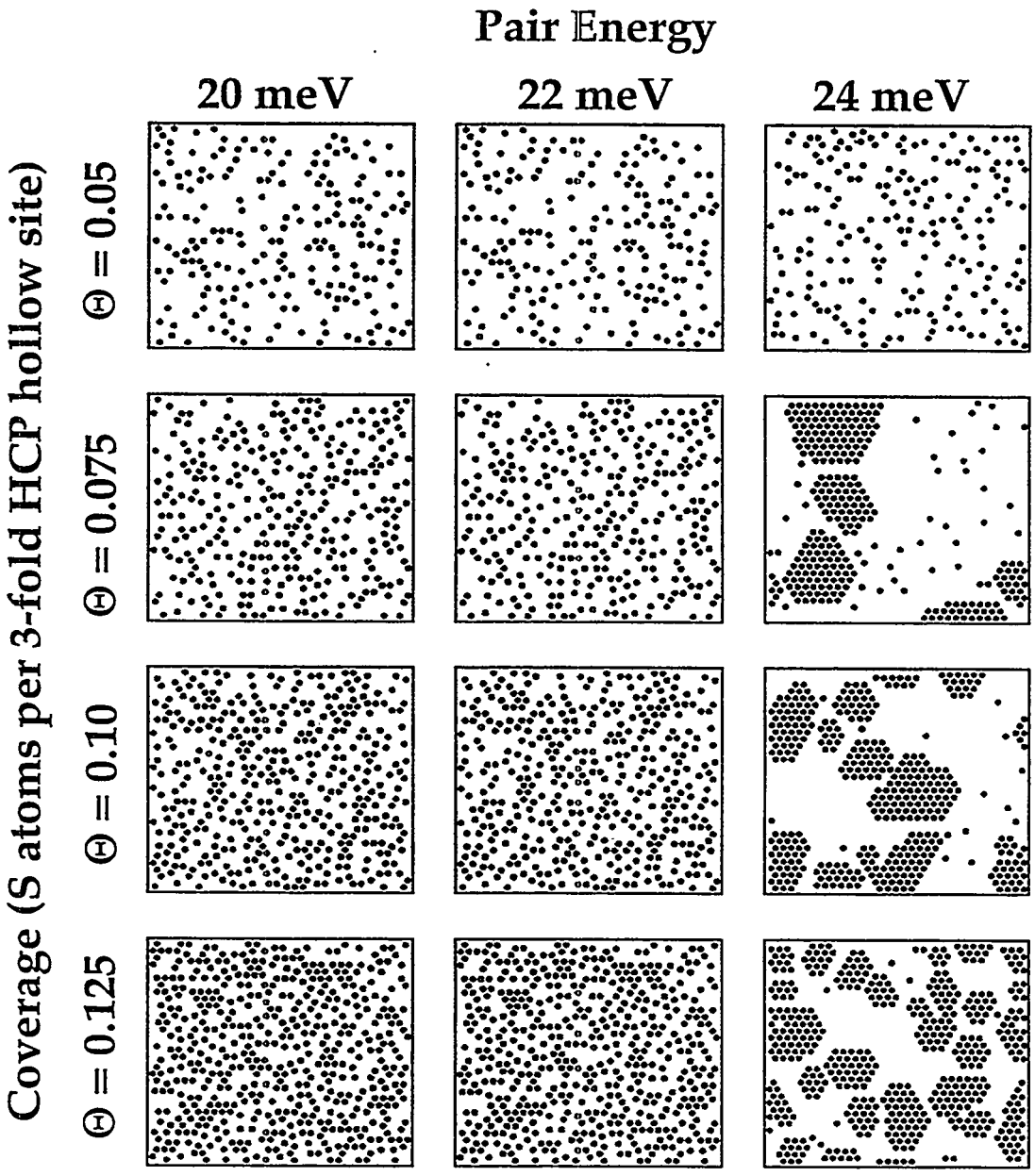

Figure 9.9 Phase Transition

Output of the Monte Carlo simulation showing representative equilibrium surface state at four different sulfur coverage values and three pair interaction energies. At high coverage and interaction energy a phase transition occurs between lattice gas and solid islands in equilibrium with a dilute lattice gas.

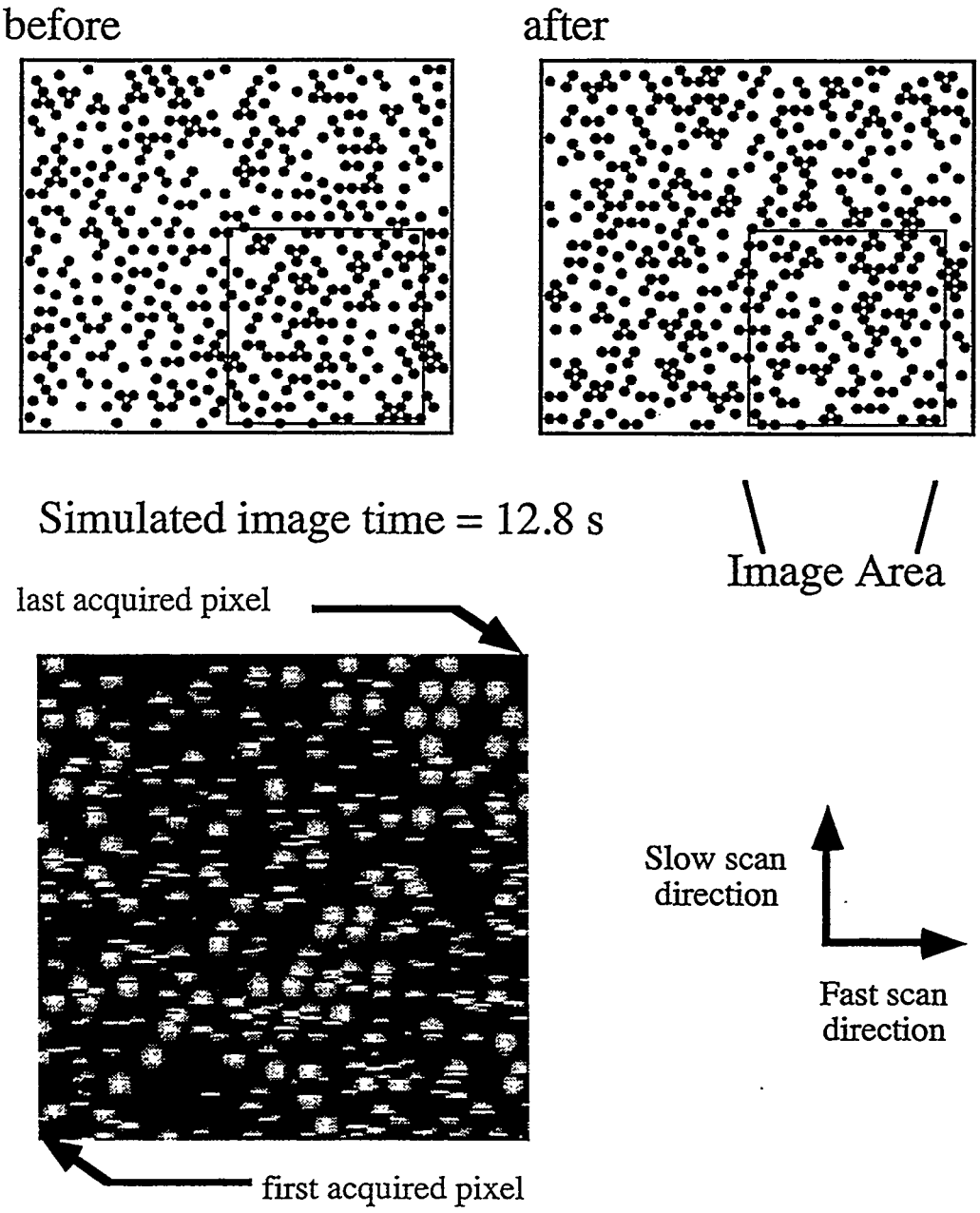

Figure 9.10 A Monte Carlo Simulation of an STM Image

At the top are instantaneous images of the entire surface at the beginning and end of the simulated image acquisition. The value of each pixel in the simulated image is determined at a different time, corresponding to the finite time acquisition of experimental images. The resulting image is similar to the experimental ones, exhibiting horizontal "dashes" due to diffusing atoms.

9.6.4 Simulated STM Images

Besides determining the static equilibrium state of the surface, the Monte Carlo technique was used to simulate STM images acquired over a finite time. In these simulations, the value of each pixel of the STM image is determined one or more simulation time-steps after the previous pixel. The time scale of the image acquisition relative to the diffusion rate in the simulation is set to the experimental value. Figure 9.10 shows the simulation results. On the top of the figure are instantaneous images of the state of the surface at the beginning and end of the acquisition of the simulated STM image. Many atoms have moved to new locations during the STM image acquisition. The simulated STM image shows the same features indicative of diffusing atoms as the experimental ones. While complete atoms are visible in some portions of the image, much of the area is covered with the "dashes" produced by atoms which diffuse to a new location in between scan lines.

Simulated images can be produced for different sulfur coverage values, interaction energies, and STM scan rates. Correlation images can be calculated from the simulations in the same manner as for the experimental images. In figure 9.11 the resulting correlation images are shown for a wide range of scan speeds. At high scan speeds the correlation image is nearly isotropic, consistent with the experimental images acquired at those rates. At lower scan speeds, the order in the y direction is lost, resulting in a decay of the correlation spots in this direction. Unlike the experimental images, the correlation maxima decay over four to six lattice spacing distances. This indicates that some additional mechanism is promoting long range order of the sulfur in the experiment which is not accounted for in the pairwise interaction model. This mechanism could be longer range interactions, such as attractive interactions at $4a$ or repulsive interactions at $3a$. It could also be that a defect on the surface establishes a reference point, promoting ordering of the sulfur around it.

9.7 Conclusions

These results have demonstrated the application of STM to study diffusion of individual adatoms on a surface, even when the diffusion time is small compared to the imaging time. The usefulness of a spatial correlation function to extract quantitative information from the images was demonstrated. By applying this technique quantitative measurements of the interactions between the diffusing atoms and of the diffusion energy barrier could be made. The Monte Carlo simulations confirmed the interpretation of the results, but indicated that more complex than pairwise interactions are present between the adsorbate atoms. STM studies of diffusion would be even more informative if the temperature of the system could be varied. This was not possible in this experiment, but an instrument which allows imaging at variable temperatures is discussed in a chapter 13. Application of the analysis methods used here to other adsorbate systems will allow phenomena such as surface diffusion and phase transformations to be studied in great detail.

Figure 9.11 (NEXT PAGE)

Correlation images may be calculated from simulated STM images. The shape of the correlation image changes as a function of scan speed. At high scan speeds, the image shows $p(2x2)$ order and is isotropic in x and y. At lower scan speeds, order is lost in the y direction.

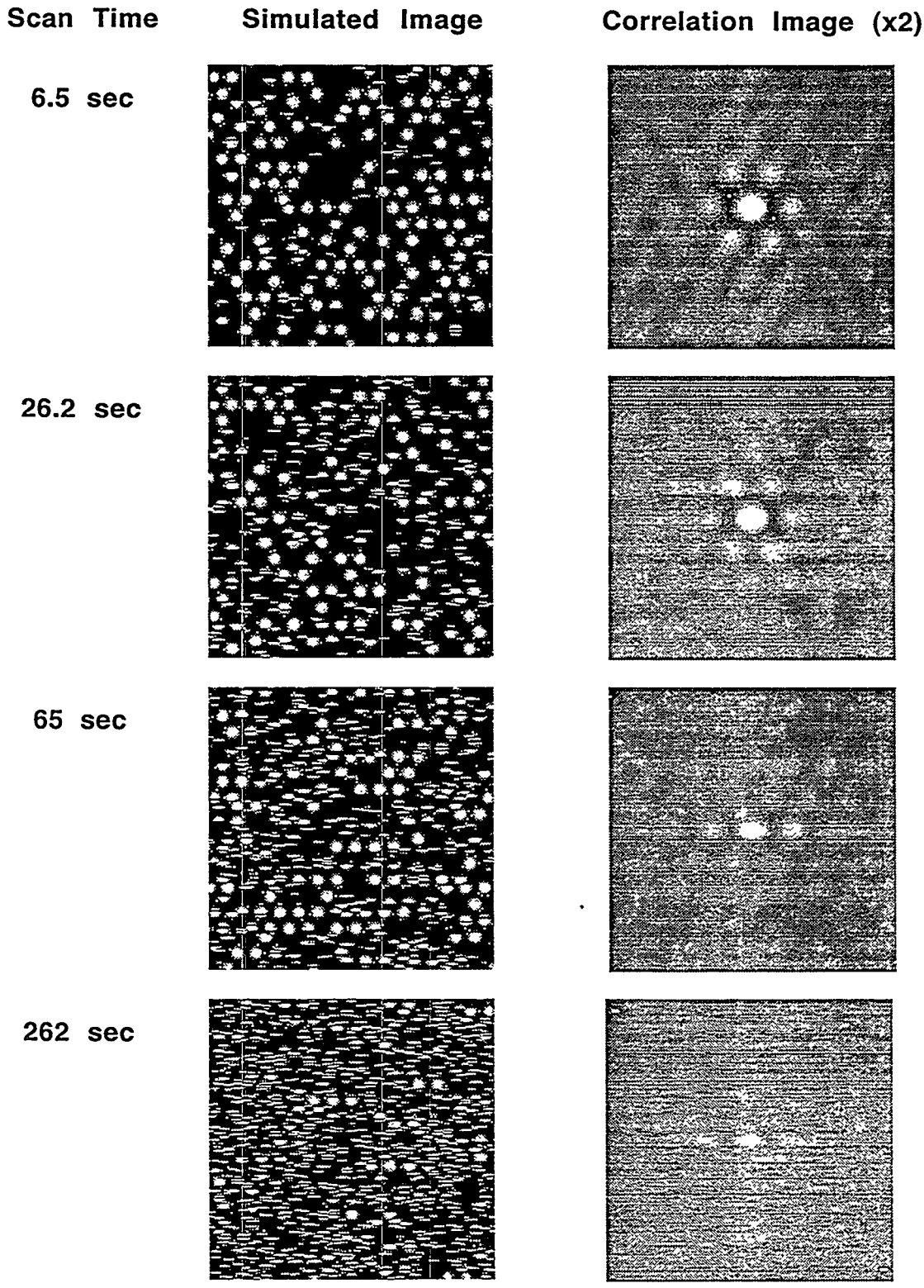

Figure 9.11 Simulated Correlation Images vs. Scan Rate

Chapter 9 References

[1] V.M. Hallmark, S. Chiang, J.K. Brown and C. Wöll, Phys. Rev. Lett. **66** (1991) 48.

[2] C. Günther and R.J. Behm, to be submitted to Surface Science

[3] E. Ganz, S.K. Theiss, I.S. Hwang and J. Golovchenko, Phys. Rev. Lett. **68** (1992) 1567.

[4] R.M. Feenstra, A.J. Slavin, G.A. Held and M.A. Lutz, Phys. Rev. Lett. **66** (1991) 3257.

[5] M. Poensgen, J.F. Wolf, J. Frohn, M. Giesen and H. Ibach, Surf. Sci. **274** (1992) 430.

[6] R. Gomer, Rep. Prog. Phys. **53** (1990) 917.

[7] D.A. Sommerfeld, R.T. Cambron and T.P.B. Jr., J. Phys. Chem. **94** (1990) 8926.

[8] D.J. Trevor and C.E.D. Chidsey, J. Vac. Sci. Technol. B **9** (1991) 964.

[9] J.H. Neave, B.A. Joyce, P.J. Dobson and N. Norton, Appl. Phys. A (1983) 1.

[10] B.J. Hinch, J.W.M. Frenken, G. Zhang and J.P. Toennies, Surf. Sci. **259** (1991) 288.

[11] S.M. George, A.M. DeSantolo and R.B. Hall, Surf. Sci. Lett. **159** (1985) L425.

[12] R. Gomer. *Field Emission and Field Ionization*. (Harvard University Press, Cambridge, MA, 1961).

[13] R. Gomer, Surf. Sci. **38** (1973) 373.

[14] G. Ehrlich and K. Stolt, An. Rev. Phys. Chem. **31** (1980) 603.

[15] T. Tsong, Rep. Prog. Phys. **51** (1988) 759.

[16] H.B. Elswijk, A.J. Hoeven, E.J.v. Loenen and D. Dijkkamp, J. Vac. Sci. Technol. B **9** (1991) 451.

[17] Y.-M. Mo, R. Kariotis, B.S. Swatrzentruber, M.B. Webb and M.G. Lagally, J. Vac. Sci. Technol. A **8** (1990) 201.

[18] Y.-W. Mo, J. Kleiner, M.B. Webb and M.G. Lagally, Phys. Rev. Lett. **66** (1991) 1998.

[19] G. Binnig, H. Fuchs and E. Stoll, Surf. Sci. Lett. **169** (1986) L295.

[20] A. Zangwill. in *Physics at Surfaces* p. 260 (Cambridge University Press, New York, 1988).

[21] J.A. Stroscio and D.M. Eigler, Science **254** (1991) 1319.

[22] F. Reif. *Fundamentals of Statistical and Thermal Physics*. (McGraw-Hill, San Fransisco, 1965).

[23] R.Q. Hwang, D.M. Zeglinski, D.F. Ogletree, A.L. Vazquez-de-Parga, G.A. Somorjai and M. Salmeron, Phys. Rev. B **44** (1991) 1914.

[24] T.L. Einstein, Langmuir **7** (1991) 2520.

[25] A. Zangwill. in *Physics at Surfaces* p. 362 (Cambridge University Press, New York, 1988).

[26] P. Sautet and J.-F. Paul, Cat. Lett. **9** (1991) 245.

[27] G.L. Kellogg, J. Chem. Phys. **72** (1985) 6332.

[28] D.G. Kelly, A.J. Gellman, M. Salmeron, G.A. Somorjai, V. Maurice, M. Huber and J. Oudar, Surf. Sci. **204** (1988) 1.

[29] J.G. McCarty and H. Wise, J. Chem. Phys. **72** (1980) 6332.

Chapter 10. COADSORPTION INDUCED COMPRESSION

10.1 Introduction

The last chapter described the dynamics and lateral interactions of sulfur atoms adsorbed on Re(0001). Lateral interactions were found to exist between sulfur atoms on the surface, and the magnitude of these interactions was determined by a special image analysis technique. In addition to lateral interactions between similar atoms or molecules, there are interactions between different species adsorbed on a surface. Studying these interactions is important for understanding surface chemical reactions, catalysis[1], and surfactant mediated epitaxial growth.[2] In these processes, more than one adsorbate is present on the surface, and the kinetics which govern the process depend strongly on how these adsorbates interact.

10.2 Coadsorption of CO and S

During the investigation of sulfur diffusion at low coverage it was found that the $p(2x2)$ ordering of the sulfur covered surface at low coverage was unstable when it was exposed to CO. In UHV the $p(2x2)$ LEED pattern was found to degrade over a period of hours to days. The spots of the LEED pattern became less sharp, and eventually the pattern disappeared completely, indicating that the sulfur on the surface was disordered. The rate of this disordering was dependent on the background pressure in the UHV chamber. As the major component of the residual gas in the chamber was CO, adsorption of this gas was a plausible cause of the disarrangement of the sulfur. This speculation was verified by leaking in CO through a variable leak valve. The disordering rate was found to be closely related to the CO pressure.

Sulfur is known to block the adsorption of CO on Re(0001) at a coverage above one quarter monolayers.[3] The disordering rate was found to increase as the sulfur coverage was decreased below one quarter monolayer. Therefore, it appears that CO

adsorbs onto clean areas of the surface, but that continued adsorption affects nearby sulfur covered regions. This process was studied further by STM and LEED.

10.3 Experiment

The $p(2x2)$ S overlayer was prepared as described in chapter 5. The crystal was then cooled to room temperature. The large scale ordering of the sulfur overlayer was determined with LEED, and the sulfur coverage checked by AES. As expected the LEED pattern had the highest contrast at a coverage near one quarter monolayer. STM images of the surface showed the $p(2x2)$ overlayer. The LEED pattern was shown to be stable for several hours in the residual gas in the UHV chamber.

A background pressure of CO from 1 x 10^{-9} to 1 x 10^{-8} Torr was produced in the chamber by introducing CO through a leak valve. The LEED pattern of the surface was observed and STM images obtained in this background pressure.

10.4 LEED Results

Figure 10.1 shows the LEED pattern transition which occurs when the $p(2x2)$ sulfur overlayer is exposed to CO. First the surface was shown to be stable for several hours in the absence of CO. No significant change in the LEED pattern occurred during this time. CO at a pressure of 5 X 10^{-9} Torr was then introduced into the chamber. Over five minutes the fractional order spots of the $p(2x2)$ LEED pattern faded and lines connecting the spots formed in a six pointed star pattern (figure 10.1B). This pattern also faded with time, leaving the rhenium $(1x1)$ spots and a diffuse background. After fifteen minutes exposure to CO a diffuse $\left(3\sqrt{3}x3\sqrt{3}\right)R30°$ pattern appeared (figure 10.1C and 10.1D). This LEED pattern corresponds to a more densely packed layer of sulfur in trimers described in chapter 5. No further changes in the LEED pattern occurred (figure 10.1E) despite continued exposure to CO. Heating the surface to 600°C for several seconds reversed the transition back to a $p(2x2)$ pattern as shown in figure 10.1F. The sulfur coverage on the surface, as measured by AES, was unchanged during the transition.

The time required for the transition depended on the sulfur coverage and CO pressure, with the longest times corresponding to coverage values closest to a full quarter monolayer and lowest CO pressures.

10.5 STM Results

The reordering of the sulfur due to CO adsorption was also studied by STM. After atomic resolution was attained on a $p(2x2)$ ordered surface, CO was leaked into the chamber at a pressure of 1 x 10^{-8} Torr and the surface imaged while exposed to CO. As has been reported by others, CO molecules were not resolved by the STM under these pressure and temperature conditions[4], presumably because they are highly mobile on the surface. However, as time progressed an increasing number of defects in the sulfur overlayer were observed. These defect regions consisted of a mixture of the sulfur trimers which, when ordered, make up the $\left(3\sqrt{3}x3\sqrt{3}\right)R30°$ overlayer and apparently "clean" areas of the surface. An example of such a defect is shown in figure 10.2B. By counting atoms and trimers of atoms the average coverage of the sulfur on the surface surrounding these defects was found to be within 10% of the original quarter monolayer. Only the ordering of the sulfur has changed and not the average coverage. The dark areas of the surface correspond to patches that are probably covered by CO.

As was shown in the LEED experiments, the $p(2x2)$ S ordering could be restored by annealing the sample to 600°C for several seconds. During the heating the sample had to be removed from the microscope, but when it was returned $p(2x2)$ ordered sulfur was again imaged.

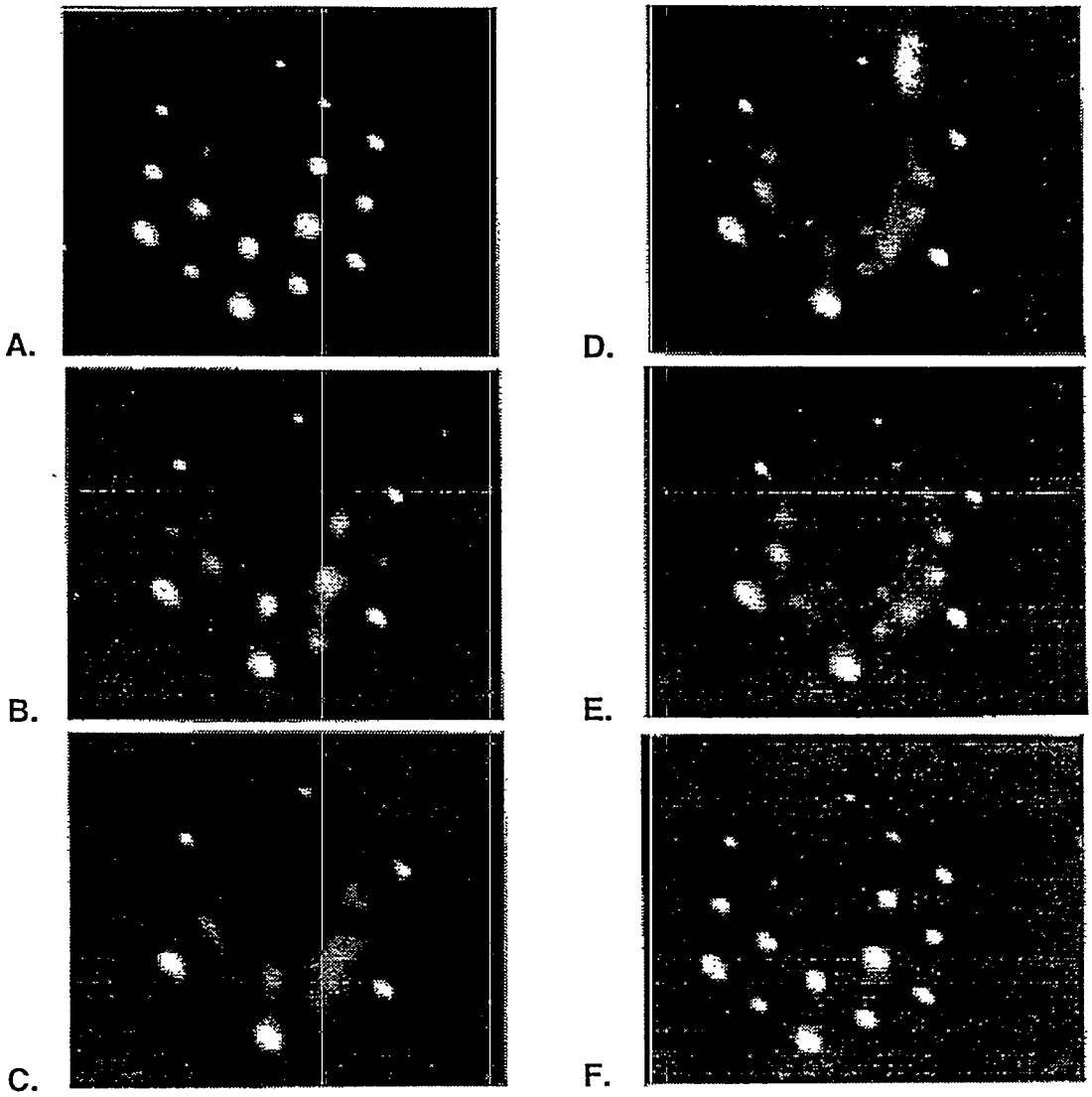

Figure 10.1 LEED Pattern Evolution of a S Layer Exposed to CO

The S covered Re surface exposed to 5 x 10^{-9} Torr of CO. A) Initial $p(2x2)$ LEED pattern. B) After 5 minutes of CO exposure. C) After 10 minutes. D) after 15 minutes the LEED pattern is diffuse with $\left(3\sqrt{3}x3\sqrt{3}\right)R30°$ spots. E) The LEED pattern after 35 minutes. F) After annealing for several seconds at 600°C to desorb the CO the LEED pattern returns to $p(2x2)$.

A.

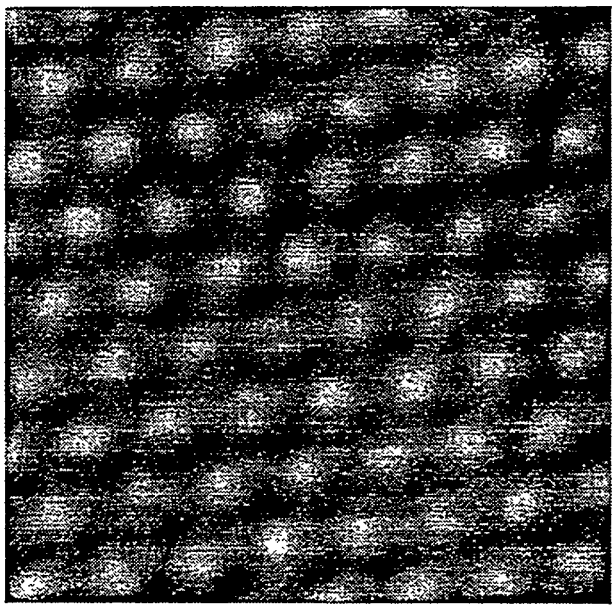

B.

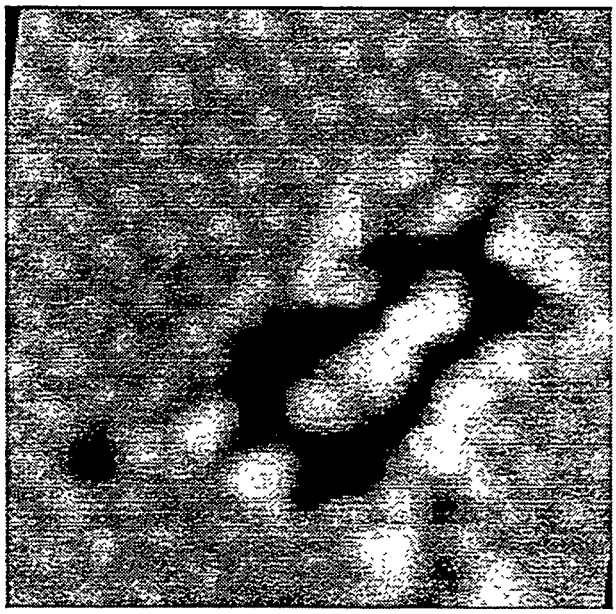

Figure 10.2 STM Images of the CO Induced Reordering of Sulfur

A) The round maxima are due to individual $p(2x2)$ ordered sulfur atoms adsorbed at the hcp three-fold hollow site on the surface. B) A hole has formed in the $p(2x2)$ layer where CO has adsorbed (CO molecules are not visible in the STM image). The sulfur atoms which had previously been in the hole have been compressed.

10.6 Discussion

10.6.1 Energy Balance

The adsorption of CO in the holes on the Re(0001) surface created by the compression of the ordered sulfur overlayer was observed. Because one of the two coadsorbed species (sulfur) forms ordered arrays, it was possible to monitor this process by STM and by LEED. The reverse process, the healing of the original overlayer of sulfur by back-diffusion upon CO desorption, was also observed by LEED.

The compression of the sulfur overlayer by CO is surprising as the correlation function results of the previous chapter showed that the interactions between the sulfur atoms at a distance less than twice the Re surface lattice spacing is repulsive. The correlation function of the diffusing sulfur had a deep minima surrounding the central peak indicating that sulfur atoms were rarely separated by these distances as they diffused over the surface. At higher coverage, however, the sulfur does form trimers. Clearly the energy to overcome the sulfur-sulfur repulsion is provided by the sulfur adsorption energy although the mechanism is not yet understood. A similar mechanism must occur when CO is adsorbed on the surface. The adsorption energy of CO must be high enough to provide the energy to overcome sulfur repulsion allowing them to form trimers. As the adsorption energy of CO is much less than that of sulfur, it is surprising that relatively weakly bound CO is able to displace much more strongly bound sulfur. We can analyze the energy balance of the reordering induced by CO based on known energies.

The adsorption energy of CO on the Re surface has been measured to be 1.0 eV per molecule.[5] The maximum saturation coverage of CO at low pressures is 0.49 monolayers[6], or approximately one CO molecule per two Re surface layer atoms. Therefore, the energy gained by freeing a Re surface atom of sulfur so that it can adsorb CO is 0.5 eV. In the $p(2x2)$ structure there are 4 surface Re atoms per sulfur while in the $\left(3\sqrt{3}x3\sqrt{3}\right)R30°$ structure there are only 2.25 surface Re atoms. Therefore each sulfur

atom moved to the more compact structure frees 1.75 Re surface atoms releasing 0.87 eV of energy when CO adsorbs on this area. If the energy per sulfur atom required to form a trimer is less than this value, the process will be energetically favorable. Based on this model, we can give a maximum energy per sulfur atom of trimer formation of 0.87 eV. This is larger than the energy derived from the sulfur Thermal Programmed Desorption (TPD) data of Kelly et al.[7] They find a desorption peak which appears at coverage above one quarter monolayer and has an adsorption energy 0.56 eV less than the sulfur desorption peak from the $p(2x2)$ structure.

An Extended Hückel calculation, similar to the one described in the last chapter, was used to determine the energy of formation of trimers on the surface. The difference in energy between sulfur atoms adsorbed separately and in a trimer was calculated. It was found to be 1.0 eV. This is slightly higher than the maximum value found in our experiments of 0.87 eV. The higher value may be explained by the neglect of Re restructuring in our calculation. Relaxation of the real surface would be expected to lower the energy.

10.6.2 Implications for Catalysis

Similar effects of the interaction between adsorbates and coadsorbed CO have been observed in the case of $p(2x2)$ sulfur[8]and $p(2x2)$ Se on Pt(111).[9] In both these systems CO adsorption compressed the other adsorbate into a higher coverage structure.

If this phenomenon of adsorption of molecules by compression of adsorbates that are already present and perhaps chemically inert during surface reaction is generally valid, it could provide the mechanism by which molecules adsorb and react on transition metal surfaces that are crowded with inert adsorbates while they are subjected to the usual conditions used in metal catalysis.

One of the puzzles of heterogeneous catalysis carried out on transition metal surfaces is that the active metal is usually covered with a strongly chemisorbed overlayer that does not participate in the catalytic turnover. During ammonia synthesis ($N_2 + 3H_2 \Rightarrow$

$2NH_3$) iron catalyst surfaces are covered by a monolayer of chemisorbed nitrogen[10] . During hydrocarbon dehydrogenation reactions (for example, cyclohexane ⇒ benzene + 3 H_2) on platinum, the surface is covered by a carbonaceous deposit of CH or C_2H stoichiometry[11]. Also, during the hydrodesulfurization of thiophene (thiophene + $2H_2$ ⇒ butadiene + H_2S) the molybdenum or rhenium surfaces are covered by sulfur[12]. Isotope labeling studies of the atoms in the chemisorbed overlayer (^{14}C and ^{35}S) indicate that the molecules participating in the catalytic reaction turnover 10^4 - 10^6 times before the atoms in the topmost overlayer desorb.

Based on the S and CO coadsorption results, a mechanism which could explain this phenomenon can be postulated. The non-reactive adsorbate may be temporarily displaced locally on the surface in order to accommodate the adsorption of the reactants analogous to the displacement of the sulfur layer by CO. Once the catalytic reaction of these adsorbates is completed, the reaction products could desorb and allow the inert layer to re-expand, covering the surface.

If one of the coadsorbates has a low heat of adsorption, the thermodynamic driving force is absent, thus preventing hole creation in the adsorbed overlayer to produce adsorption sites. The adsorption energy of one adsorbate must be sufficient to overcome the self-repulsion of the other adsorbate in order for it to be compressed into a more compact layer. One also expects the interaction between the two coadsorbates to play a role in the coadsorbate-induced compression phenomenon.

Chapter 10 References

[1] G.A. Somorjai. *Chemistry in Two Dimensions: Surfaces*. (Cornell University Press, Ithaca, 1981).

[2] Z. Zhang and M.G. Lagally, Phys. Rev. Lett. **72** (1994) 693.

[3] D.G. Kelly, A.J. Gellman, M. Salmeron, G.A. Somorjai, V. Maurice, M. Huber and J. Oudar, Surf. Sci. **204** (1988) 1.

[4] T. Gritsch, D. Coulman, R.J. Behm and G. Ertl, Phys. Rev. Lett. **63** (1989) 1086.

[5] J.-W. He and D.W. Goodman, J. Phys. Chem. **94** (1990) 1502.

[6] R. Ducros, J. Fusy, J. Jupille, P. Pareja and S. Tatarenko, Appl. Surf. Sci. **29** (1987) 179.

[7] D.G. Kelley, R.F. Lin, M.A.V. Hove and G.A. Somorjai, Surf. Sci. **224** (1989) 97.

[8] J.C. Dunphy, B.J. McIntyre, J. Gomez, D.F. Ogletree, G.A. Somorjai and M.B. Salmeron, J. Chem. Phys. **100** (1994) 6092.

[9] M. Kiskinova, A. Szabo and J.T. Yates, Vacuum **41** (1990) 82.

[10] D.R. Strongin and G.A. Somorjai, J. Cat. **118** (1989) 99.

[11] S.M. Davis, F. Zaera and G.A. Somorjai, J. Cat. **77** (1982) 439.

[12] M.E. Bussell, A.J. Gellman and G.A. Somorjai, Cat. Lett. **1** (1988) 195.

Chapter 11. DEPOSITION OF Au ON SULFIDED Mo(100)

11.1 Introduction

Chemisorbed layers on surfaces influence every aspect of their behavior. They determine their chemical reactivity, the growth of thin metal films, and the adhesion between solids. Adhesion involves the formation and rupture of bonds across interfaces. This process may be modeled by studying the growth of one metal onto another that is covered by a monolayer of a different species. In this manner, the influence of adsorbates on adhesion can be investigated. Since only a few layers of the surface are involved in the model, it can be investigated by surface science techniques, including Low Energy Electron Diffraction (LEED), Auger Electron Spectroscopy (AES), and STM.

Some of the issues addressed in this study include the wetting of the metal deposited, its interaction with the chemisorbed layer, the formation of coadsorbed structures, and the possible formation of sandwich structures (metal/adsorbate/metal). The Au/S/Mo(100) system was chosen because the previous work on the sulfur overlayers on molybdenum described in chapter 7 provides background knowledge. Gold deposited on other chemisorption systems has been shown to have interesting behavior.[1, 2]

Deposited gold could interact with the sulfur overlayers in a number of ways. It could form a layer on top of the sulfur producing a "sandwich" structure similar to that proposed for Cu/O/W(110) and Cu/CO/W(110).[3, 4] Gold could also migrate under the sulfur and the sulfur over the gold. This "floating" of chemisorbed species has been observed in a number of systems.[5] Gold could also adsorb onto the surface displacing the sulfur laterally as was observed in the Au/O/Ru(0001) system.[1, 2] In this system the displaced O ordered in a 0.75 monolayer coverage $(2x2)$ structure which could not be produced by chemisorption of oxygen at low pressures.

11.2 Experiment

Clean and sulfided Mo(100) surfaces were produced as described in chapter 7. Gold was evaporated onto the clean or sulfided surface by heating gold wire with a tungsten wire resistive heater. Except as noted the sample was kept at room temperature during gold deposition. AES was used to determine sulfur and gold coverage on the surface by measurement of spectral peak ratios.

Compared to the surfaces without gold, STM tip stability was often a problem on the surfaces with a higher gold coverage at higher scan rates. Apparently, on the rougher gold covered surfaces gold was easily transferred between the tip and surface during imaging. The STM images were corrected for distortions using the second order fit procedure described in chapter 7.

11.3 Results

11.3.1 Gold on the clean Mo surface

Experiments on the structure of gold overlayers on the clean Mo(100) surface were complicated by the difficulty in keeping the Mo(100) surface free of contamination in the residual vacuum of 3×10^{-10} Torr. With a low gold coverage (< 1 monolayer), AES showed that the surface often became contaminated by carbon and oxygen (but not sulfur) during the gold deposition. The source of this contamination was primarily CO in the residual vacuum which is known to partially dissociate upon adsorption on the surface at room temperature.[6] Deposition of multilayers of gold onto the surface was found to inhibit the contamination, perhaps by blocking Mo sites required for the dissociation of CO. However, at a low coverage of gold contamination could not be prevented.

Deposition of gold on the surface with no annealing produced a very rough surface, characterized by the presence of clusters with a corrugation of approximately 2 to 4 Å and size of 10 to 20 Å. Annealing the gold covered surface after or during gold deposition to approximately 800 K produced a surface with one of a number of LEED patterns

depending on the gold coverage, notably a $c(2x2)$ and a $c(4x2)$ pattern. At a coverage of 0.5 monolayers or less the LEED pattern of the gold covered surface was $c(2x2)$. Figure 11.1 shows an STM image of this surface. The corrugation of the maxima in STM images of the overlayer was not constant; some of the maxima were significantly smaller than the majority. We attribute the largest and most frequent maxima (approximately 0.8 Å) in the $c(2x2)$ lattice to gold atoms and the lesser maxima to contaminant atoms, most likely carbon or oxygen. These elements also form layers with $c(2x2)$ periodicity on Mo(100). Interestingly, the gold and contamination atoms produce a mixed overlayer with $c(2x2)$ ordering. When the gold $c(2x2)$ structure is complete, the ratio of the Au_{69} and Mo_{186} peaks in the Auger spectrum was 0.91.

After several monolayers of gold were deposited and the surface annealed to 800 K for 20 seconds the STM images show a smooth surface with steps due to the underlying Mo substrate. AES showed no contamination of this surface above the noise level (approximately 1% of a monolayer). No atomic resolution was achieved on these surfaces in spite of the observation of LEED patterns with $c(4x2)$ symmetry.

11.3.2 Gold on the partially sulfided surface

STM images, such as those show in chapter 7, of the $c(2x2)$ sulfur overlayer prepared by exposure of the surface to H_2S gas show a nearly perfect lattice over most of the surface. A few defects near the terrace edges, and an occasional small hole in the overlayer can be seen in the image. In contrast to the clean Mo surface, AES showed that this surface did not become contaminated by CO dissociation when the sulfur coverage was half of a monolayer or greater. As long as sulfur was deposited on the surface immediately after cleaning the sample, the contamination level was kept below the AES detection limit before and after gold deposition.

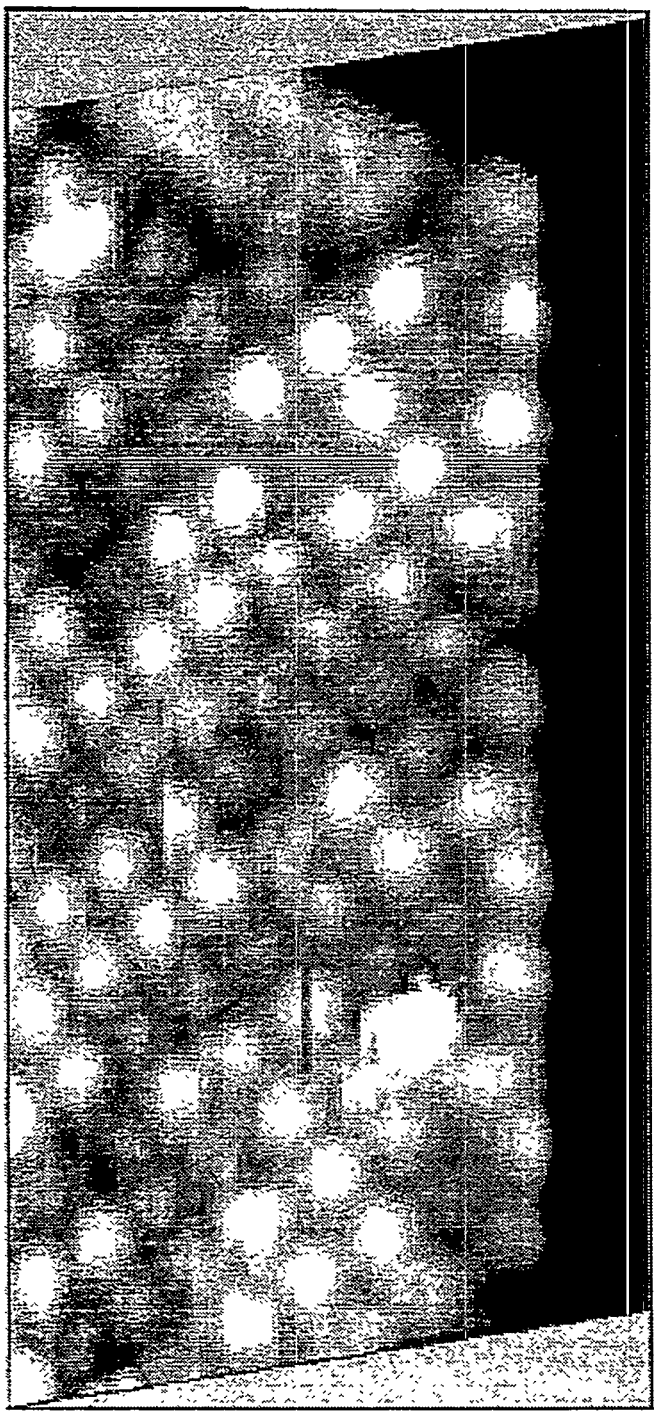

A mixed $c(2x2)$ overlayer of gold (bright maxima) and contamination (O and C) atoms (weaker maxima) on Mo(100). The corrugation of the gold atoms was approximately 0.8 Å, while it was significantly less (~0.3 Å) for the contamination atoms.

Figure 11.1 STM Images Of Gold On The Mo(100) Surface

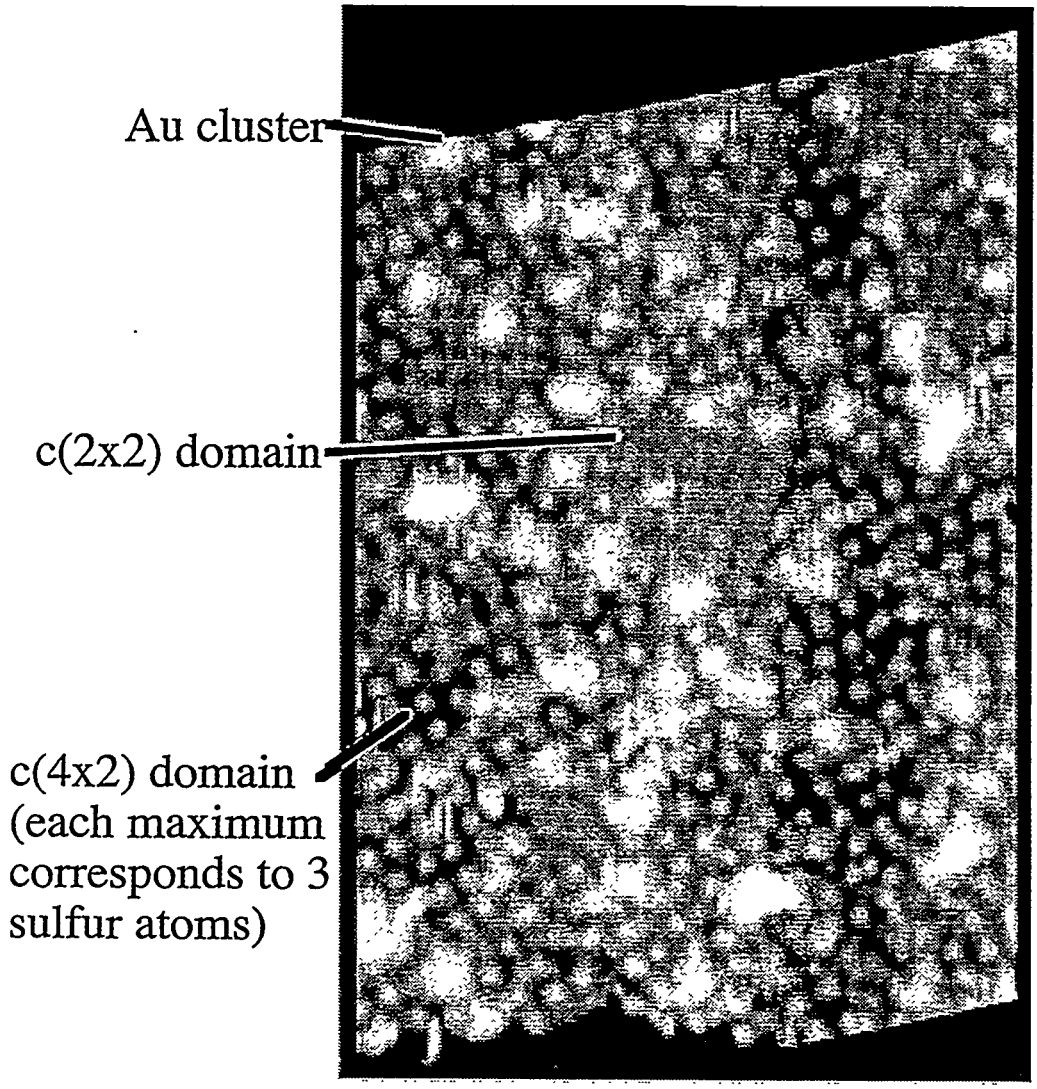

Figure 11.2 Gold Deposition on the Mo(100) $c(2x2)$ S surface

A topographic image of the surface showing both gold clusters and ordered sulfur regions between them. The sulfur overlayer has reordered into structures consistent with a higher local coverage. The square lattice in the center and top right edge of the image is $c(2x2)$ ordered sulfur. Along one edge of this region is a single row of the $\begin{bmatrix} 2 & \bar{1} \\ 1 & 1 \end{bmatrix}$ structure. The large bright spots are gold atoms and clusters. The lesser round spots in the dark background are associated with a single unit cell of the $c(4x2)$ structure which contains 3 atoms.

After deposition of a tenth of a monolayer of gold on this surface the appearance of the surface changed in STM images. The surface was covered with small clusters approximately 2 Å high (one atomic layer) and 5 to 20 Å across, interspersed with ordered regions of S which appear as bright spots in figure 11.2. Some small islands of the $c(2x2)$ S structure remain on the surface and appear as a square lattice, but much of the sulfur on the surface has reordered into the $\begin{bmatrix} 2 & \bar{1} \\ 1 & 1 \end{bmatrix}$ structure or the $c(4x2)$ structure. These structures in the images are identified by comparison to the images of complete overlayers shown in chapter 7. A single double row of sulfur atoms which makes up the $\begin{bmatrix} 2 & \bar{1} \\ 1 & 1 \end{bmatrix}$ overlayer is visible at the edge of the $c(2x2)$ ordered region. The $c(4x2)$ regions appear as isolated spots in the dark background. Each of these spots corresponds to a single $c(4x2)$ unit cell which contains three sulfur atoms located at four-fold hollow sites. As discussed in chapter 7, the sulfur atoms in this structure are too close together on the surface to be individually resolved, but the periodicity of the maxima in these regions is $c(4x2)$. These regions have a 50% higher sulfur coverage than the $c(2x2)$ regions although they have a lower density of maxima in the STM image. The domains of the $c(4x2)$ structure are very small, often consisting of less than five unit cells.

It is clear from the STM images that gold adsorbs and bonds to Mo displacing the sulfur atoms in the $c(2x2)$ regions laterally to form denser structures. This reordering is accomplished at room temperature and many defects are left in the reordered areas.

The close proximity of the various sulfur structures in these images allowed the relative registry of the maxima in the images to be easily determined. The maxima of all the structures fit onto a $(1x1)$ Mo lattice. In all cases the results are consistent with those described in chapter 7.

11.3.3 Gold on the sulfur saturated surface

While gold was able to laterally compress the $c(2x2)$ S overlayer it is not clear if compression is possible on a fully sulfur saturated surface. With the sulfur overlayer already compressed to its saturation structure, the gold might have to form a layer on top of the sulfur. A $c(4x2)$ overlayer of sulfur was prepared. The S_{150} to Mo_{186} AES peak ratio for this structure was found to be 2.58. Approximately half monolayer of Au was deposited on the surface at room temperature. AES showed that the surface remained completely uncontaminated by O and C during the deposition. The LEED pattern did not change significantly with the deposition of gold, although the background intensity increased, indicating some disorder on the surface. The AES S_{150}/Mo_{186} ratio increased to 2.65 while the Au_{69}/Mo_{186} ratio increased from 0 to 0.39. Approximately one quarter of the increase in S_{150}/Mo_{186} ratio can be explained by a small gold AES peak at the same energy (150 eV) as the sulfur peak. STM images such as figure 11.3 show that this surface is covered with round clusters of gold approximately 10 to 30 Å in diameter and 5 to 10 Å high corresponding to a height of 2 to 5 monolayers. In between these clusters the surface appeared flat. Atomic resolution of the sulfur layer between the gold clusters was obtained in single line scans and found to be unchanged from its initial $c(4x2)$ structure. As the total gold coverage on the surface found by relating the height of the clusters to the AES peak ratios was only enough for the islands to cover approximately one tenth of the surface, we believe that the diameter of the clusters in the image is a result of the convolution with a finite tip.

11.4 Discussion

When deposited onto clean Mo(100) and annealed to 800 K, gold forms epitaxial monolayers with $c(2x2)$ and $c(4x2)$ symmetries as revealed by LEED. The Au $c(2x2)$ structure contained numerous defects, which appeared as dimmer spots in the STM images that are presumably due to residual carbon and oxygen impurities as these were the only impurities present in the AES spectrum. Even if each of these adsorbates would form by

itself a $c(2x2)$ structure, it is not obvious that a mixed Au-C or Au-O adlayer could form with the same symmetry. The existence of these structures indicates that the short range interactions between adsorbates might be mediated by similar substrate or electronic distortions around each adatom. More detailed studies of mixed layers could be helpful in determining the nature of the interactions.

In our study, only the $c(2x2)$ structure of gold could be resolved by STM. This might be due to the termination of the imaging tip with Pt or Au atoms. As shown in chapter 6, large atoms (as determined by the spatial extent of the outermost orbitals, 6s in Pt or Au) at the tip apex tend to produce lower corrugations in the image. This effect is more important the closer the atoms to be imaged. Therefore the $c(4x2)$ with a denser packing of large Au atoms is less resolved than the more open $c(2x2)$. It might be possible then to resolve the $c(4x2)$ with a tip terminated in a small atom such as C, O, or S.

One of the important findings of out study is the competition for high energy bonding sites between gold and sulfur. While the sulfur can be compressed into a denser structure at a moderate cost in energy $\left(E^{S}_{c(2x2)} - E^{S}_{c(4x2)} << E_{Au-Mo}\right)$ gold will not grow "on top" of the S. This is fully supported by the present observations. It is less obvious what will happen when the surface is initially saturated by sulfur. Various possibilities exist: (a) A new structure that is denser than the $c(4x2)$ $(\theta = 0.75)$ might form that is not stable in the absence of gold, like a $(1x1)$ with $\theta = 1$. (b) Au grows on top of S and a "sandwiched" S interface is created. (c) Sulfur diffuses on top of gold and the result is a

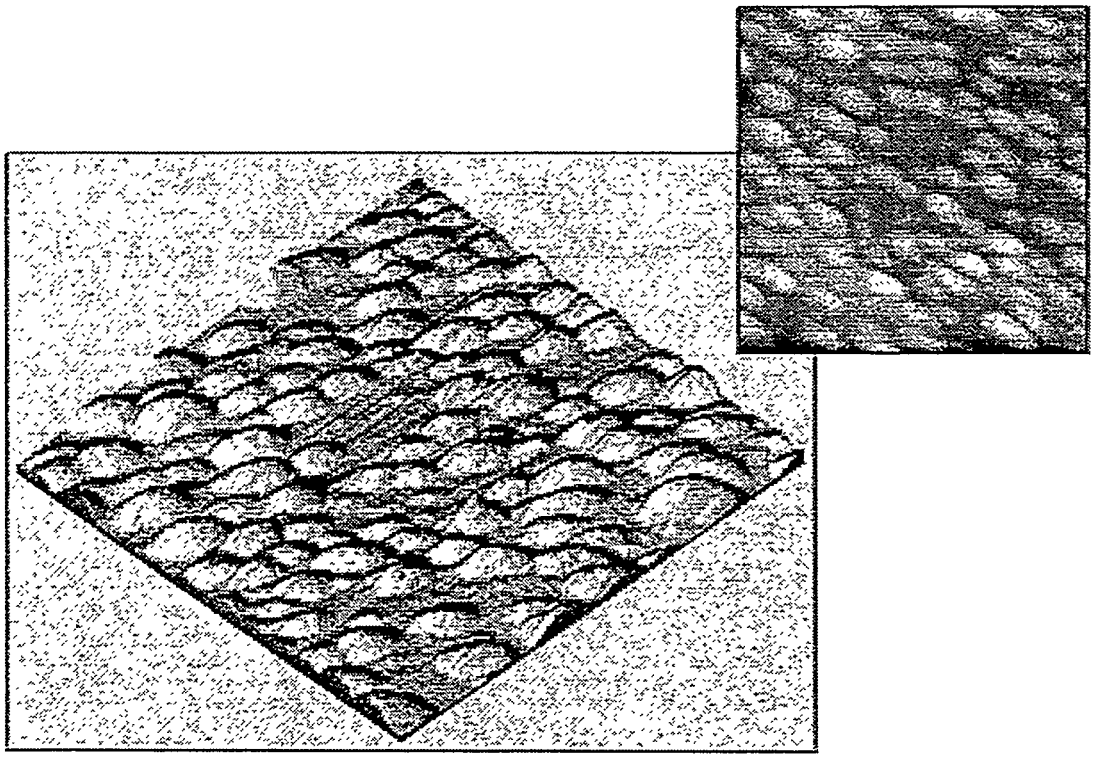

Figure 11.3 Gold Clusters on the $c(4x2)$ S Covered Mo(100)

A 300 Å square topographic STM image of the gold clusters which form when gold is deposited on the $c(4x2)$ S covered Mo(100) surface. The clusters are approximately 5 to 10 Å high and appear 10 to 30 Å in diameter although the apparent lateral size may be due to the finite radius of the STM tip termination. The flat areas between the clusters are still covered by $c(4x2)$ ordered sulfur.

"sandwiched" Au interface. It is apparent from the lack of change in the LEED pattern that (a) can be excluded. This indicates that the $E^{S}_{c(2x2)} - E^{S}_{c(4x2)}$ is too large and cannot be provided by E_{Au-Mo}. It is difficult to distinguish cases (b) and (c) by STM imaging. However, the increase in the sulfur to Mo ratio in the AES after deposition of gold indicates that the gold layer shields the Mo on the surface more than it does the sulfur. This indicates that some of the sulfur on the surface is floating to the top of the gold islands.

11.5 Conclusions

The competition for binding sites with the Mo substrate atoms leads to repulsive interactions between coadsorbed sulfur and gold atoms. As a result segregated structures form whereby preadsorbed sulfur is forced into denser arrangements whenever possible. Thus the $c(2x2)$ is compressed into the $\begin{bmatrix} 2 & \bar{1} \\ 1 & 1 \end{bmatrix}$ and $c(4x2)$ structures. The previously proposed denser structure with one monolayer coverage and $p(2x1)$ symmetry could not be formed and therefore can be ruled out.

If the Mo surface is initially covered by the saturation sulfur structure, $c(4x2)$, gold grows in three dimensional clusters that are at least in part binding to the Mo substrate at their base. Sulfur is displaced and partially covers the gold clusters. This study indicates that strong adhesion between gold and sulfur covered Mo can occur in places where S can be displaced.

Chapter 11 References

[1] R.Q. Hwang, C. Günther, J. Schröder, S. Günther, E. Kopatski and R.J. Behm, J. Vac. Sci. Technol. A **10** (1992) 1970.

[2] J. Schröder, C. Günther, R.Q. Hwang and R.J. Behm, Ultramicroscopy **42-44** (1992) 475.

[3] J.E. Houston, D. G. O'Neill and R. Gomer, Surf. Sci. **244** (1991) 221.

[4] N. Shamir, J.C. Lin and R. Gomer, J. Chem. Phys. **90** (1989) 5135.

[5] J. W. F. Egelhoff and D.A. Steigerwald, J. Vac. Sci. Technol. A **7** (1989) 2167.

[6] E.I. Ko and R.J. Madix, Surf. Sci. Lett. **100** (1980) L505.

Chapter 12. EFFECT OF SULFUR ADSORPTION ON STEPS

12.1 Background

In the course of obtaining the STM images of sulfur overlayers on Mo(100), changes in the distribution and height of steps on the surface were noticed. Monatomic steps predominate on the clean surface. When sulfur was adsorbed on the surface, however, steps coalesced to form groups of steps, double atomic height steps, and multiple height steps, depending on the sulfur coverage and initial step density.

Adsorbates have been shown to affect the step structure of a number of metal surfaces by causing steps to coalesce or, conversely, causing an increase in the number of steps. Early work on the effect of adsorbates on surface structure by D. W. Blakely[1] et al. showed that adsorbates could cause the formation of multiple height steps and faceting on surfaces which were stable when clean. A.-M. Lanzillotto[2] et al. investigated the behavior of sulfur on a stepped Pt(111) surface. They found that sulfur orders in a $p(2x2)$ overlayer at the step edges at a coverage between 0.1 and 0.15 monolayers. These are coverage values lower than those necessary to form the $p(2x2)$ overlayer on the flat (111) surface. These authors have also shown that sulfur leads to a doubling of the step height on this vicinal surface. G. Comsa[3] et al. used He-scattering in conjunction with LEED to study the dynamics of step doubling that occurs when oxygen is adsorbed on the Pt (997) surface. E. Bauer et al.[4] and C. Zhang[5] et al. have shown that a high coverage of oxygen induce (110) faceting on W(100) and both (110) and (112) faceting on Mo(100), respectively. In contrast to these results, P. A. Dowben[6] et al. showed that adsorption of nitrogen on a stepped Fe(100) surface increases the single step density. This was also found for S adsorption on Pd(111) by A. J. Gellman[7] et al., and the increase in the number of steps was shown to be correlated with the chemical activity of the surface. Step doubling has been studied on vicinal sulfided Mo surfaces by LEED.[8] Reports of step modification and faceting have been compiled by G. A. Somorjai et al.[9]

12.2 Observations

On the clean Mo(100) surface STM images show that the steps on the surface are of single atomic height and relatively evenly spaced. Images of the clean surface, such as figure 12.1, appear noisy due to some carbon and oxygen contamination of the highly reactive surface even at background pressures in the 10^{-10} Torr range, but the steps in these images are clearly of monatomic height. Depositing a half a monolayer of $c(2x2)$ ordered sulfur and annealing the sample appeared not to change this. By adding more sulfur while annealing we obtained a mixture of the $c(2x2)$ and $\begin{bmatrix} 2 & \bar{1} \\ 1 & 1 \end{bmatrix}$ structures at an approximately coverage of 0.6 monolayers. At this sulfur coverage there was modification of the step structure. The steps formed pairs, triplets, and quadruplets of monatomic height steps separated by 30-50 Å terraces. These groups were separated by much larger terraces in between. An example of this step grouping is displayed in figure 12.2. The two

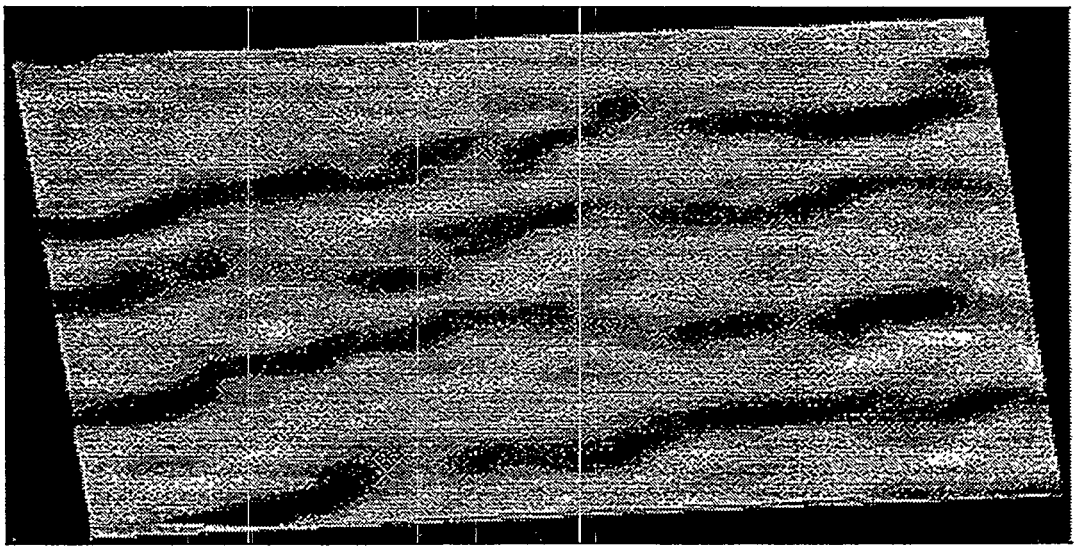

Figure 12.1 STM Image of Non-sulfided Mo(100)

STM image (200Å X 200Å) of Mo(100) surface without a sulfur overlayer. The steps are approximately equally spaced and monatomic. The noise in this image is due to contamination of the reactive surface by carbon and oxygen.

individual steps in a pair remained locked to each other over thousands of Angstroms along the step with only small variation in their separation. This indicates that the steps in the groups were spaced by an equilibrium distance and that the observed structure is not due to insufficient annealing preventing the steps from fully coalescing.

A further increase in the quantity of sulfur to approximately 0.8 monolayers on the surface causes the steps to coalesce into microfacets. The process appears to be limited by the time the sample is annealed. On samples which are only annealed for a short time, a combination of single, double and triple atomic height steps are found. On samples annealed for long periods of time (10 minutes at 800 K) with a background pressure of H_2S, the steps coalesce into multiple height steps or microfacets of up to twelve atomic layers. Most of these microfacets are two, four, and eight atomic layers high. Occasionally other sizes may be found as well. STM images of terraces separated by these microfacets are shown in figure 12.3.

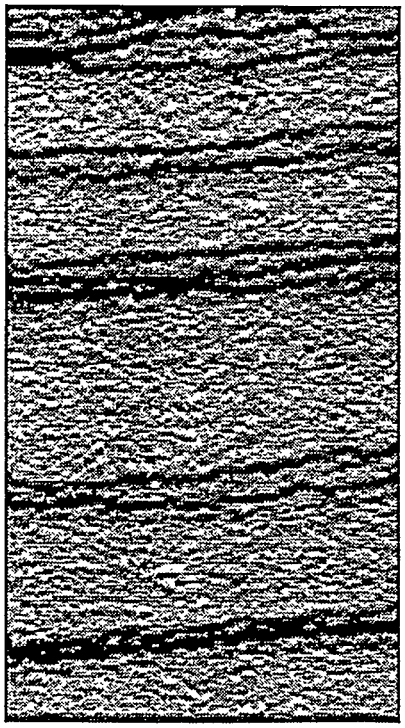

An STM image (1500Å X 400Å) of Mo(100) covered by 0.6 monolayers of sulfur. Steps on the surface form closely spaced groups, showing that there is a long range attractive interaction between steps. The steps in the groups are spaced by approximately 30-50 Å.

Figure 12.2 Mo(100) Covered With 0.6 Monolayers Sulfur

While microfacets smaller than four atomic layers in height follow random directions across the crystal surface and contain many kinks, large ones follow strictly the crystallographic directions. Steps of approximately twelve atomic layers or more in height are faceted in the (310) direction. Figure 12.3 shows an example of such a microfacet. The largest step in this image is 12 atomic layers high. Observation of the orientation of $c(4x2)$ overlayer relative to the step establishes that this step runs exactly along the [001] direction of the crystal. The slope of the cross section of the step is 1/3 within the error of

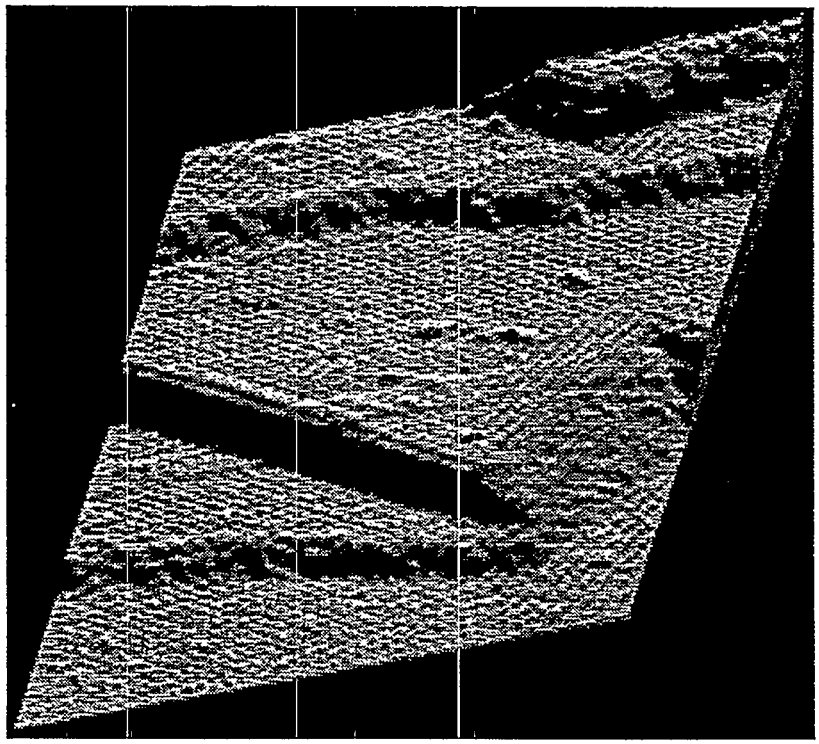

Figure 12.3 Mo(100) Covered With 0.8 Monolayers Sulfur

An STM image showing large steps and facets which form on the Mo surface with approximately 0.8 monolayers of sulfur after annealing. Steps of eight or more layers follow the crystallographic directions on the surface, while the smaller steps follow random directions and contain many kinks. This image (300Å X 400Å) shows a (310) facet on which individual atomic layers are resolved.

the piezoelectric calibration. This indicates that the step can be viewed as a (310) oriented facet or 12 one atom wide (100) terraces separated by (110) oriented monatomic steps. On some STM images of these (310) microfacets the individual atomic layers are resolved.

Removal of the sulfur and sufficient annealing will return the surface to its original condition. However, if the surface is not annealed sufficiently, the partial breakup of the large steps will leave areas of the surface with a higher step density than average. Adsorbing a $c(2x2)$ overlayer of sulfur on this surface causes double height steps to form in these high step density areas, while they did not form for the same coverage on the lower step density areas characteristic of the average orientation of the surface. We also observed that the sulfur overlayer was better ordered around the bottom edge of the double steps. An area of high step density with half a monolayer of $c(2x2)$ sulfur is shown in figure 12.4. This figure shows ordered sulfur covered regions near the bottoms of steps, while the area not covered by sulfur appears noisy. Clearly, the formation of multiple height steps depends on both sulfur coverage and step density.

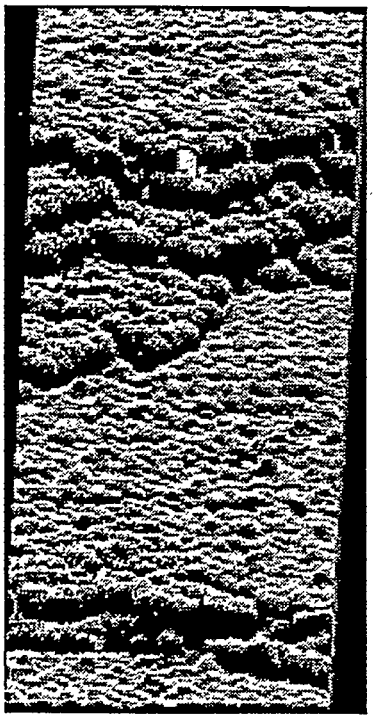

An STM image (50Å X 190Å) showing groups of double atomic height steps which form in areas of high step density on the Mo(100) surface even at low sulfur exposure. There is a group of four of these diatomic steps at the top of the image and a group of two at the bottom.

Figure 12.4 Step Grouping at Low Sulfur Exposure

12.3 Comparison With LEED Results

LEED experiments[8, 10] on the stepped (910) and (911), and the kinked (28,4,1) Mo surfaces found that S adsorption both modifies the formation of ordered overlayers and promotes step doubling. The results of both the LEED and STM experiments on this system may be displayed as a rough phase diagram, figure 12.5. It shows where single, double, and multiple height steps have been found to form as a function of sulfur coverage and step density. Roughly defined boundaries have been drawn between these regions. The left side of the diagram is based on STM results, while the right side displays the LEED results on the three vicinal surfaces which were studied. This diagram shows a trend toward increasing step height as either sulfur coverage or step density is increased. Further work is needed to fill in some regions of the diagram. As LEED is only able to distinguish what type of step structure predominates on the surface, it is unclear whether the step pairing and multiple height steps observed with the STM also exist at some sulfur coverage values on the higher step density surfaces studied by LEED.

12.4 Interactions Between Steps

The strong interaction between sulfur and the steps on this surface is manifested by the change in step structure which occurred upon sulfur adsorption. The first indication of the effect of sulfur on the interactions between steps on the Mo(100) surface observed by STM was the grouping of steps. The theory of Equilibrium Crystal Shapes (ECS) is useful in interpreting this observation. However, it fails to be valid when steps combine to form double height steps and facets. Therefore, the formation of multiple height steps and facets will be discussed later. It must be kept in mind that in the experiments discussed here the surface is only in a local equilibrium at the temperature at which the state of the surface is quenched. However it is possible to predict from the local equilibrium structures what shape the crystal is tending toward.

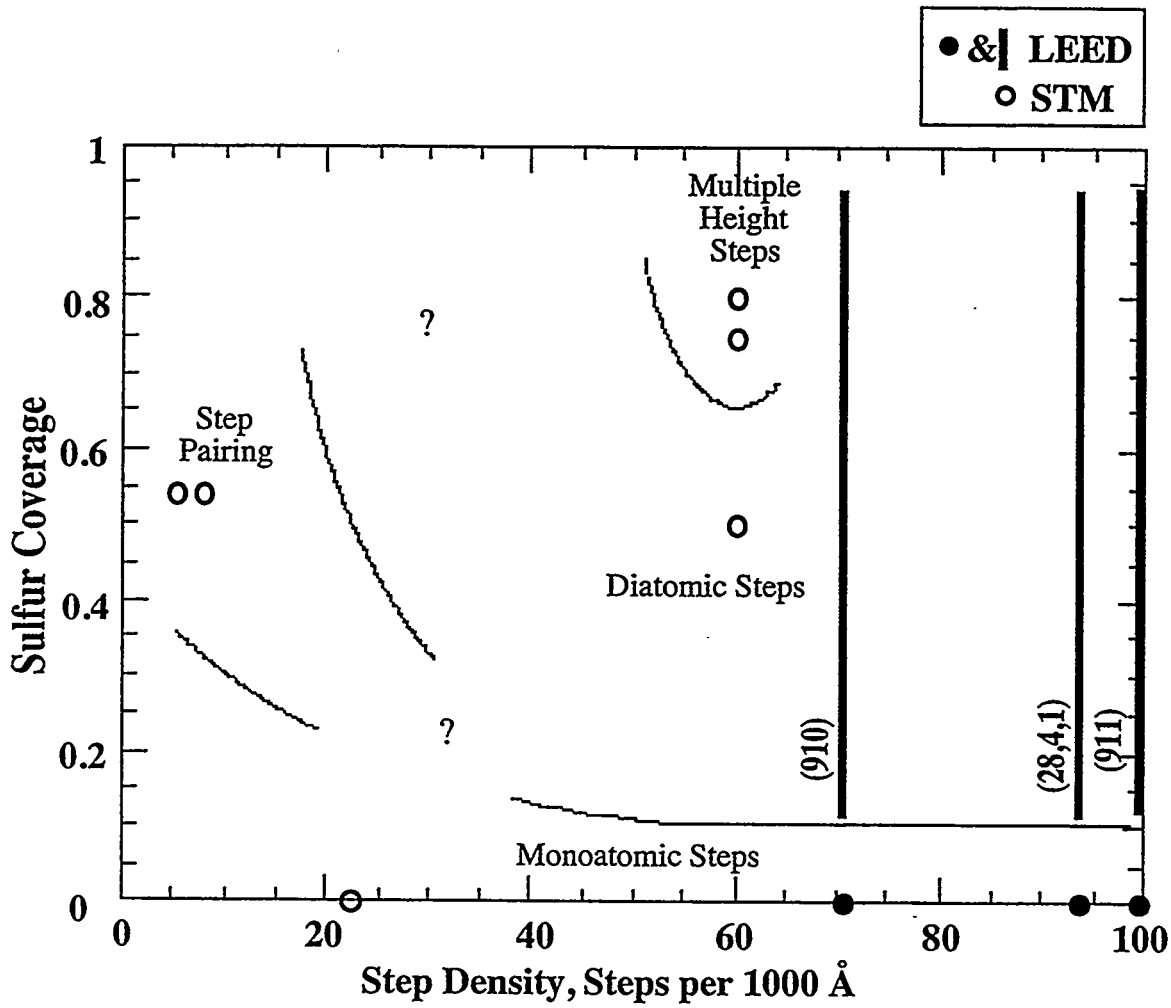

Figure 12.5 A Phase Diagram of Step Structure on Sulfided Mo(100)

The horizontal axis represents the step density on the surface and the vertical axis represents the sulfur coverage. Dark experimental points and lines represent LEED results. Hollow points represent STM results. Roughly defined regions of different steps structures are shown. The diagram shows a trend toward increasing step height as either sulfur coverage or step density is increased.

The equilibrium shape of a crystal is determined by minimizing the surface free energy while holding the volume constant.[11, 12] Near a (100) oriented facet, the solution of this variational problem leads to a continuous approximation of the shape function of the surface $z(x)$ determined by

$$\lambda z(x) = [f(s) + s\lambda x]_{\text{minimum on } s} \tag{12.1}$$

where λ is a distance scaling factor and $f(s)$ is the surface free energy per unit area as a function of step density or average surface slope $s = \frac{dz}{dx}$. The z and x axes are in the (100) and (010) directions, respectively. The shape of the surface therefore depends on the form of $f(s)$, which in turn depends on the form and strength of the interactions between the steps on the surface. Statistical mechanics techniques have been developed which allow $f(s)$ to be calculated from the step-step interactions on the surface in the Terrace-Step-Kink (TSK) model.[13, 14] This calculation may be done by mapping the statistical mechanics transfer matrix problem onto a system of interacting spinless fermions.[13] The surface free energy $f(s)$ is directly related to the ground state energy in the fermion problem, and it may be expanded in powers of s about $s = 0$.

Analysis of equation (12.1) shows that there are two types of transitions between facets on the surface. First order transitions produce facets connected by a surface which contains points of discontinuous slope s. Second order transitions exhibit a surface which is smoothly rounded from one facet to the next. In this case the shape of the surface $z(x)$ varies as $x^{3/2}$ near the facet[13] characterizing it as a Pokrovsky-Talapov[15] or Gruber-Mullins[14] transition. In the experimental data, the sulfur covered surfaces contain either groups of steps at low coverage or (110) and (310) facets at high coverage. This indicates that the transition from the (100) facet is first order as the surface is breaking up into these two phases with no intermediate orientation in between. On the clean surface with evenly spaced steps, the transition appears to be second order.

A first order transition occurs when the free energy function $f(s)$ contains a negative s^3 term.[13] Let us consider possible contributions to this term. As steps may

not cross, placing them too close together reduces their ability to wander. The reduction of step wandering amplitude increases the free energy by decreasing the entropy. This contributes a term to the total surface free energy which varies as s^3 and is always positive (repulsive). Step-step interaction potentials also contribute to the total surface free energy as s^3 as long as they fall as $1/r^2$ or slower with step-step distance $r = 1/s$.[13]

There are two interactions between steps which vary as $1/r^2$. The first of these, mechanical stress in the bulk due to the steps, is always repulsive for identical steps.[16, 17] However, sulfur adsorption, by modifying the displacements of the surface atoms may change the strength of this interaction. The second interaction which falls off as $1/r^2$ is the longest range part of the electronic interaction between steps, the dipolar interaction. Steps have a higher electron density at the bottom than at the top, due to electronic relaxation smoothing out the electronic density around the step.[18] Steps therefore form line dipoles which point at an angle outward from the surface and along the surface perpendicular to the steps. The dipole moment of steps has been measured experimentally on W(110) with (100) steps and found to be 0.37 Debye per lattice site.[19] The interaction between these dipoles can be attractive or repulsive, depending on their orientation relative to the local average surface. The horizontal component of the dipoles is attractive, while the vertical component is repulsive. Sulfur atoms adsorbed on the surface also form dipoles which have been measured to be 0.218 Debye per sulfur atom on Mo (100).[20] Since sulfur is electronegative the dipoles point inward toward the surface, opposite to the vertical component of the step dipoles. Placement of sulfur atoms along the step edge will therefore decrease the vertical repulsive component of the step dipole. This causes a reversal of the sign of the interaction between steps from repulsive to attractive, leading to a net negative s^3 term in the expression for free energy $f(s)$. This changes the phase transition at facets from second to first order as observed experimentally.

Equation (12.1) also shows that the step density will diverge (i.e. a facet will form) in a first order transition unless there is a higher order positive term in $f(s)$. Interactions

of range shorter than $1/r^2$ contribute to the free energy as s^4.[13] The observed grouping of steps that remain separated by 30-50 Å terraces at higher coverage shows that there must be a short range repulsive interaction between steps preventing faceting. This comes from higher order electronic interactions than the dipole interaction between steps discussed earlier. As sulfur adsorption changes the local electronic structure of the surface, adding more sulfur could change this short range interaction from net repulsive to net attractive, leading to faceting instead of step grouping.

While the theory of equilibrium crystal shapes is useful in interpreting the mechanism behind the grouping of steps on the surface, it is not applicable once the steps coalesce into microfacets. Equation (12.1) describes a surface in which there is a finite step density at each point on the surface. Once steps form pairs or facets, it is no longer valid. Pairs of steps may have different electrostatic dipole and mechanical stress interactions than single steps. Therefore, steps may come together to form diatomic steps, but the different interactions between the diatomic steps may prevent them from coalescing into larger steps. Since both LEED and STM results agree that separated double steps can remain stable on the surface at some sulfur coverage, we can conclude that the long range stress and dipole interactions between double steps is more repulsive than that between single steps at this sulfur coverage.

It is clear that diatomic steps will form only when the twice the free energy of a monatomic step is greater than the free energy of a diatomic step.[21] This condition corresponds to the energy of single step formation exceeding the temperature times the entropy gained by splitting a double step into two single steps. Sulfur adsorption appears to increase the energy of single step formation, causing the formation of diatomic steps. This increase in step formation energy may come from the energy needed to break up an overlayer domain into two parts, with one on each side of the step, upon formation of a new step.

12.5 Conclusion

Adsorbed sulfur and steps have a strong interaction on the vicinal Mo(100) surface. The bottom edge of steps act as sites for nucleating the sulfur overlayer. The strong interaction of sulfur with steps also causes changes in the structure of steps on the surface. Sulfur adsorption on the Mo(100) surface makes the interaction between steps more attractive at long range. This changes the transition between facets from second to first order, leading to a breakup of the surface into two phases with different orientation. At lower sulfur coverage there is a short range repulsive interaction which prevents faceting, but this interaction diminishes or becomes attractive at higher sulfur coverage allowing step doubling and the formation of microfacets.

Chapter 12 References

[1] D.W. Blakely and G.A. Somorjai, Surf. Sci. **65** (1977) 419.

[2] A.-M. Lanzillott and S.L. Bernasek, J. Chem. Phys. **84** (1986) 3553.

[3] G. Comsa, G. Mechtersheimer and B. Poelsema, Surf. Sci. **119** (1982) 159.

[4] E. Bauer, H. Poppa and Y. Viswanath, Surf. Sci. **58** (1976) 517.

[5] C. Zhang, M.A.V. Hove and G.A. Somorjai, Surf. Sci. **149** (1985) 326.

[6] P.A. Dowben, M. Grunze and R.G. Jones, Surf. Sci. Lett. **109** (1981) L519.

[7] A.J. Gellman, J.C. Dunphy and M. Salmeron, Langmuir **8** (1992) 534.

[8] C.C. Knight and G.A. Somorjai, Surf. Sci. **272** (1992) 326.

[9] G.A. Somorjai and M.A.V. Hove, Prog. Surf. Sci. **30** (1989) 201.

[10] J.C. Dunphy, C. Knight, P. Sautet, D.F. Ogletree, M. Salmeron and G.A. Somorjai, Surf. Sci. **280** (1993) 313.

[11] N. Cabrera. *Symposium on Properties of Surfaces* 1-24 (Special Publication, No. 340 ASTM, Philadelphia, 1962).

[12] L.D. Landau and E.M. Lifshitz. *Statistical Physics*. (Pergamon Press, 1978).

[13] C. Jayaprakash, C. Rottman and W.F. Saam, Phys. Rev. B **30** (1984) 6549.

[14] E.E. Gruber and W.W. Mullins, J. Phys. Chem. Solids **28** (1967) 875.

[15] V.L. Pokrovsky and A.L. Talapov, Phys. Rev. Lett. **42** (1979) 65.

[16] V.I. Marchenko and A.Y. Parshin, Soviet Physics JETP **52** (1980) 129.

[17] M.B. Gordon and J. Villain, J. Phys. C **12** (1979) L151.

[18] M.D. Thompson and M.B. Huntington, Surf. Sci. **116** (1982) 522.

[19] B. Krahl-Urban, E.A. Niekisch and H. Wagner, Surf. Sci. **64** (1977) 52.

[20] V. Maurice, L. Peralta, Y. Berthier and J. Oudar, Surf. Sci. **148** (1984) 623.

[21] T.L. Einstein, T.M. Jung, N.C. Barlelt and E.D. Williams, J. Vac. Sci. Technol. A **10** (1992) 2600.

Chapter 13. CRYOGENIC STM DESIGN

13.1 Motivation

At cryogenic temperatures some of the difficulties in deriving quantitative results from STM experiments are eliminated. The severely restricted surface diffusion at these temperatures insures that both the surface and tip are likely to be static during imaging. Thermal expansion coefficients fall towards zero at low temperature, greatly decreasing the thermal drift of the tunneling gap. These two facts allow image acquisition time to be increased from minutes to days, if required. The same nanoscopic area of the surface can be studied for hours. As changes in the tip termination structure are rare, different surface structures can be studied with precisely the same tip. In addition, the resolution of tunneling spectroscopy improves with kT. For instance, narrowly separated quantum states in confined electron systems can be more easily resolved.

Besides simply improving the performance of the instrument, imaging at low temperatures opens up a wide new range of experiments which are possible. For instance, at low temperatures it is possible to adsorb species at metastable sites. In this manner, the contrast of STM images of benzene molecules as a function of their adsorption site on Pt(111) has been investigated.[1] As Eigler et al. have demonstrated, at low sample temperatures the STM can be used to fabricate new structures. Under these conditions weakly bound adsorbate species do not naturally diffuse, but they can be manipulated through their interaction with the STM tip. Using this technique Eigler et al.[2] have built "quantum corrals", or rings of adsorbed Fe atoms, in which electrons in a surface state of Cu(111) are partially confined. Recently, molecules have been constructed on the surface by manipulation of adsorbed atoms with the STM tip.

For other potential experiments, the ability to vary the sample temperature is required. For example, variable sample temperature is necessary for the experimental observation of phase transitions such as that simulated with the Monte Carlo technique in

chapter 9. Working just at 4° K prevents the study of nearly all chemical and dynamic processes because they do not occur at this temperature. At room temperature, however, many surface processes, including diffusion of most small atomic and molecular species, and reactions of these species, are too fast to be observable. For instance, the diffusion of sulfur on Re described in chapter 9 is at the edge of the time scale observable with the current STM design. By cooling the sample, the rates of many of the processes of interest are slowed to the time scale of imaging. In chemical reactions, the reactants, products, and perhaps even intermediate species may be observable. The rates of most of these processes follow the Ahrenius law. From a measurement of the rates as a function of temperature, the energy barrier and Ahrenius prefactor can be determined. From these parameters, the rate can be extrapolated to higher temperatures.

13.2 Design

13.2.1 Overview

A number of groups have developed[3, 4], or are in the process of developing, UHV STM systems which incorporate liquid He sample cooling. The earliest such design was built by Eigler, and first produced results in 1989-90.[5] In this design the STM resides inside a liquid He dewar. After preparation the sample is lowered into the dewar with a long transfer arm. This instrument has produced a number of unique and exciting results, including the demonstration of atom manipulation with the STM tip[6], single atom switch[7], construction of molecules on a surface, and "quantum corrals."[2] However, in this design the sample cannot be cooled while using UHV instruments besides the STM. When located on the STM stage, the temperature is limited to that of liquid He.

The experiments planned for our low temperature STM, such as atomic level study of chemistry, the measurement of diffusion rates, and observation of phase transitions, require sample temperatures other than 4 K. However, obtaining the absolute lowest temperatures possible with liquid He cooling is not necessary. Some sacrifice in the lowest

achievable temperature is necessary because the degree of thermal coupling between the sample and the liquid He must not be too great in order for the sample temperature to be varied.

It is extremely useful to be able to apply other surface science techniques, such as AES and LEED, while the sample is cooled to the same temperatures at which it is studied with the STM. Therefore, the sample is mounted to a manipulator incorporating sample cooling and temperature control. The chosen design differs from that of Eigler et al. in that the liquid He is brought into the UHV system with a flow cryostat instead of transferring the sample in UHV into a liquid He dewar.

Figure 13.1 (NEXT PAGE)

The system sits on a steel frame on top of air damping legs. An inner frame, which holds the chamber and dewar may be tilted by several degrees with respect to the outer frame. Liquid He is stored in the dewar on the left. During operation it travels through a transfer line into a combination cryostat-manipulator which has linear translation and rotation capability.

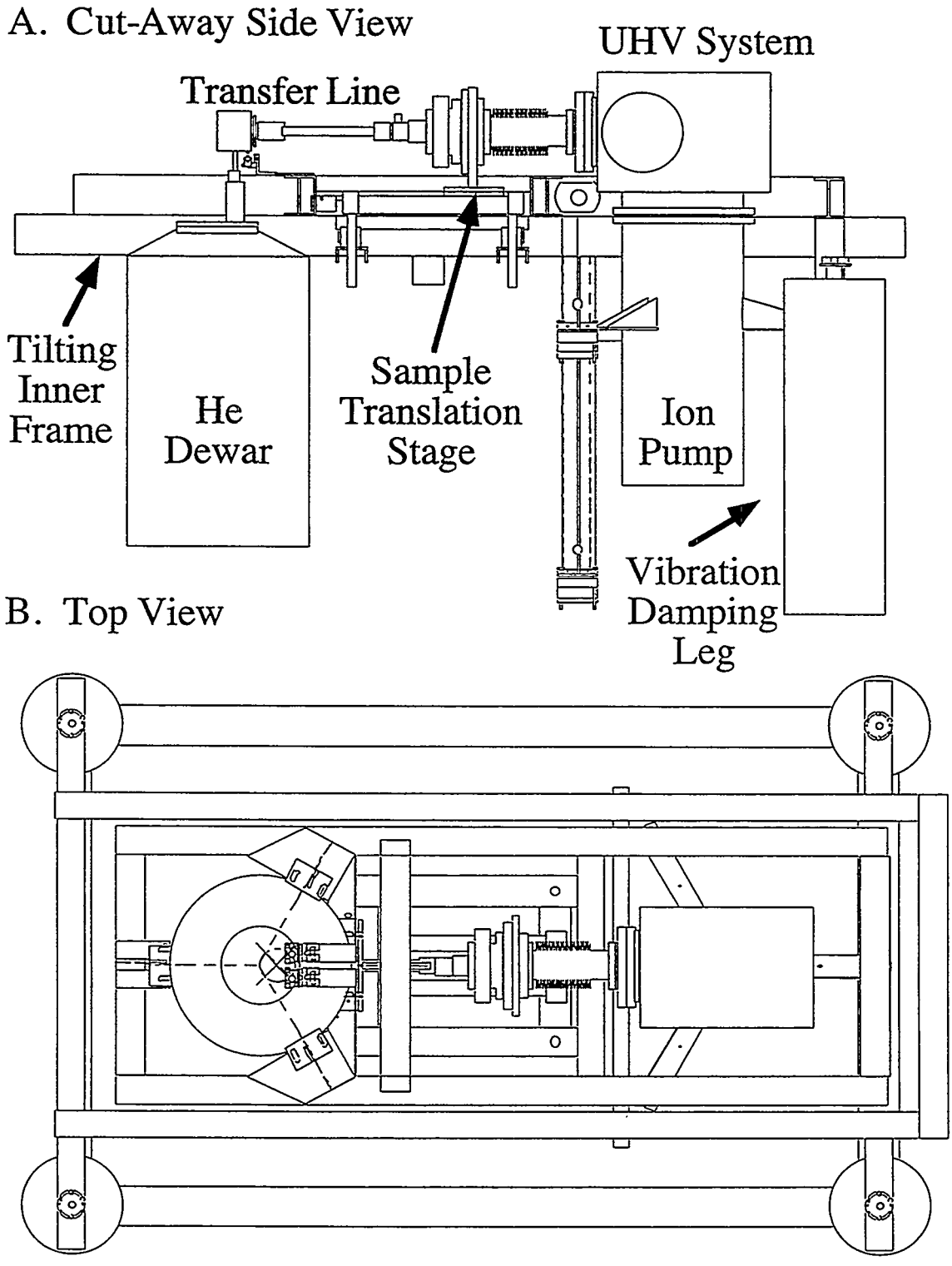

Figure 13.1 Diagram of the Complete System

An overview of the instrument is shown in figure 13.1. The entire system is mounted onto a steel frame which sits on air damping legs for vibration isolation from the building. The main components of the system are attached to a smaller frame which rests on an axle held by the larger frame. The smaller frame can be tilted on this axle by several degrees from horizontal in order to reduce convection currents within the cryostat. The

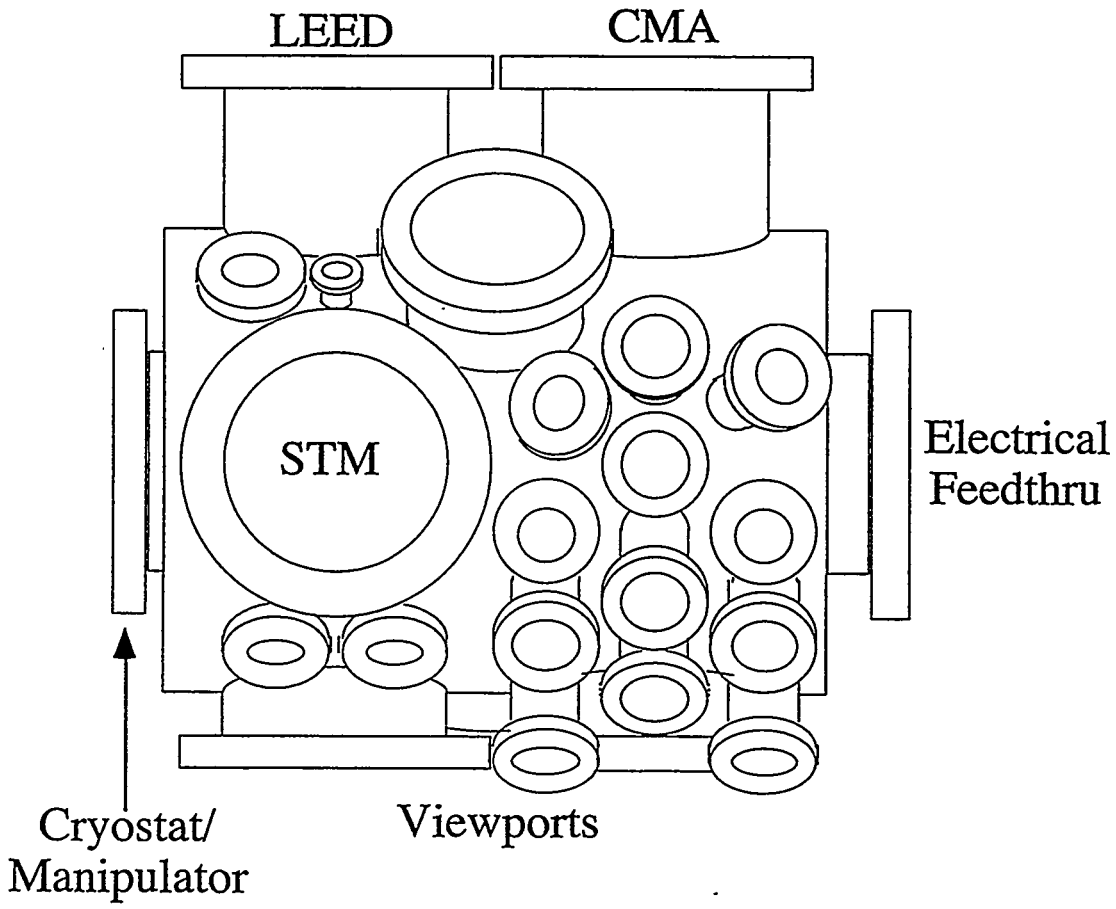

Figure 13.2 Top View of the UHV Chamber

The UHV chamber sits on top of an ion pump. Eight inch flanges on the back hold a LEED and a CMA for AES. The STM attaches to an eight inch flange on the top. A combination cryostat-manipulator with rotation and one dimensional on-axis translation capability is attached to another flange. Smaller ports on the right side of the chamber hold an ion gun, electron gun, RGA, ion gauge, and variable leak valves.

UHV chamber and ion pump are attached to one side of the smaller frame. A manipulator with rotation and on axis translation capability is mounted horizontally through an eight inch flange of the chamber. This manipulator is specially designed to operate as a cryostat. To minimize its thermal conductivity, it is constructed from concentric layers of thin wall stainless steel. A liquid He transfer line fits into its hollow interior. Within the cryostat a vacuum insulated space surrounds the transfer line, and a return path for the He gas surrounds this insulation layer.

A 30 liter dewar holding liquid He is attached to the other side of the frame. A vacuum shielded transfer line connects the dewar to the cryostat-manipulator. During operation, liquid He is transferred from the dewar through the transfer line to the end of the cryostat inside the UHV chamber. The sample is thermally coupled to the cryostat. The transfer line remains stationary when the sample and cryostat are translated.

13.2.2 UHV Chamber

The UHV system is built around the horizontal axis manipulator. The geometry of the system is designed to maximize the number of surface analysis techniques and depositions sources with access to the sample. The linear translation of the manipulator moves the sample between two clusters of instruments on opposite ends of the chamber. The instruments on the right are primarily employed for sample preparation. They include an AES system, ion gun, mass spectrometer, thermal deposition sources, and gas dosing sources. The AES system is made up of a CMA mounted to an eight inch flange and an electron gun aimed 70° off the sample surface normal during operation.

A LEED system and the STM are mounted on the left side of the chamber. The STM is attached to a manipulator mounted on an eight inch flange on top of the chamber. The design will be described shortly. Currently a standard Varian front view LEED is installed in the left rear eight inch flange. The diffraction pattern is observed through the viewports on the front of the chamber. Because the manipulator blocks the view of much of the LEED screen, it will eventually be replaced with a rear view LEED system. The new

LEED system will be capable of operating as a Retarding Field Analyzer (RFA) electron spectrometer providing a second, but less sensitive, system for obtaining AES spectra.

Below the chamber is an ion pump and titanium sublimation pump. A turbomolecular pump is used to produce a rough vacuum. The system is baked to 150-200° C after exposure to air with both resistive strip heaters and an infrared lamp installed inside the chamber. The temperature is measured by approximately 10 thermocouples attached on both the outside and inside of the chamber which are interfaced to a PC. The heaters are controlled by the PC.

13.2.3 Microscope Design

The STM is a Besoke or "walker" type design.[8] This design has been successfully employed in a number of STM and AFM systems which operate at low and variable sample temperatures.[4, 9] The design is small, mechanically simple, and rigid. Therefore, its lowest frequency resonance modes are at a relatively high frequency compared to other STM designs. This allows a higher feedback gain and faster image acquisition, as explained in section 2.3. The rigid design is also less sensitive to externally produced vibrations, such as those produced by flowing and boiling He. The symmetry of the design provides first order thermal compensation.

The microscope, shown in figure 13.3, consists of a 0.60" diameter nickel plated aluminum disk onto which four parallel piezoelectric tubes are soldered. The three outer tubes, arranged in a triangle, function as legs. The inner tube holds the STM tip. The outside of each tube is cut into four sectors allowing control of the position of its end in three dimensions, as described in section 2.2. An etched ring electrically insulates the four sectors from the end of the tube which is soldered to the disc.

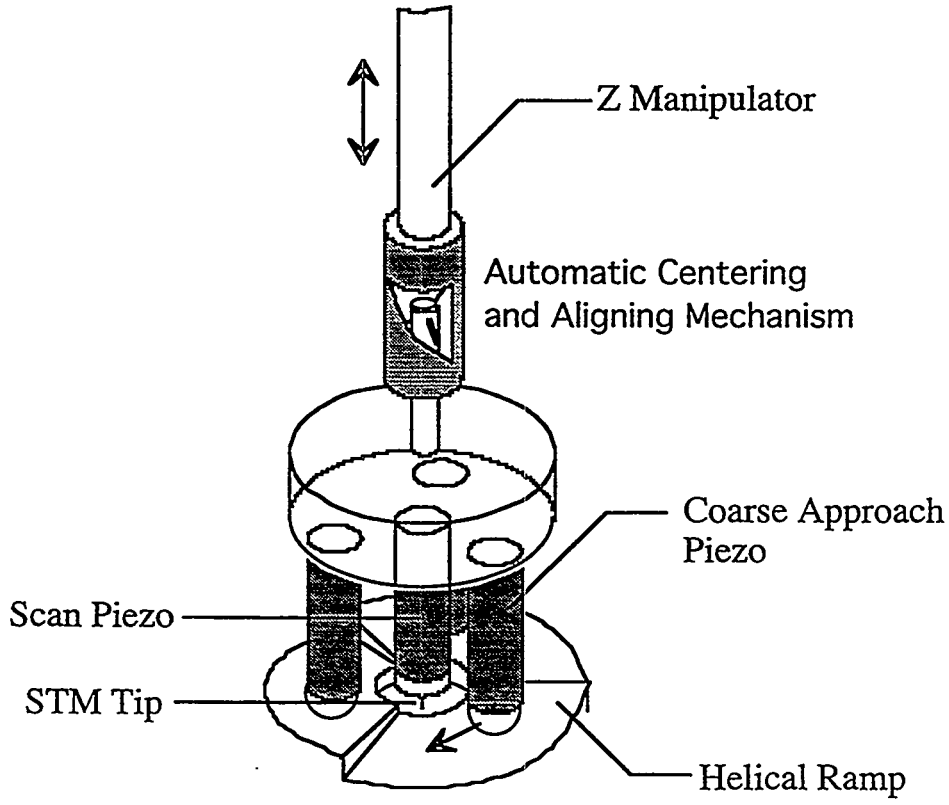

Figure 13.3 The "Walker" STM Head

In operation the STM head stands on three 0.5" long piezoelectric tube legs ending in sapphire balls on a helical Mo ramp. The outer electrode of each leg is cut into four sectors allowing motion in x, y, and z. The legs can walk the microscope laterally or rotate it on its axis by inertial approach. Rotation of the microscope translates the tip toward and away from the sample by the screw action of the ramp. The center piezoelectric tube of the microscope holds the tip and is used for scanning. The STM may be lifted off of the ramp with a z manipulator ending in a mechanism which automatically centers and rotates the microscope such that the legs are at the top of the ramp.

The microscope stands on a three segment shallow helical ramp. The sample is located below a hole in the center of the ramp. Each of the three ramps covers an angle of 120° and has a total height of 0.5 mm. Large scale offsets of the tip are produced by "walking" the microscope on its three legs. Sapphire balls are glue to the end of the legs. These balls stick or slip against the ramp depending on the speed of the motion of the leg. Lateral motion is produced directly by walking the microscope. The tip is approached toward the sample by rotating the microscope around its own vertical axis and down the helical ramp.

A linear motion manipulator holds the STM. When not in use, the STM hangs from a horizontal Cu-Be wire hooked into two asymmetric V-shaped holes cut into the opposite sides of a short vespel tube. The weight of the microscope pulls the wire to the bottom of the holes, rotating it to a specific angle. At this angle the legs of the microscope are centered over the top of the ramps.

The wires from the microscope piezoelectric tubes exit through holes in the Al disc. The holes are evenly distributed around the circumference of the disk in between the outer piezoelectric legs. The wires are coated with Kapton insulation and protected from

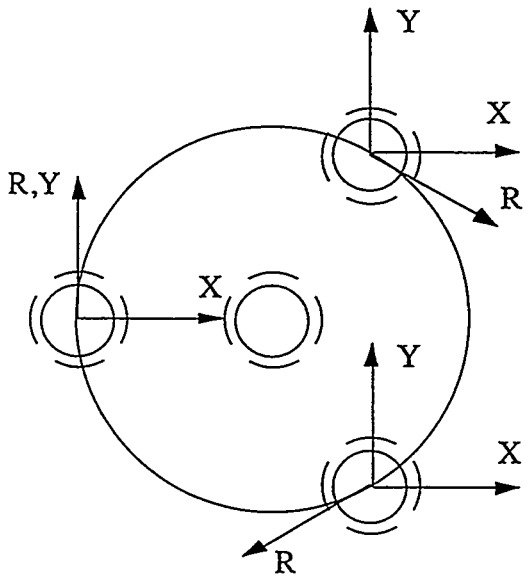

This diagram of a top view of the microscope (not to scale) shows the direction of the "walking" or inertial approach of the three outer legs to produce an offset of the tip in X, Y, and Z. The Z motion is produced by rotation of the microscope on the ramp (vectors labeled R).

Figure 13.4 Inertial Approach and Lateral Motion of the STM Head

abrasion against the microscope by Teflon tube. The wires pass from the microscope head upward to a Teflon ring which holds gold plated Cu-Be connectors to which they are soldered. Matching Cu-Be connectors on the top side of the Teflon ring connect to wires which go to electrical feedthrus on the flange holding the microscope manipulator.

During operation, the sample manipulator holds the ramp centered below the microscope. The microscope is lowered onto the ramp with its manipulator. It lands with its legs at the top of the three ramps and with the tip as far from the sample surface as possible. Once the microscope is on the ramp, the Cu-Be wire which holds the microscope on the manipulator no longer touches the vespel tube. This decouples the microscope from vibrations of its manipulator. Using the piezoelectric tube legs, the microscope is rotated about its own axis down the ramp until tunneling current is detected. After use, the microscope is walked part of the way up the ramp and then lifted off it with the manipulator. Upon lifting, the microscope rotates back to the starting angle.

13.2.4 Sample Holder

The sample holder, shown in figure 13.5, is designed to allow heating of the single crystal samples to the temperatures needed to clean them (at least 1200° C for most materials), and also to provide controlled cryogenic cooling to below 20° K. The base of the sample holder is a flat Cu plate attached to the end of the cryostat. This plate is cooled to as low as approximately 5° K when liquid He is flowing through the transfer line. A Si diode sensor measures the temperature of this plate. An external temperature controller maintains the desired temperature by heating the cryostat with a resistor.

The Mo ramp is clamped to the Cu plate by four hollow stainless steel screws. The screws are held tight by Cu-Be washer springs. These screws are designed to have low thermal conductivity to avoid heating the cryostat with the thermal radiation which hits the ramp.

The sample is clamped between the ramp and the cryostat. It is insulated thermally and electrically from the ramp by an alumina disk. A type E thermocouple measures the

sample temperature. While less accurate than a Si diode, especially at low temperatures, the thermocouple can survive heating to the temperatures needed to clean and prepare the crystal. At the back of the sample is an alumina insulated electron bombardment heater made from a 0.005" tungsten filament. This heater is used during sample preparation.

The sample is thermally coupled to the cryostat through a sapphire disc and three sapphire rods. Sapphire was chosen because it has (relative to other materials) a high thermal conductance at cryogenic temperatures relative to high temperatures. This provides a good thermal link between the sample and the cryostat at low temperatures, allowing sample temperatures of approximately 15° K to be reached. When the crystal is heated during cleaning, however, the thermal link is weak enough to prevent excessive heating of the cryostat. The Si diode on the cryostat cannot be heated above 200° C without suffering damage.

13.2.5 Cryostat Design

The complete sample cooling system is shown in figure 13.6. The sample holder, at the right, is shielded from thermal radiation from the chamber walls by a gold plated Cu tube. The opposite end of the cryostat is connected to a differentially pumped rotation stage. This mechanism is held to a linear translator through a Viton sealed vibration isolation stage which eliminates all direct metal to metal contact paths between the STM and the chamber. The translation stage moves the sample between the two sets of instruments in the chamber.

The transfer line carries liquid He from the dewar to the cryostat end at the sample holder. The He flow from the dewar is switched on with a ball valve governed by a screw control at the top of the dewar. Like the cryostat, the transfer line consists of several layers of concentric thin walled stainless steel tube. The liquid He flows through the center tube which is vacuum insulated from the inside of the dewar to the end in the cryostat. In the section from the evacuated box above the dewar to the end of the transfer line, two layers of vacuum shielding are used. In between these layers is a return path for He gas.

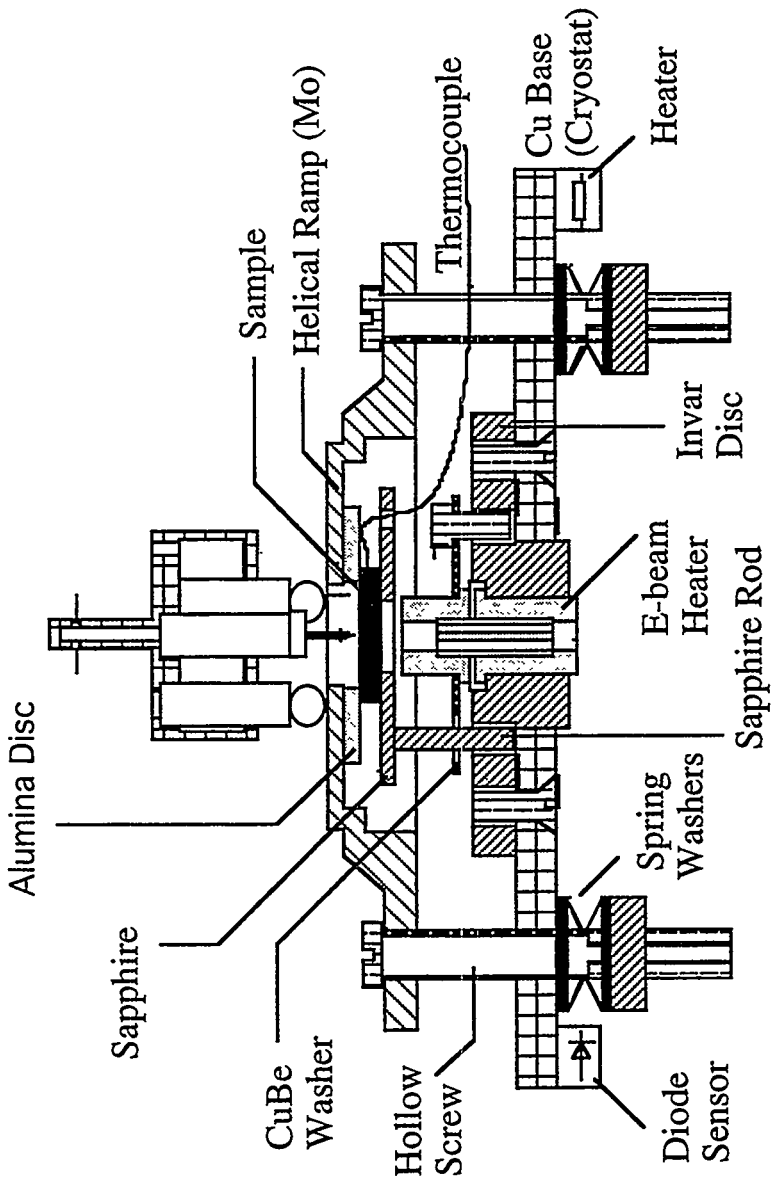

Figure 13.5 Drawing of the Sample Holder

The single crystal sample sits under the center of the helical approach ramp of the microscope. The ramp is pressed down towards the cryostat by three spring loaded insulating hollow screws. The sample is insulated thermally and electrically from the ramp by an alumina disc. It is mounted on top of a sapphire disc which is thermally coupled to the cryostat through three sapphire rods. A Si diode sensor measures the cryostat temperature.

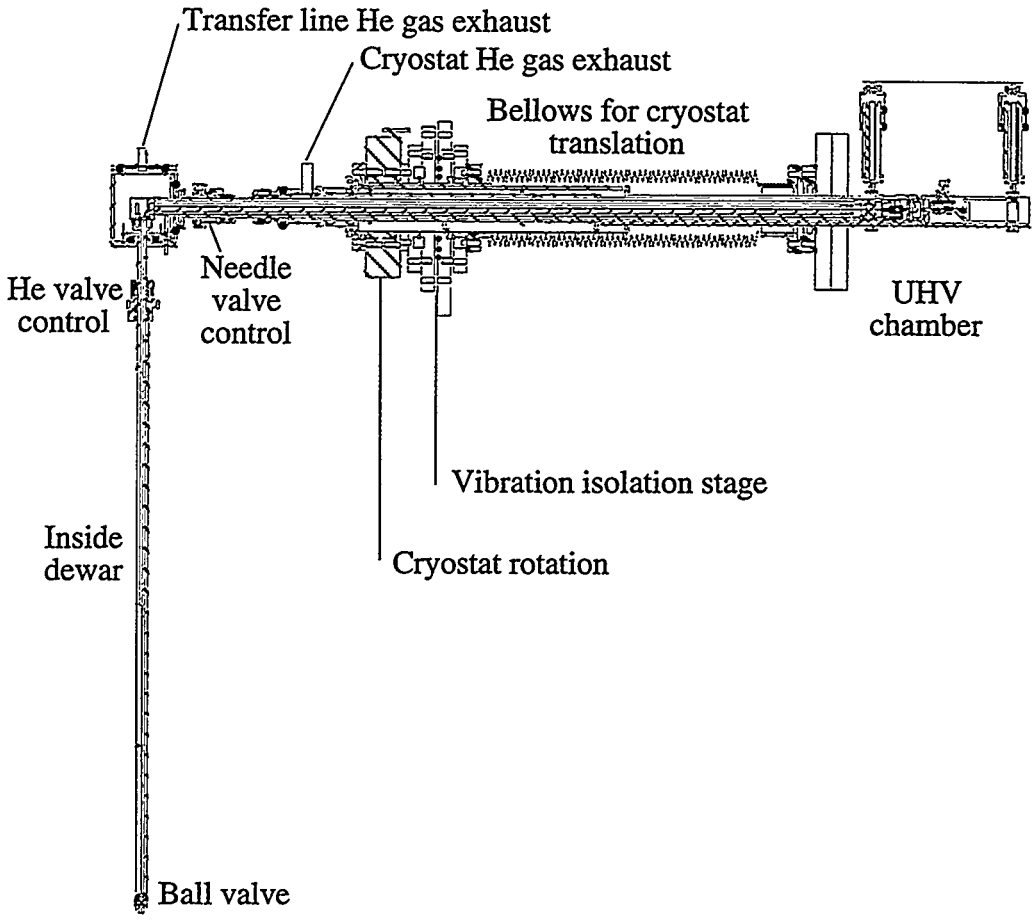

Figure 13.6 Liquid He Transfer Line and Cryostat

(1:10 Scale)

The L shaped transfer line carries the liquid He into the cryostat. A ball valve inside the pressurized dewar activates the flow of He. The He travels up a 1/8" stainless steel tube into an evacuated box, and then travels through a vacuum and superinsulation shielded tube into the cryostat. The cryostat is attached to a double differentially pumped rotation stage. This stage is decoupled from vibrations from the rest of the chamber through a differentially pumped Viton sealed connection. The entire cryostat is held by a linear translation stage with a range of 10".

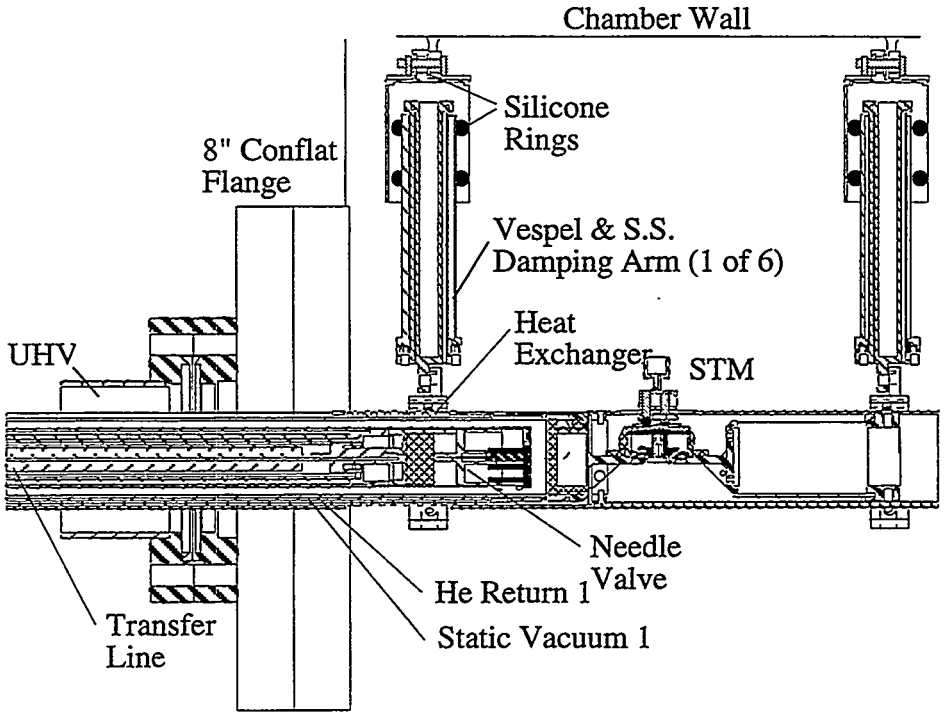

Figure 13.7 Termination of the Cryostat and Transfer Line

(1/3 Scale)

Liquid He and cold He gas are deposited at the end of the transfer line inside of the cryostat. In order to prevent vibrations from being transmitted, the transfer line does not make mechanical contact with the cryostat at its cold end. The He flow is governed by an externally controlled needle valve inside the transfer line. After boiling, He gas returns through a helical Cu heat exchanger which cools the shields surrounding the sample. Vibrations of the cryostat end are damped by two rings coupled to the cryostat through spring loaded vespel balls and held to the chamber by three arms each. The arms are made of vespel and stainless steel. They are folded back within themselves to increase their effective length and thermal resistance. The arms are attached to the chamber wall through silicone O-rings which are clamped inside a cylinder.

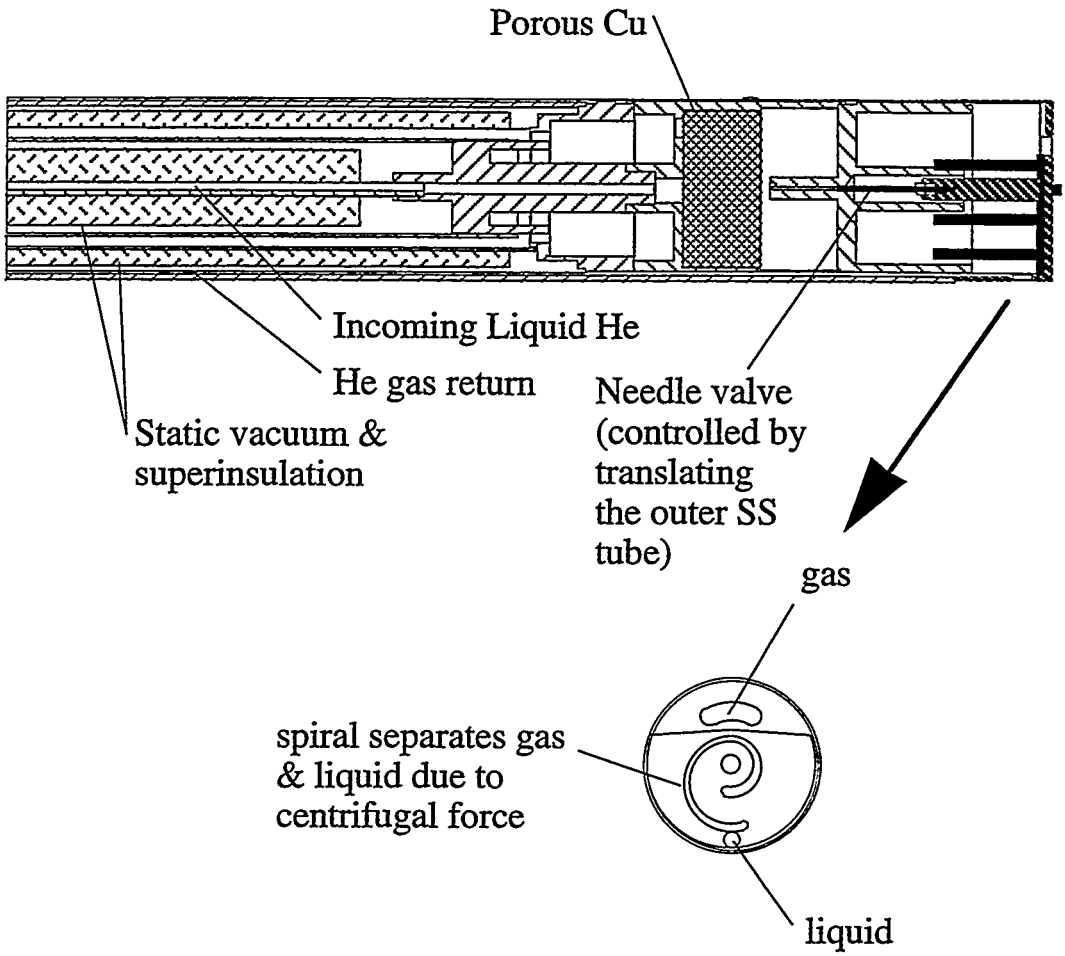

Figure 13.8 Transfer Line End

(1 X Scale)

Liquid He arrives through the center double vacuum insulated and superinsulated stainless steel tube. It passes through a porous Cu block which disrupts large gas bubbles to provide a smoother flow. Some He gas returns from this point though an outer layer of the transfer line. The remaining He passes through a needle valve into a phase separator. The needle valve is externally controlled with a screw mechanism which moves the outer stainless steel tube relative to the rest of the transfer line. Liquid and gas pass out into the cryostat through separate holes at the end of the transfer line.

During operation the dewar is pressurized to 5-10 psi, which forces the liquid He through the transfer line. The He gas returns through two paths. The first path is the shield surrounding the transfer line. Cold He gas returning along this path blocks most thermal radiation from reaching the liquid He and causing it to boil within the transfer line. The second gas return path is through the cryostat. Gas returning along this path is produced by the liquid He which boils in the process of cooling the sample holder. The flow rate through each of these paths is set with independent mass flow controllers which apply back pressure on the two exhausts.

Figure 13.7 shows the end of the cryostat and sample holder. A gold plated tube surrounding the sample holder shields it from thermal radiation from the chamber walls. A hole through this tube provides access to the sample for LEED, AES, and the STM.

Vibrations of the cryostat end are damped by arms which loosely attach it to the chamber. Two rings are each clamped to the end of the cryostat by three spring loaded vespel balls. The rings are held to the walls of the chamber by three stainless steel and vespel arms each. In order to reduce their thermal conductivity, the arms are folded internally such that their effective length is three times their physical length. The end of the arms at the chamber wall are at room temperature. They are coupled to the chamber wall by cylinders which compress silicone O-rings against the arms. These silicone rings provide vibration isolation as well as damping vibrations of the end of the cryostat.

The transfer line, visible in the figure inside of the cryostat, does not touch the cryostat anywhere on the chamber side. This prevents vibration from the He flow within the line from being transmitted to the STM. However, this design introduces a problem. Convection currents inside the horizontal dead space between the inside of the cryostat and transfer line transport heat from the warm end of the cryostat to the cold end. This heat transport reduces the efficiency of the system and increases He consumption. By tilting the cryostat so that its warm end is above its cold end, these convection currents can be

reduced or eliminated. This is accomplished by tilting the smaller steel frame on which the entire UHV system, transfer line, and dewar are mounted.

Figure 13.8 shows a close-up of the end of the transfer line. A porous Cu block breaks up large gas bubbles, stabilizing the flow. A needle valve, controlled by moving the outer wall of the transfer line with respect to the rest of it, controls the flow of He into the cryostat. After passing through the needle valve the He goes into a phase separator. Here, a metal spiral separates the liquid and gas He by a centrifugal action. Vibrations produced by boiling are decreased by separating the liquid and gas. The separate phases pass through two holes at the end of the transfer line.

13.3 Initial Test Results and Design Changes

At present, no successful tests of the STM with the sample at cryogenic temperatures have been accomplished, but this should change in the near future. The UHV system has produced a vacuum in the 10^{-10} Torr range. The sample preparation systems, including the electron beam heater, gas dosing, LEED, and AES systems are all operating. The STM and cryostat have been independently tested. The results of the tests are described below.

13.3.1 STM Tests

The STM inertial approach was tested outside of the chamber. At first, an approach ramp with a height of 1.0 mm was used. While the STM could walk down this ramp easily, it would often get stuck or slip when walking laterally or up the ramp. Reducing the ramp height to 0.5 mm alleviated this problem. In early tests, 0.003" diameter Cu wires were used to connect the STM head. These wires were found to put too much torque on the microscope when it rotated, often causing it to get stuck. Reducing the wire diameter to 0.002", using slightly longer wires, and straightening them before use solved this problem. Additionally, an aluminum guard ring was added to the ramp. This ring prevents the microscope from walking off of the edge of the ramp.

As a test of the STM, a Rh(110) surface with a small amount of sulfur was imaged at room temperature in UHV. An atomic resolution image obtained of this surface is shown in figure 13.9. The individual Rh atoms are resolved. Some adsorbed sulfur atoms are also visible in between the Rh rows. A LEED study[10] has indicated that sulfur adsorbs in between the Rh rows, as is visible in the image and indicated in the model. In some areas of the image these atoms are ordering into a $c(2x2)$ overlayer.

Scanning rates as high as 1500 Å/second could be achieved while maintaining atomic resolution in topographic mode without inducing resonances of the microscope head. This scan rate is more than an order of magnitude faster than could be obtained with the double tube design UHV STM described in chapter 3.

13.3.2 Cryostat Tests

The cryostat was tested with a dummy sample made of polycrystalline Cu onto which a diode temperature sensor was glued. Initially the dewar was pressurized to 8.5 psi and the flow controllers on the He gas exhaust were opened to the maximum of 20 liters/minute. The temperature of the cryostat end dropped to 30° K over approximately 40 minutes. After around one hour the sample temperature has stabilized at a minimum of 13.4 ° K and the cryostat temperature had reached 6.0° K. At the time of this test the alumina ring which insulates the sample from the Mo ramp was not installed. Thus, a lower sample temperature may well be possible.

The best operating parameters of the cryostat were determined by experimentation. A transfer line exhaust flow rate of 2 liters/minute was found to be sufficient to prevent boiling of He in the transfer line. The cryostat temperature was maintained at the minimum value by a cryostat exhaust flow rate of 12 liters/minute or greater. Tilting the inner frame was found to be necessary to stop oscillations of the temperature, perhaps induced by convection currents in the space between the cryostat and transfer line. At too small a tilt angle the temperature at the cryostat oscillated from near its minimum value to 10-20 ° K. Some trade off between tilt angle and He consumption was possible. The minimum value

of cryostat tilt angle at which the He consumption was low is 2.7 degrees. Translating the sample and cryostat to the far side of the chamber had a negligible effect on the sample temperature as long as the system was tilted. At a total consumption rate of 14 (gas) liters/minute the filled 30 liter dewar is consumed in 25 hours, ample time for an experiment to be completed.

Using the resistive heater on the cryostat, its temperature could be increased to approximately 20° K. Above this temperature, the cryostat temperature oscillated because at times the liquid helium cooling it boiled completely away. However, by reducing the He flow rate through the cryostat until only cold He gas was present at the end of the transfer line, stable temperatures from 20° K to room temperature could be obtained.

Simultaneous tests of the STM and cryostat are currently underway. The first application of this apparatus will be the molecularly resolved study of the cyclization reaction of acetylene into benzene on the Pd(111) surface.[11]

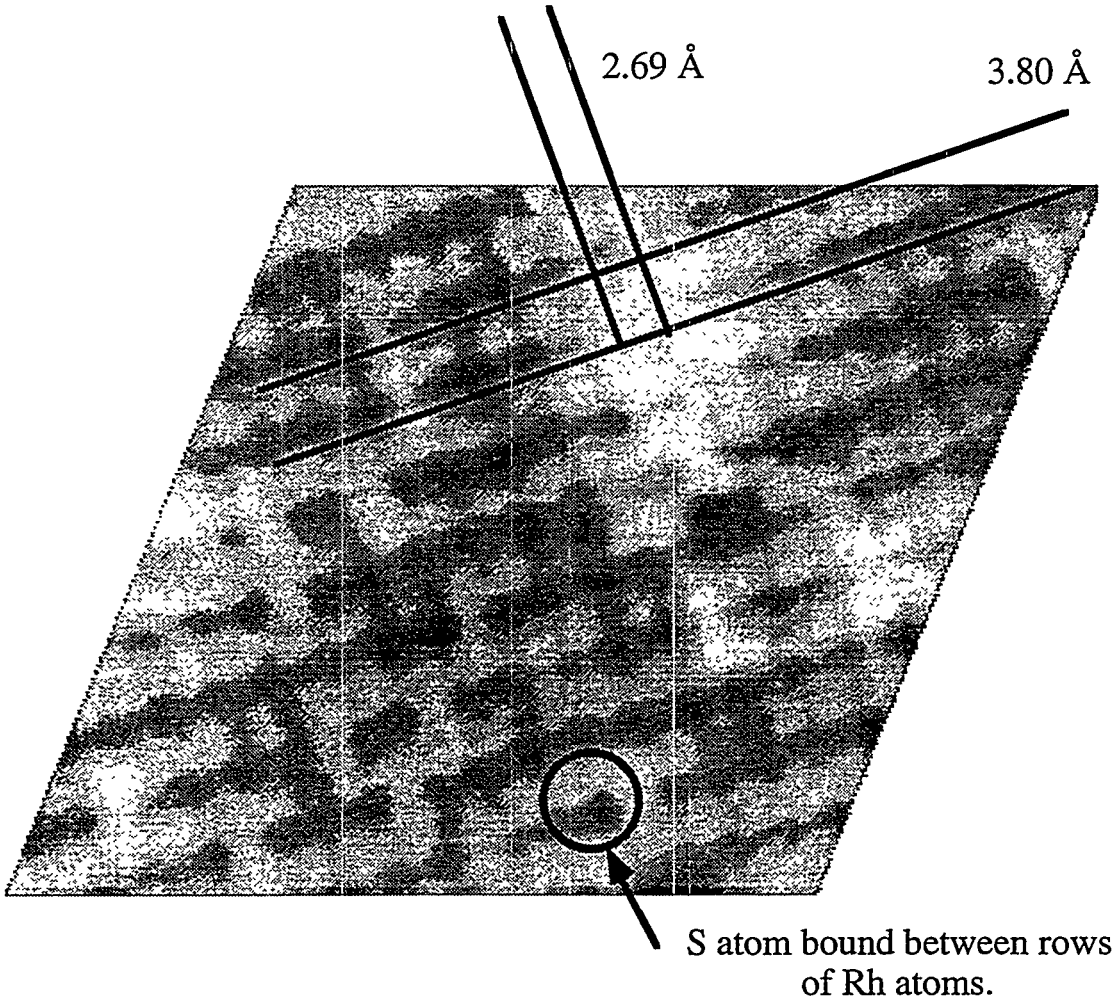

Rh(110) surface model

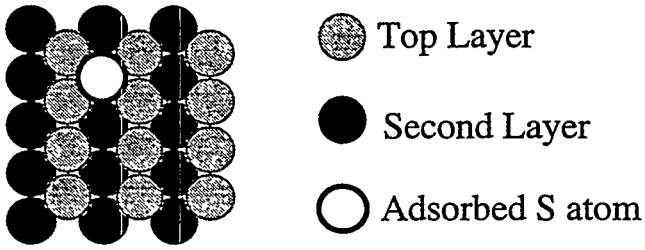

Figure 13.9 STM Test Result - Atomic Resolution of Rh(110)

Atomic resolution of the Rh(110) surface was obtained with the STM at room temperature. The surface has a small (~0.1 monolayer) coverage of sulfur adsorbed on it. Sulfur atoms appear as bright lines in between the rows of Rh atoms. A model of the surface is below the image.

Chapter 13 References

[1] P.S. Weiss and D.M. Eigler, Phys. Rev. Lett. **71** (1993) 3139.

[2] M.F. Crommie, C.P. Lutz and D.M. Eigler, Science **262** (1993) 218.

[3] S. Horch, P. Zeppenfeld, R. David and G. Comsa, Rev. Sci. Instr. **65** (1994) 3204.

[4] S.J. Stranick, M.M. Kamna and P.S. Weiss, Rev. Sci. Instr. **65** (1994) 3211.

[5] D.M. Eigler and E.K. Schweizer, Nature **344** (1990) 524.

[6] J.A. Stroscio and D.M. Eigler, Science **254** (1991) 1319.

[7] D.M. Eigler, C.P. Lutz and W.E. Rudge, Nature **352** (1991) 600.

[8] J. Frohn, J.F. Wolf, K. Besoke and M. Teske, Rev. Sci. Instr. **60** (1989) 1200.

[9] Q. Dai, R. Vollmer, R. Carpick, D.F. Ogletree and M. Salmeron, submitted to Review of Scientific Instruments (1995)

[10] S. Hengrasmee, P.R. Watson, D.C. Frost and K.A.R. Mitchell, Surf. Sci. **92** (1980) 71.

[11] C.J. Baddeley, R.M. Ormerod, A.W. Stephenson and R.M. Lambert, J. Phys. Chem. **99** (1995) 5146.

Chapter 14. CONCLUSIONS & FUTURE WORK

14.1 Summary of Results

The experimental results described in this thesis can generally be divided into two areas: static surface structure and the dynamics of adsorbates on surfaces. The first part of the work can be further subdivided into structural information derived from image symmetry and that derived from comparison with theoretical calculations. While the experiments were performed on two specific chemisorption systems, the techniques and many of the concepts derived from this work is quite general and can be applied to atomic scale STM studies of other surfaces.

14.1.1 Diffusion and Lateral Interactions

Surface diffusion and the lateral interactions were studied on a Re(0001) surface with a low coverage of sulfur which allowed the adsorbate atoms room to move. At low coverage the sulfur forms a $p(2x2)$ ordered overlayer of single atoms indicating that lateral interactions between atoms at this separation are more attractive than at closer and further distances. STM images of this surface showed horizontal dashes in the fast scan direction of the image which were interpreted as diffusing atoms. At room temperature isolated sulfur atoms were present at one site on the surface for approximately the time required to acquire one scan line of an image (~50 ms) before diffusing to a neighboring site.

A pair correlation function was calculated from the images of diffusing sulfur. The resulting correlation images represent statistical information on the relative positions of the adsorbate atoms. The maxima in this image were located on a $p(2x2)$ lattice with respect to the substrate, indicating that the sulfur diffuses as a lattice gas between low energy sites and that an attractive lateral interaction between the sulfur atoms induce a local $p(2x2)$ order of the diffusing atoms.

By comparison of the statistical information derived from the correlation function with an Ising model of the lattice gas system, the attractive interaction between the atoms at a spacing of twice the Re surface lattice distance was found to be 24 meV per pair of atoms. These results were also compared with a more accurate, but less analytical Monte Carlo simulation. The Monte Carlo results indicate that, at the interaction energy derived from the Ising model, the surface was very close to a phase transition between a lattice gas and solid islands, in agreement with the observation of small islands in the images at higher coverage values. Simulated STM images produced with the Monte Carlo technique compare well with the experimental images.

Besides the lateral interactions between equivalent adsorbates, the interactions between different adsorbed species were studied. On Re(0001) CO adsorption was found to induce compression of the sulfur overlayer to that corresponding to a higher local sulfur coverage. This compression, while costing energy due to the repulsion of the sulfur atoms, was favorable because of the adsorption energy gained by CO chemisorption. The existence of this coadsorbate induced compression process has implications on catalytic systems, in which the active metal surface is usually covered with a tightly bound passivating inactive layer. It provides a mechanism by which reactants may adsorb onto and react on a passivated catalyst surface.

A similar mechanism was observed when gold was deposited on the sulfided Mo(100) surface. At a low coverage the sulfur was pushed aside by the gold and compressed into higher density ordered structures. At higher coverage values at which the sulfur could not easily be compressed, the gold formed three dimensional mounds on the surface.

This portion of the work demonstrates the use of STM to study the atomic scale kinetics and thereby the underlying interaction energies of surfaces which are non-static, both between similar and heterogeneous adsorbates.

14.1.2 Image Symmetry and Structure

On the static sulfur covered Mo(100) surface, the crystallography of the ordered structures formed by sulfur was determined by investigating the symmetry of domain boundaries of the sulfur overlayers. Most of the proposed structural models could be excluded because they were incompatible with the observed symmetry.

Sulfur was found to affect the step distribution on the Mo(100) surface. It promoted the grouping and eventual coalescence of steps. These results were interpreted in the framework of the theory of equilibrium crystal shapes.

14.1.3 The Relationship Between Image Contrast and Structure

Electron Scattering Quantum Chemistry (ESQC) theory calculations were compared to experimental STM images. The contrast in STM images of sulfur overlayers on Re(0001) were found to change spontaneously, independent of any experimentally controllable variables. These contrast changes could be explained by the theory as being a result of changes in the precise structure and atomic identity of the STM tip termination. Calculations were made of STM images with sulfur located at four different high symmetry sites on the surface. These experimental images were only consistent with the calculations with sulfur located on the three-fold hollow site, although there was no discernible difference between the hcp and fcc hollow sites. In addition, the images were also only consistent with a small range of sulfur adsorbate height over the Re surface. The height derived from this analysis was consistent with the results of a LEED structural determination.

With the ESQC theory, the mechanisms governing the contrast in STM images were investigated. Unlike the $p(2x2)$ overlayer , the contrast in images of a fictitious $p(4x4)$ overlayer was not found to change drastically with the tip termination. Only the size of the maxima at the position of the sulfur atom varied. Hence, the images of the $p(2x2)$ overlayer were not a simple superposition of four laterally displaced images of the $p(4x4)$ overlayer. The contrast is dependent on the close proximity of the adsorbed

atoms. It was found to be a result of the interference between electrons tunneling from several nearby adsorbate atoms. Within the theory, specific matrix elements between orbitals of the surface and tip could be selectively set to zero. The contribution coming through single atoms was compared to the complete current through several adsorbate atoms including the interference between these channels.

These results indicate that STM images are sensitive to the structure of the surface, opening up the possibility of using STM to determine quantitative structural information such as bond lengths. This was attempted on the $c(2x2)$ ordered sulfur overlayer on Mo(100). The method used is analogous to dynamical LEED structure determination. The results of ESQC calculations for a number of tips and a range of trial surface structures were compared with experimental data. The experimental data was acquired using a new multiple gap technique in which data is acquired at eight exponentially distributed tunneling gap resistance values while preserving information on the registry and z separation of the images. The results of the fit between experiment and theory indicated that the STM tip was terminated with a Pt atom and provided two parameters of the surface structure which matched the results of LEED within 0.1 Ångstroms. Future development of this technique should improve its accuracy. STM will be particularly valuable for determining the structure of defects on surfaces which is inaccessible by other structure sensitive techniques.

14.2 Future Directions

14.2.1 Kinetics of Adsorbate Processes

The application of STM to study lateral interactions between adsorbates on surfaces has great potential for future studies. Due to its real-space nature, STM can determine directly the relative positions of adsorbates on surfaces. Obviously, knowledge of these interactions is crucial for a complete understanding of chemical processes at surfaces. Molecules must come into contact in order to react, and thus their distribution and mobility

on surfaces controls their reaction rate. In addition, this knowledge is necessary for understanding and controlling epitaxial growth, which, besides its fundamental interest, is becoming increasingly important for technological applications. It is well known that the kinetics and interactions of the atoms arriving at the surface control the morphology of the grown structures.

The development of low and variable temperature STM systems, such as the one described in the last chapter, will greatly enhance the ability to study the interaction of adsorbates on surfaces. STM is a slow technique, limited by the speed of mechanical displacement of the tip or resonance modes of the microscope, and cannot be applied to study adsorbates which are diffusing at rates faster than ~ 1 ms per hop. However, by cooling the surface, processes of interest, whether diffusion, decomposition, the merging of an atom with an island, or reaction of two molecules, can be slowed to a rate observable by STM. The diffusing adsorbate image analysis by pair correlation described in chapter 9 can be applied directly to these studies. This method allows the statistics of the relative positions of atoms to be determined on surfaces on which the adsorbates are mobile, and therefore clearly in equilibrium at the current temperature. This allows statistical mechanics to be used to derive the interactions energies from the statistics of the relative positions of the atoms. No other technique can provide such information on a wide range of surface adsorbate systems.

14.2.2 STM Surface Structure Determination

Another area for future study is quantitative structural determination by the combination of STM and theoretical calculations. The results presented in chapter 8 show the potential of this technique. The methods used for theoretical calculations of images are becoming increasingly accurate through the use of *ab-initio* calculations of surface electronic structure. On the experimental side, the low temperature STM will greatly facilitate this work. Imaging at low temperature will decrease thermal drift and tip instabilities allowing more data to be acquired on precisely the same area of the surface.

The development of atom manipulation methods with the STM opens the possibility of directly controlling the tip termination by picking up adsorbates on the surface onto the end of the tip and imaging the surface with them. This eliminates the main unknown factor in the theoretical models, the composition and structure of the tip termination.

Besides continuing these current topics, the low temperature STM system provides new possibilities for future research. Surface phase transitions can be studied as a function of temperature. Chemical reactions and the intermediate species often present in catalysis can be observed one molecule at a time. Atom manipulation can be used to produce new structures on the surface, and their chemical and electronic properties studied. The higher resolution of tunneling spectroscopy at low temperatures facilitates the study of quantized energy states in confined electron systems such as semiconductor clusters.

While the scanning tunneling microscopy technique has now existed for more than ten years, there is still much valuable research to be done even in the subfield of surface/adsorbate systems. The variable temperature STM system provides unique opportunities for studying many surface processes at the most fundamental level.